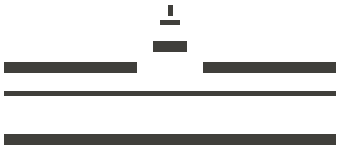

Westfälische
Wilhelms-Universität
Münster

Precision Calculations for Coloured Supersymmetric Particle Production at the Large Hadron Collider

Christoph Julian Borschensky

29 March 2016

Theoretische Physik

Precision Calculations for Coloured Supersymmetric Particle Production at the Large Hadron Collider

Inaugural-Dissertation
zur Erlangung des Doktorgrades
der Naturwissenschaften im Fachbereich Physik
der Mathematisch-Naturwissenschaftlichen Fakultät
der Westfälischen Wilhelms-Universität Münster

vorgelegt von
Christoph Julian Borschensky
aus Offenburg
- 2016 -

Dekan:	Prof. Dr. Christian Weinheimer
Erste Gutachterin:	Jun. Prof. Dr. Anna Kulesza
Zweiter Gutachter:	Prof. Dr. Michael Klasen
Tag der mündlichen Prüfung:	.....
Tag der Promotion:	.....

Abstract

The search for supersymmetry is one of the main quests of the Large Hadron Collider. There, coloured supersymmetric particles, the squarks and gluinos, are expected to be produced dominantly. As long as no supersymmetry is found, the current mass limits set by the ATLAS and CMS experiments require the squarks and gluinos to be heavy. Consequently, they will always be produced close to threshold. Near this threshold, higher-order logarithms that stem from the emission of soft gluons become large and endanger the validity of perturbation theory. A systematic treatment of these terms up to all orders in the strong coupling is given by means of threshold resummation. Further threshold-enhanced contributions for heavy final-state particles originate from Coulomb gluon exchange, even forming bound states in the case of an attractive Coulomb interaction.

In this thesis, a variety of threshold-improved predictions for squark and gluino production is presented. We find that future colliders will be able to probe squark and gluino masses towards and even beyond 10 TeV. While theshold-improved parton distribution functions can change the behaviour of the cross sections noticeably, we see that the deviations are always within the uncertainties of conventional fixed-order sets. Contributions at NNLL lead to an enhancement of the cross section for all squark and gluino production processes, with the biggest effect for gluinos due to large colour factors. We also observe a reduction in scale dependence with the exception of gluino-pair production. In the case of stops, we even see an increased dependence on additional stop mixing parameters due to the hard-matching coefficients. While additional contributions from Coulomb resummation are small compared to the two-loop Coulomb terms, bound states lead to an enhancement of a few percent for gluino-pair and squark-antisquark production processes. At last, we discuss double parton scattering for J/ψ-pair production which is of importance for estimating the background of Standard Model processes. We find double parton scattering to be of similar size as single scattering at collider energies of 7 and 8 TeV, while for 13 TeV, the former will be larger than the latter by almost a factor of two.

Zusammenfassung

Die Suche nach Supersymmetrie ist eine der Hauptaufgaben des Large Hadron Collider. Dort wird erwartet, dass farbgeladene supersymmetrische Teilchen, die Squarks und Gluinos, vorranging produziert werden. Solange Supersymmetrie nicht gefunden wird, fordern die aktuellen Massenlimits der ATLAS- und CMS-Experimente von den Squarks und Gluinos, dass sie schwer sind. Daher findet ihre Produktion ständig in der Nähe der Produktionsschwelle statt. Nahe dieser Schwelle werden logarithmische Terme, welche von der Abstrahlung weicher Gluonen herrühren, groß und gefährden die Aussagekraft der Störungstheorie. Eine systematische Behandlung dieser Terme bis zu allen Ordnungen in der starken Kopplung ist durch Schwellenresummation gegeben. Weitere Beiträge, die nahe der Produktionsschwelle verstärkt sind, stammen vom Austausch der Coulomb-Gluonen zwischen schweren Endzustandsteilchen, welche außerdem zur Bildung von gebundenen Zuständen führen.

In dieser Doktorarbeit wird eine Auswahl an Vorhersagen, die Verbesserungen durch Schwelleneffekte enthalten, für die Produktion von Squarks und Gluinos vorgestellt. Wir finden, dass zukünftige Teilchenbeschleuniger in der Lage sein werden, Squarks und Gluinos mit einer Masse um oder sogar über 10 TeV zu erforschen. Während Partonverteilungsfunktionen mit Schwelleneffekten eine merkbare Veränderung in den Wirkungsquerschnitten hervorrufen, sehen wir, dass die Unterschiede zu den konventionellen Sets immer innerhalb der PDF-Unsicherheiten liegen. Beiträge ab NNLL führen zu einer Vergrößerung der Wirkungsquerschnitte für alle Squark- und Gluino-Produktionsprozesse, wobei der größte Effekt für Gluinos auftritt aufgrund der großen Farbfaktoren. Wir beobachten weiterhin eine Verringerung der Skalenabhängigkeit mit Ausnahme von Gluino-Paarproduktion. Für die Produktion von Stops erhalten wir außerdem eine stärkere Abhängigkeit von den zusätzlichen Stop-Mischungsparametern aufgrund der Korrektur durch die Koeffizienten des harten Prozesses. Während zusätzliche Beiträge durch die Resummation von Coulomb-Gluonen gegenüber den Coulomb-Termen auf Zwei-Schleifen-Niveau klein sind, führen Effekte von Bindungszuständen zu Korrekturen von ein paar Prozent für Gluino-Paar- und Squark-Antisquark-Produktion. Schließlich diskutieren wir Doppelpartonstreuung für die Paarproduktion von J/ψ-Mesonen, was von Bedeutung für Berechnungen des Untergrunds von Standardmodell-Prozessen ist. Wir erhalten, dass bei Beschleunigerenergien von 7 und 8 TeV Doppelpartonstreuung vergleichbar ist mit normaler Einfachstreuung, während bei 13 TeV erstere um fast einen Faktor zwei größer ist.

Contents

1 Introduction **1**

2 The Standard Model and QCD **5**
2.1 Particle content and interactions 5
2.2 QCD and collider physics 6
2.2.1 Running coupling 7
2.2.2 Factorisation 8
2.2.3 Parton distribution functions 10

3 Supersymmetry **11**
3.1 The need for an extension 11
3.2 Supersymmetry transformations 15
3.3 The Minimal Supersymmetric Standard Model 16
3.3.1 Supersymmetry breaking 16
3.3.2 Constraining the parameter space 17
3.3.3 Particle content 18
3.3.4 Mass diagonalisation 19
3.4 Production of SUSY particles at the LHC 20
3.4.1 Progress in theoretical predictions for electroweak sparticle production 22
3.4.2 Progress in theoretical predictions for coloured sparticle production . 22

4 Threshold Resummation **25**
4.1 Infrared divergences 26
4.1.1 Drell-Yan up to next-to-leading order 28
4.1.2 Potentially large logarithms and the threshold 32
4.1.3 Eikonal approximation 34
4.1.4 Mellin-moment space 37
4.1.5 Factorisation of the phase space 37
4.2 Factorisation and Resummation 39
4.2.1 Refactorisation near threshold 40
4.2.2 Renormalisation group approach to resummation 42

4.3 Soft-gluon resummation for massive coloured final-state particles 46
4.3.1 Colour structures of QCD scattering processes 46
4.3.2 The soft anomalous dimension matrix 47
4.3.3 All-order expressions for the hadronic cross section 49
4.4 Absolute threshold 54
4.5 Coulomb resummation 56
4.5.1 Derivation of all-order Coulomb corrections from $e^+e^- \to t\bar{t}$ production 56
4.5.2 All-order expressions for Coulomb contributions to a general case . . 61
4.5.3 Bound states 64
4.6 Physical predictions and the "Minimal Prescription" 64
4.7 Implementation of the PDFs 67
4.7.1 The "derivative method" 68
4.8 Matching to a fixed-order calculation 69

5 NLL Threshold Resummation for Future Colliders 71
5.1 Ingredients for NLL resummation 71
5.1.1 Colour decomposition 72
5.2 Predictions for future colliders 75
5.2.1 Total cross sections for all processes of squark and gluino production . 75
5.2.2 Special cases of squark and gluino production 75
5.2.2.1 Gluino-pair production with decoupled squarks 76
5.2.2.2 Squark production with decoupled gluinos 76
5.2.2.3 Stop-antistop production 79

6 NLL Threshold Resummation with Threshold-Improved PDF Sets 81
6.1 NNPDF2.3 analysis 82
6.2 NLO+NLL cross section predictions at 13 TeV with NNPDF3.0 83
6.3 NLO+NLL cross sections with threshold-improved NNPDF3.0 sets 88
6.3.1 The necessity for a prescription 91

7 NNLL Threshold Resummation for Squarks and Gluinos 95
7.1 Ingredients for NNLL resummation 95
7.1.1 Hard-matching coefficients 96
7.1.2 Coulomb contributions 96
7.1.3 Approximated NNLO 98
7.2 Treatment of p-wave channels 98
7.3 Numerical results at $\sqrt{S} = 8$ TeV 99
7.3.1 Analysis of the scale dependence of gluino-pair production 104

8 NNLL Threshold Resummation for Stops 111
8.1 Initial-state contributions to stop-antistop production 112
8.2 Extraction of the hard-matching coefficient 113
8.3 Numerical results for stop-antistop production at $\sqrt{S} = 8, 13$ TeV 116
8.3.1 Threshold behaviour of the partonic cross section 117

8.3.2 Predictions for stop-antistop production at the LHC . . . 119
8.3.3 Comparison to squark-antisquark production . . . 124
8.3.4 Comparison to SCET results . . . 126
8.3.5 Subleading terms in $\text{NNLO}_{\text{Approx}}$ . . . 128
8.3.6 Estimating the p-wave contributions at higher logarithmic accuracies . 129

9 Coulomb Resummation and Bound-State Contributions 131
9.1 Implementation of Coulomb resummation into the framework in Mellin-moment space . . . 132
9.2 Implementation of bound-state contributions . . . 132
9.3 Choice of the scale . . . 134
9.4 Numerical results and comparison to SCET . . . 135

10 Double Parton Scattering for J/ψ-Pair Production 143
10.1 Theoretical setup . . . 144
10.1.1 Factorisation approach for double parton scattering . . . 144
10.2 Monte Carlo simulation . . . 145
10.2.1 LHCb cuts . . . 146
10.2.2 ATLAS cuts . . . 146
10.3 Cross sections and kinematic distributions . . . 147
10.3.1 LHCb predictions . . . 148
10.3.1.1 Predictions at 13 TeV . . . 150
10.3.2 ATLAS predictions . . . 151
10.3.2.1 Predictions at 13 TeV . . . 152
10.3.3 Comparison to CMS measurement . . . 153
10.3.4 Comparison to Lansberg et al. . . . 154

11 Conclusions 159

A Full scale dependence of the resummed expressions 163

B Evaluation of the integrals in the exponentiated expressions 165

C Resummed exponential functions up to NNLL 169

Bibliography 173

1 Introduction

The foundation of physics lies in the description of nature in terms of a mathematical model. In order to achieve this, it is necessary to zoom into the microscopic world which is governed by the laws of quantum mechanics. In this world, the elementary particles reside which form the matter, consisting of fermions, and constitute the interactions, mediated by bosons, between matter particles. A very successful model that describes the elementary particles which were observed so far is the Standard Model of particle physics. Its predictions have been tested experimentally over many years and at an exceptionally high accuracy with a very good agreement between theory and experiment. The discovery of the Higgs boson in 2012 resulted in one of the last missing puzzle pieces being found, leading to a consistent picture of the observable universe.

Despite the success of the Standard Model, there are strong indications that the picture is not complete, and that there is additional content beyond its borders. The question of a quantum field theoretic description of gravitation, dark matter, the origin of the matter-antimatter asymmetry in the universe, neutrino masses – all these are examples of issues that the Standard Model cannot tackle. Out of the wide range of models describing physics beyond the Standard Model, the famous theory of supersymmetry extends the fundamental symmetry between representations of the Poincaré group. Due to its relation to space-time symmetries and its additional particle content, it is capable of offering explanations for some of the open questions such as dark matter. Albeit being thoroughly tested, no indications for supersymmetry have been found so far. Nevertheless, the large parameter space of supersymmetry makes it possible that its proof lies in a region where experiments have not yet looked into. Therefore, theoretical predictions are required at high precision to point experimental searches into the direction where supersymmetry may hide.

Big particle colliders such as the Large Hadron Collider (LHC) have been built to produce particles at high energies. They open a window to the time right after the Big Bang where all different kinds of particles might have existed and all fundamental forces might have been of the same strength. They are the only possibility next to astrophysical processes to create and observe very heavy particles directly. Hadron colliders such as the LHC accelerate

and collide protons and are therefore strongly affected by the strong interaction, which is described on the theoretical side by quantum chromodynamics (QCD). Contrary to e.g. the electromagnetic interaction, the strength of the strong interaction increases with decreasing collision energies, and decreases for increasing energies. This has a few interesting effects such as confinement and asymptotic freedom, causing the constituents of the strong interaction, quarks and gluons, on one hand not to be detectable by themselves, but only as colour-neutral objects such as baryons and mesons which show up as jets in detectors, and on the other hand behaving like quasi-free particles in high-energy collisions.

Theoretical calculations rely on the applicability of perturbation theory. The scattering matrix of a process is expanded in the coupling strength of the fundamental interactions and, assuming small enough couplings, might be described well by calculations up to a certain fixed order in the coupling. They are translated into cross sections which denote the probability for a process to occur in a collision experiment. In particular, when particles carrying colour charge are involved, QCD interactions lead to large contributions to the cross sections and need to be known to high orders in the coupling. When analysing the production of two particles, the region close to the production threshold of the particles, i.e. when there is just enough energy available for the creation of their rest mass, often is the main contribution to the total cross section. A precise theoretical description requires all processes with the same final-state particles to be taken into account. These involve higher-order loop calculations as well as the emission of extra particles which show up as jets. Close to the production threshold, the extra emission of gluons is forced to be soft. This means that the emission of an arbitrary number of extra particles needs to be included in the theoretical predictions for inclusive cross sections, as their contributions become large despite a suppression of higher orders in the strong coupling. The reason for this are large logarithmic terms which occur in this extreme kinematical limit, spoiling the validity of perturbation theory. A systematic treatment of these logarithms up to all orders is given by means of threshold resummation. It relies on the factorisation of these extra emissions from the underlying hard scattering process. Additional contributions which are enhanced near threshold stem from the exchange of Coulomb gluons between heavy final-state particles. A framework has also been developed to take these contributions into account at all orders. A consequence of the Coulomb interaction is the formation of bound states below threshold in the case of an attractive force.

One of the main goals of the LHC is the search for supersymmetry. The main processes of supersymmetric particle production involve the partners of the quarks and gluons, the squarks and gluinos, in the final state due to their colour charge. As no supersymmetric particles have been found so far, the mass limits for the coloured sparticles have grown above 1 TeV, requiring them to be heavy. This means that they are practically always produced near threshold, making the inclusion of threshold resummation effects and Coulomb contributions a necessity in order to properly predict their cross sections.

Besides a precise description of the production process, also a good description of the background originating from Standard Model particles and leading to similar signatures in the detectors as new physics processes is necessary to increase the possibility to find signals of new particles. In particular, multi-parton interactions cause multiple independent

scattering processes in the same proton-proton collision to occur, and they become more relevant at higher LHC energies.

Thus, the goal of this thesis is to improve the current theoretical calculations for coloured supersymmetric particle production by taking into account threshold resummation effects from soft gluons at higher accuracies and combine them with contributions from Coulomb gluon exchange and bound-state formation. Additionally, the effect of double parton scattering for the production of J/ψ pairs is analysed, which will lead to an improved treatment of background estimates for the Standard Model and Beyond the Standard Model processes. The structure of the thesis is as follows: Chapter 2 briefly introduces the Standard Model and mainly discusses several properties of QCD which build the foundation of the theoretical description of collider processes. Afterwards, supersymmetry will be introduced in chapter 3. A thorough discussion on the emergence of threshold-enhanced contributions, starting from the structure of infrared divergencies and deriving the well-established equations for soft-gluon and Coulomb resummation, will be performed in chapter 4. A first application of the threshold resummation formalism will be done in chapter 5, where current predictions of squark and gluino production will be updated for future collider experiments. Chapter 6 discusses the inclusion of threshold-improved predictions in fits for parton distribution functions and its consequences for squark and gluino production. The focus will then be put on an improvement of the logarithmic accuracy, first for squarks and gluinos in chapter 7, and then separately for stops as the third-generation squarks in chapter 8. Chapter 9 will formulate the combined resummation of soft-gluon and Coulomb effects with bound-state formation below threshold and analyse the impact of it on squark and gluino production. The evaluation of double parton scattering effects for J/ψ production will be done in chapter 10, followed by the conclusions in chapter 11.

2 The Standard Model and QCD

Various models exist that attempt to explain all of the observations made so far in different experiments and even propose yet unseen effects. The best studied model is the Standard Model (SM), consisting of the electroweak model of Glashow, Weinberg, and Salam [1–4], unifying quantum electrodynamics (QED) and the weak interaction, quantum chromodynamics (QCD) as the theory describing the strong interaction [5–7], as well as the Higgs sector [8–10] with the postulated Higgs boson having been found in 2012 by the ATLAS and CMS experiments at the LHC [11, 12]. Since the completion of the Standard Model in the 1970s, it was shown to be very consistent with the results from experiments made at particle colliders, and most of its free parameters have been measured to an extremely high precision.

After a short introduction on the Standard Model, the emphasis will be put on the application of QCD to collider physics, as the main interest of this thesis is the study of the strong interactions at hadronic colliders in extreme kinematical regions.

2.1 Particle content and interactions

The Standard Model of particle physics consists of 12 fermionic spin-½ and 12 bosonic spin-1 particles, the former describing the matter content of the universe, and the latter describing their interactions: the strong, electromagnetic, and weak interactions. Additionally, a scalar spin-0 particle, the Higgs boson, is added as the remainder of the Higgs mechanism to render fermions and the bosons of the weak interaction massive.

The fermions are split up into quarks (up u, down d, charm c, strange s, top t, bottom b), interacting strongly and electroweakly, and leptons (electron e, electron-neutrino ν_e, muon μ, muon-neutrino ν_μ, tau τ, tau-neutrino ν_τ), only interacting electroweakly. Quarks and leptons can be grouped together into three generations according to their weak interaction states:

$$\begin{pmatrix} u \\ d \end{pmatrix}, \begin{pmatrix} c \\ s \end{pmatrix}, \begin{pmatrix} t \\ b \end{pmatrix} \quad \text{and} \quad \begin{pmatrix} \nu_e \\ e \end{pmatrix}, \begin{pmatrix} \nu_\mu \\ \mu \end{pmatrix}, \begin{pmatrix} \nu_\tau \\ \tau \end{pmatrix}.$$

The spin-1 bosons mediating the interactions between the matter particles consist of 8 gluons g (strong), the photon γ (electromagnetic), and the Z^0 and W^+ and W^- bosons (weak). The gravitational interaction is not included in the Standard Model.

The gauge group describing the interactions mathematically is given as the direct product of the following Lie groups:

$$\mathrm{SU}(3)_C \times \mathrm{SU}(2)_L \times \mathrm{U}(1)_Y \tag{2.1}$$

with the labels C denoting colour, L denoting the left-handedness of the weak interaction, and Y denoting hypercharge. The quantum numbers defining a certain representation of a quantum mechanical state in this gauge group are colour charge, weak isospin, and hypercharge. After electroweak symmetry breaking, weak isospin and hypercharge combine to a new conserved quantity, the electric charge, via the Gell-Mann-Nishijima formula [13, 14]. The crucial ingredients denoting the strengths of the different interactions are the coupling of the electroweak interaction α, which coincides with the fine-structure constant $\alpha_0 \approx 1/137$ at a low scale, and the coupling of the strong interaction α_s. In general, these couplings are not constant in theoretical calculations due to the application of perturbation theory and the truncation of the series up to a certain order, and will depend on the energy scale of a collision process. For high-energy collisions at the LHC with typical scales above 1 GeV up to a few TeV, both couplings are in the perturbative range with α and α_s being $\mathcal{O}(10^{-2})$ and $\mathcal{O}(10^{-1})$ in size, respectively.

The quantum-field-theoretic basis for being able to make theoretical predictions for scattering processes of two particles is the applicability of perturbation theory. The requirement for a perturbative treatment is the smallness of the expansion parameter which is the interaction strength, making it possible to write an observable such as a cross section in the following way:

$$\sigma = \sigma^{(0)} + \frac{\alpha_\mathrm{s}}{\pi}\sigma^{(1)} + \left(\frac{\alpha_\mathrm{s}}{\pi}\right)^2 \sigma^{(2)} + \ldots \tag{2.2}$$

with the first term $\sigma^{(0)}$ being called the leading order (LO) result, $\sigma^{(1)}$ the next-to-leading order (NLO) result, $\sigma^{(2)}$ the next-to-next-to-leading order (NNLO) result, and so on. In this thesis, perturbation theory is always implied to be carried out as a series in α_s, unless specified otherwise.

2.2 QCD and collider physics

Quantum chromodynamics is the fundamental theory of the strong interaction. It plays an important role in the understanding of collision processes at hadron colliders, such as the LHC, as the dominant production channels will proceed through the exchange of gluons, the gauge bosons of the strong interaction. The description through a non-abelian SU(N_c) group, where $N_c = 3$ denotes the number of colours, leads to a multitude of interesting effects such as the possibility for a self-coupling of the gluons, which is not present for abelian theories such as QED. While quarks transform according to the fundamental representation

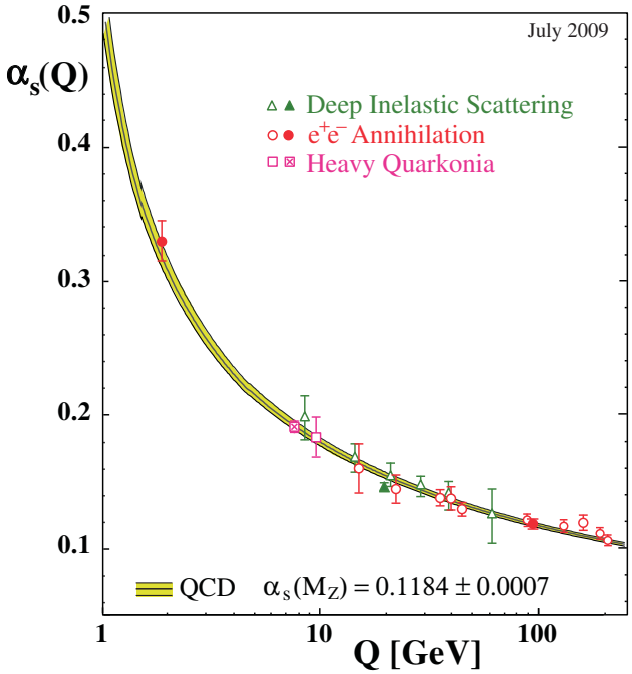

Figure 2.1: Running of the strong coupling constant α_s with the scale Q. Shown is the theoretical prediction as well as experimentally measured values at different scales. Plot taken from ref. [15].

of SU(N_c), gluons live in the adjoint representation. This means that both quarks and gluons carry a *colour charge*, in analogy to the electric charge with the difference that there are three colours and the corresponding anti-colours.

Experimentally, it has not been possible to isolate a single quark or gluon and measure its colour charge, but only complex bound states, the *hadrons*, of two (mesons) or three (baryons) quarks and antiquarks (and sometimes even exotic cases with more than three quarks) which always appear as colour-neutral. Contrary to the electromagnetic and the gravitational forces, which decrease in strength with increasing distance, the strong force increases with increasing distance, requiring a lot of energy to isolate a single quark or gluon, and in reality causing a new colour-neutral quark-antiquark pair to be formed if the distance becomes large enough. On the other hand, observations show that at high energies, it is possible to dissolve the inner structure of hadrons through *deep inelastic scattering* experiments, where photons scatter off quasi-free quarks inside a hadron. Both effects are strongly related to the *running coupling* which will be discussed in the following section.

2.2.1 Running coupling

The strong coupling parameter α_s is defined in terms of the coupling g_s which appears as the strength of the interaction between a quark, an antiquark, and a gluon in the QCD Lagrangian:

$$\alpha_s(\mu_R) = \frac{g_s(\mu_R)^2}{4\pi}. \tag{2.3}$$

Due to the necessity of renormalisation at higher orders of α_s in perturbation theory, the unphysical *renormalisation scale* μ_R is introduced, causing the renormalised coupling to depend on it. The *renormalisation group equation* for the running coupling is given by:

$$\mu_R^2 \frac{\mathrm{d}\alpha_s}{\mathrm{d}\mu_R^2} = \beta(\alpha_s) = -b_0\,\alpha_s^2 - b_1\,\alpha_s^3 - b_2\,\alpha_s^4 + \mathcal{O}(\alpha_s^5) \tag{2.4}$$

with the beta function of QCD $\beta(\alpha_s)$, written as a perturbative series in α_s with coefficients $b_0, b_1, b_2, \ldots$. The latter are in general dependent on the structure of the gauge group and the contributing particles in loop corrections. Up to three loops, the coefficients are [16]:

$$b_0 = \frac{11\,C_A - 4 n_f\,T_R}{12\pi}, \tag{2.5}$$

$$b_1 = \frac{17\,C_A^2 - n_f\,T_R\,(10\,C_A + 6\,C_F)}{24\pi^2}, \tag{2.6}$$

$$b_2 = \frac{1}{64\pi^3}\left[\frac{2857}{54}C_A^3 - \frac{1415}{54}C_A^2\,n_f - \frac{205}{18}C_A\,C_F\,n_f + C_F^2\,n_f + \frac{n_f^2}{9}\left(\frac{79}{6}C_A + 11\,C_F\right)\right] \tag{2.7}$$

with n_f the number of light quark flavours, usually to be taken to $n_f = 5$, and the SU(N_c) colour factors and quadratic Casimir invariants

$$C_F = \frac{N_c^2 - 1}{2N_c}, \quad C_A = N_c, \quad T_R = \frac{1}{2}. \tag{2.8}$$

The differential equation (2.4) can be solved, here given up to two-loop order:

$$\alpha_s(\mu_R) = \frac{\alpha_s(\mu_0)}{1 + b_0\,\alpha_s(\mu_0)\ln\left(\frac{\mu_R^2}{\mu_0^2}\right)}\left[1 - \frac{\alpha_s(\mu_0)}{4\pi}\frac{b_1 \ln\left(1 + b_0\,\alpha_s(\mu_0)\ln\left(\frac{\mu_R^2}{\mu_0^2}\right)\right)}{b_0\left(1 + b_0\,\alpha_s(\mu_0)\ln\left(\frac{\mu_R^2}{\mu_0^2}\right)\right)} + \ldots\right], \tag{2.9}$$

where μ_0 is a reference scale at which the value of α_s has to be known, the latter usually being determined experimentally. A feature of QCD with three colours and five light flavours is now that b_0 is positive. This leads to a leading behaviour of α_s increasing at lower scales, and decreasing at higher scales, see figure 2.1. The decrease of α_s at high energies is called *asymptotic freedom*, as the coupling strength of the strong interaction becomes so weak that the quarks behave like quasi-free particles. Furthermore, a small coupling enables perturbation theory to be carried out. On the other hand, the rise of α_s at low scales (and in fact a divergence, the *Landau pole*, at a certain energy called the QCD scale Λ_{QCD}) constitutes the non-perturbative domain of *confinement*.

2.2.2 Factorisation

One of the properties mentioned in the previous section is confinement, i.e. the formation of hadronic bound states which cannot be described perturbatively due to α_s becoming

large. However, at hadronic colliders such as the LHC where beams of protons are shot at each other, confinement becomes a problem as it is not possible to theoretically describe the structure of the proton with the known perturbative methods. At high collision energies or momentum exchange, this issue can be circumvented due to asymptotic freedom which allows for a description of the collision process as two partons (quarks, gluons) inside the protons scattering. The hadronic cross section can then be understood as the product of a partonic cross section describing the partonic scattering process, and another function for each proton describing its internal structure, the so-called *parton distribution functions* (PDFs). This split-up into short- and long-distance functions is called *factorisation* and one of the fundamental properties which enables theoretical predictions to be made for hadronic collisions. At leading order in the coupling, the PDFs can be regarded as the probability that a parton with a certain flavour and a specific fraction of the momentum is extracted from the full proton.

A physical interpretation of this separation relies on the different time scales involved in the scattering process [17]: in the centre-of-mass frame, the two hadrons are Lorentz-contracted with respect to each other, meaning that a parton will travel through the hadron in a shorter time frame compared to any interactions within the hadron. Furthermore, the internal interactions are affected by time dilation and can therefore be regarded as frozen in time with respect to a high-energy parton travelling through the hadron. As a result, the point in time when the internal interactions become relevant will be long past the scattering of two partons from each hadron.

At higher orders in perturbation theory, the PDFs lose their probabilistic interpretation and a factorisation procedure has to be carried out, as the occurrence of collinear singularities in the partonic cross section (see section 4.1.1) spoil the predictive nature. The singularities are then absorbed into a redefinition of the PDFs. As a result, a *factorisation scale* μ_F is introduced. Schematically, this redefinition of the PDFs within the factorisation procedure can be written as:

$$\begin{aligned}\sigma_{\text{hadr}} &= \sum_{\text{partons i,j}} \hat{f}_i \otimes \hat{C}_i(\mu_F) \otimes \hat{f}_j \otimes \hat{C}_j(\mu_F) \otimes \hat{\sigma}_{ij}(\mu_F) \\ &= \sum_{\text{partons i,j}} f_i(\mu_F) \otimes f_j(\mu_F) \otimes \hat{\sigma}_{ij}(\mu_F), \end{aligned} \tag{2.10}$$

where i, j are the flavours of the partons, $\hat{f}$ denote the bare PDFs, $f(\mu_F)$ denote the factorised PDFs depending on the factorisation scale, $\hat{C}_{i,j}(\mu_F)$ are the collinear singularities for each parton, and $\hat{\sigma}_{ij}(\mu_F)$ is the partonic cross section with the collinear subtraction having been carried out. The operator $\otimes$ stands for a convolution, as both the PDFs as well as the partonic cross section depend on the momentum fractions of the full proton momenta that the partons carry and these momentum fractions are integrated over. This split-up is only valid when it is possible to neglect power corrections that are suppressed due to high momentum exchange. There is an ambiguity in the sense that also finite terms can be absorbed in $\hat{C}_{i,j}(\mu_F)$ [18]. The specific choice of these finite terms fixes the factorisation scheme of the PDFs, where usually the $\overline{\text{MS}}$ scheme is chosen. The application of the factorisation theorem will be described

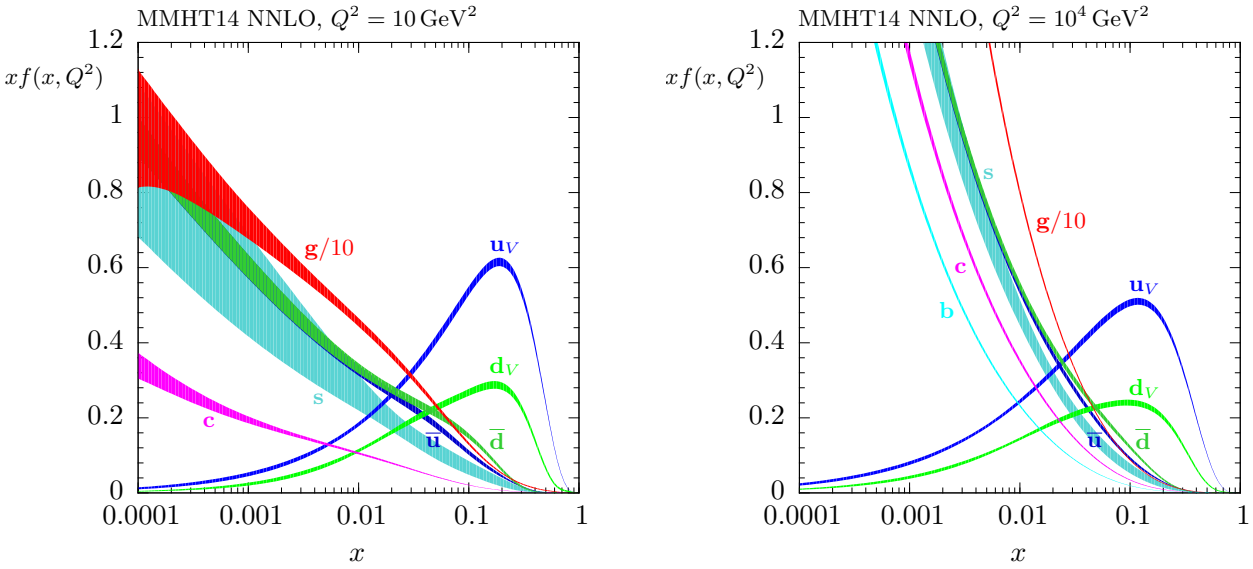

Figure 2.2: Parton distribution functions at NNLO accuracy of the MMHT collaboration. On the left side, the behaviour of several flavours is shown for a factorisation scale of 10 GeV, while on the right side, the scale is chosen to be 1 TeV. Plots taken from ref. [19].

more rigorously in chapter 4.

2.2.3 Parton distribution functions

Parton distribution functions are universial functions that only depend on the incoming hadrons of a collision process, and not on the inner details of the actual process. Therefore, they can be determined experimentally from well known and clean (in the sense of having a clear signal in experiments) processes such as deep inelastic scattering and Drell-Yan, and then be applied to a multitude of other processes. Commonly, the shape of the PDFs are given through a fit to a theoretical model, although also other methods exist which offer a completely unbiased way of describing the PDFs. The three biggest groups providing the PDFs for a proton are the MMHT [19] (formerly MSTW [20]), CTEQ [21], and NNPDF collaborations [22]. In figure 2.2, the MMHT14 NNLO PDFs [19] are shown for different parton flavours at two values of the factorisation scale with the x-axis denoting the momentum fraction x of the full proton momentum which the parton carries. A prescription how to best combine theoretical results obtained from calculations with the different PDF sets and provide these predictions to the experimental community is given by the PDF4LHC working group [23]. The recommendations have recently been updated and the PDF4LHC group provides a special PDF set created as a combination of the the MMHT, CTEQ, and NNPDF PDF sets.

3 Supersymmetry

While the Standard Model sufficiently describes the observed particles and their interactions, there is reason to believe that it does not cover the full matter content of the universe, e.g. from cosmological observations, the need for so-called dark matter arises, which cannot be described by the Standard Model. Furthermore, the Standard Model is not a "theory of everything" in the sense that it does not incorporate the gravitational interaction. These and other problems make it necessary to extend the Standard Model. There are several ways to achieve this, e.g. by adding new interactions and particles or by changing the structure of space-time. One possible extension is supersymmetry (SUSY). Albeit not being a "theory of everything" either, the step towards a grand unified theory (GUT) is made easier by the realisation of gauge coupling unification at some high energy scale, and the very nature of supersymmetry being related to space-time transformations. The first attempt at writing an explicitely supersymmetric Lagrangian was in 1974, when Julius Wess and Bruno Zumino formulated their model consisting of a fermion and a complex scalar field [24]. Since then, a lot of work has been done and many extensions of the Standard Model in a supersymmetric context have been developed.

After a short discussion on why the Standard Model needs to be extended, supersymmetry as one of the most widely studied new physics models will be presented. The additional particle content of the minimal realisation of supersymmetry in the framework of the Standard Model is shown, followed by a short summary of the status of current experimental searches for supersymmetric particles as well as the theoretical status of cross section calculations. The introductory part mainly follows refs. [25, 26].

3.1 The need for an extension

Although the Standard Model has been very successful so far, it is incomplete in the sense that both on the theoretical as well as the experimental side, there are strong indications for a theory beyond the Standard Model which can fill its gaps and solve its problems. It is therefore assumed to be an *effective theory* only valid in a certain energy range with new

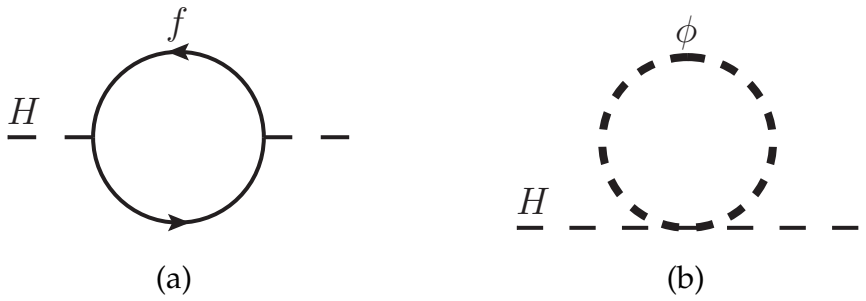

Figure 3.1: Radiative corrections to the Higgs boson mass from fermion loops (a) and scalar loops (b).

effects becoming important at least at the Planck scale $M_P \sim 10^{19}$ GeV or maybe even earlier, at lower scales. The following list presents some of the issues present in the Standard Model and how they can be solved by supersymmetry, the theory presented in this chapter:

- A general problem of quantum field theories with scalar particles is the occurrence of quadratic divergencies in loop diagrams, leading to the **hierarchy problem** [27–31]. This affects the Higgs field as the only scalar present in the Standard Model. It leads to *unnaturally large* fine-tuning of the Higgs mass which receives quantum corrections proportional to the square of a cut-off scale Λ_{UV} regulating the diverging loop integral. In particular, any fermion loop as depicted in figure 3.1 (a) leads to radiative corrections to the Higgs mass of the following type:

$$\Delta m_H^2 = -\frac{y_f^2}{8\pi^2}\Lambda_{\text{UV}}^2 + \dots , \tag{3.1}$$

  where y_f is the Yukawa coupling of a fermion-antifermion-Higgs interaction. Formally, these quadratic divergences can be dealt with by renormalising the Higgs mass and introducing the corresponding counter-terms in the Lagrangian. A very unnatural fine-tuning of these counter-terms would however be required at every loop order to keep the Higgs mass at its present value of 125 GeV.

  Additionally, terms that are proportional to the quadratic mass of the particle in the loop occur in the Higgs mass corrections. Assuming that a heavy scalar particle S which couples to the Higgs boson is added to the Standard Model, it would cause a loop contribution to the Higgs mass as shown in figure 3.1 (b), which gives:

$$\Delta m_H^2 = \frac{\lambda_S}{16\pi^2}\left[\Lambda_{\text{UV}}^2 - 2m_S^2 \ln\left(\frac{\Lambda_{\text{UV}}}{m_S}\right) + \dots\right], \tag{3.2}$$

  where λ_S denotes the coupling of the scalar S to the Higgs boson. Even in a different regularisation scheme (such as dimensional regularisation) where no cut-off scale is present, the term proportional to m_S^2 leads to the Higgs mass being sensitive to the mass of S, or in fact every mass, so in particular the largest mass in the theory.

  It does not seem too far-fetched to propose the addition of two complex scalar fields for every fermion field (to match the same number of degrees of freedom) with $\lambda_S = y_f^2$.

Due to the different sign in eqs. (3.1) and (3.2), the quadratic divergences would then cancel exactly, and only a logarithmic divergence proportional to the difference of the squared masses between the fermion and the scalar would remain. Assuming these two masses to be equal, or at least none of them being much bigger than $\mathcal{O}(1\text{ TeV})$, the Higgs mass would not receive any large radiative contributions, so no extreme fine-tuning would be needed to keep it at the magnitude of the electroweak scale. In fact, supersymmetry was originally proposed to solve the hierarchy problem due to its increased particle spectrum and symmetry between bosons and fermions.

- Cosmological observations require a certain type of gravitationally interacting matter, so-called **dark matter**. It is responsible for the formation of large-scale clusters as seen in galaxies and systems of galaxies in the universe. The amount of luminous, that is strongly and electromagnetically interacting matter does not suffice to account for these structures. Analyses of the *cosmic microwave background* from the COBE [32], WMAP [33–37], and Planck satellites [38–43] revealed an amount of roughly 27% of dark matter to be present, which, however, has not been directly observed yet. Coincidentally, weakly interacting massive particles (WIMPs) seem to describe today's amount of dark matter well enough. The neutrinos as the only purely weakly interacting particles of the Standard Model are not massive enough and only might make up *hot dark matter*, which is moving at relativistic speeds, whereas more non-relativistic *cold dark matter* is needed for the structure formation to have taken place at a very early age of the universe. Under certain conditions, supersymmetry can provide such a candidate for cold dark matter which is stable and fulfils the requirements of being a WIMP.

- A mathematical treatment of the **gravitational interaction** on a quantum level is difficult, as quantum gravity is non-renormalisable and the known methods of quantum field theory lack a way to deal with gravity. String theories as an active research area to unify the gauge interactions and also include quantum gravity in fact require supersymmetry to be consistent. Furthermore, supersymmetry by itself causes gravitational interactions to appear when it is considered to be a local (i.e. dependent on space-time coordinates) instead of a global symmetry.

- Following the unification of the electromagnetic and weak interactions to the electroweak model by Glashow, Weinberg, and Salam, a remaining unification with the strong interactions would lead to a **Grand Unified Theory** (GUT), with only one gauge force present at high enough energies, described by e.g. SU(5). The running coupling of all the three interactions suggest that they do not meet in a single point. Due to the increase particle content of supersymmetric theories, the renormalisation group equations are changed slightly, so that at a certain unification scale, all the three couplings meet at the same point (see figure 3.2), building the groundwork for a GUT.

- The Higgs mechanism for electroweak symmetry breaking requires certain conditions to the parameters of the scalar potential, i.e. that the squared mass parameter of the Higgs field has a negative sign for the scalar potential to develop a non-zero vacuum expectation value (VEV). While in the Standard Model, these parameters are simply

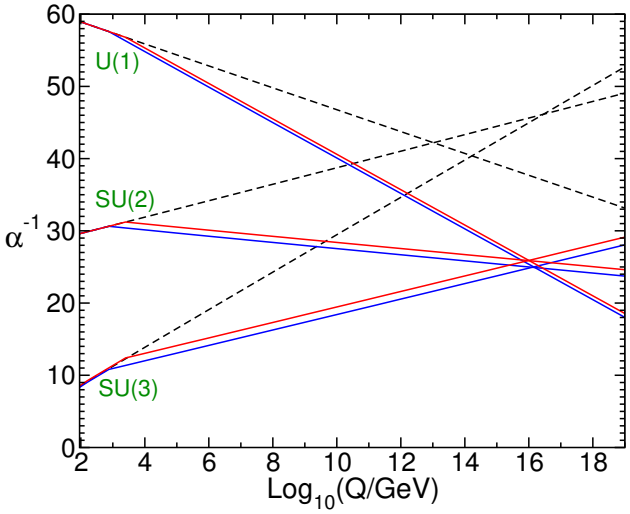

Figure 3.2: One-loop running of the reciprocal of the gauge couplings in the Standard Model and the Minimal Supersymmetric Standard Model. While the Standard Model couplings (black dashed lines) miss each other at a high scale, supersymmetry leads to them meeting at a scale of approximately 10^{16} GeV. Plot taken from ref. [25].

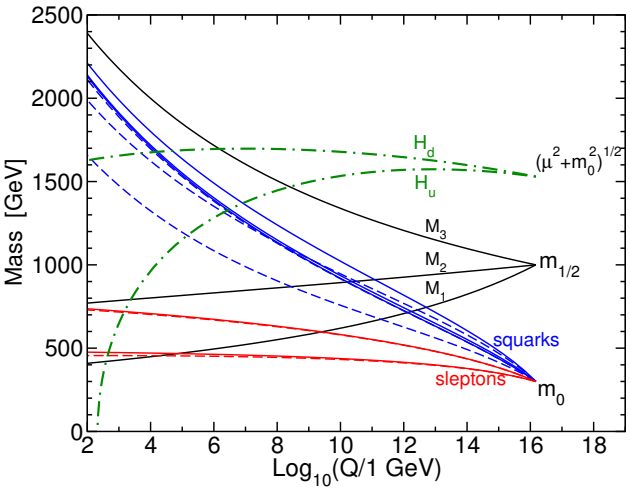

Figure 3.3: Running of mass parameters in the Minimal Supersymmetric Standard Model. It can be seen that at the electroweak scale, the mass parameter of the H_u field becomes negative, fulfiling the requirement for electroweak symmetry breaking. Plot taken from ref. [25].

added ad-hoc and tuned in such a way that the minima of the potential allow for such a non-zero VEV, supersymmetry offers the possibility to **dynamically generate electroweak symmetry breaking** by providing a way to make the squared mass parameter negative through renormalisation group runnings (see figure 3.3), and furthermore express the ad-hoc parameters through the gauge couplings of the electroweak interactions, making it possible to even give an estimate of the Higgs mass (which requires radiative corrections to reach the observed mass of 125 GeV, however).

Supersymmetry is a symmetry between fermionic and bosonic degrees of freedom. This symmetry is based on a modification of the Poincaré group, the group of Lorentz transformations including translations. Extending the Poincaré group is strongly restricted by the Coleman-Mandula theorem [44]. The only possibility is given by the Haag-Łopuszański-Sohnius theorem [45]: the inclusion of anticommuting, i.e. fermionic generators. These generators change the spin of a particle by ½, from fermion to boson and vice versa, but leave all of the other quantum numbers invariant. Such a transformation is called *supersymmetry transformation*. The mathematical structure of such a transformation will be outlined in the following section.

3.2 Supersymmetry transformations

A SUSY transformation mediated by the generator Q turns fermionic states into bosonic ones and vice versa:

$$Q\,|\text{fermion}\rangle = |\text{boson}\rangle, \qquad Q\,|\text{boson}\rangle = |\text{fermion}\rangle. \tag{3.3}$$

Due to its nature, the generator Q itself has to be fermionic, i.e. with the transformation properties of a spinor. It requires the introduction of fermionic coordinates, enlarging the known space-time to additional "fermionic dimensions" [26]. The full list of commutation relations for the generators of the Poincaré algebra read:

$$\begin{aligned}
[P^\mu, P^\nu] &= 0, \\
[P^\mu, M^{\rho\sigma}] &= i(g^{\mu\rho}P^\sigma - g^{\mu\sigma}P^\rho), \\
[M^{\mu\nu}, M^{\rho\sigma}] &= -i(g^{\mu\rho}M^{\nu\sigma} - g^{\mu\sigma}M^{\nu\rho} - g^{\nu\rho}M^{\mu\sigma} + g^{\nu\sigma}M^{\mu\rho}),
\end{aligned} \tag{3.4}$$

and including the SUSY generator Q

$$\begin{aligned}
[P^\mu, Q_a] &= 0, \\
[M^{\mu\nu}, Q_a] &= -\Sigma^{\mu\nu}_{ab} Q_b, \\
\{Q_a, Q_b\} &= 2\gamma^\mu_{ab} P_\mu,
\end{aligned} \tag{3.5}$$

where P^μ is the operator generating translations, and $M^{\rho\sigma}$ the operator generating rotations and boosts, and the γ^μ are the Dirac matrices with $\Sigma^{\mu\nu} = \frac{i}{4}[\gamma^\mu, \gamma^\nu]$ and a, b being Dirac indices.

The Poincaré algebra including the SUSY transformations form the supersymmetric algebra.

The SUSY transformation assigns superpartners to each particle. In $N = 1$-supersymmetry, there is only one SUSY generator Q, resulting in only one superpartner per particle. From the (anti-)commutation relations follows the equality of the masses of particle and superpartner. Furthermore, as SUSY transformations should not have an effect on the gauge interactions present in the Standard Model, also the gauge quantum numbers must be the same from particle to superpartner [26]. This has quite an interesting consequence, as one might try to pair particle fields that differ in their spin by ½, but behave the same under a gauge transformation, such as the left-handed $SU(2)_L$ lepton doublet and the charge-conjugated Higgs doublet. As the former carries lepton number, which is conserved within the Standard Model, and the latter does not, this would cause a disparity between one type of particle conserving this quantum number and another one related to the first through SUSY not conserving it. Therefore, new fields are required for supersymmetry to be realised.

The suggested equality of the masses of Standard Model and SUSY particles poses a problem, as experimentally, no particles consistent with the additional properties of a SUSY particle have been detected. In fact, if SUSY were exactly realised in nature, superpartners of light particles such as the electron would be produced in copious amounts at a particle collider. Thus, as no supersymmetric particles have been found so far, supersymmetry must be broken, at least at the scale of electroweak interactions, where the Standard Model "lives". The exact dynamics of such a breaking mechanism, be it spontaneous, as it is the case for the Higgs mechanism with a non-zero vacuum expectation value, or explicit, are yet unknown and are usually considered to be decoupled from the phenomenological content of a supersymmetric theory in a hidden sector that interacts only through messenger particles with the phenomenologically accessible part.

Minimally extending the Standard Model by one additional field per Standard Model particle leads to the minimal supersymmetric Standard Model (MSSM), which will be presented briefly in the following section.

3.3 The Minimal Supersymmetric Standard Model

The MSSM extends the Standard Model by including $N = 1$-supersymmetry, that is, by exactly one copy of each particle, with spin-½ fermions being assigned scalar superpartners, and spin-1 bosons (as well as the Higgs boson) being assigned spin-½ fermionic superpartners. Consequently, the gauge interactions stay the same as in the Standard Model. Furthermore, the Higgs sector of the MSSM must be enlarged by adding one additional Higgs doublet, which is required for the Lagrangian to be invariant under a supersymmetry transformation.

3.3.1 Supersymmetry breaking

The lack of knowledge regarding the SUSY breaking mechanism is parametrised simply by adding additional mass or interaction terms to the Lagrangian that are allowed by gauge invariance, but only contain supersymmetric fields, and therefore explicitely break the invariance under a SUSY transformation. The additional terms are in general independent of

each other, and lead to over 100 new parameters, compared to the Standard Model. Many of them, in particular flavour-mixing terms, are, however, strongly contrained by experiments, leading to the assumption that the SUSY breaking terms might not be entirely general and independent after all [25]. The supersymmetry breaking is constructed to be *soft*, in the sense that the mass dimension of the coupling is positive and therefore leaves the Lagrangian renormalisable [46].

Various breaking mechanisms have been proposed, the most famous ones being the Planck-scale-mediated supersymmetry breaking (PMSB) (or gravity-mediated supersymmetry breaking) [47–53] and gauge-mediated supersymmetry breaking (GMSB) [54–59]. Whereas the former relates SUSY breaking to a hidden sector that interacts through gravitational interactions with the MSSM, naturally raising the scale where the spontaneous symmetry breaking occurs up to the Planck scale M_P, the latter achieves this through the ordinary QCD and electroweak interactions by introducing new heavy messenger fields that occur in self-energy loop corrections to sparticle lines, coupling at the known gauge coupling strength and radiatively generating corrections to the masses of the sparticles. Other breaking models are extra dimensions [60–63], gaugino-mediated [64–68], and anomaly-mediated (AMSB) supersymmetry breaking [69,70]. In the end, all of these mechanisms generate the soft SUSY-breaking terms as mentioned above, eliminating the need to add them ad-hoc.

3.3.2 Constraining the parameter space

Due to the large number of free parameters added with the soft SUSY-breaking Lagrangian, it is difficult to make efficient phenomenological studies as the parameter space is too complex. Various scenarios have therefore been suggested to assume a more manageable set of parameters at some high scale and relate these to all of the parameters at a lower scale through renormalisation group (RG) equations, making supersymmetric models more predictable and experimentally testable.

In particular, from the PMSB model, a scenario called *Minimal Supergravity* (mSUGRA), or *Constrained Minimal Supersymmetric Standard Model* (CMSSM), emerges. It relates all the different parameters that are generated from the SUSY breaking to just four parameters at the scale of gauge coupling unification $M_U \sim 10^{16}$ GeV which are then evolved through RG equations down to the electroweak scale, with only one more parameter needed to describe the full parameter space of the MSSM. Commonly, the following parameters are chosen:

$$m_0, \quad m_{1/2}, \quad A_0, \quad \tan(\beta), \quad \mathrm{sgn}(\mu), \tag{3.6}$$

where m_0 is the common mass of scalar fields (sleptons, squarks, Higgs fields), $m_{1/2}$ is the common mass of gaugino and higgsino fields, A_0 is the common trilinear coupling parameter (appearing in the soft SUSY-breaking Lagrangian as a coupling of three scalar fields), $\tan(\beta)$ is the ratio of the vacuum expectation values of the two Higgs doublets, and $\mathrm{sgn}(\mu)$ is the sign of the Higgs self-coupling parameter μ.

Supermultiplet	$SU(3)_C$	×	$SU(2)_L$	×	$U(1)_Y$	Particles
$\hat{Q} \equiv \begin{pmatrix} \hat{u} \\ \hat{d} \end{pmatrix}$	**3**		**2**		$\frac{1}{3}$	$\begin{pmatrix} u_L \\ d_L \end{pmatrix}, \begin{pmatrix} \tilde{u}_L \\ \tilde{d}_L \end{pmatrix}$
$\hat{U}$	**3**		**1**		$\frac{4}{3}$	$u_R, \tilde{u}_R$
$\hat{D}$	**3**		**1**		$-\frac{2}{3}$	$d_R, \tilde{d}_R$
$\hat{L} \equiv \begin{pmatrix} \hat{\nu} \\ \hat{e} \end{pmatrix}$	**1**		**2**		-1	$\begin{pmatrix} \nu_L \\ e_L \end{pmatrix}, \begin{pmatrix} \tilde{\nu}_L \\ \tilde{e}_L \end{pmatrix}$
$\hat{E}$	**1**		**1**		-2	$e_R, \tilde{e}_R$
$\hat{H}_d \equiv \begin{pmatrix} \hat{H}_d^0 \\ \hat{H}_d^- \end{pmatrix}$	**1**		**2**		-1	$\begin{pmatrix} H_d^0 \\ H_d^- \end{pmatrix}, \begin{pmatrix} \tilde{H}_d^0 \\ \tilde{H}_d^- \end{pmatrix}$
$\hat{H}_u \equiv \begin{pmatrix} \hat{H}_u^+ \\ \hat{H}_u^0 \end{pmatrix}$	**1**		**2**		1	$\begin{pmatrix} H_u^+ \\ H_u^0 \end{pmatrix}, \begin{pmatrix} \tilde{H}_u^+ \\ \tilde{H}_u^0 \end{pmatrix}$
$\hat{G}^a$	**8**		**1**		0	$G_\mu^a, \tilde{g}^a$
$\hat{W}^i$	**1**		**3**		0	$W_\mu^i, \tilde{w}^i$
$\hat{B}$	**1**		**1**		0	$B_\mu, \tilde{b}$

Table 3.1: Particle content of the MSSM. The generation indices for quarks and leptons have been suppressed. Bold numbers below the $SU(3)_C$ and $SU(2)_L$ groups show the representation under which the supermultiplet transforms (e.g. **3**: triplet, **1**: singlet), and numbers below $U(1)_Y$ denote the hypercharge quantum number.

3.3.3 Particle content

In table 3.1, an overview of all supermultiplets containing the fields and supersymmetric partners and their behaviour under gauge transformations is shown. A supermultiplet is an irreducible representation of the supersymmetric algebra. Since the supersymmetric generators commute with all the generators from the gauge groups, it is possible to write both fields and superfields in the same gauge representation. For a supersymmetric theory, the Lagrangian has to be invariant under SUSY transformations. Writing the Lagrangian in terms of the supermultiplets ensures this invariance.

In the upper part of table 3.1, quark and lepton fields are shown, with left- and right-handed fields transforming differently under the gauge group. Furthermore, the two Higgs doublets ensure that both up-type and down-type quarks (and leptons) can get mass. In the bottom part, the gauge fields are shown. After electroweak symmetry breaking, the gauge fields mix to form new mass eigenstates. In particular, the neutral gaugino and Higgsino fields mix to form the *neutralinos*, which can be regarded as the partners of the photon, the Z-boson, and the Higgs bosons, while the charged gauginos and Higgsinos form the *charginos*, being the partners of the W- and the charged Higgs bosons. The electroweak sector of the MSSM is completed by the *sleptons* as the partner fields of the charged leptons and the neutrinos.

The coloured sector of the MSSM is made up of the quark and gluon supermultiplets,

containing the *squarks* and the *gluino* as the supersymmetric partners of the quarks and the gluon. These particles will be the main interest of this thesis, as the colour charge which they carry enables them to be produced in large numbers at hadron collider experiments due to the strong interaction.

Lepton-number (L) and baryon-number (B) violating interactions are strongly suppressed by experiments. In particular, they would lead to protons decaying more quickly than what has been observed experimentally so far. In general, the MSSM can contain terms that do allow such interactions, however. In order to prevent these from occurring, a new symmetry called R-parity is introduced, defined as a multiplicative quantum number

$$R = (-1)^{3(B-L)+2s} \tag{3.7}$$

with s denoting the spin of the particle. Every Standard Model particle has an R-parity of +1, whereas a superpartner has −1. Assuming R-parity conservation and an invariance of the Lagrangian under an R-parity transformation, all couplings must contain an even number of supersymmetric particles. Phenomenologically, this means that supersymmetric particles can only be produced in pairs, and that there must be a lightest supersymmetric particle (LSP) which is stable because it cannot decay any further into only Standard Model particles. Consequently, R-parity conservation has a very interesting consequence for dark matter: in many benchmark scenarios, the LSP is the lightest neutralino which neither carries colour nor electric charge and only interacts weakly and gravitationally. These properties result in the neutralino being a perfect candidate for dark matter, being a WIMP and stable to form galaxy clusters.

3.3.4 Mass diagonalisation

In the MSSM, the physical particles in general do not correspond to the fields that appear in the Lagrangian. After electroweak symmetry breaking, fields with the same quantum numbers, i.e. spin as well as colour and electric charge, can however mix to form physical states with a defined mass. For squarks as the scalar partners of the quarks, this means that the supersymmetric components corresponding to the left- and right-handed chiral fields of the Standard Model, $\tilde{q}_L$ and $\tilde{q}_R$[1], will form a superposition which are then the physical fields $\tilde{q}_1$ and $\tilde{q}_2$. In the general MSSM, different flavours can mix, which is, however, strongly constrained due to phenomenological reasons. Furthermore, the squark mixing is proportional to the mass of the corresponding quark, making it negligible for the first two generations, and important for the third one. In particular, for the stops as the partners of the top quarks, the contributing mass terms from the MSSM Lagrangian can be written in form of a 2×2 matrix in the basis of $\tilde{t}_L$ and $\tilde{t}_R$ states [25]:

$$\mathcal{L}_{\text{stop masses}} = -\begin{pmatrix}\tilde{t}_L^*, & \tilde{t}_R^*\end{pmatrix}\begin{pmatrix}\left(M_{LL}^{\tilde{t}}\right)^2 & \Delta_{LR}^{\tilde{t}} \\ \Delta_{RL}^{\tilde{t}} & \left(M_{RR}^{\tilde{t}}\right)^2\end{pmatrix}\begin{pmatrix}\tilde{t}_L \\ \tilde{t}_R\end{pmatrix} \tag{3.8}$$

[1] Of course, chirality is not a property of scalar particles like the squarks, and the labels L and R only serve to distinguish between the partners of left- and right-handed quarks.

with the components

$$\begin{aligned}
\left(M_{LL}^{\tilde{t}}\right)^2 &= m_{\tilde{t}_L}^2 + m_t^2 + \left(\frac{1}{2} - \frac{2}{3}\sin^2(\theta_W)\right)\cos(2\beta)\, m_Z^2, \\
\left(M_{RR}^{\tilde{t}}\right)^2 &= m_{\tilde{t}_R}^2 + m_t^2 + \frac{2}{3}\sin^2(\theta_W)\cos(2\beta)\, m_Z^2, \\
\Delta_{LR}^{\tilde{t}} &= \Delta_{RL}^{\tilde{t}*} = m_t\left(A_t - \mu\cot(\beta)\right),
\end{aligned} \tag{3.9}$$

depending on various Standard Model (m_t^2, θ_W, m_Z^2) and SUSY parameters (β, $m_{\tilde{t}_L}^2$, $m_{\tilde{t}_R}^2$, A_t, μ). Most importantly, the off-diagonal elements of the matrix, denoting the mixing of the L and R stop fields, are proportional to the stop mass, and for first and second generation squarks, they would be proportional to the corresponding "light-flavoured" quark mass. Therefore, while the mixing is negligible for the first two generations, it can be significant for stops.

The physical mass eigenstates of the stops, $\tilde{t}_1$ and $\tilde{t}_2$, are related to the L and R states of the weak interaction through a rotation with a unitary matrix

$$\begin{pmatrix}\tilde{t}_1\\ \tilde{t}_2\end{pmatrix} = \begin{pmatrix}\cos\theta_{\tilde{t}} & \sin\theta_{\tilde{t}}\, e^{i\phi_{\tilde{t}}}\\ -\sin\theta_{\tilde{t}}\, e^{-i\phi_{\tilde{t}}} & \cos\theta_{\tilde{t}}\end{pmatrix}\begin{pmatrix}\tilde{t}_L\\ \tilde{t}_R\end{pmatrix} \tag{3.10}$$

which diagonalises the stop mass matrix of eq. (3.8). The phase $\phi_{\tilde{t}}$ is often chosen to be zero, resulting in the components of the basis rotation matrix to be real which then depends only on the stop mixing angle $\theta_{\tilde{t}}$. The eigenvalues of the diagonalised matrix, corresponding to the masses of the $\tilde{t}_1$ and $\tilde{t}_2$ states, can then simply be read off [71]. They are:

$$\begin{aligned}
m_{\tilde{t}_{1,2}}^2 = \frac{1}{2}&\left\{\left(m_{\tilde{t}_L}^2 + m_{\tilde{t}_R}^2\right) + \frac{1}{2}m_Z^2\cos(2\beta) + 2m_t^2\right\} \\
&\mp \frac{1}{2}\sqrt{\left[m_{\tilde{t}_L}^2 - m_{\tilde{t}_R}^2 + \left(\frac{1}{2} - \frac{4}{3}\sin^2(\theta_W)\right)\cos(2\beta)\, m_Z^2\right]^2 + 4m_t^2\left(A_t - \mu\cot(\beta)\right)^2}.
\end{aligned} \tag{3.11}$$

Due to the appearance of the off-diagonal entries of the matrix in eq. (3.8) inside the square root of eq. (3.11), the splitting between the two mass eigenstates is usually very large, often making the ligher eigenstate the lighest squark and one of the lightest supersymmetric particles in the whole SUSY particle spectrum. As stops therefore take a special role, they are usually looked at separately from the light-flavoured squarks of the first two generations, while additionally, the latter are often assumed to be mass-degenerate.

3.4 Production of SUSY particles at the LHC

Searches for supersymmetric particles are one of the main quests of the ATLAS and CMS experiments at the LHC. A lot of effort has been put both into improving detection mechanisms as well as theoretical calculations to provide the best possible framework for an

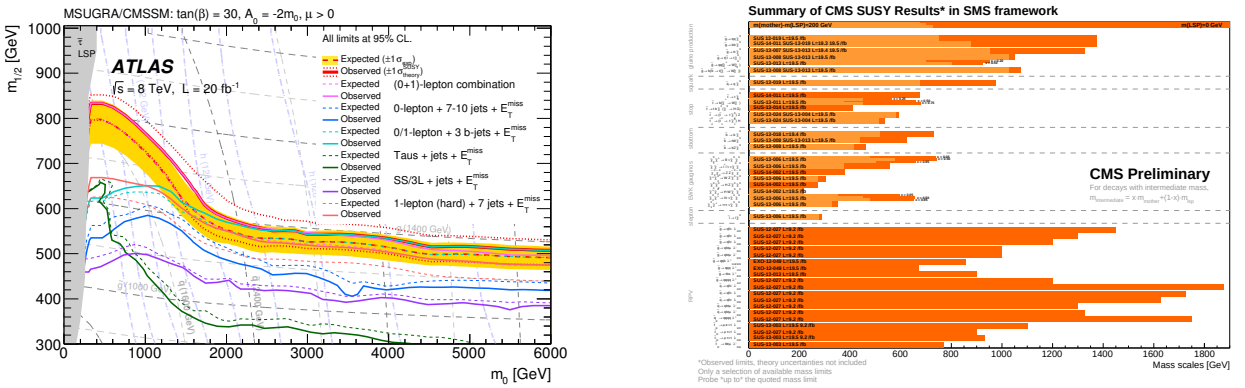

Figure 3.4: Left: CMSSM exclusion plot of the ATLAS experiment when varying the parameters m_0 and $m_{1/2}$ [72]. Right: mass exclusion limits for different SUSY particles from the CMS experiment [73].

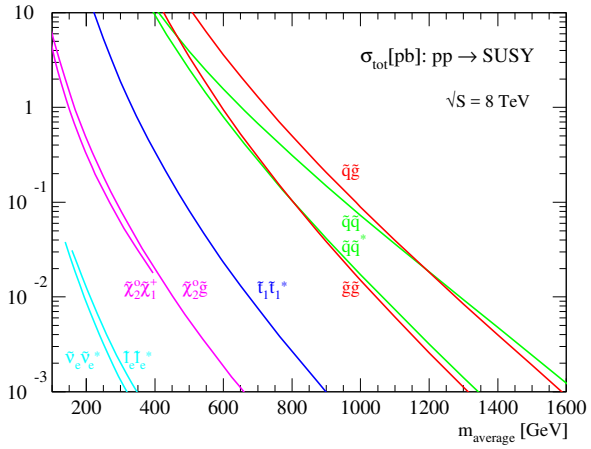

Figure 3.5: NLO production cross sections for SUSY particle production at the LHC with a centre-of-mass energy of 8 TeV, calculated with the public code `Prospino` [74]. Plot taken from the referenced `Prospino` website.

analysis of the proton collisions happening at 7, 8, and by now 13 TeV of centre-of-mass energy, with plans to upgrade the LHC to even higher energies and luminosities in the future to increase the number of collisions in which supersymmetric particles could be produced. Figure 3.4 show two plots visualising the current mass exclusion limits of supersymmetric particles, one from the CMS experiment and the other for the CMSSM scenario from the ATLAS experiment, both with data collected up to 8 TeV. In figure 3.5, the theoretical LHC production cross sections at NLO for SUSY particles is shown. Since no supersymmetric particles have been found so far, the production cross sections can directly be translated into the mass exclusion limits.

3.4.1 Progress in theoretical predictions for electroweak sparticle production

Theoretical predictions for purely electroweak SUSY particles like sleptons, neutralinos, and charginos have been made up to NLO, see refs. [76–78], with a growing number being implemented at NLO+NLL[2] accuracy including transverse-momentum and invariant-mass resummation, see refs. [79–86]). A public code for the calculation of gaugino-pair and slepton-pair production up to NLO+NLL is available under the name of `Resummino` [87]. While the production of electroweak sparticles usually offers signal channels that are cleaner than those for coloured sparticle production, their cross sections are significantly smaller and depend on many SUSY parameters.

3.4.2 Progress in theoretical predictions for coloured sparticle production

Coloured SUSY particles, the squarks and gluinos which are the main interest of this thesis, are expected to be produced in substantial amounts due to the large coupling of the strong interaction. LO predictions have been made in the 1980s [88–94], while approximately 10 years later, the NLO corrections were computed [95–98], showing significant contributions of the order of tens of percents. Electroweak corrections at LO and NLO in the electroweak coupling α have been analysed in much detail [99–108], leading to corrections of the order of a few percents.

Resummed soft-gluon corrections for squarks and gluinos up to NLO+NLL accuracy have been calculated in refs. [109–113], where in ref. [110], also the separate resummation of leading-order Coulomb contributions via the Sommerfeld factor has been looked at. In the formalism of soft-collinear effective theory (SCET) [114–121], similar results at NLO+NLL have been obtained [122, 123], including also the resummation of Coulomb and bound-state contributions.

First steps towards the computation of a full NNLO result have been made in refs. [124–127] (see also ref. [128]), where the threshold-enhanced contributions have been expanded up to NNLO. The inclusion of soft-gluon corrections up to NNLL has been done in refs. [129–131], and for SCET in refs. [132–134], again including the resummation of Coulomb and bound-state corrections. Additional studies regarding finite-width effects [135] and bound-state effects [136–139] have also been made.

[2] For the definition of LL, NLL, NNLL etc., see section 4.4.

Parts of the results of this thesis, describing the increase of accuracy up to NNLL in the so-called Mellin-space formalism, have been published in refs. [140,141] and [142], where in the latter, the effect of threshold-improved PDFs has been applied to the NLO+NLL calculations.

4 Threshold Resummation

Higher-order corrections in the perturbative series to production processes are important for the validity of theoretical predictions, in particular for the LHC, as the large coupling strength of the strong interaction, large colour factors, and restrictions to the available phase space can lead to higher-order corrections being significant contributions ranging from $\mathcal{O}(10\%)$ up to $\mathcal{O}(100\%)$ with respect to leading order. Sometimes, processes take place in extreme kinematical regions, close to a *threshold*, which forces the produced particles to have very little kinetic energy. Such situations occur when the produced particles are very heavy, and the centre-of-mass energy of the collider is just large enough for the formation of the rest mass of the final-state particles. At higher orders, large logarithmic corrections arise due to an imbalanced cancellation of infrared divergencies, stemming from the possibility of emitting an arbitrary number of low-energy gluons. These logarithms appear at all orders and lead to very large corrections in the vicinity of the threshold, opening up the question if perturbation theory is still reliable in this kinematic limit. It turns out that the structure of the logarithmic terms allows for a *resummation* of all of these contributions up to all orders in α_s.

Furthermore, in the case of coloured final-state particles, *QCD Coulomb contributions* stemming from gluon exchange between slowly-moving particles lead to another source of threshold-enhanced corrections that need to be treated in a similar way up to all orders for perturbation theory to stay applicable. Under certain conditions, bound states between the final-state particles can form and contribute to the cross section from below threshold.

This chapter introduces the techniques to soft-gluon resummation, starting from the results of a NLO calculation and moving on to show how factorisation properties of the cross section lead to the appearing logarithms being resummed up to all oders. Subsequently, the resummation of Coulomb contributions and bound-state formation is presented. All processes will be assumed to be $2 \to 2$ processes, being the main interest of this thesis, with real emission corrections of n additional particles appearing as $2 \to 2 + n$.

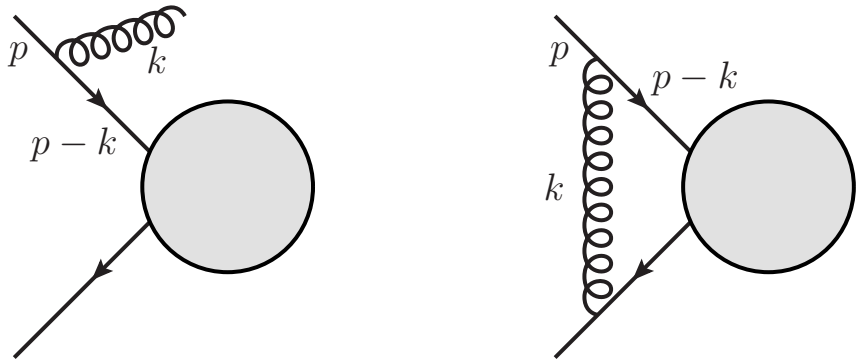

(a) (b)

Figure 4.1: Feynman diagrams of a gluon being radiated off a massless quark line (a), and a virtual gluon forming a loop (b), with the momenta as labels. The grey circle denotes further interactions between the two quark lines.

4.1 Infrared divergences

At higher orders in perturbation theory, there exist two types of contributions to a Born process: virtual corrections, i.e. loop diagrams, and real corrections, i.e. the emission of additional particles to the final state. The computation of real emission diagrams is of great importance because, even though they formally do not lead to the same final state as the underlying $2 \to 2$ process, they still contribute to the same order in α_s as their corresponding loop diagrams. Experimental detectors are not able to resolve additional particles with arbitrarily small energies or when they are travelling in the same direction as the particle that they were emitted from. Therefore, in order to fully describe a $2 \to 2$ scattering process at a collider, real emission corrections need to be taken into account at higher orders in perturbation theory.

In theories with massless particles, one encounters peculiarities when internal propagators of Feynman diagrams become on-shell. This is possible both for virtual diagrams, where the integration over unconstrained momenta – in addition to being responsible for divergences in the ultraviolet regime – causes the internal particle's momentum to satisfy its on-shell condition, as well as for the real emission of additional particles, where extra phase space integration factors play a similar role to the integration over loop momenta.

As an example, the real radiation of a gluon off a massless quark line is looked at, see figure 4.1 (a). The corresponding matrix element is proportional to the propagator of the intermediate quark line labelled $p - k$,

$$\mathcal{M}_{\text{real}} \sim \frac{1}{(p-k)^2} = -\frac{1}{2p \cdot k} = -\frac{1}{2p_0 k_0 (1 - \cos\theta)} \tag{4.1}$$

with θ the angle between the spatial momentum components of the quark and the gluon. Obviously, eq. (4.1) has two singularities, assuming that the energy of the incoming quark, p_0, is larger than zero:

- a *soft* or *infrared* (IR) singularity for $k_0 \to 0$, i.e. when the emitted gluon is *soft* and has very little energy (and consequently for all components, $k \to 0$),
- and a *collinear* singularity for $\cos\theta \to 1$, i.e. when the gluon is emitted at a very small angle θ relative to the quark.

Subsequently, for the computation of a cross section, the phase space integration over these momentum components will cause the propagators to diverge. In dimensional regularisation, $D = 4-2\varepsilon$ with $\varepsilon < 0$ (i.e. enlarging the number of space-time dimensions), these divergences can be regularised and appear as singularities $\varepsilon^{-1}, \varepsilon^{-2}$ for $\varepsilon \to 0$. It should be noted that, while both soft and collinear divergences are associated with massless vector bosons like photons and gluons, only the latter require also the emitting particle to be massless.

A slightly more physical interpretation of the soft divergence can be made when considering the phase space integration in coordinate space (or x-space): the phase-space integral $\int \mathrm{d}^D x \ldots$ in D dimensions "sums" over all the end points of the field of an emitted gluon in space, since the integration boundaries reach to infinity. For a minimum value of D (which happens to be $D = 4$), this integral will diverge. Gluons extending out to infinite distances are associated with an infinite Compton wavelength, which is furthermore related via the uncertainty principle to a vanishing momentum $k \to 0$ [143].

Now, calculating the virtual diagram in figure 4.1 (b) leads to a very similar result, as the same propagator term appears in the matrix element and the phase space integration over k is replaced by a loop integration, leading to a similar structure of IR divergences. There is one crucial difference, however, and that is the different sign with which the singularities from the virtual contributions appear. The consequence is the complete cancellation of the IR divergencies in the sum of real and virtual contributions. This property is valid to all orders in perturbation theory. For the case of e.g. e^+e^- in the initial state, it is a consequence of the Bloch-Nordsieck theorem for QED [144], and the Kinoshita-Lee-Nauenberg (KLN) theorem for the full Standard Model [145, 146].

For massless partons in the initial state, the KLN theorem does not apply, however, due to the appearance of collinear singularities. In that case, a factorisation procedure is required to separate long- and short-distance quantities, the former describing all the infrared and collinear behaviour, the latter therefore being *infrared safe*. Infrared safety applies to quantities which are independent of the long-distance behaviour. This means that they are finite for vanishing parton masses $m_i \to 0$, i.e.:

$$\sigma\left(\frac{Q^2}{\mu_R^2}, \frac{m_i^2}{\mu_R^2}, \alpha_\mathrm{s}(\mu_R)\right) = \sigma\left(\frac{Q^2}{\mu_R^2}, 0, \alpha_\mathrm{s}(\mu_R)\right)\left\{1 + \mathcal{O}\left(\frac{m_i^2}{Q^2}\right)\right\} \tag{4.2}$$

with Q "large invariants" of the process, such as $\sqrt{s}$, and μ_R the renormalisation scale [147]. As a consequence of asymptotic freedom, infrared safe quantities can then be calculated in perturbation theory. A systematic way to identify infrared and collinear divergences at all orders follows from finding the solutions to the Landau equations [149] and applying the method of Coleman and Norton [150] through the use of reduced diagrams, see also ref. [151].

When a cross section or another physical quantity becomes sufficiently exclusive, e.g.

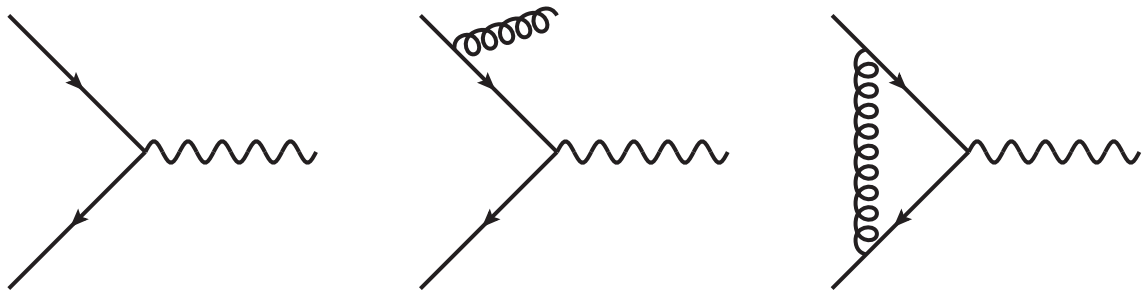

Figure 4.2: Quark-antiquark annihilation into a virtual off-shell photon, as part of the Drell-Yan process. Shown is the Born diagram (a), the real emission of a gluon (b), and the virtual gluon correction (c) as the two NLO contributions proportional to the strong coulping constant α_s. The second real emission diagram, where the gluon is radiated off the antiquark line, as well as the self-energy corrections on the external quark legs are not depicted here.

when analysing a kinematical region where the emission of additional particles is strongly constrained as it is the case close to the production threshold of a certain final state, there is a mismatch between the kinematic dependence of the virtual and real corrections. While in the sum of the two, the ε-singularities will still cancel, only little phase space is available for the emission of real gluons, leading to the appearance of potentially large finite terms. They manifest as logarithms of quantities that vanish in this kinematical limit, schematically written as $\ln(w)$ with $w \to 0$, resulting in large contributions that can spoil the perturbative expansion by nullifying the suppression due to the coupling constant in which the expansion is carried out, e.g. $\alpha_s \ln(w) \approx 1$.

In the following, it will be shown how these logarithms arise from a next-to-leading order calculation of the Drell-Yan process.

4.1.1 Drell-Yan up to next-to-leading order

One of the most important and fundamental processes in the high-energy physics of the strong interaction is the Drell-Yan process [152]. It describes the scattering of two hadrons h_1 and h_2 through quark-antiquark annihilation into an off-shell photon or Z-boson to form an oppositely charged lepton pair:

$$h_1 + h_2 \to \gamma^*, Z^0 \to l^+ + l^- + X. \tag{4.3}$$

By now, the Drell-Yan process has been studied rigorously and many other processes, also in beyond the Standard Model theories, show a similar structure and can therefore easily be evaluated. On the experimental side, due to Drell-Yan being solely an electroweak process at leading order, it offers a clean signature in a detector, making the process easy to discover and convenient for reproducing the invariant mass of the off-shell photon. Because of its clean signal, it is also used for the determination of the parton distribution functions.

The Drell-Yan process is described at leading order by the partonic process

$$q(p_1) + \bar{q}(p_2) \to (l^+ + l^-)(Q), \tag{4.4}$$

where p_1 and p_2 are the momenta of the quark and antiquark, and Q is the momentum of lepton-antilepton final state. While the initial state can receive corrections from the strong interaction, the two leptons in the final state only interact electroweakly. Therefore, the final-state corrections are much smaller than the ones from the initial state and can be neglected. This means that it is sufficient to calculate the subprocess of an off-shell photon or Z-boson splitting into the lepton pair at leading order, while higher-order corrections are only applied to the initial-state particles. The cross section can then be split into two parts [153, 154]:

$$\frac{\mathrm{d}\hat{\sigma}}{\mathrm{d}Q^2}(q + \bar{q} \to l^+ + l^-) = \frac{\mathrm{d}\hat{\sigma}_\gamma}{\mathrm{d}Q^2}(q + \bar{q} \to \gamma^*, Z^0) \times \frac{\mathrm{d}\Gamma_{l\bar{l}}}{\mathrm{d}Q^2}(\gamma^*, Z^0 \to l^+ + l^-). \tag{4.5}$$

In the following, only the contribution from off-shell photon will be considered. The factor describing the splitting is then given as $\mathrm{d}\Gamma_{l\bar{l}}/\mathrm{d}Q^2 = \alpha/(3\pi Q^2)$, where α is the fine structure constant and Q^2 is the invariant mass of the lepton-antilepton system. At leading order, no gluons are present, so the quark annihilation part of the cross section is itself simply proportional to α:

$$\frac{\mathrm{d}\hat{\sigma}_\gamma}{\mathrm{d}Q^2}(q + \bar{q} \to \gamma^*) = \frac{4\pi^2 \alpha e_q^2}{3\hat{s}} \delta(1 - z) \tag{4.6}$$

with e_q the fractional charge of the quark, $\hat{s} = (p_1 + p_2)^2$ a Mandelstam variable, and $z := Q^2/\hat{s}$. The physical interpretation of the variable z can be viewed as the fraction of the total energy that is used up for the creation of the off-shell photon, with $1 - z$ consequently denoting the fraction of the total energy that is available for the creation of additional particles, which will become important when moving on to NLO. The partonic cross section can now be written as

$$\frac{\mathrm{d}\hat{\sigma}}{\mathrm{d}Q^2} = \frac{\alpha}{3\pi Q^2} \frac{\mathrm{d}\hat{\sigma}_\gamma}{\mathrm{d}Q^2} = \frac{4\pi\alpha^2 e_q^2}{9Q^2\hat{s}} \omega_{q\bar{q}} \tag{4.7}$$

where $\omega_{q\bar{q}}$ denotes the contributions from higher orders in the strong interaction:

$$\omega_{q\bar{q}} = \omega_{q\bar{q}}^{(0)} + \left(\frac{\alpha_\mathrm{s}}{\pi}\right) \omega_{q\bar{q}}^{(1)} + \left(\frac{\alpha_\mathrm{s}}{\pi}\right)^2 \omega_{q\bar{q}}^{(2)} + \mathcal{O}(\alpha_\mathrm{s}^3), \tag{4.8}$$

with the normalisation $\omega_{q\bar{q}}^{(0)} = \delta(1-z)$. Figure 4.2 shows the Feynman diagrams that contribute to $\omega_{q\bar{q}}^{(0)}$ (a), and to $\omega_{q\bar{q}}^{(1)}$ (b) and (c).

NLO corrections to the Drell-Yan process have first been computed in [153] using the $\overline{\mathrm{MS}}$ renormalisation scheme. Their calculation is a bit more involved due to additional loop and phase-space integrations and the subsequent appearance of the three types of divergences: UV, IR, and collinear divergences. In order to make these divergences apparent,

dimensional regularisation is applied in the usual manner, i.e. shifting the number of space-time dimensions from 4 to $D = 4 - 2\varepsilon$ with the sign of ε denoting if ultraviolet ($\varepsilon > 0$) or infrared and collinear ($\varepsilon < 0$) divergences are regulated. Furthermore, as the sum of all contributions to the NLO cross section must be independent of the gauge chosen for the gluon field and since also the dimensional regularisation scheme is explicitely gauge independent, a gauge can freely be chosen in order to simplify the calculations. It turns out that the Landau gauge is a well-motivated choice as it renders both the quark self-energies as well as the vertex correction of figure 4.2 (c) individually UV-finite and even causes the quark self-energies to vanish completely, leaving the vertex correction as the only virtual contribution to be calculated.

Following the calculations of refs. [153, 154], the contribution from the real emission diagram after performing the phase-space integrations is:

$$\omega^{(1)}_{q\bar{q}}\big|_{\text{real}} = \frac{C_F}{2}\left(\frac{4\pi\mu_R^2}{Q^2}\right)^{\varepsilon}\frac{\Gamma(1-\varepsilon)}{\Gamma(1-2\varepsilon)}\left\{-\frac{2}{\varepsilon}\left[(1-z)^{1-2\varepsilon}z^{\varepsilon} + 2z^{1+\varepsilon}(1-z)^{-1-2\varepsilon}\right]\right\}. \tag{4.9}$$

Here, the pole term $(-2/\varepsilon)$ stems from the integration over the angle between the quark and the emitted gluon, parametrising the divergence for the collinear splitting into a gluon. All terms with positive powers of ε will vanish after taking the limit $\varepsilon \to 0$ and therefore have been suppressed. Additional singularities in the expressions inside the square brackets can be made explicit by introducing the following expansion:

$$(1-z)^{-1-2\varepsilon} = -\frac{1}{2\varepsilon}\delta(1-z) + \frac{1}{[1-z]_+} - \varepsilon\left[\frac{\ln(1-z)}{1-z}\right]_+ + \mathcal{O}(\varepsilon^2). \tag{4.10}$$

The terms in eq. (4.10) have to be understood in a distributional sense and are only defined under an integral. The expressions written in square brackets of the form $[g(z)]_+$ are called plus distributions, defined with a smooth test function $f(z)$:

$$\int_0^1 \mathrm{d}z\, f(z)\Big[g(z)\Big]_+ = \int_0^1 \mathrm{d}z\,\Big(f(z) - f(1)\Big)\, g(z). \tag{4.11}$$

Plus distributions serve to regulate a divergence of $g(z)$ at the upper integration limit, making the integral converge. Inserting the expansion of eq. (4.10) and again neglecting terms that vanish for $\varepsilon \to 0$, the real emission corrections turn into the following form with all poles in ε having been made explicit:

$$\begin{aligned}\omega^{(1)}_{q\bar{q}}\big|_{\text{real}} = \frac{C_F}{2}&\left(\frac{4\pi\mu_R^2}{Q^2}\right)^{\varepsilon}\frac{\Gamma(1-\varepsilon)}{\Gamma(1-2\varepsilon)}\\ &\times\left\{\frac{2}{\varepsilon^2}\delta(1-z) - \frac{2}{\varepsilon}\frac{1+z^2}{[1-z]_+} + 4(1+z^2)\left[\frac{\ln(1-z)}{1-z}\right]_+ - 2\frac{1+z^2}{1-z}\ln z\right\}.\end{aligned} \tag{4.12}$$

The pole in eq. (4.10) that turns into a double pole in eq. (4.12) stems from a soft singularity, which can be seen from the proportionality to $\delta(1-z)$, forcing z to be 1 and therefore only

allowing the emission of soft gluons.

The virtual corrections are calculated from the diagram of figure 4.2 (c) which is the only diagram contributing to the virtual piece for the reasons mentioned above. Evaluating the loop integral of the vertex corretion and making the poles in ε explicit results in the following expression:

$$\omega^{(1)}_{q\bar{q}}\big|_{\text{virtual}} = \frac{C_F}{2}\left(\frac{4\pi\mu_R^2}{Q^2}\right)^{\varepsilon}\frac{\Gamma(1-\varepsilon)}{\Gamma(1-2\varepsilon)}\left\{-\frac{2}{\varepsilon^2}-\frac{3}{\varepsilon}-8+\frac{2}{3}\pi^2\right\}\delta(1-z). \tag{4.13}$$

The virtual correction is, similarly to the Born cross section, proportional to $\delta(1-z)$ as no additional particles are emitted and all of the initial-state energy turns into the invariant mass of the off-shell photon. According to the KLN-theorem, the sum of real and virtual corrections is IR-finite, which is achieved by the cancellation of the double pole in ε proportional to $\delta(1-z)$:

$$\begin{aligned}\omega^{(1)}_{q\bar{q}} &= \omega^{(1)}_{q\bar{q}}\big|_{\text{real}} + \omega^{(1)}_{q\bar{q}}\big|_{\text{virtual}} \\ &= \frac{C_F}{2}\left(\frac{4\pi\mu_R^2}{Q^2}\right)^{\varepsilon}\frac{\Gamma(1-\varepsilon)}{\Gamma(1-2\varepsilon)}\left\{-\frac{2}{\varepsilon}\frac{1+z^2}{[1-z]_+}-\frac{3}{\varepsilon}\delta(1-z)-2\frac{1+z^2}{1-z}\ln(z)\right. \\ &\qquad \left.+4(1+z^2)\left[\frac{\ln(1-z)}{1-z}\right]_+ + \left(\frac{2\pi^2}{3}-8\right)\delta(1-z)\right\}.\end{aligned} \tag{4.14}$$

While the double poles related to the soft singularity vanish, a single pole in ε, denoting a purely collinear divergence, remains. A factorisation procedure absorbs this pole into a collinear counter term, effectively separating sufficiently collinear gluons, i.e. gluons with vanishing transverse momentum, from the hard partonic subprocess, where no collinear or soft divergences are present. Analogously to UV-renormalisation, one has to choose a specific scheme to determine which additional finite terms are subtracted from the partonic cross section and absorbed into the counter term. Commonly, PDFs are defined in the $\overline{\text{MS}}$ scheme, which leads to the subtraction of the following term from the cross section:

$$\omega^{(1)}_{q\bar{q}}\big|_{\text{coll}} = \frac{1}{\varepsilon\Gamma(1-\varepsilon)}\left(\frac{4\pi\mu_R^2}{\mu_F^2}\right)^{\varepsilon}P_{qq}(z) \tag{4.15}$$

where P_{qq} is the leading-order quark-quark splitting function and μ_F is the factorisation scale. Splitting functions $P_{ba}(x)$ denote the probability that a parton a turns into another parton b, possibly of a different type, carrying a fraction x of the momentum of a by emitting a quark or gluon [18]. The quark-quark splitting function, which is of interest here, is defined as:

$$P_{qq}(z) = C_F\left(\frac{1+z^2}{[1-z]_+}+\frac{3}{2}\delta(1-z)\right) = C_F\left[\frac{1+z^2}{1-z}\right]_+. \tag{4.16}$$

Subtracting this term from eq. (4.14) leads to the final result for the NLO correction to the

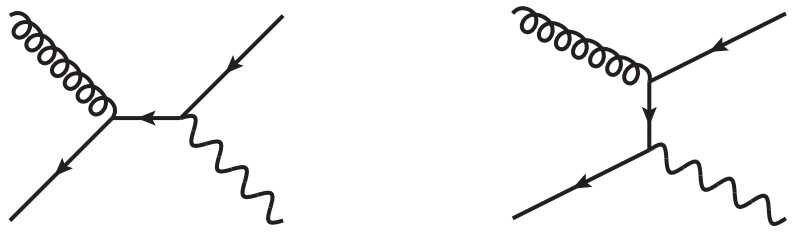

Figure 4.3: Drell-Yan correction at $\mathcal{O}(\alpha_s)$ from the so-called QCD Compton scattering of a quark and a gluon. Whereas these two diagrams contribute to the process $g + \bar{q} \to \gamma^* + \bar{q}$, inverting the arrows on the fermion lines gives the contribution to $g + q \to \gamma^* + q$.

Drell-Yan process with a $q\bar{q}$ initial state in the $\overline{\text{MS}}$ scheme:

$$\begin{aligned}\omega_{q\bar{q}}^{(1),\overline{\text{MS}}} &= \lim_{\varepsilon\to 0}\left(\omega_{q\bar{q}}^{(1)}\big|_{\text{real}} + \omega_{q\bar{q}}^{(1)}\big|_{\text{virtual}} - \omega_{q\bar{q}}^{(1)}\big|_{\text{coll}}\right)\\ &= C_F\left\{2(1+z^2)\left[\frac{\ln(1-z)}{1-z}\right]_+ - \frac{1+z^2}{1-z}\ln(z) + \left(\frac{\pi^2}{3} - 4\right)\delta(1-z)\right\} + P_{qq}(z)\ln\frac{Q^2}{\mu_F^2}. \quad (4.17)\end{aligned}$$

Since all poles in ε are cancelled, this expression is now explicitely UV-, IR-, and collinear-finite and the limit $\varepsilon \to 0$ can be taken, resulting in all terms proportional to ε to vanish. It is interesting to note that the collinear subtraction introduces a factorisation scale dependence in the partonic cross section.

At higher orders in the perturbative expansion, additional initial-state configurations offer the possibility to contribute to the Drell-Yan process. At next-to-leading order, there is one such process called QCD Compton scattering, see figure 4.3, describing the scattering of a gluon and a(n) (anti-)quark, leading to an additional (anti-)quark in the final state:

$$g + q/\bar{q} \to \gamma^* + q/\bar{q}. \quad (4.18)$$

For completeness, the result is quoted here [153, 154]:

$$\omega_{qg}^{(1),\overline{\text{MS}}} = \frac{1}{2}T_R\left\{\left(z^2 + (1-z^2)\right)\ln\frac{(1-z)^2}{z} - \frac{3}{2}z^2 + z + \frac{3}{2}\right\} + \frac{1}{2}P_{qg}(z)\ln\frac{Q^2}{\mu_F^2} \quad (4.19)$$

with the leading-order gluon-quark splitting function

$$P_{qg}(z) = T_R\left[z^2 + (1-z)^2\right]. \quad (4.20)$$

and the colour factor $T_R = 1/2$.

4.1.2 Potentially large logarithms and the threshold

In order to solidify the significance of the previous section, a small recap of the singularity structures observed in the NLO correction to Drell-Yan production will be given. Due to the expansion of eq. (4.10), the real emission correction, eq. (4.12), exhibits the following infrared

and collinear divergencies for $\varepsilon \to 0$:

- Double pole $\propto \varepsilon^{-2}$: this first term stems from the emitted gluon being soft or both soft and collinear to the particle it is being radiated off; the double or soft pole proportional to $\delta(1-z)$ is cancelled by a corresponding term from the virtual correction.

- Single pole $\propto \varepsilon^{-1}$: the single pole term results from the emitted gluon being collinear to the quark direction, with vanishing transverse momentum, but large momentum components otherwise, so not soft. It is not cancelled by similar terms in the sum of real and virtual corrections, but absorbed into the definition of the PDFs through a factorisation procedure. The emerging factorisation scale can roughly be seen as a measure up to which transverse energy a gluon is still considered as collinear.

- Finite term $\propto \varepsilon^{0}$: finite terms arise from a cancellation of a pole by the expansion in ε. While these finite terms are formally convergent, they can lead to potentially large contributions in certain kinematical regimes. They are the result of an incomplete cancellation of kinematical degrees of freedom in the sum of real and virtual contributions: while the loop momentum of a virtual gluon is unconstrained and can take every value, a real gluon is limited to the available energy that remains after the actual process, e.g. the production of an off-shell photon or a lepton-antilepton pair.

Out of the finite terms, of particular interest are the plus distributions containing a logarithmic term that remain in the NLO correction to the cross section. In fact, it has been shown that these logarithms appear at every order (while the infrared poles cancel, of course), corresponding to an arbitrary number of gluon emissions, in the combination

$$\alpha_s^n \left[\frac{\ln^k(1-z)}{1-z} \right]_+ , \quad k \leq 2n-1. \tag{4.21}$$

These types of logarithms are associated with the emission of soft particles: as $z = Q^2/\hat{s}$ becomes close to 1, which is the case for large invariant masses Q^2 or limited collision energies $\hat{s}$, there is insufficient energy available for the production of additional particles as described by real emission corrections. Thus, all additional radiation is forced to be soft. These logarithms are then strongly enhanced, nullifying the suppression from the small expansion parameter α_s. A truncation of the perturbative series in α_s at any order would therefore lead to significant contributions being neglected. The terms of eq. (4.21) are usually called *threshold logaritms* due to their dependence on a parameter that is associated with a certain threshold, in this case the minimum partonic energy that is needed to create an off-shell photon with invariant mass Q^2, for which $z = 1$. Due to the appearance of these terms up to all orders in perturbatin theory, it is customary to associate another perturbative series in factors of $\alpha_s^n L^k$, where L denote the logarithmic corrections, with the calculation of cross sections.

Other definitions of threshold exist, one in particular being the *production* or *absolute*

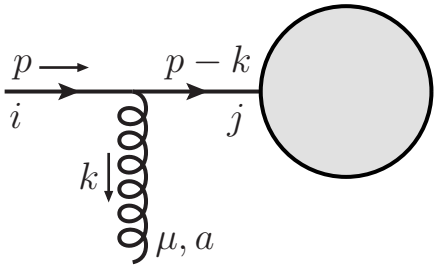

Figure 4.4: Simplified diagram for the emission of a gluon off a quark line. p, $p-k$, and k label the momenta of the lines, while μ is a Lorentz index, i, j are fundamental SU(3) indices, and a is an adjoint SU(3) index.

threshold given by the sum of the rest masses of all final-state particles:

$$\hat{s} \to \left(\sum_i m_i\right)^2 . \tag{4.22}$$

It is of importance when analysing total cross sections or in general where quantities like the invariant mass are not accessible and have already been integrated over. For the processes of interest in this thesis, total cross sections will be computed, and therefore the production threshold will be used.

For all these definitions of threshold, logarithmic contributions like the ones from eq. (4.21) arise at all orders. In order to regain the predictive power of perturbation theory, a systematic reorganisation of these terms valid for all orders is required. This is what *threshold resummation* techniques achieve. By summing the large contributions stemming from the logarithms to all orders in α_s, one does not have to worry about introducing a large uncertainty due to the truncation of the perturbative series anymore. Usually, resummation is limited to the kinematical region where the logarithms are enhanced, relying on factorisation properties of multi-particle emission from a hard subprocess which is free from any infrared or collinear divergences. As the kinematical limit is the soft region, forcing all gluons to be soft, one also refers to this type of threshold resummation as *soft-gluon resummation*.

In the following sections, the factorisation properties of cross sections in the soft limit are reviewed, leading to an exponentiation of the enhanced contributions and providing general formulas that can be applied to a multitude of processes. To achieve factorisation at a cross section level, both the amplitudes as well as the phase space have to factorise into contributions associated with the hard process which is free of any soft or collinear divergences and quantities that describe the soft and collinear behaviour of the emitted gluons. First, it will be shown how amplitudes factorise in the soft limit, followed by a trick that is required to write the phase space into a factorised expression.

4.1.3 Eikonal approximation

Considering a diagram of the type of figure 4.4 which depicts a real gluon radiated off a quark line, and, for the sake of generality, allowing for the possibility of a non-vanishing

quark mass $m > 0$, the matrix element of this real emission process is given as:

$$\mathcal{M}_{\text{real}} = \widetilde{\mathcal{M}}_{\text{hard}} \frac{i(\not{p} - \not{k} + m)}{(p-k)^2 - m^2 + i\epsilon} \left(-ig_{\text{s}} T^a_{ji} \gamma^\mu\right) u(p)\, \varepsilon^*_\mu(k), \tag{4.23}$$

where $\widetilde{\mathcal{M}}_{\text{hard}}$ is the matrix element of the remaining hard subprocess, as shown with the grey circle, $g_{\text{s}} = \sqrt{4\pi\alpha_{\text{s}}}$ is the strong coupling, T^a_{ji} are the generators of the fundamental representation of the SU(N_c) gauge group with a being an adjoint and i, j being fundamental indices, and $u(p)$ and $\varepsilon^*_\mu(k)$ are the usual spinors and polarisation vectors for external quarks and gluons. Slashed variables correspond to Feynman's shorthand notation: $\not{p} = p_\mu \gamma^\mu$. Taking the soft limit $k \to 0$ makes it possible to neglect $\not{k}$ in comparison to $\not{p}$ in the numerator as $k^\mu \ll p^\mu$ for all components[1]. The soft limit with the consequent suppression of small momenta is also referred to as the *eikonal approximation*. Using the following identity:

$$\not{p}\gamma^\mu u(p) = \left[-\gamma^\mu \not{p} + 2p^\mu\right] u(p) = \left[-\gamma^\mu m + 2p^\mu\right] u(p) \tag{4.24}$$

which simply is the anticommutation relation for γ matrices, $\left\{\gamma^\mu, \gamma^\nu\right\} = 2g^{\mu\nu}$, with the second equation corresponding to an application of the Dirac equation, $\left(\not{p} - m\right) u(p) = 0$, while furthermore using the on-shell property of $p^2 = m^2$ in the denominator, the matrix element simplifies to:

$$\begin{aligned} \mathcal{M}_{\text{real}} &\xrightarrow{k \to 0} \widetilde{\mathcal{M}}_{\text{hard}}\, u(p) \frac{2p^\mu}{-2p \cdot k + i\epsilon} g_{\text{s}} T^a_{ji}\, \varepsilon^*_\mu(k) \\ &= \mathcal{M}_{\text{hard}} \times \left(-g_{\text{s}} T^a_{ji} \frac{v^\mu}{v \cdot k - i\epsilon} \varepsilon^*_\mu(k)\right). \end{aligned} \tag{4.25}$$

$\mathcal{M}_{\text{hard}}$ now denotes the full hard matrix element as if the additional radiated gluon were absent (while the tilde was indicating that a spinor for the external quark was missing). It is completely factorised from the second factor in the sense that they do not share any Lorentz or spinor indices or kinematical dependencies with each other. To make the kinematical independence of the two factors even more explicit, the quark momentum p^μ is written in terms of a dimensionless vector v^μ, only depending on the direction of the quark:

$$p^\mu = Q v^\mu = \sqrt{\frac{\hat{s}}{2}} v^\mu, \tag{4.26}$$

where Q denotes a characteristic scale of the process, often chosen to be $\sqrt{\hat{s}/2}$. The second factor in eq. (4.25) constitutes the *eikonal Feynman rule* for the emission of a gluon from an incoming quark line, the latter being called an *eikonal line*.

The eikonal Feynman rules can be generalised to soft-gluon emission from quark, antiquark,

[1] It also leads to a suppression of the k^2 term in the denominator when expanding the product $(p-k)^2 - m^2 = p^2 - 2p \cdot k + k^2 - m^2 \approx -2p \cdot k$; this is automatic for the real emission of gluons due to the on-shell relation. However, since the factorisation in the soft limit can also be applied to virtual diagrams, it is worth mentioning here.

Direction	Emitting particle	Eikonal Feynman rule
incoming	quark	$-g_s T^a_{ji} \frac{v^\mu}{v \cdot k - i\epsilon} \varepsilon^*_\mu(k)$
	antiquark	$g_s T^a_{ij} \frac{v^\mu}{v \cdot k - i\epsilon} \varepsilon^*_\mu(k)$
	gluon	$-ig_s f^{ija} \frac{v^\mu}{v \cdot k - i\epsilon} \varepsilon^*_\mu(k)$
outgoing	quark	$g_s T^a_{ij} \frac{v^\mu}{v \cdot k + i\epsilon} \varepsilon^*_\mu(k)$
	antiquark	$-g_s T^a_{ji} \frac{v^\mu}{v \cdot k + i\epsilon} \varepsilon^*_\mu(k)$
	gluon	$-ig_s f^{ija} \frac{v^\mu}{v \cdot k + i\epsilon} \varepsilon^*_\mu(k)$

Table 4.1: List of eikonal Feynman rules for different cases of incoming and outgoing particles. For quarks, i, j denote fundamental SU(N_c) indices, whereas for gluons, i, j are adjoint indices, with a always denoting the adjoint index of the radiated gluon. The colour index i always belongs to the "outermost" (or external) parton, with v^μ (see the definition in the accompanying text) always pointing in the direction of a momentum flowing into the diagram for incoming lines, and out of the diagram for outgoing lines. The T^a_{ij} correspond to the colour generators of the fundamental representation of SU(N_c), while the f^{ija} are the totally antisymmetric structure constants.

or gluon lines (and in principle other particles with a similar colour structure as those mentioned) by doing the corresponding calculations. Table 4.1 lists all eikonal Feynman rules that appear in QCD (and in principle also SUSY-QCD by considering squarks instead of quarks and gluinos instead of gluons).

It can be shown that this factorisation property is valid also for multiple soft gluons attached to a hard matrix element with an eikonal factor for each additional gluon (see e.g. ref. [143]). As a result, when considering soft-gluon emission up to all orders in α_s, the eikonal factors exponentiate, where one only has to pay attention to keeping the correct order of the colour generators which is usually dealt with by introducing additional colour- or path-ordering operators. The eikonal approximation can also be used on a virtual gluon in a loop, leading to the same factorised form. As the eikonal factors are independent of the kinematics of the hard process (in fact, they only depend via v^μ on the direction of the quark), they can be regarded as their own subdiagrams, being calculable independently from the hard process.

Before proceeding to go into details regarding the factorisation of the phase space in the soft limit, a mathematical tool is introduced which is required for the following calculations.

4.1.4 Mellin-moment space

The Mellin transform $\tilde{f}(N)$ of an arbitrary function $f(x)$ with respect to x is defined as an integral transform of the following type:

$$\tilde{f}(N) := \int_0^\infty \mathrm{d}x\, x^{N-1} f(x), \tag{4.27}$$

where N is Mellin-moment variable. Most of the functions of interest in this thesis generally vanish for an argument $x > 1$ due to kinematical constraints, so that the Mellin transform is usually defined with an upper limit of 1:

$$\tilde{f}(N) := \int_0^1 \mathrm{d}x\, x^{N-1} f(x). \tag{4.28}$$

Taking the limit $x \to 1$ in $f(x)$ correspond to $N \to \infty$ in $\tilde{f}(N)$. This can easily be seen in the fact that for large N, the factor x^{N-1} reweights the integrand, leading to a strong suppression towards the lower integration boundary, $x = 0$, effectively only taking into account the contributions of $f(x)$ at $x \approx 1$.

The inverse Mellin transform then follows as:

$$f(x) = \frac{1}{2\pi i} \int_{c-i\infty}^{c+i\infty} \mathrm{d}N\, x^{-N} \tilde{f}(N), \tag{4.29}$$

where the notation denotes a line integral along a straight curve parallel to the imaginary axis in the complex plane, shifted by a real value c from the origin.

4.1.5 Factorisation of the phase space

The general three-body phase space for real gluon emission is given as:

$$\begin{aligned}\mathrm{dPS}_3(P = q_1 + q_2; k_1, p_1, p_2) = \frac{\mathrm{d}^3 p_1}{(2\pi)^3 2p_{1,0}} \frac{\mathrm{d}^3 p_2}{(2\pi)^3 2p_{2,0}} (2\pi)^4 \delta^{(4)}(P - p_1 - p_2 - k_1) \\ \times \frac{\mathrm{d}^3 k_1}{(2\pi)^3 2k_{1,0}} \mathrm{d}Q^2\, \delta([P - k_1]^2 - Q^2)\end{aligned} \tag{4.30}$$

with q_1, q_2 the momenta of the incoming particles, p_1, p_2 the momenta of the final-state particles, and k_1 the momentum of the radiated gluon. Q^2 denotes the invariant mass of the final-state system. Neglecting the k_1 in the first delta function with respect to p_1 and p_2, corresponding to taking the soft limit, leads to the first line turning into the two-body phase space of the Born process. For the real emission of n gluons, the phase space then changes into:

$$\mathrm{dPS}_{2+n}(P = q_1 + q_2; k_1, \dots, k_n, p_1, p_2) \approx \mathrm{dPS}_2(P = q_1 + q_2; p_1, p_2)$$

$$\times \delta\left(\left[P - \sum_i k_i\right]^2 - Q^2\right) \mathrm{d}Q^2 \prod_{l=1}^{n} \frac{\mathrm{d}^3 k_l}{(2\pi)^3 2k_{l,0}}, \tag{4.31}$$

where the approximation denotes the fact that in the $2 \to 2$ phase space, the soft gluon momenta have been neglected. The delta function can be rewritten:

$$\begin{aligned}
\delta\left(\left[P - \sum_i k_i\right]^2 - Q^2\right) &= \delta\left(\hat{s} - 2\sqrt{s}\sum_i k_{i,0} + \left[\sum_i k_i\right]^2 - Q^2\right) \\
&\approx \delta\left(\hat{s} - 2\sqrt{\hat{s}}\sum_i k_{i,0} - Q^2\right) \\
&= \frac{1}{\hat{s}}\delta\left(1 - \frac{2\sum_i k_{i,0}}{\sqrt{\hat{s}}} - \frac{Q^2}{\hat{s}}\right) \\
&= \frac{1}{\hat{s}}\delta\left(1 - z - \sum_i z_i\right)
\end{aligned} \tag{4.32}$$

with $\hat{s} = (q_1 + q_2)^2$ the centre-of-mass energy, $z = Q^2/\hat{s}$, and $z_i = 2k_{i,0}/\sqrt{\hat{s}}$. In the second line of eq. (4.32), squared terms in the soft-gluon momenta have been neglected. For a differential cross section in the invariant mass, i.e. not integrating over Q^2, the remaining phase space is:

$$\begin{aligned}
\mathrm{dPS}_{2+n}(P = q_1 + q_2; k_1, \ldots, k_n, p_1, p_2) &= \mathrm{dPS}_2(P = q_1 + q_2; p_1, p_2) \\
&\times \frac{1}{\hat{s}}\delta\left(1 - z - \sum_i z_i\right) \prod_{l=1}^{n} \frac{\mathrm{d}^3 k_l}{(2\pi)^3 2k_{l,0}}.
\end{aligned} \tag{4.33}$$

The delta function causes an entanglement between the integrations, preventing a factorisation of the soft gluons from the two-body phase space. However, representing the delta function as its Fourier transform results in an exponential function,

$$\begin{aligned}
\delta\left(1 - z - \sum_i z_i\right) &= \frac{1}{2\pi}\int_{-\infty}^{\infty} \mathrm{d}\tilde{N}\, e^{i\tilde{N}(1 - z - \sum_i z_i)} = \frac{1}{2\pi i}\int_{c-i\infty}^{c+i\infty} \mathrm{d}N\, e^{N(1 - z - \sum_i z_i)} \\
&\overset{z\to 1}{\approx} \frac{1}{2\pi i}\int_{c-i\infty}^{c+i\infty} \mathrm{d}N\, z^{-N} \prod_i e^{-N z_i},
\end{aligned} \tag{4.34}$$

where in the second step, the substitution $N = i\tilde{N}$ and a shift of the integration contour by a real constant c have been carried out, to turn the Fourier transform into a Laplace transform. In the third step, the soft limit $z \to 1$ has been used to express $1 - z$ as $\ln(z)$, and subsequently $e^{N(1-z)} \approx e^{-N \ln z} = z^{-N}$. The result after the last step denotes an inverse Mellin transform with respect to the variable z.

Obviously, the delta function factorises completely under such a Mellin transform. In the

soft limit ($z_i \to 0$, $z \to 1$), the delta function can be approximated as

$$\delta\left(1 - z - \sum_i z_i\right) \approx \delta\left(z - \prod_i (1 - z_i)\right) \tag{4.35}$$

by neglecting quadratic terms and higher in the z_i. Such a multiplicative relation factorises exactly under a Mellin transform:

$$\int_0^1 \mathrm{d}z\, z^{N-1}\, \delta\left(z - \prod_i (1 - z_i)\right) = \prod_i (1 - z_i)^{N-1}. \tag{4.36}$$

Finally, in summary, in this section it has been shown that the phase space of a differential cross section $\mathrm{d}\sigma/\mathrm{d}Q^2$ with n extra real gluons factorises in the soft limit under a Mellin transform:

$$\int_0^1 \mathrm{d}z\, z^{N-1} \mathrm{dPS}_{2+n} \approx \mathrm{dPS}_2 \times \frac{1}{\hat{s}} \prod_{i=1}^{n} \left[\frac{\mathrm{d}^3 k_i}{(2\pi)^3 2k_{i,0}} (1 - z_i)^{N-1}\right]. \tag{4.37}$$

With both the amplitudes as well as the phase space having been shown to factorise in the soft limit, the next section will discuss how such factorisation properties of a cross section automatically lead to the resummation of the logarithms of eq. (4.21).

4.2 Factorisation and Resummation

The QCD factorisation theorem plays an important role in calculating inclusive hadronic cross sections, the quantities measured by the experiments. It is based upon a separation of long-distance effects, which describe non-perturbatively the hadronic structure of the colliding hadrons, from short-distance effects, those are the partonic cross sections which can be calculated perturbatively. While factorisation plays a role in a lot of different types of processes (deep inelastic scattering, Drell-Yan, fragmentation), the following discussion will focus only on Drell-Yan-like processes, i.e. the collision of two hadrons (usually protons) in the initial state producing a colour-singlet final state, and later also the production of massive coloured final-state particles (see also e.g. ref. [155] for a more in-depth discussion on factorisation from an analytic point of view).

An important requirement for factorisation, as can also be deduced from the physical interpretation in section 2.2.2, is that the characteristic scale of the process (e.g. for a Drell-Yan-like process, $Q^2 = (p_1 + p_2)^2$ with p_1 and p_2 the momenta of the observed final-state particles) is large enough. For a production cross section of a final state X through the scattering of two hadrons, $h_1 + h_2 \to X$, differential with respect to the invariant mass Q^2, the general factorisation formula, using the variables $z = Q^2/\hat{s}$ and $\rho_Q = Q^2/S$, is given as:

$$\frac{\mathrm{d}\sigma_{h_1 h_2 \to X}}{\mathrm{d}Q^2}\left(S, Q^2, \alpha_\mathrm{s}(\mu_R^2)\right) = \sum_{i,j} \int \mathrm{d}z\, \mathrm{d}x_1\, \mathrm{d}x_2\, f_{i/h_1}(x_1, \mu_F^2)\, f_{j/h_2}(x_2, \mu_F^2)\, \delta\left(z - \frac{\rho_Q}{x_1 x_2}\right)$$

$$\times\, \omega_{ij\to X}\left(z, \alpha_s(\mu_R^2), \mu_F^2\right). \tag{4.38}$$

Here, $S = (P_1 + P_2)^2$ is the hadronic centre-of-mass energy, with the proton momenta P_1 and P_2. x_1 and x_2 denote the momentum fractions from the full proton momenta that the scattered partons carry, $q_1 = x_1 P_1$, $q_2 = x_2 P_2$. The partonic centre-of-mass energy is given by $\hat{s} = (q_1 + q_2)^2 \approx x_1 x_2 S$. The function $f_{i/h_1}(x_1, \mu_F^2)$ denotes the parton distribution function, which can be interpreted at lowest order as the probability that a parton with flavour i is involved in the partonic scattering process, and $\omega_{ij\to X}\left(z, \alpha_s(\mu_R^2), \mu_F^2\right)$ is the partonic hard-scattering function. The dependence on a factorisation scale μ_F stems from the factorisation procedure the PDFs and the partonic cross section, as the latter develops (non-soft) collinear divergences at higher orders which are absorbed into the PDFs. Furthermore, PDFs are non-perturbative quantities, and consequently being extracted from experiments. Integrating eq. (4.38) over the invariant mass results in the total inclusive hadronic cross section.

For the following discussion, as is commonly done, the renormalisation and factorisation scales are set equal, $\mu = \mu_R = \mu_F$. At a later point, after deriving the resummed equations, explicit dependencies on the two different scales will be introduced again.

4.2.1 Refactorisation near threshold

One important property of factorisation is the freedom to choose the long- and short-distance parts which are convoluted. An alternative choice of parton densities then simply needs to be compensated by a corresponding change of the partonic cross section [156]. Furthermore, the factorisation theorem is also valid for a partonic scattering process instead of a hadronic one. The groundwork for the resummation of divergent structures using these properties of factorisation has been established by the works of Sterman, Catani, and Trentadue in refs. [156, 157]. The main idea will therefore strongly follow these references.

In particular, one can define *parton-in-parton densities* that describe the probability for a splitting of a parton with flavour i, e.g. reinterpreting eq. (4.38) for a partonic process gives [158]:

$$\begin{aligned}\frac{\mathrm{d}\sigma_{ij\to X}}{\mathrm{d}Q^2}\left(z, \alpha_s(\mu^2)\right) = \int \mathrm{d}z'\, \mathrm{d}x_1\, \mathrm{d}x_2\, f_{i/i}(x_1, \mu^2)\, f_{j/j}(x_2, \mu^2)\, \delta\left(z' - \frac{z}{x_1 x_2}\right) \\ \times\, \omega_{ij\to X}\left(z', \alpha_s(\mu^2), \mu^2\right),\end{aligned} \tag{4.39}$$

with $f_{i/i}$ and $f_{j/j}$ so-called light-cone parton-in-parton densities (defined at a fixed light-cone momentum fraction). The hard-scattering functions $\omega_{ij\to X}$ are the same as in eq. (4.38).

This partonic scattering can alternatively be described in terms of a different kind of parton densities that separate the collinear contributions as discussed in the previous section from the hard function where no collinear particles are present [156]:

$$\frac{\mathrm{d}\sigma_{ij\to X}}{\mathrm{d}Q^2}\left(z, \alpha_s(\mu^2)\right) = \int \mathrm{d}\xi_1\, \mathrm{d}\xi_2\, \psi_{i/i}(\xi_1, \mu^2)\, \psi_{j/j}(\xi_2, \mu^2)\, \omega^{\psi}_{ij\to X}\left(\xi_1, \xi_2, z, \alpha_s(\mu^2), \mu^2\right), \tag{4.40}$$

The $\psi_{i/i}$ and $\psi_{j/j}$ are now centre-of-mass parton-in-parton densities, defined at a fixed energy,

which are more suitable to describe the emission of collinear particles close to threshold. In the following, these functions will also be referred to as the jet functions[2]. The change in the hard part $\omega^{\psi}_{ij\to X}$ compensates the changes in the parton-in-parton densities when going from eq. (4.39) to eq. (4.40).

Additionally, it is not possible to neglect the radiation of soft gluons when their energies are comparable to the remaining particles. Therefore, close to threshold, $\omega^{\psi}_{ij\to X}$ splits up into a hard function H, containing only infrared-safe interactions, and a soft function S:

$$\omega^{\psi}_{ij\to X}\left(\xi_1,\xi_2,z,\alpha_s(\mu^2),\mu^2\right) = H\left(Q^2,\alpha_s(\mu^2),\mu^2\right) \times \int \mathrm{d}w\, S\left(w,Q^2,\alpha_s(\mu^2),\mu^2\right)\,\delta\left(1-z-\xi_1-\xi_2-w\right), \tag{4.41}$$

where the delta function serves to keep the proper kinematical relations between the energy fractions z, ξ_1, ξ_2, and w. As it has been shown in section 4.1.5, for small energy fractions ξ_1, ξ_2, and w, the delta function can also be written as $\delta\left(1-z-\xi_1-\xi_2-w\right) \approx \delta\left(z-(1-\xi_1)(1-\xi_2)(1-w)\right)$. The near-threshold factorisation now has the form:

$$\begin{aligned}\frac{\mathrm{d}\sigma_{ij\to X}}{\mathrm{d}Q^2}\left(z,\alpha_s(\mu^2)\right) = {} & H\left(Q^2,\alpha_s(\mu^2),\mu^2\right) \\ & \times \int \mathrm{d}\xi_1\,\mathrm{d}\xi_2\,\mathrm{d}w\,\delta\left(z-(1-\xi_1)(1-\xi_2)(1-w)\right) \\ & \times \psi_{i/i}(\xi_1,\mu^2)\,\psi_{j/j}(\xi_2,\mu^2)\,S\left(w,Q^2,\alpha_s(\mu^2),\mu^2\right) \\ & + \mathcal{O}(1-z)\end{aligned} \tag{4.42}$$

with corrections that vanish as powers of $(1-z)$. For the purpose of showing the exponentiation of the threshold-enhanced contributions, the notation of refs. [158, 159] regarding the arguments of the hard, soft, and the jet functions as well as the normalisation of the cross section σ_0 will be used:

$$\begin{aligned}\frac{\mathrm{d}\sigma_{ij\to X}}{\mathrm{d}Q^2}\left(z,\alpha_s(\mu^2)\right) = {} & \sigma_0\, H\left(\frac{p_1}{\mu},\frac{p_2}{\mu},\zeta_i\right) \\ & \times \int \mathrm{d}\xi_1\,\mathrm{d}\xi_2\,\mathrm{d}w\,\delta\left(z-(1-\xi_1)(1-\xi_2)(1-w)\right) \\ & \times \psi_{i/i}\left(\frac{p_1\cdot\zeta_1}{\mu},\xi_1\frac{Q}{\mu}\right)\,\psi_{j/j}\left(\frac{p_2\cdot\zeta_2}{\mu},\xi_2\frac{Q}{\mu}\right)\,S\left(w\frac{Q}{\mu},v_i,\zeta_i\right) \\ & + \mathcal{O}(1-z),\end{aligned} \tag{4.43}$$

where ζ_i are gauge-fixing vectors and $v_{i=1,2}$ are dimensionless vectors pointing in the same direction as p_1 and p_2, see eq. (4.26). Applying a Mellin transform with respect to the variable

[2] See e.g. eq. (2.1) of ref. [156] for a definition of such a jet function for quarks in operator matrix element notation.

z to eq. (4.43) results in a simple product of the hard, soft, and jet functions:

$$\begin{aligned}\tilde{\sigma}(N) &:= \int_0^1 \mathrm{d}z\, z^{N-1} \frac{1}{\sigma_0} \frac{\mathrm{d}\sigma_{ij\to X}}{\mathrm{d}Q^2}\left(z, \alpha_\mathrm{s}(\mu^2)\right) \\ &= H\left(\frac{p_1}{\mu}, \frac{p_2}{\mu}, \zeta_i\right) \tilde{S}\left(\frac{Q}{\mu N}, v_i, \zeta_i\right) \tilde{\psi}_{i/i}\left(\frac{p_1\cdot\zeta_1}{\mu}, \frac{Q}{\mu N}\right) \tilde{\psi}_{j/j}\left(\frac{p_2\cdot\zeta_2}{\mu}, \frac{Q}{\mu N}\right) \end{aligned} \tag{4.44}$$

with

$$\begin{aligned}\tilde{S}\left(\frac{Q}{\mu N}, v_i, \zeta_i\right) &:= \int_0^1 \mathrm{d}w\, (1-w)^{N-1}\, S\left(w\frac{Q}{\mu}, v_i, \zeta_i\right), \\ \tilde{\psi}_{i/i}\left(\frac{p_1\cdot\zeta_1}{\mu}, \frac{Q}{\mu N}\right) &:= \int_0^1 \mathrm{d}\xi_1\, (1-\xi_1)^{N-1}\, \psi_{i/i}\left(\frac{p_1\cdot\zeta_1}{\mu}, \xi_1\frac{Q}{\mu}\right), \\ \tilde{\psi}_{j/j}\left(\frac{p_2\cdot\zeta_2}{\mu}, \frac{Q}{\mu N}\right) &:= \int_0^1 \mathrm{d}\xi_2\, (1-\xi_2)^{N-1}\, \psi_{j/j}\left(\frac{p_2\cdot\zeta_2}{\mu}, \xi_2\frac{Q}{\mu}\right). \end{aligned} \tag{4.45}$$

Eq. (4.44) separates all threshold-enhanced contributions appearing in the cross section, i.e. the plus distributions of section 4.1.2, in the convenient form of a simple product.

4.2.2 Renormalisation group approach to resummation

Another property of the physical all-order cross section – besides the factorisation near threshold – is the independence of the unphysical renormalisation scale, which is only introduced in the regularisation process of ultraviolet divergences while truncating the perturbative series in α_s. This property is unchanged by the Mellin transform, thus causing the derivative of $\tilde{\sigma}(N)$ with respect to μ to vanish:

$$\mu\frac{\mathrm{d}}{\mathrm{d}\mu}\tilde{\sigma}(N) = 0. \tag{4.46}$$

The renormalisation scale dependence of the hard, soft, and jet functions is therefore multiplicative and leads to the following relations defining the anomalous dimensions:

$$\begin{aligned}\mu\frac{\mathrm{d}}{\mathrm{d}\mu}\ln H &= -\gamma_H(\alpha_\mathrm{s}), \\ \mu\frac{\mathrm{d}}{\mathrm{d}\mu}\ln\tilde{\psi}_i &= -\gamma_{\psi_i}(\alpha_\mathrm{s}), \quad (i=1,2) \\ \mu\frac{\mathrm{d}}{\mathrm{d}\mu}\ln\tilde{S} &= -\gamma_S(\alpha_\mathrm{s}). \end{aligned} \tag{4.47}$$

To simplify the expressions, the subscripts of the jet functions are changed to $\tilde{\psi}_{i/i} = \tilde{\psi}_1$ and $\tilde{\psi}_{j/j} = \tilde{\psi}_2$. The independence of $\tilde{\sigma}(N)$ from μ furthermore requires that the sum of these

anomalous dimensions vanishes:

$$\gamma_H + \gamma_S + \sum_i \gamma_{\psi_i} = 0. \tag{4.48}$$

The solutions for the functions from eq. (4.47), determined from separation of variables, are:

$$\begin{aligned}
\tilde{S}\left(\frac{Q}{\mu N}, v_i, \zeta_i, \alpha_s(\mu^2)\right) &= \tilde{S}\left(1, v_i, \zeta_i, \alpha_s(Q^2/N^2)\right) \exp\left[-\int_{Q/N}^{\mu} \frac{\mathrm{d}\lambda}{\lambda} \gamma_S\left(\alpha_s(\lambda^2)\right)\right] \\
\tilde{\psi}_i\left(\frac{p_i \cdot \zeta_i}{\mu}, \frac{Q}{\mu N}, \alpha_s(\mu^2)\right) &= \tilde{\psi}_i\left(\frac{(p_i \cdot \zeta_i)N}{Q}, 1, \alpha_s(Q^2/N^2)\right) \exp\left[-\int_{Q/N}^{\mu} \frac{\mathrm{d}\lambda}{\lambda} \gamma_{\psi_i}\left(\alpha_s(\lambda^2)\right)\right]
\end{aligned} \tag{4.49}$$

At this point, it should be noted that the exponentiation of the functions in eq. (4.49) constitutes the resummation, however not yet completely. From the structure of the integrals, it becomes clear that the exponents contain only single logarithms in N, while the leading terms should be proportional to double logarithms in N. This can be understood from the reasoning that every divergent structure of gluon emission (soft or collinear) produces one logarithm in N, while a gluon that is both soft and collinear at the same time, radiated off an initial-state parton, results in a squared logarithmic term.

Fortunately, yet another property of the cross section helps to fix this apparent issue regarding the missing logarithm. In eq. (4.43), gauge-fixing vectors ζ_i were introduced. As the physical cross section should deliver the same results regardless of the gauge chosen, it cannot depend on the gauge vectors and the gauge dependence must cancel between the hard, soft, and jet functions:

$$p_i \cdot \zeta_i \frac{\mathrm{d}}{\mathrm{d}p_i \cdot \zeta_i} \tilde{\sigma}(N) = 0. \tag{4.50}$$

Focussing on just one gauge vector ζ_1 and noting that $\tilde{\psi}_2$ is independent of ζ_1, the following relation needs to hold:

$$0 = \left(p_1 \cdot \zeta_1 \frac{\partial}{\partial p_1 \cdot \zeta_1} H\right) \tilde{\psi}_1 \tilde{\psi}_2 \tilde{S} + H \left(p_1 \cdot \zeta_1 \frac{\partial}{\partial p_1 \cdot \zeta_1} \tilde{\psi}_1\right) \tilde{\psi}_2 \tilde{S} + H \tilde{\psi}_1 \left(p_1 \cdot \zeta_1 \frac{\partial}{\partial p_1 \cdot \zeta_1} \tilde{S}\right) \tilde{\psi}_2, \tag{4.51}$$

or divided by $\tilde{\sigma}(N)$:

$$\begin{aligned}
p_1 \cdot \zeta_1 \frac{\partial}{\partial p_1 \cdot \zeta_1} \ln \tilde{\psi}_1\left(\frac{p_1 \cdot \zeta_1}{\mu}, \frac{Q}{\mu N}, \alpha_s(\mu^2)\right) &= -p_1 \cdot \zeta_1 \frac{\partial}{\partial p_1 \cdot \zeta_1} \ln H\left(\frac{p_1}{\mu}, \frac{p_2}{\mu}, \zeta_i, \alpha_s(\mu^2)\right) \\
&\quad - p_1 \cdot \zeta_1 \frac{\partial}{\partial p_1 \cdot \zeta_1} \ln \tilde{S}\left(\frac{Q}{\mu N}, v_i, \zeta_i, \alpha_s(\mu^2)\right).
\end{aligned} \tag{4.52}$$

The derivative of $\tilde{\psi}_1$ with respect to $p_1 \cdot \zeta_1$ therefore splits up additively into one function depending only on the hard scale $Q \sim p_1 \cdot \zeta_1$, and another one depending only on the soft scale Q/N. By defining two functions which describe the variation of H and $\tilde{S}$ with respect

to ζ_1,

$$G\left(\frac{p_1\cdot\zeta_1}{\mu},\alpha_s(\mu^2)\right) := -p_1\cdot\zeta_1\frac{\partial}{\partial p_1\cdot\zeta_1}\ln H\left(\frac{p_1}{\mu},\frac{p_2}{\mu},\zeta_i,\alpha_s(\mu^2)\right) + C\left(\alpha_s(\mu^2)\right),$$
$$K\left(\frac{Q}{\mu N},\alpha_s(\mu^2)\right) := -p_1\cdot\zeta_1\frac{\partial}{\partial p_1\cdot\zeta_1}\ln\tilde{S}\left(\frac{Q}{\mu N},v_i,\zeta_i,\alpha_s(\mu^2)\right) - C\left(\alpha_s(\mu^2)\right) \tag{4.53}$$

with $C\left(\alpha_s(\mu^2)\right)$ an arbitrary perturbative function only depending implicitely on the renormalisation scale through $\alpha_s(\mu^2)$, eq. (4.52) becomes:

$$p_1\cdot\zeta_1\frac{\partial}{\partial p_1\cdot\zeta_1}\ln\tilde{\psi}_1\left(\frac{p_1\cdot\zeta_1}{\mu},\frac{Q}{\mu N},\alpha_s(\mu^2)\right) = G\left(\frac{p_1\cdot\zeta_1}{\mu},\alpha_s(\mu^2)\right) + K\left(\frac{Q}{\mu N},\alpha_s(\mu^2)\right). \tag{4.54}$$

Due to the multiplicative renormalisation of $\tilde{\psi}_1$ in eq. (4.47) and the independence of the anomalous dimension γ_{ψ_1} from the combination $p_1\cdot\zeta_1$, the sum $G+K$ is renormalisation scale invariant:

$$p_1\cdot\zeta_1\frac{\mathrm{d}}{\mathrm{d}p_1\cdot\zeta_1}\gamma_{\psi_i}\left(\alpha_s(\mu^2)\right) = \mu\frac{\mathrm{d}}{\mathrm{d}\mu}\left[G\left(\frac{p_1\cdot\zeta_1}{\mu},\alpha_s(\mu^2)\right) + K\left(\frac{Q}{\mu N},\alpha_s(\mu^2)\right)\right] = 0, \tag{4.55}$$

and one can define a so-called Sudakov anomalous dimension γ_K:

$$\mu\frac{\mathrm{d}}{\mathrm{d}\mu}K\left(\frac{Q}{\mu N},\alpha_s(\mu^2)\right) = -\gamma_K\left(\alpha_s(\mu^2)\right) \tag{4.56}$$

$$\mu\frac{\mathrm{d}}{\mathrm{d}\mu}G\left(\frac{p_1\cdot\zeta_1}{\mu},\alpha_s(\mu^2)\right) = \gamma_K\left(\alpha_s(\mu^2)\right). \tag{4.57}$$

Solving these differential equations separately with different initial conditions then results in the following solution for $G+K$:

$$G\left(\frac{p_1\cdot\zeta_1}{\mu},\alpha_s(\mu^2)\right) + K\left(\frac{Q}{\mu N},\alpha_s(\mu^2)\right) = G\left(1,\alpha_s\left((p_1\cdot\zeta_1)^2\right)\right) + K\left(1,\alpha_s\left(\frac{Q^2}{N^2}\right)\right) - \int_{Q/N}^{p_1\cdot\zeta_1}\frac{\mathrm{d}\xi}{\xi}\gamma_K\left(\alpha_s(\xi^2)\right). \tag{4.58}$$

Now, the scale of the α_s argument in K can be changed to the same one as in G by adding the following term to the integral:

$$K\left(1,\alpha_s\left(\frac{Q^2}{N^2}\right)\right) = K\left(1,\alpha_s((p_1\cdot\zeta_1)^2)\right) + \int_{p_1\cdot\zeta_1}^{Q/N}\frac{\mathrm{d}\mu}{\mu}\left\{2\beta\left(\alpha_s(\mu^2)\right)\frac{\partial}{\partial\alpha_s}K\left(1,\alpha_s\right)\right\} \tag{4.59}$$

with $\beta(\alpha_s)$ the QCD beta function, as introduced in section 2.2.1. This shift in the argument

of α_s results in an expression of the form

$$G\left(\frac{p_1\cdot\zeta_1}{\mu},\alpha_s(\mu^2)\right)+K\left(\frac{Q}{\mu N},\alpha_s(\mu^2)\right)=A'\left(\alpha_s((p_1\cdot\zeta_1)^2)\right)-\int_{Q/N}^{p_1\cdot\zeta_1}\frac{d\xi}{\xi}A\left(\alpha_s(\xi^2)\right) \tag{4.60}$$

with

$$\begin{aligned}A'\left(\alpha_s(\mu^2)\right)&=G\left(1,\alpha_s(\mu^2)\right)+K\left(1,\alpha_s(\mu^2)\right),\\ A\left(\alpha_s(\mu^2)\right)&=\gamma_K\left(\alpha_s(\mu^2)\right)+2\beta(\alpha_s(\mu^2))\frac{\partial}{\partial\alpha_s}K(1,\alpha_s).\end{aligned} \tag{4.61}$$

It is possible to solve eq. (4.54) now by again separating the variables and integrating over $p_1\cdot\zeta_1$:

$$\begin{aligned}\tilde{\psi}_1\left(\frac{p_1\cdot\zeta_1}{\mu},\frac{Q}{\mu N},\alpha_s(\mu^2)\right)&=\tilde{\psi}_1\left(1,\frac{Q}{\mu N},\alpha_s(\mu^2)\right)\\ &\times\exp\left[-\int_\mu^{p_1\cdot\zeta_1}\frac{d\lambda}{\lambda}\left(\int_{Q/N}^{\lambda}\frac{d\xi}{\xi}A\left(\alpha_s(\xi^2)\right)-A'\left(\alpha_s(\lambda^2)\right)\right)\right].\end{aligned} \tag{4.62}$$

The double integral in the exponent will evaluate to the double logarithms in N for soft-collinear gluon emission. The renormalisation scale dependence can be expressed with eq. (4.49) through another exponential function to get the final form of the jet function:

$$\begin{aligned}\tilde{\psi}_i\left(\frac{p_i\cdot\zeta_i}{\mu},\frac{Q}{\mu N},\alpha_s(\mu^2)\right)&=\tilde{\psi}_i\left(1,1,\alpha_s(Q^2/N^2)\right)\exp\left[-\int_{Q/N}^{\mu}\frac{d\lambda}{\lambda}\gamma_{\psi_i}\left(\alpha_s(\lambda^2)\right)\right]\\ &\times\exp\left[-\int_{Q/N}^{p_i\cdot\zeta_i}\frac{d\lambda}{\lambda}\left(\int_{Q/N}^{\lambda}\frac{d\xi}{\xi}A\left(\alpha_s(\xi^2)\right)-A'\left(\alpha_s(\lambda^2)\right)\right)\right].\end{aligned} \tag{4.63}$$

Assuming that the gauge vectors and scales are chosen in such a way that $p_i\cdot\zeta_i=Q$ $(i=1,2)$ and $\mu=Q$, the fully resummed cross section, together with the solution of the soft function from eq. (4.49), becomes:

$$\begin{aligned}\tilde{\sigma}(N)&=H\left(1,1,\alpha_s(Q^2)\right)\,\tilde{S}\left(1,\alpha_s(Q^2/N^2)\right)\,\tilde{\psi}_1\left(1,1,\alpha_s(Q^2/N^2)\right)\,\tilde{\psi}_2\left(1,1,\alpha_s(Q^2/N^2)\right)\\ &\times\exp\left[-2\int_{Q/N}^{Q}\frac{d\lambda}{\lambda}\left(\int_{Q/N}^{\lambda}\frac{d\xi}{\xi}A\left(\alpha_s(\xi^2)\right)-B\left(\alpha_s(\lambda^2)\right)\right)\right]\end{aligned} \tag{4.64}$$

with $B\left(\alpha_s(\mu^2)\right)=A'\left(\alpha_s(\mu^2)\right)-\frac{1}{2}\left[\gamma_{\psi_1}\left(\alpha_s(\mu^2)\right)+\gamma_{\psi_2}\left(\alpha_s(\mu^2)\right)+\gamma_S\left(\alpha_s(\mu^2)\right)\right]$. One can now write the functions appearing in eq. (4.64) as a perturbative series in α_s, $f(\alpha_s)=f^{(0)}+(\alpha_s/\pi)f^{(1)}+(\alpha_s/\pi)^2f^{(2)}+\ldots$, and compare the expansion of eq. (4.64) to a fixed-order calculation to determine e.g. the coefficients $A^{(i)}$, $B^{(i)}$.

4.3 Soft-gluon resummation for massive coloured final-state particles

While in the previous section, the exponentiation of logarithms in N has been shown for a Drell-Yan-like process only, ignoring the possibility for any soft-gluon radiation from final-state particles, this section serves to extend the formalism to massive coloured particles being present in the final state, as it is the case for squark and gluino production. In general, it will be necessary to split up the amplitudes into the different colour structures: considering that an initial state may only form colour states given by the direct product of their SU(N_c) representations – that is, irreducible representations thereof –, the final-state particles will be produced in the same colour structure. The soft gluon being emitted from such a final-state particle will then depend on the details of this colour structure. The consequence is that the hard and soft functions turn into matrices in colour space and in general require a diagonalisation procedure to evaluate and incorporate them into the resummed formulas.

4.3.1 Colour structures of QCD scattering processes

The SU(N_c) colour structures of interest for the processes examined in this thesis are, with the corresponding initial state mentioned in the first column [17, 131]:

$$q\bar{q}: \qquad \mathbf{N_c} \otimes \overline{\mathbf{N}}_\mathbf{c} = \mathbf{1} \oplus (\mathbf{N_c^2 - 1}), \tag{4.65}$$

$$\begin{aligned} gg: \qquad (\mathbf{N_c^2 - 1}) \otimes (\mathbf{N_c^2 - 1}) = {} & \mathbf{1} \oplus (\mathbf{N_c^2 - 1})_\mathbf{A} \oplus (\mathbf{N_c^2 - 1})_\mathbf{S} \oplus (\mathbf{N_c^2 - 1})(\mathbf{N_c^2 - 4})/\mathbf{4} \\ & \oplus \overline{(\mathbf{N_c^2 - 1})(\mathbf{N_c^2 - 4})/\mathbf{4}} \oplus \mathbf{N_c^2}(\mathbf{N_c + 3})(\mathbf{N_c - 1})/\mathbf{4} \\ & \oplus \mathbf{N_c^2}(\mathbf{N_c - 3})(\mathbf{N_c + 1})/\mathbf{4}, \end{aligned} \tag{4.66}$$

$$qq: \qquad \mathbf{N_c} \otimes \mathbf{N_c} = \mathbf{N_c}(\mathbf{N_c - 1})/\mathbf{2} \oplus \mathbf{N_c}(\mathbf{N_c + 1})/\mathbf{2}, \tag{4.67}$$

$$qg: \qquad \mathbf{N_c} \otimes (\mathbf{N_c^2 - 1}) = \mathbf{N_c} \oplus \overline{\mathbf{N_c}(\mathbf{N_c + 1})(\mathbf{N_c - 2})/\mathbf{2}} \oplus \mathbf{N_c}(\mathbf{N_c - 1})(\mathbf{N_c + 2})/\mathbf{2}, \tag{4.68}$$

denoting the dimensions of each of the representations, with the subscripts **A** and **S** referring to antisymmetric and symmetric properties of the representations, and an overline meaning conjugate representations. These colour structures will not be derived at this point. Instead, it is noted that such calculations may be performed in the framework of Young tableaux which offer a simple but powerful method to extract the irreducible representations from product representations, applying group theory relations in a diagrammatic form (see e.g. refs. [160, 161]). Not all of the mentioned structures are relevant for all processes, e.g. for the production of a squark-antisquark pair from gluon-fusion, $gg \to \tilde{q}\tilde{q}^*$, and setting $N_c = 3$, only $\mathbf{8} \otimes \mathbf{8} = \mathbf{1} \oplus \mathbf{8_A} \oplus \mathbf{8_S}$ of eq. (4.66) will be of interest, as the squark-antisquark pair may, for instance, not be produced in a **27** state. Additionally, for gluino-pair production as the only process possible in the following channels, the $(\mathbf{N_c^2 - 1})(\mathbf{N_c^2 - 4})/\mathbf{4} \oplus \overline{(\mathbf{N_c^2 - 1})(\mathbf{N_c^2 - 4})/\mathbf{4}}$ representation does not contribute at all, while $\mathbf{N_c^2}(\mathbf{N_c - 3})(\mathbf{N_c + 1})/\mathbf{4}$ is absent in the physical case of SUSY-QCD with $N_c = 3$ due to being zero-dimensional.

4.3.2 The soft anomalous dimension matrix

Having introduced the colour representations, eq. (4.44) can now be generalised to the case of massive coloured particles in the final state by writing both the hard as well as the soft functions as matrices in colour representation space:

$$\begin{aligned}\tilde{\sigma}(N) &= \mathrm{Tr}\left\{\mathbf{H}\left(\frac{p_1}{\mu},\frac{p_2}{\mu},\zeta_i\right)\tilde{\mathbf{S}}\left(\frac{Q}{\mu N},v_i,\zeta_i\right)\right\}\tilde{\psi}_1\left(\frac{p_1\cdot\zeta_1}{\mu},\frac{Q}{\mu N}\right)\tilde{\psi}_2\left(\frac{p_2\cdot\zeta_2}{\mu},\frac{Q}{\mu N}\right)\\ &= \sum_{I,J} H_{ij\to kl,IJ}\left(\frac{p_1}{\mu},\frac{p_2}{\mu},\zeta_i\right)\tilde{S}_{ij\to kl,JI}\left(\frac{Q}{\mu N},v_i,\zeta_i\right)\tilde{\psi}_1\left(\frac{p_1\cdot\zeta_1}{\mu},\frac{Q}{\mu N}\right)\tilde{\psi}_2\left(\frac{p_2\cdot\zeta_2}{\mu},\frac{Q}{\mu N}\right),\end{aligned} \tag{4.69}$$

where $ij\to kl$ stands for the partonic process with the final state kl and I,J denote the final-state colour channels into which the hard and soft functions are split up and that are summed over. The existence of two colour channel indices per function stems from the split-up into the representations happening on the amplitude level (so one index is from the amplitude itself and the other one from its complex conjugate). Due to the decoupling of soft gluons from jet functions, the latter will not depend on the specific colour channel, as it is the case for the factorisation of the hadronic cross section into colour-representation independent PDFs describing long-range behaviour and the short-range partonic cross sections. It should be noted that massive coloured particles cannot generate collinear divergences, and their jet functions are therefore absent, whereas for multi-jet production, an additional jet function for every final-state jet present in the process is required in eq. (4.69) to describe the final-state collinear divergences.

The independence of the cross section $\tilde{\sigma}(N)$ from the renormalisation scale again leads to relations between the anomalous dimensions and renormalisation constants of the hard, soft, and jet functions. In particular, the UV divergences arising in the soft function have to be cancelled by similar ones in the hard function, resulting in the following multiplicative renormalisation with the unrenormalised functions $H^{\mathrm{bare}}_{ij\to kl}$ and $\tilde{S}^{\mathrm{bare}}_{ij\to kl}$ and the renormalised ones $H_{ij\to kl}$ and $\tilde{S}_{ij\to kl}$ [158]:

$$\begin{aligned}H^{\mathrm{bare}}_{ij\to kl,IJ} &= Z_i^{-1}\,Z_j^{-1}\left(Z_{ij\to kl}\right)^{-1}_{IK} H_{ij\to kl,KL}\left(Z^{\dagger}_{ij\to kl}\right)^{-1}_{LJ},\\ \tilde{S}^{\mathrm{bare}}_{ij\to kl,JI} &= \left(Z^{\dagger}_{ij\to kl}\right)_{JK}\tilde{S}_{ij\to kl,KL}\left(Z_{ij\to kl}\right)_{LI}.\end{aligned} \tag{4.70}$$

Here, Z_i, Z_j are the renormalisation constants of the external initial-state fields, and $Z_{ij\to kl}$ is a matrix denoting the renormalisation of the soft function, already including the renormalisation of the external final-state particles. The jet functions do not require a separate renormalisation as composite operators (see also appendix A). Therefore, the renormalisation group equation for the soft function becomes:

$$\mu\frac{\mathrm{d}}{\mathrm{d}\mu}\tilde{S}_{ij\to kl,IJ} = -\Gamma^{\dagger}_{ij\to kl,IK}\tilde{S}_{ij\to kl,KJ} - \tilde{S}_{ij\to kl,IK}\Gamma_{ij\to kl,KJ}, \tag{4.71}$$

where $\Gamma_{ij\to kl}$ is the soft anomalous dimension matrix, defined in terms of the residues of the renormalisation constant:

$$\Gamma_{ij\to kl,IJ} := -\alpha_s \frac{\partial}{\partial \alpha_s} \mathrm{Res}_{\varepsilon\to 0} \left(Z_{ij\to kl}\right)_{IJ} (\alpha_s, \varepsilon). \tag{4.72}$$

The solution for eq. (4.71) is generally written in terms of path-ordered exponentials [162]:

$$\begin{aligned}\tilde{S}_{ij\to kl,IJ}\left(\frac{Q}{N\mu}, \alpha_s(\mu^2)\right) = &\left(\bar{\mathrm{P}} \exp\left\{\int_\mu^{Q/N} \frac{\mathrm{d}\lambda}{\lambda} \Gamma^\dagger_{ij\to kl}\left(\alpha_s(\lambda^2)\right)\right\}\right)_{IK} \tilde{S}_{ij\to kl,KL}\left(1, \alpha_s\left(\frac{Q^2}{N^2}\right)\right) \\ &\times \left(\mathrm{P} \exp\left\{\int_\mu^{Q/N} \frac{\mathrm{d}\lambda}{\lambda} \Gamma_{ij\to kl}\left(\alpha_s(\lambda^2)\right)\right\}\right)_{LJ},\end{aligned} \tag{4.73}$$

with P and $\bar{\mathrm{P}}$ denoting path-ordering and anti path-ordering operators in the integration variable owing to the non-commutative nature of the soft anomalous dimension matrices, and formally being defined as:

$$\begin{aligned}\mathrm{P} \exp\left\{\int_{\mu_0}^{\mu} \mathrm{d}\mu' \, \Gamma(\mu')\right\} := 1 &+ \int_{\mu_0}^{\mu} \mathrm{d}\mu_1 \, \Gamma(\mu_1) + \int_{\mu_0}^{\mu} \mathrm{d}\mu_1 \, \Gamma(\mu_1) \int_{\mu_0}^{\mu_1} \mathrm{d}\mu_2 \, \Gamma(\mu_2) \\ &+ \int_{\mu_0}^{\mu} \mathrm{d}\mu_1 \, \Gamma(\mu_1) \int_{\mu_0}^{\mu_1} \mathrm{d}\mu_2 \, \Gamma(\mu_2) \int_{\mu_0}^{\mu_2} \mathrm{d}\mu_3 \, \Gamma(\mu_3) + \dots,\end{aligned} \tag{4.74}$$

i.e. ordering terms closer to the lower integration boundary to the left and terms closer to the upper integration boundary to the right after expanding the exponential. The anti path-ordering is then defined in an analogous manner, in a reverse sense to path-ordering. In the case of diagonal soft anomalous dimension matrices,

$$\Gamma_{ij\to kl}(\alpha_s) = \mathrm{diag}\left(\dots, \lambda_{ij\to kl,I}(\alpha_s), \dots\right) \tag{4.75}$$

with $\lambda_{ij\to kl,I}$ the eigenvalues of the soft anomalous dimension matrix, the solution simplifies significantly:

$$\begin{aligned}\tilde{S}_{ij\to kl,IJ}\left(\frac{Q}{N\mu}, \alpha_s(\mu^2)\right) = &\, \tilde{S}_{ij\to kl,IJ}\left(1, \alpha_s\left(\frac{Q^2}{N^2}\right)\right) \\ &\times \exp\left\{\int_\mu^{Q/N} \frac{\mathrm{d}\nu}{\nu} \left[\lambda^*_{ij\to kl,I}\left(\alpha_s(\nu^2)\right) + \lambda_{ij\to kl,J}\left(\alpha_s(\nu^2)\right)\right]\right\},\end{aligned} \tag{4.76}$$

where the right-hand side of eq. (4.76) is understood with no summation over I or J.

The soft function at unit argument $\tilde{S}_{ij\to kl,IJ}\left(1, \alpha_s\left(\frac{Q^2}{N^2}\right)\right)$ is given at leading order as follows:

$$\tilde{S}_{ij\to kl,IJ}\left(1, \alpha_s\left(\frac{Q^2}{N^2}\right)\right) = \tilde{S}^{(0)}_{ij\to kl,IJ} := \mathrm{Tr}\left(c_I^\dagger c_J\right) \tag{4.77}$$

with $\{c_I\}$ the corresponding colour basis for the process $ij \to kl$ with a colour structure according to eqs. (4.65)–(4.68). If this colour basis is furthermore orthogonal, the soft function itself becomes diagonal:

$$\tilde{S}_{ij\to kl,IJ}\left(\frac{Q}{N\mu}, \alpha_s(\mu^2)\right) = \delta_{IJ}\, \tilde{S}^{(0)}_{ij\to kl,IJ}\, \exp\left\{\int_\mu^{Q/N} \frac{d\nu}{\nu} 2\,\mathrm{Re}\left(\lambda_{ij\to kl,I}(\alpha_s(\nu^2))\right)\right\}. \tag{4.78}$$

The diagonalisation of $\Gamma_{ij\to kl}$ as assumed in eq. (4.75) conveniently happens automatically in the absolute threshold limit by a clever choice of a colour basis. The so-called *s*-channel basis [110], tracking the colour flow of a diagram through the *s*-channel, achieves this and is used for the computation of the exponent. Alternatively, a diagonalisation procedure, as illustrated in [163], can be used, in particular if one requires the soft anomalous dimension matrix for a different definition of threshold. The calculation of the soft function and the soft anomalous dimensions require a special type of diagrams, the so-called *eikonal diagrams*, to be evaluated [164]. Alternatively, the soft function can also be calculated using *webs* [143].

4.3.3 All-order expressions for the hadronic cross section

To finalise the calculation of the resummed cross section and to convolute the results from eq. (4.64) with the parton distribution functions, it is necessary to return to the beginning of section 4.2. In eqs. (4.39) and (4.40), two different ways of factorising the partonic cross sections were shown. By computing the Mellin moments of the two expressions, the hard-scattering function $\omega_{ij\to kl}\left(z, \alpha_s(\mu^2), \mu^2\right)$ can be expressed through the exponentiated soft and jet functions. The Mellin transform of eq. (4.40) has been computed in eq. (4.44), while the Mellin transform of eq. (4.39) is:

$$\begin{aligned}\tilde{\sigma}(N) &= \int_0^1 dz\, z^{N-1} \frac{1}{\sigma_0} \frac{d\sigma_{ij\to kl}}{dQ^2}\left(z, \alpha_s(\mu^2)\right) \\ &= \tilde{f}_{i/i}(N+1, \mu^2)\, \tilde{f}_{j/j}(N+1, \mu^2)\, \tilde{\omega}_{ij\to kl}\left(N, \alpha_s(\mu^2), \mu^2\right),\end{aligned} \tag{4.79}$$

where σ_0 corresponds to the same normalisation taken in eq. (4.44), and with the Mellin-moment functions

$$\begin{aligned}\tilde{f}_{i/i}(N, \mu^2) &:= \int_0^1 dx\, x^{N-1} f_{i/i}(x, \mu^2), \\ \tilde{\omega}_{ij\to kl}\left(N, \alpha_s(\mu^2), \mu^2\right) &:= \int_0^1 dz'\, z'^{N-1}\, \omega_{ij\to kl}\left(z', \alpha_s(\mu^2), \mu^2\right).\end{aligned} \tag{4.80}$$

In the threshold limit, the argument $N+1$ of the Mellin-transformed parton-in-parton distributions can be replaced by N, neglecting terms that are suppressed by at least $1/N$ [158]. Setting eq. (4.79) equal to eq. (4.44) and also setting $\mu = Q$ results in a relation for the

Mellin-transformed hard-scattering function:

$$\tilde{\omega}_{ij\to kl}\left(N,Q^2,\alpha_\mathrm{s}(Q^2)\right)=\frac{\tilde{\psi}_{i/i}(N,Q^2,\varepsilon)\,\tilde{\psi}_{j/j}(N,Q^2,\varepsilon)}{\tilde{f}_{i/i}(N,Q^2,\varepsilon)\,\tilde{f}_{j/j}(N,Q^2,\varepsilon)}\sum_I H_{ij\to kl,I}\left(\alpha_\mathrm{s}(Q^2)\right)\tilde{S}_{ij\to kl,I}\left(N,\alpha_\mathrm{s}(Q^2)\right). \tag{4.81}$$

The notation for most of the functions has been simplified a bit, while the collinear poles in the two types of parton-in-parton distributions have been made explicit by showing a dependence on ε. As the hard-scattering function is an infrared-safe quantity, these collinear poles of the light-cone and centre-of-mass parton-in-parton distributions cancel exactly. Furthermore, as the process of interest in this thesis is the production of massive coloured particles, the notation from section 4.3 will be applied, already assuming a diagonal soft (and therefore also hard) function through a suitable choice of the colour basis, with I an index denoting the corresponding colour representation.

In ref. [159], the resummed form of the hard-scattering function for Drell-Yan from a $q\bar{q}$ initial state has been calculated up to one loop in the exponent, with $\mu = Q$. The result is written in an alternative form to eq. (4.64) by making the Mellin transform explicit in the exponent (see e.g. ref. [165] for a prescription how to relate the two forms):

$$\omega_{q\bar{q}}^{\overline{\mathrm{MS}}}\left(N,\alpha_\mathrm{s}(Q^2)\right)=R_{q\bar{q}}\left(\alpha_\mathrm{s}(Q^2)\right)\exp\left[2\int_0^1\mathrm{d}z\frac{z^{N-1}-1}{1-z}\right.$$
$$\left.\times\left\{\int_1^{(1-z)^2}\frac{\mathrm{d}\lambda}{\lambda}A_q\left(\alpha_\mathrm{s}(\lambda Q^2)\right)+B_q\left(\alpha_\mathrm{s}\left(Q^2(1-z)^2\right)\right)\right\}\right]. \tag{4.82}$$

This result can be obtained by dividing eq. (4.64) by the light-cone parton-in-parton distribution functions $f_{i/i}$, $f_{j/j}$. Here, $R(\alpha_\mathrm{s})$ is a function of the strong coupling and independent of N, and the coefficients $A(\alpha_\mathrm{s})$ and $B(\alpha_\mathrm{s})$ are written as a perturbative series, see the comments below eq. (4.64). In particular, the one-loop coefficients are $A_q^{(1)} = C_F$ and $B_q^{(1)} = 0$ in the $\overline{\mathrm{MS}}$ scheme [159].

As the soft-collinear divergences in the initial state are independent of the process and consequently only depend on the type of parton, eq. (4.82) can be used to identify the resummed parton-in-parton distributions in the following way:

$$\left[\frac{\tilde{\psi}_{i/i}(N,Q^2,\varepsilon)}{\tilde{f}_{i/i}(N,Q^2,\varepsilon)}\right]^2\tilde{S}_{i\bar{i}}\left(N,\alpha_\mathrm{s}(Q^2)\right)=R_{i\bar{i}}\left(\alpha_\mathrm{s}(Q^2)\right)\exp\left[2\int_0^1\mathrm{d}z\frac{z^{N-1}-1}{1-z}\right.$$
$$\left.\times\left\{\int_1^{(1-z)^2}\frac{\mathrm{d}\lambda}{\lambda}A_i\left(\alpha_\mathrm{s}(\lambda Q^2)\right)+B_i\left(\alpha_\mathrm{s}\left(Q^2(1-z)^2\right)\right)\right\}\right]. \tag{4.83}$$

Here, the assumption that $\tilde{\psi}_{i/i}=\tilde{\psi}_{\bar{i}/\bar{i}}$ and $\tilde{f}_{i/i}=\tilde{f}_{\bar{i}/\bar{i}}$ has been used, while flavour mixing in parton splitting is neglected due to a suppression of at least $1/N$. $\tilde{S}_{i\bar{i}}$ is the Drell-Yan soft function, describing purley soft gluon emission from eikonal lines of the initial-state partons.

It is written explicitely, because the ratio of the parton-in-parton distributions should only contain both soft and collinear contributions. Its contribution will be presented shortly.

Taking the square root of eq. (4.83) results in [110]:

$$\frac{\tilde{\psi}_{i/i}(N,Q^2,\varepsilon)}{\tilde{f}_{i/i}(N,Q^2,\varepsilon)} = R_i\left(\alpha_s(Q^2)\right)\,\Delta_i\left(N,Q^2,\alpha_s(Q^2)\right)\left[\tilde{S}_{i\bar{i}}\left(N,\alpha_s(Q^2)\right)\right]^{-\frac{1}{2}}. \tag{4.84}$$

with

$$\Delta_i\left(N,Q^2,\alpha_s(Q^2)\right) := \exp\left[\int_0^1 \mathrm{d}z\frac{z^{N-1}-1}{1-z}\left\{\int_1^{(1-z)^2}\frac{\mathrm{d}\lambda}{\lambda}A_i\left(\alpha_s(\lambda Q^2)\right)+D_i\left(\alpha_s\left(Q^2(1-z)^2\right)\right)\right\}\right] \tag{4.85}$$

and $R_i(\alpha_s) := \sqrt{R_{i\bar{i}}(\alpha_s)}$. The coefficients B_i have been renamed to D_i to denote their origin being the purely soft gluon emission, since the same symbol will be used for the coefficients for final-state soft-gluon emission, see eq. (4.93). The square root of the Drell-Yan soft function effectively isolates the contribution from one single eikonal line with parton flavour i. Therefore, it can also be applied to initial states with two different partons or ones that cannot form a colour singlet (like qg or qq).

The Drell-Yan soft function is now written as:

$$\tilde{S}_{i\bar{i}}\left(N,\alpha_s(Q^2)\right) = \tilde{S}_{i\bar{i}}\left(1,\alpha_s\left(\frac{Q^2}{N^2}\right)\right)\exp\left[\int_0^1 \mathrm{d}z\frac{z^{N-1}-1}{1-z}\Gamma_{S_{i\bar{i}}}\left(\alpha_s\left((1-z)^2Q^2\right)\right)\right] \tag{4.86}$$

with the soft anomalous dimension for a colour singlet state, written as a perturbative series in α_s:

$$\Gamma_{S_{i\bar{i}}}(\alpha_s) = \sum_{n=1}^{\infty}\left(\frac{\alpha_s}{\pi}\right)^n\Gamma^{(n)}_{S_{i\bar{i}}}. \tag{4.87}$$

The calculation of the one-loop coefficient then leads to the following expression:

$$\Gamma^{(1)}_{S_{i\bar{i}}} = C_i\left(1-\ln\left(2\frac{(v_i\cdot\zeta_i)}{|\zeta_i|^2}\right)-i\pi\right), \tag{4.88}$$

with $C_i = C_F, C_A$ for $i = q, g$. It should be noted that the gauge dependence ζ_i in the Drell-Yan soft anomalous dimension cancels at every order with gauge dependent terms in the jet and hard functions.

The hard-scattering function from eq. (4.81) can so far be written as:

$$\begin{aligned}\tilde{\omega}_{ij\to kl}\left(N,Q^2,\alpha_s(Q^2)\right) = \sum_I & R_i\left(\alpha_s(Q^2)\right)\,R_j\left(\alpha_s(Q^2)\right)\,H_{ij\to kl,I}\left(\alpha_s(Q^2)\right)\\ & \times\Delta_i\left(N,Q^2,\alpha_s(Q^2)\right)\,\Delta_j\left(N,Q^2,\alpha_s(Q^2)\right)\,\bar{\tilde{S}}_{ij\to kl,I}\left(N,\alpha_s(Q^2)\right),\end{aligned} \tag{4.89}$$

where the QCD scattering soft function has been redefined to absorb the Drell-Yan soft

function, preventing a double counting of these terms, with

$$\bar{\tilde{S}}_{ij\to kl,I} := \frac{\tilde{S}_{ij\to kl,I}}{\sqrt{\tilde{S}_{\bar{i}\bar{i}}}\sqrt{\tilde{S}_{\bar{j}\bar{j}}}}. \tag{4.90}$$

This leads to a shift in the soft anomalous dimension defined in eq. (4.72) which, at one-loop, is

$$\bar{\Gamma}_{ij\to kl,IJ} = \Gamma_{ij\to kl,IJ} - \delta_{IJ}\sum_{p=i,j} C_p \left(1 - \ln\left(2\frac{(v_p\cdot\zeta_p)}{|\zeta_p|^2}\right) - i\pi\right). \tag{4.91}$$

Similarly to the jet functions, the soft function is now written in the following form:

$$\bar{\tilde{S}}_{ij\to kl,I}\left(N,\alpha_s(Q^2)\right) = \tilde{S}_{ij\to kl,I}\left(1,\alpha_s\left(\frac{Q^2}{N^2}\right)\right)\Delta^{(s)}_{ij\to kl,I}\left(N,Q^2,\alpha_s(Q^2)\right) \tag{4.92}$$

with the exponential

$$\Delta^{(s)}_{ij\to kl,I}\left(N,Q^2,\alpha_s(Q^2)\right) := \exp\left\{\int_0^1 dz\frac{z^{N-1}-1}{1-z}D_{ij\to kl,I}\left(\alpha_s(Q^2(1-z)^2)\right)\right\}, \tag{4.93}$$

where the $D_{ij\to kl,I}$ are coefficients which are related to the eigenvalues $\bar{\lambda}_{ij\to kl,I}$ of the shifted soft anomalous dimension matrix, eq. (4.91), e.g. for the one-loop coefficient:

$$\frac{\alpha_s}{\pi}D^{(1)}_{ij\to kl,I} := 2\,\mathrm{Re}\left(\bar{\lambda}^{(1)}_{ij\to kl,I}(\alpha_s)\right). \tag{4.94}$$

The hard-scattering function is now:

$$\begin{aligned}\tilde{\omega}_{ij\to kl}\left(N,Q^2,\alpha_s(Q^2)\right) = \sum_I R_i\left(\alpha_s(Q^2)\right)R_j\left(\alpha_s(Q^2)\right)H_{ij\to kl,I}\left(\alpha_s(Q^2)\right)\tilde{S}_{ij\to kl,I}\left(1,\alpha_s\left(\frac{Q^2}{N^2}\right)\right)\\ \times\Delta_i\left(N,Q^2,\alpha_s(Q^2)\right)\Delta_j\left(N,Q^2,\alpha_s(Q^2)\right)\Delta^{(s)}_{ij\to kl,I}\left(N,Q^2,\alpha_s(Q^2)\right),\end{aligned} \tag{4.95}$$

The normalisation taken in eq. (4.43) for Drell-Yan prevents an immediate application of the derived equations to the case of massive coloured particles. However, a small trick will allow the resummed Drell-Yan expressions to be used. Following refs. [110, 166], the PDF convolution of eq. (4.38) is (but renaming $\omega_{ij\to kl}$ to $\hat{\sigma}_{ij\to kl}$ to avoid confusing it with the resummed expression from eq. (4.95)):

$$\begin{aligned}\frac{\mathrm{d}\sigma_{h_1h_2\to kl}}{\mathrm{d}Q^2}\left(\rho_Q,\alpha_s(\mu_R^2)\right) = \sum_{i,j}\sum_I\int \mathrm{d}z\,\mathrm{d}x_1\,\mathrm{d}x_2\,f_{i/h_1}(x_1,\mu_F^2)\,f_{j/h_2}(x_2,\mu_F^2)\,\delta\left(z-\frac{\rho_Q}{x_1x_2}\right)\\ \times\hat{\sigma}_{ij\to kl,I}\left(z,\mu_F^2,\alpha_s(\mu_R^2)\right)\end{aligned}$$

$$= \sum_{i,j} \sum_{I} \int \frac{\mathrm{d}z}{z} \hat{\sigma}_{ij\to kl,I}\left(z, \mu_F^2, \alpha_\mathrm{s}(\mu_R^2)\right) \times \int_{c-\infty}^{c+\infty} \frac{\mathrm{d}N}{2\pi i} \left(\frac{\rho_Q}{z}\right)^{-N+1} \tilde{f}_{i/h_1}(N, \mu_F^2)\, \tilde{f}_{j/h_2}(N, \mu_F^2). \tag{4.96}$$

Here, $\hat{\sigma}_{ij\to kl,I}$ can now be written with long- and short-distance effects factorised, both depending on the colour structure:

$$\begin{aligned}
\frac{\mathrm{d}\sigma_{h_1h_2\to kl}}{\mathrm{d}Q^2}\left(\rho_Q, \alpha_\mathrm{s}(\mu_R^2)\right) &= \sum_{i,j} \sum_{I} \int \frac{\mathrm{d}z}{z} H_{ij\to kl,I}\left(z, \mu_F^2, \alpha_\mathrm{s}(\mu_R^2)\right) \\
&\quad \times \int_{c-\infty}^{c+\infty} \frac{\mathrm{d}N}{2\pi i} \left(\frac{\rho_Q}{z}\right)^{-N+1} \tilde{f}_{i/h_1}(N, \mu_F^2)\, \tilde{f}_{j/h_2}(N, \mu_F^2)\, \tilde{\omega}_{ij\to kl}\left(N, Q^2, \alpha_\mathrm{s}(Q^2)\right) \\
&= \sum_{i,j} \sum_{I} \int \frac{\mathrm{d}z}{z} \hat{\sigma}^{(0)}_{ij\to kl,I}\left(z, \mu_F^2, \alpha_\mathrm{s}(\mu_R^2)\right) \mathcal{C}_{ij\to kl,I}\left(z, N, \mu_F^2, \alpha_\mathrm{s}(\mu_R^2)\right) \\
&\quad \times \int_{c-\infty}^{c+\infty} \frac{\mathrm{d}N}{2\pi i} \left(\frac{\rho_Q}{z}\right)^{-N+1} \tilde{f}_{i/h_1}(N, \mu_F^2)\, \tilde{f}_{j/h_2}(N, \mu_F^2) \\
&\quad \times \Delta_i\left(N, Q^2, \alpha_\mathrm{s}(Q^2)\right)\, \Delta_j\left(N, Q^2, \alpha_\mathrm{s}(Q^2)\right)\, \Delta^{(\mathrm{s})}_{ij\to kl,I}\left(N, Q^2, \alpha_\mathrm{s}(Q^2)\right)
\end{aligned} \tag{4.97}$$

with

$$\hat{\sigma}^{(0)}_{ij\to kl,I} \mathcal{C}_{ij\to kl,I} := R_i\, R_j\, H_{ij\to kl,I}\, \tilde{S}_{ij\to kl,I}. \tag{4.98}$$

Performing the integration over z (which is, in fact, another Mellin transform) and shifting $N \to N+1$ results in the finalised resummation formula:

$$\frac{\mathrm{d}\sigma^{(\mathrm{res})}_{h_1h_2\to kl}}{\mathrm{d}Q^2}\left(\rho_Q, \alpha_\mathrm{s}(\mu_R^2)\right) = \int_{c-\infty}^{c+\infty} \frac{\mathrm{d}N}{2\pi i} \rho_Q^{-N} \tilde{\sigma}^{(\mathrm{res})}_{h_1h_2\to kl}\left(N, Q^2, \alpha_\mathrm{s}(\mu_R^2)\right) \tag{4.99}$$

with

$$\begin{aligned}
\tilde{\sigma}^{(\mathrm{res})}_{h_1h_2\to kl}\left(N, Q^2, \alpha_\mathrm{s}(\mu_R^2)\right) &= \sum_{i,j} \sum_{I} \tilde{f}_{i/h_1}(N+1, \mu_F^2)\, \tilde{f}_{j/h_2}(N+1, \mu_F^2)\, \tilde{\sigma}^{(0)}_{ij\to kl,I}\left(N, \mu_F^2, \alpha_\mathrm{s}(\mu_R^2)\right) \\
&\quad \times C_{ij\to kl,I}\left(N, \mu_F^2, \alpha_\mathrm{s}(\mu_R^2)\right)\, \Delta_i \Delta_j \Delta^{(\mathrm{s})}_{ij\to kl,I}\left(N+1, Q^2, \mu_R^2, \mu_F^2, \alpha_\mathrm{s}(\mu_R^2)\right)
\end{aligned} \tag{4.100}$$

and where

$$\tilde{\sigma}^{(0)}_{ij\to kl,I}(N)\, C_{ij\to kl,I}(N) := \int_0^1 \mathrm{d}z\, z^{N-1}\, \hat{\sigma}^{(0)}_{ij\to kl,I}(z) \mathcal{C}_{ij\to kl,I}(z, N). \tag{4.101}$$

The correct renormalisation and factorisation scale dependences in the exponential functions of eq. (4.100) have been readded by taking into account the scale dependences of the parton-in-parton distribution functions, see appendix A.

The matching coefficient $\mathcal{C}_{ij\to kl,I}(z,N)$ (or $C_{ij\to kl,I}(N)$ in Mellin-moment space) contains higher-order corrections to the cross section. It has been shown that close to theshold, the corrections originate from two different sources which factorise [122, 167, 168]: higher-order terms from virtual diagrams that do not contain any soft or collinear divergences and therefore only contribute to the hard part, and *QCD Coulomb corrections*. The former will become constant terms when taking the threshold limit, and in the next chapter, they will be referred to as the *hard-matching coefficients*. Coulomb contributions on the other hand also lead to an enhancement of the cross section close to threshold and will be explored more in detail in section 4.5 where additionally, a formalism for the resummation of these terms up to all orders in α_s will be outlined.

The integrals appearing in the resummed exponentials eqs. (4.85) and (4.93) can be solved with the all-order prescription outlined in appendix B, leading to the evaluated expressions in appendix C.

4.4 Absolute threshold

While the formulas so far have been derived for a differential cross section depending on the invariant mass of the final-state particles, the same discussion is valid for total cross sections – only the latter will be used for the analysis of squark and gluino production in the following chapters 5 to 9. As the invariant mass has been integrated out for a total cross section and is not accessible anymore, the threshold is now commonly chosen to be the partonic production threshold of the particles described by the variables ρ and $\hat{\rho}$,

$$\begin{aligned}\rho &:= \frac{4m^2}{S},\\ \rho &:= \frac{4m^2}{\hat{s}} = \frac{\rho}{x_1 x_2}\end{aligned} \tag{4.102}$$

with $m = (m_k + m_l)/2$ denoting the average of m_k and m_l, the masses of the final-state particles. While $\rho \to 1$ describes the true production threshold in terms of collider variables, the partonic threshold $\hat{\rho} \to 1$ is the one that is actually realised in the partonic subprocess that is factorised and exponentiated. This corresponds to replacing the variables ρ_Q and z of eq. (4.38) in the sense $\rho_Q \to \rho, z \to \hat{\rho}$. Instead of the plus distributions of eq. (4.21), logarithms of a variable β,

$$\beta := \sqrt{1-\hat{\rho}}, \tag{4.103}$$

are now resummed, appearing at an arbitrary order in α_s while calculating higher-order corrections, and being of the following form:

$$\alpha_s^n \ln^k \beta, \quad k \leq 2n. \tag{4.104}$$

The total hadronic cross section with resummed corrections taken into account then turns into:

$$\sigma^{(\mathrm{res})}_{h_1 h_2 \to kl}\left(\rho, \alpha_s(\mu_R^2)\right) = \sum_{i,j} \int \mathrm{d}\hat{\rho}\, \mathrm{d}x_1\, \mathrm{d}x_2\, f_{i/h_1}(x_1, \mu_F^2)\, f_{j/h_2}(x_2, \mu_F^2)\, \delta\left(\hat{\rho} - \frac{\rho}{x_1 x_2}\right) \times \hat{\sigma}^{(\mathrm{res})}_{ij\to kl}\left(\hat{\rho}, \alpha_s(\mu_R^2), \mu_F^2\right) \tag{4.105}$$

with the resummed partonic cross section:

$$\hat{\sigma}^{(\mathrm{res})}_{ij\to kl}\left(\hat{\rho}, \alpha_s(\mu_R^2), \mu_F^2\right) = \int \frac{\mathrm{d}N}{2\pi i} \hat{\rho}^{-N} \tilde{\sigma}^{(\mathrm{res})}_{ij\to kl}\left(N, m^2, \mu_R^2, \mu_F^2\right) \tag{4.106}$$

and

$$\tilde{\sigma}^{(\mathrm{res})}_{ij\to kl}\left(N, m^2, \mu_R^2, \mu_F^2\right) = \sum_I \tilde{\sigma}^{(0)}_{ij\to kl,I}(N, m^2, \mu_R^2)\, C_{ij\to kl,I}(N, m^2, \mu_R^2, \mu_F^2) \times \Delta_i \Delta_j \Delta^{(\mathrm{s})}_{ij\to kl,I}(N+1, Q^2, \mu_R^2, \mu_F^2). \tag{4.107}$$

As the invariant mass has been integrated over, the parameter Q now takes the value of the typical hard scale of the process, $Q = 2m$.

Eq. (4.107) is the final expression for the partonic cross section including fully resummed soft-gluon corrections. The resummed logarithms are contained in the exponential functions $\Delta_i \Delta_j \Delta^{(\mathrm{s})}_{ij\to kl,I}$, where $\Delta_i \Delta_j$ describe the soft-collinear and $\Delta^{(\mathrm{s})}_{ij\to kl,I}$ the soft wide-angle gluon emission. The integral representation is given in eqs. (4.85) and (4.93). The method of appendix B can be used to calculate the integrals up to a given logarithmic accuracy. Schematically, the exponentials can then be written as a sum of functions:

$$\Delta_i \Delta_j \Delta^{(\mathrm{s})}_{ij\to kl,I}(N) = \exp\left[L\, G^{(1)}_{ij}(\alpha_s \ln N) + G^{(2)}_{ij\to kl,I}(\alpha_s \ln N) + \alpha_s G^{(3)}_{ij\to kl,I}(\alpha_s \ln N) + \ldots\right]. \tag{4.108}$$

The first function $G^{(1)}_{ij}$, together with the enhancement due to the factor L, solely collects contributions from soft-collinear gluon emission off the initial-state partons which are called the *leading logarithmic* (LL) terms. The second function $G^{(2)}_{ij\to kl,I}$ also depends on the colour structure of the final-state particles, in addition to the initial-state partons, and denotes the *next-to-leading logarithmic* (NLL) contribution. The third function $G^{(3)}_{ij\to kl,I}$ is suppressed by a factor of α_s and is called the *next-to-next-to-leading logarithmic* (NNLL) contribution. Higher orders in this expansion, denoted by the three dots, are suppressed by higher orders of α_s. Explicit expressions for the functions up to NNLL are given in appendix C.

The matching coefficients $C_{ij\to kl,I}$ can be split up into the hard-matching and Coulomb

coefficients which can furthermore be separately expanded in α_s:

$$C_{ij\to kl,I}(N) = \left(1 + \frac{\alpha_s}{\pi}\mathcal{C}^{\text{Coul},(1)}_{ij\to kl,I}(N) + \frac{\alpha_s^2}{\pi^2}\mathcal{C}^{\text{Coul},(2)}_{ij\to kl,I}(N) + ...\right)\left(1 + \frac{\alpha_s}{\pi}\mathcal{C}^{(1)}_{ij\to kl,I} + \frac{\alpha_s^2}{\pi^2}\mathcal{C}^{(2)}_{ij\to kl,I} + ...\right). \tag{4.109}$$

Here, $\mathcal{C}^{\text{Coul},(1)}_{ij\to kl,I}$ denotes the N-dependent one-loop Coulomb coefficient in Mellin-moment space, $\mathcal{C}^{(1)}_{ij\to kl,I}$ denotes the N-independent one-loop hard-matching coefficient, and so on. In this thesis, the convention will be used that up to NLL accuracy, $C_{ij\to kl,I} = 1$.

4.5 Coulomb resummation

While for now, only the threshold-enhanced contributions from soft gluons have been considered, there is a second type of terms that receive a notable enhancement near threshold: the *Coulomb contributions*. These are corrections stemming from gluons that are exchanged between slowly moving final-state particles which carry a colour charge. Close to threshold, the final-state particles just have enough energy to account for their rest mass, preventing them from gaining a lot of kinetic energy. As a result, they move slowly and – just as it is the case for charged particles in QED – exchange gluons leading to an attractive or repulsive Coulomb force between them. In particular, for very massive particles, like for soft-gluon logarithms, the Coulomb effects are strongly enhanced due to the kinematical constraints. In terms of the threshold variable β, which has been introduced in the previous section, Coulomb gluon effects are proportional to

$$\frac{\alpha_s^n}{\beta^n}, \quad n \geq 1. \tag{4.110}$$

Since β stands for the relative velocity of the produced particles, slowly moving particles with $\beta \to 0$ cause the suppression from factors of the strong coupling being compensated, so that $\alpha_s/\beta \sim 1$. Therefore, it is also necessary to account for these terms up to all orders in perturbation theory to avoid introducing large uncertainties close to threshold.

Coulomb gluon effects have first been studied for the case of heavy top production in e^+e^- colliders [169–171]. As they solely depend on the colour structure of the final-state particles, the methods derived for top production can straightforwardly be applied to other processes like the production of squarks and gluinos. While Coulomb contributions with a leading-order Coulomb interaction can be described by the Sommerfeld factor (see e.g. ref. [169]), higher-order corrections to the Coulomb potential can be conveniently implemented through Green's functions.

4.5.1 Derivation of all-order Coulomb corrections from $e^+e^- \to t\bar{t}$ production

The idea of the all-order exchange of Coulomb gluons is an application of the Bethe-Salpeter equation [172]. Based on this idea are the calculations of ref. [171], which will be followed here. In ref. [171], Coulomb gluon effects up to all orders are resummed as corrections to

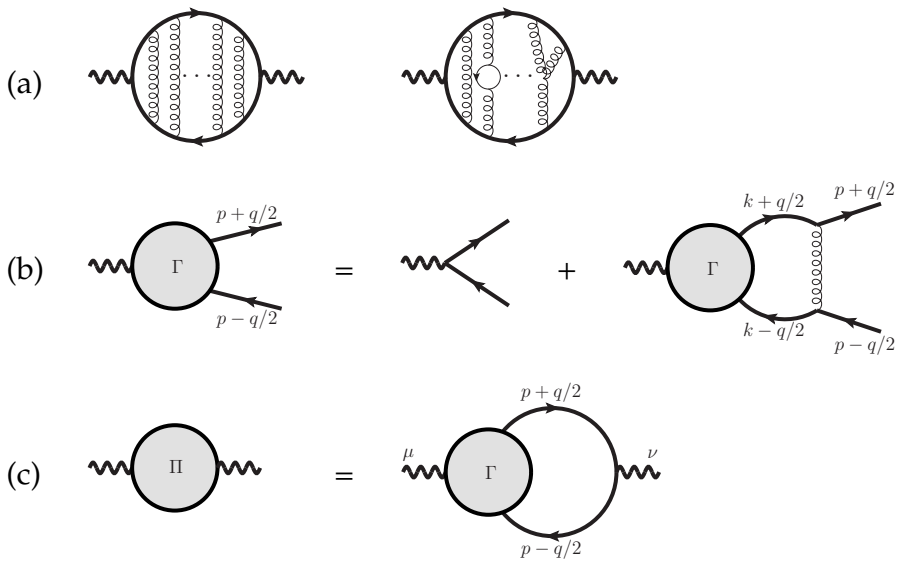

Figure 4.5: Calculation of the Green's function for the QCD Coulomb corrections with the contributing diagrams to the vacuum polarisation of the photon (a), the recursive relation for the vertex correction from ladder diagrams (b), and the application of the vertex correction to compute the vacuum polarisation diagrams (c).

the two-point Green's function of the photon propagator, calculated in a non-relativistic approximation, which is valid for slowly moving particles. The first type of diagrams of figure 4.5 (a) is the leading contribution to the Green's function, consisting of so-called ladder diagrams with the exchange of an arbitrary number of uncrossed gluon lines, which contribute to the vacuum polarisation of the photon. Higher-order corrections to the Green's function also require diagrams of the second type of figure 4.5 (a) to be evaluated. As it will be seen later, these corrections can be taken into account by a modification of the Coulomb potential.

The ladder diagrams can easily be evaluated by constructing the vertex function Γ^μ in a recursive manner, as shown in figure 4.5 (b). Closing the fermion lines to a loop, the vacuum polarisation of the photon propagator Π_t can be expressed through the vertex function, figure 4.5 (c):

$$i(g^{\mu\nu}q^2 - q^\mu q^\nu)\,\Pi_t(q^2) = -\left(ie_q\right)^2 \int \frac{\mathrm{d}^4p}{(2\pi)^4}\,\mathrm{Tr}\left[S_F\left(p+\frac{q}{2}\right)\Gamma^\mu(p,q)\,S_F\left(p-\frac{q}{2}\right)\gamma^\nu\right], \qquad (4.111)$$

where e_q is the electromagnetic charge of the top quark, i.e. $e_q = (2/3)e$, and S_F is the fermion propagator. The factor (-1) stems from the closed fermion loop. The momenta are as labelled in figure 4.5, with q being the momentum flowing into the photon vertex. The leading contributions to this vacuum polarisation will come from the regime where the particles are slowly moving, so it is justified to approximate the fermion propagators in the non-relativistic limit near threshold. In this approximation, the photon momentum is set to $q = (2m_t + E, \mathbf{0})$ where E now represents the binding energy of the $t\bar{t}$ system. The fermion propagators can

then be approximated through their non-relativistic poles:

$$S_F(p+q/2) = \frac{i\left(\not{p} + \frac{1}{2}\not{q} + m_t\right)}{\left(p+\frac{1}{2}q\right)^2 - m_t^2 + i\Gamma_t m_t} \to i\frac{1+\gamma^0}{2}\frac{1}{\frac{E}{2} - \frac{|\mathbf{p}|^2}{2m_t} + p^0 + i\frac{\Gamma_t}{2}},$$

$$S_F(p-q/2) \to -i\frac{1-\gamma^0}{2}\frac{1}{\frac{E}{2} - \frac{|\mathbf{p}|^2}{2m_t} - p^0 + i\frac{\Gamma_t}{2}}. \tag{4.112}$$

Bold quantities denote the spacial components of a four-vector in relativistic notation. The finite width of the top, Γ_t, takes the role of the ϵ-prescription for the on-shell poles of the propagator. Within the non-relativistic approximation, it can be assumed to be constant and corresponding to its on-shell value, independent of the top quark momentum [169, 171]. Eq. (4.111) becomes in this approximation:

$$i(g^{\mu\nu}q^2 - q^\mu q^\nu)\,\Pi_t(q^2) = e_q^2 \int \frac{\mathrm{d}^4 p}{(2\pi)^4}\,\mathrm{Tr}\left[\frac{1+\gamma^0}{2}\Gamma^\mu(p,q)\frac{1-\gamma^0}{2}\gamma^\nu\right] \times \frac{1}{\left[\frac{E}{2} - \frac{|\mathbf{p}|^2}{2m_t} + p^0 + i\frac{\Gamma_t}{2}\right]\left[\frac{E}{2} - \frac{|\mathbf{p}|^2}{2m_t} - p^0 + i\frac{\Gamma_t}{2}\right]}. \tag{4.113}$$

Now, the recursive relation of figure 4.5 (b) is applied the vertex function Γ^μ. Consequently, in the non-relativistic limit, the gluon propagator which appears in the vertex function is only needed in the form of a static or instantaneous Coulomb interaction. Including also the quark-antiquark-gluon vertices at the end points of the propagator, this part is given by:

$$(-ig_\mathrm{s})^2(T^a\gamma^0)(T^a\gamma^0)\frac{+i}{|\mathbf{p}-\mathbf{k}|^2}, \tag{4.114}$$

where T^a are the usual SU(3) generators of the fundamental representation. In general, the colour generators depend on the type of the vertex, so for the case of gluino-pair production presented later, these colour matrices take the form corresponding to the adjoint representation. However, following the case of $t\bar{t}$ production for now, the gluon propagator plus vertices for a colour-singlet final state can be written in the form

$$i(\gamma^0)(\gamma^0)\tilde{V}(\mathbf{p}-\mathbf{k}) := -i(\gamma^0)(\gamma^0)\,T^a \cdot T^a \frac{g_\mathrm{s}^2}{|\mathbf{p}-\mathbf{k}|^2} \tag{4.115}$$

with the QCD Coulomb potential $\tilde{V}$ in momentum space. Replacing $T^a \cdot T^a = C_F = 4/3$ for top quarks, the Coulomb potential becomes:

$$\tilde{V}(\mathbf{p}-\mathbf{k}) = -\frac{4}{3}\frac{4\pi\alpha_\mathrm{s}}{|\mathbf{p}-\mathbf{k}|^2}. \tag{4.116}$$

Taking into account the second type of diagrams in figure 4.5 (a) will lead to higher-order

corrections in α_s to this potential.

Collecting all the approximations made so far, the relation of figure 4.5 (b) for the vertex function Γ^μ can be written as the following recursive equation:

$$\Gamma^\mu(p,q) = \gamma^\mu + i\int \frac{\mathrm{d}^4k}{(2\pi)^4}\gamma^0\left(\frac{1+\gamma^0}{2}\Gamma^\mu(k,q)\frac{1-\gamma^0}{2}\right)\gamma^0 \times \frac{\tilde{V}(\mathbf{p}-\mathbf{k})}{\left[\frac{E}{2}-\frac{|\mathbf{k}|^2}{2m_t}+k^0+i\frac{\Gamma_t}{2}\right]\left[\frac{E}{2}-\frac{|\mathbf{k}|^2}{2m_t}-k^0+i\frac{\Gamma_t}{2}\right]}. \tag{4.117}$$

As $\Gamma^\mu(p,q)$ is independent of the component p^0, it follows from the recursive relation that $\Gamma^\mu(k,q)$ consequently does not depend on k^0 either. Thus, the k^0 integration can simply be carried out with the residue theorem:

$$\int_{-\infty}^{\infty}\frac{\mathrm{d}k^0}{2\pi}\frac{1}{\left[\frac{E}{2}-\frac{|\mathbf{k}|^2}{2m_t}+k^0+i\frac{\Gamma_t}{2}\right]\left[\frac{E}{2}-\frac{|\mathbf{k}|^2}{2m_t}-k^0+i\frac{\Gamma_t}{2}\right]} = 2\pi i\frac{1}{E+i\Gamma_t-\frac{|\mathbf{k}|^2}{m_t}}, \tag{4.118}$$

so that eq. (4.117) becomes:

$$\Gamma^\mu(p,q) = \gamma^\mu - \int\frac{\mathrm{d}^3k}{(2\pi)^3}\left(\frac{1+\gamma^0}{2}\Gamma^\mu(k,q)\frac{1-\gamma^0}{2}\right)\frac{\tilde{V}(\mathbf{p}-\mathbf{k})}{E+i\Gamma_t-\frac{|\mathbf{k}|^2}{m_t}}. \tag{4.119}$$

Here, $(\gamma^0)^2 = 1$ has been used to simplify

$$\gamma^0\frac{1+\gamma^0}{2}\ldots\frac{1-\gamma^0}{2}\gamma^0 = \frac{1+\gamma^0}{2}\ldots\frac{1-\gamma^0}{2}. \tag{4.120}$$

For the same reason,

$$\frac{1\pm\gamma^0}{2}\frac{1\pm\gamma^0}{2} = \frac{1\pm\gamma^0}{2}. \tag{4.121}$$

The recursive relation allows eq. (4.119) to be written in a simplified manner:

$$\frac{1+\gamma^0}{2}\Gamma^\mu(p,q)\frac{1-\gamma^0}{2} = \frac{1+\gamma^0}{2}\gamma^\mu\frac{1-\gamma^0}{2}\tilde{\Gamma} \tag{4.122}$$

where the remaining equation with the scalar function $\tilde{\Gamma}$ now becomes:

$$\tilde{\Gamma}(\mathbf{p},E) = 1 - \int\frac{\mathrm{d}^3k}{(2\pi)^3}\tilde{V}(\mathbf{p}-\mathbf{k})\frac{1}{E+i\Gamma_t-\frac{|\mathbf{k}|^2}{m_t}}\tilde{\Gamma}(\mathbf{k},E). \tag{4.123}$$

Defining a function $\tilde{G}$ in the following way:

$$\tilde{G}(\mathbf{k}; E + i\Gamma_t) := -\frac{1}{E + i\Gamma_t - \frac{|\mathbf{k}|^2}{m_t}} \tilde{\Gamma}(\mathbf{k}, E) \tag{4.124}$$

turns eq. (4.123) into

$$-\left(E + i\Gamma_t - \frac{|\mathbf{p}|^2}{m_t}\right) \tilde{G}(\mathbf{p}; E + i\Gamma_t) = 1 + \int \frac{\mathrm{d}^3 k}{(2\pi)^3} \tilde{V}(\mathbf{p} - \mathbf{k}) \tilde{G}(\mathbf{k}; E + i\Gamma_t). \tag{4.125}$$

Applying an inverse Fourier transform with respect to $\mathbf{p}$ to both sides turns the equation into a Schrödinger equation in coordinate space of the form:

$$\left[H - (E + i\Gamma_t)\right] G(\mathbf{r}; E + i\Gamma_t) = \delta^{(3)}(\mathbf{r}) \tag{4.126}$$

where

$$H = \frac{(-i\nabla)^2}{m_t} + V(\mathbf{r}) \tag{4.127}$$

is the Hamiltonian. V and G are the inverse Fourier transforms of $\tilde{V}$ and $\tilde{G}$. The latter corresponds to the usual Schrödinger Green's function $G(\mathbf{r}, \mathbf{r}'; E + i\Gamma)$ at $\mathbf{r}' = 0$.

In eq. (4.113), the residue theorem can be used in a similar manner to perform the p^0-integration. Additionally inserting the results of eqs. (4.122) and (4.123) leads to:

$$\begin{aligned} i(g^{\mu\nu} q^2 - q^\mu q^\nu)\, \Pi_t(q^2) &= i e_q^2 \int \frac{\mathrm{d}^3 p}{(2\pi)^3} \operatorname{Tr}\left[\frac{1 + \gamma^0}{2} \gamma^\mu \frac{1 - \gamma^0}{2} \gamma^\nu\right] \frac{1}{E + i\Gamma_t - \frac{|\mathbf{p}|^2}{m_t}} \tilde{\Gamma}(\mathbf{p}, E) \\ &= -i \operatorname{Tr}\left[\frac{1 + \gamma^0}{2} \gamma^\mu \frac{1 - \gamma^0}{2} \gamma^\nu\right] e_q^2 \int \frac{\mathrm{d}^3 p}{(2\pi)^3} \tilde{G}(\mathbf{p}; E + i\Gamma_t). \end{aligned} \tag{4.128}$$

The trace of the Dirac matrices has been moved out of the integral, as it does not depend on $\mathbf{p}$. Using the properties of the Dirac matrices, the trace can be evaluated:

$$\begin{aligned} \operatorname{Tr}\left[\frac{1 + \gamma^0}{2} \gamma^\mu \frac{1 - \gamma^0}{2} \gamma^\nu\right] &= \frac{1}{4} \left(\operatorname{Tr}\left[\gamma^\mu \gamma^\nu\right] - \operatorname{Tr}\left[\gamma^0 \gamma^\mu \gamma^0 \gamma^\nu\right]\right) \\ &= g^{\mu\nu} - \left(2 g^{0\mu} g^{0\nu} - g^{\mu\nu}\right) \qquad (4.129) \\ &= 2\left(g^{\mu\nu} - g^{0\mu} g^{0\nu}\right), \qquad (4.130) \end{aligned}$$

where $g^{\mu\nu}$ is the metric tensor with the signature $+---$. On the left side of eq. (4.128), the 4-vector q^μ can be written in the non-relativistic approximation as $q^\mu = g^{0\mu}(2m_t + E)$, which results in the following Lorentz structure:

$$g^{\mu\nu} q^2 - q^\mu q^\nu = (2m_t + E)^2 \left(g^{\mu\nu} - g^{0\mu} g^{0\nu}\right). \tag{4.131}$$

The Lorentz structures on the left and right side of the equal sign are the same. The vacuum polarisation Π_t can therefore directly be related to the Green's function:

$$\begin{aligned}\Pi_t(q^2) &= -\frac{2e_q^2}{4m_t^2}\int\frac{\mathrm{d}^3p}{(2\pi)^3}\tilde{G}(\mathbf{p};E+i\Gamma_t)\\ &= -\frac{2}{9}\frac{e^2}{m_t^2}G(\mathbf{r}=0,\mathbf{r}'=0;E+i\Gamma_t).\end{aligned} \tag{4.132}$$

Here, $(2m_t+E)^2$ has been approximated by $(2m_t+E)^2\approx 4m_t^2$. In the second line, the Green's function evaluated at origin $G(\mathbf{r}=0,\mathbf{r}'=0;E+i\Gamma_t)$ follows from the inverse Fourier transform with $\mathbf{r}=0$. Multiplying this result by a factor of $N_c=3$ due to the three colour charges of the top quark, the result of ref. [171] is obtained:

$$\Pi_t(q^2) = -\frac{2}{3}\frac{e^2}{m_t^2}G(0,0;E+i\Gamma_t). \tag{4.133}$$

The optical theorem relates the imaginary part of a forward-scattering amplitude to the cross section. It can be used to express the production cross section of the $t\bar{t}$ state through the imaginary part of the vacuum polarisation. The physical interpretation of this property is the possibility for pair production from vacuum polarisation if the energy is large enough to form the rest mass of the final state. The electron-positron scattering cross section into a heavy top pair, including the exchange from Coulomb gluons through the Coulomb Green's function, can therefore be written as:

$$\begin{aligned}\sigma(e^+e^-\to t\bar{t}) &= \frac{4\pi\alpha}{S}\left[-\operatorname{Im}\Pi_t(q^2)\right]\\ &= \frac{8\pi^2\alpha^2}{3m_t^4}\operatorname{Im}G(0,0;E+i\Gamma_t)\end{aligned} \tag{4.134}$$

with $\alpha=e^2/(4\pi)$ and $S=q^2\approx 4m_t^2$ near threshold.

4.5.2 All-order expressions for Coulomb contributions to a general case

The evaluation of the Green's function follows as a solution to the Schrödinger equation (4.126). Its calculation is performed in refs. [173, 174], requiring a renormalisation procedure due to occuring UV-divergences, with usually the $\overline{\mathrm{MS}}$ renormalisation scheme being chosen. Higher-order corrections to the exchanged gluons lead to a more complicated Coulomb potential, which up to NLO is given by the following expression in coordinate space:

$$V(\mathbf{r}) = -\frac{\alpha_\mathrm{s}(\mu_C)\mathscr{D}_{ij\to kl,I}}{r}\left\{1+\frac{\alpha_\mathrm{s}(\mu_C)}{4\pi}\left[8\pi b_0\left(\ln(\mu_C r)+\gamma_E\right)+a_1\right]\right\},\quad (r=|\mathbf{r}|). \tag{4.135}$$

with $\gamma_E=0.57721...$ the Euler-Mascheroni constant, $a_1=31/9\,C_A-20/9\,T_R n_f$, b_0 the leading coefficient of the β-function for the running of α_s (see eq. (2.5)), $n_f=5$ the number of light

flavours, and μ_C the Coulomb scale which will be specified in chapter 9. The colour factor $\mathscr{D}_{ij\to kl,I}$ of the QCD Coulomb potential with the index I denoting the colour configuration of the final state (see section 4.3.1) is related to the colour operators T_k^a, T_l^a that appear in eq. (4.114) and can be expressed through quadratic Casimir invariants of the particle pair $C_2(R_I)$ in the colour representation R_I and its constituent particles C_k, C_l:

$$\mathscr{D}_{ij\to kl,I} := -T_k^a \cdot T_l^a = \frac{1}{2}\left[(T_k^a)^2 + (T_l^a)^2 - (T_k^a + T_l^a)^2\right] = \frac{1}{2}\left(C_k + C_l - C_2(R_I)\right). \tag{4.136}$$

The general solution to the Schrödinger equation for two particles with unequal mass and up to a NLO Coulomb potential is given in a compact form, with $E = \sqrt{\hat{s}} - 2m_{\text{av}}$ denoting the energy above threshold [138, 139, 173–175]:

$$G(0,0;E+i\Gamma) = i\frac{vm_{\text{red}}^2}{\pi} + \frac{\mathscr{D}_{ij\to kl,I}\alpha_{\text{s}}m_{\text{red}}^2}{\pi}\left[g_{\text{LO}} + \frac{\alpha_{\text{s}}}{4\pi}g_{\text{NLO}} + \ldots\right], \tag{4.137}$$

with $\Gamma = (\Gamma_k + \Gamma_l)/2$ the average decay width of the two particles, and

$$\begin{aligned} g_{\text{LO}} &:= L - \psi^{(0)}, \\ g_{\text{NLO}} &:= 4\pi b_0\Big[L^2 - 2L\left(\psi^{(0)} - \kappa\psi^{(1)}\right) + \kappa\psi^{(2)} + \left(\psi^{(0)}\right)^2 - 3\psi^{(1)} - 2\kappa\psi^{(0)}\psi^{(1)} \\ &\qquad + 4{}_4F_3(1,1,1,1;2,2,1-\kappa;1)\Big] + a_1\Big[L - \psi^{(0)} + \kappa\psi^{(1)}\Big], \end{aligned} \tag{4.138}$$

where $\psi^{(n)} = \psi^{(n)}(1-\kappa)$ is evaluated with argument $(1-\kappa)$, with $\psi^{(n)}(z) = \mathrm{d}^n/\mathrm{d}z^n\,\psi^{(0)}(z)$ denoting the n-th derivative of $\psi^{(0)}(z) = \gamma_E + \mathrm{d}/\mathrm{d}z \ln\Gamma(z)$, the digamma function, as well as

$$v := \sqrt{\frac{E+i\Gamma}{2m_{\text{red}}}}, \quad \kappa := i\frac{\mathscr{D}_{ij\to kl,I}\alpha_{\text{s}}}{2v}, \quad L := \ln\frac{i\mu_C}{4m_{\text{red}}v}. \tag{4.139}$$

${}_4F_3(1,1,1,1;2,2,1-\kappa;1)$ in eq. (4.138) is the generalised hypergeometric function. A note regarding its efficient numerical evaluation is given in ref. [138]. The masses of the final-state particles enter the solution in the form of the reduced mass $m_{\text{red}} = m_k m_l/(m_k + m_l)$. v denotes the non-relativistic velocity. The free Green's function is simply the first term, which corresponds to freely propagating particles with no Coulomb interactions present:

$$G^{\text{free}}(0,0;E+i\Gamma) = i\frac{vm_{\text{red}}^2}{\pi}. \tag{4.140}$$

Setting $\Gamma = 0$ and rewriting

$$E = 2m_{\text{red}}v^2 = \sqrt{\hat{s}} - 2m_{\text{av}} \Rightarrow \sqrt{\hat{s}} = 2m_{\text{av}} + 2m_{\text{red}}v^2, \tag{4.141}$$

v can be related to β through its definition

$$\beta = \sqrt{1 - \frac{4m_{\text{av}}}{\hat{s}}} \Rightarrow \sqrt{\hat{s}} = \frac{2m_{\text{av}}}{\sqrt{1-\beta^2}} \overset{\beta\to 0}{\approx} 2m_{\text{av}} + m_{\text{av}}\beta^2 \tag{4.142}$$

where in the last step, terms of order $\mathcal{O}(\beta^4)$, being heavily suppressed close to threshold, have been neglected. From the two relations above, it is clear that $v \approx \sqrt{m_{\text{av}}/(2m_{\text{red}})}\beta$. This also shows how β plays the role of the relativistic velocity of the particles, which of course coincides with the non-relativistic velocity at low kinetic energies, i.e. near threshold. m_{av} now explicitely denotes the average mass of the particles $m_{\text{av}} = (m_k + m_l)/2$ to distinguish it from the reduced mass m_{red}.

As the partonic leading order cross section $\hat{\sigma}^{(0)}_{ij\to kl,I}$ splits up close to threshold into a β-dependent part corresponding to the free Green's function and a β-independent hard function $\mathcal{H}^{(0)}_{ij\to kl,I}$,

$$\hat{\sigma}^{(0)}_{ij\to kl,I}(\beta) \overset{\hat{s}\to 4m_{\text{av}}^2}{\approx} \operatorname{Im} G^{\text{free}}(0,0;E)\, \mathcal{H}^{(0)}_{ij\to kl,I} \approx \frac{m_{\text{red}}^2}{\pi}\sqrt{\frac{m_{\text{av}}}{2m_{\text{red}}}}\beta\, \mathcal{H}^{(0)}_{ij\to kl,I}, \tag{4.143}$$

the proper incorporation of the Coulomb corrections is done by a rescaling of the leading-order cross section [136]:

$$\hat{\sigma}^{\text{Coul}}_{ij\to kl,I} = \hat{\sigma}^{(0)}_{ij\to kl,I} \times \frac{\operatorname{Im} G(0,0;E+i\Gamma)}{\operatorname{Im} G^{\text{free}}(0,0;E+i\Gamma)} \tag{4.144}$$

for every colour channel I separately. $\hat{\sigma}^{\text{Coul}}_{ij\to kl,I}$ denotes the Coulomb cross section which takes Coulomb gluon exchange in the threshold limit up to all orders in α_{s} into account. An example of this is eq. (4.134) for the case of top production in an e^+e^- collision.

Furthermore, it is possible to include spin-dependent corrections at NNLO to the Coulomb potential (although formally not originating from a Coulomb interaction and therefore being of non-Coulombic origin), leading to [128, 173, 174]

$$\Delta_{\text{nC}}(E+i\Gamma) = 1 - \alpha_{\text{s}}^2(\mu_C)\ln(v)\left[2\mathscr{D}^2_{ij\to kl,I}(1+v_{\text{spin}}) + \mathscr{D}_{ij\to kl,I}C_A\right], \tag{4.145}$$

where v_{spin} are spin-dependent coefficients. The inclusion of the spin-dependent corrections follow from multiplying the LO Coulomb contribution g_{LO} with Δ_{nC} [128, 134].

The Green's function presented in this section and in particular the near-threshold expansion eq. (4.143) and multiplication prescription eq. (4.144) is only valid for a final state produced with zero angular momentum, corresponding to an s-wave state. Higher partial wave contributions, such as p-wave states, require a modification of the Green's function (see e.g. ref. [123] and references therein). Whereas cross sections for s-wave states are proportional to β close to threshold, p-wave states experience an additional phase space suppression factor of β^2 relative to the s-wave states. For the discussion of squark and gluino production at NNLL accuracy in chapters 7-9, the p-wave states only give a negligible contribution and are therefore be treated differently without including the Coulomb contributions, see section 7.2.

4.5.3 Bound states

A very interesting feature of the Coulomb interactions is the possibility of bound-state formation at energies below the production threshold of the particles. The Green's function then develops single poles of the form [176]:

$$G(E + i\Gamma) \sim \sum_{n=1}^{\infty} \frac{|\psi(0)|^2}{E_n - E - i\Gamma} \tag{4.146}$$

where $|\psi(0)|^2$ is the wave function of the bound-state system at origin and $E_n < 0$ are the bound-state energies. In the narrow-width approximation $\Gamma \to 0$, the imaginary part of the Green's function turns into a sum of sharp δ-peaks,

$$\operatorname{Im} G(E + i\Gamma) = \sum_{n=1}^{\infty} |\psi(0)|^2 \frac{\Gamma}{(E_n - E)^2 + \Gamma^2} \overset{\Gamma\to 0}{\longrightarrow} \pi \sum_{n=1}^{\infty} |\psi(0)|^2 \, \delta(E - E_n). \tag{4.147}$$

Only taking into account the LO Coulomb potential, the bound-state energies can be computed by analysing eq. (4.137): the digamma function $\psi^{(0)}(1 - \kappa)$ is singular for $\kappa = n$ with $n \geq 1$ a positive integer. Rewriting κ into E gives:

$$E_n = -\frac{\alpha_s^2 \mathscr{D}_I^2 m_{\text{red}}}{2n^2}. \tag{4.148}$$

The residues of $\operatorname{Im} G(E)$ at the bound-state energies precisely give the value of the wave function at origin. It is:

$$|\psi(0)|^2 = \frac{1}{\pi} \left(\frac{\alpha_s \mathscr{D}_{ij\to kl,I} m_{\text{red}}}{n} \right)^3. \tag{4.149}$$

Therefore, the imaginary part of the bound-state Green's function for a LO Coulomb potential becomes:

$$\operatorname{Im} G^{\text{BS}}(E) = \sum_{n=1}^{\infty} \delta(E - E_n) \left(\frac{\alpha_s \mathscr{D}_{ij\to kl,I} m_{\text{red}}}{n} \right)^3, \qquad E < 0. \tag{4.150}$$

In ref. [176], bound-state energies and residues for higher-order corrections to the Coulomb potential have been calculated. In this thesis, however, only the energy levels and residues of a LO Coulomb potential will be considered.

4.6 Physical predictions and the "Minimal Prescription"

A physical interpretation of the resummation techniques presented in the previous sections requires an inverse Mellin transform of the cross section back to momentum space. It turns out that this is not exactly a straightforward procedure, as will be presented in the following.

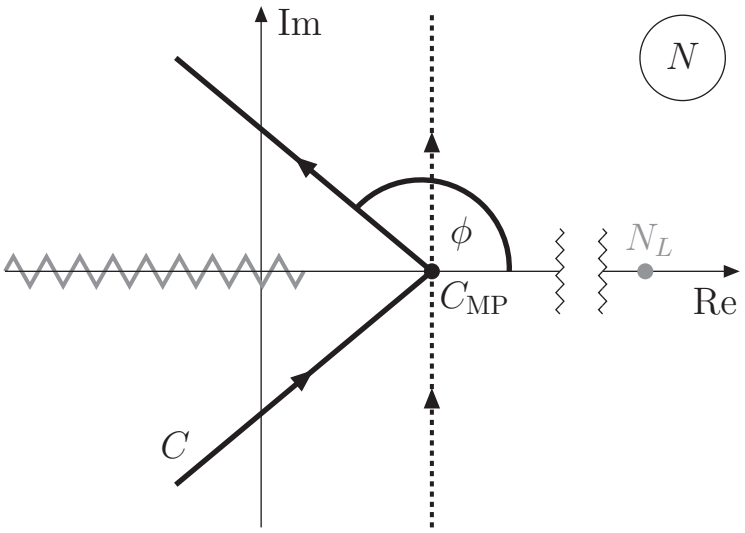

Figure 4.6: Bent integration contour C (solid black line) of the inverse Mellin transform in the complex N-plane according to the "Minimal Prescription" of ref. [166] and improved for numerical evaluation [177]. The original contour (dotted black line) parallel to the imaginary axis is also shown.

Considering the following schematical inverse transform of a cross section in Mellin space,

$$\sigma(\rho) = \int_{c-i\infty}^{c+i\infty} \frac{\mathrm{d}N}{2\pi i} \rho^{-N} \left[\tilde{f}(N)\right]^2 \Delta(N) \tag{4.151}$$

with $\tilde{f}(N)$ denoting the PDFs in Mellin space and $\Delta(N)$ being the resummed exponential functions $\Delta_i \Delta_j \Delta^{(\mathrm{s})}_{ij\to kl,I}$, the integration contour is along a path which is parallel to the imaginary axis and intersects the real axis in the point c. This point has to be chosen such that the Mellin integral $\int_0^1 \mathrm{d}\rho\, \rho^{c-1}\sigma(\rho)$ is absolutely convergent. A problem arises when including the resummed exponents of section 4.3.3: it is clear that Δ_i and $\Delta^{(\mathrm{s})}_{ij\to kl,I}$ from eqs. (4.85) and (4.93) (and therefore the Mellin transform of the resummed cross section) are divergent for every value of N due to the argument of the running coupling being integrated over and always hitting the Landau pole where the coupling diverges, which marks the transition to the non-perturbative regime. Thus, the inverse Mellin transform is ill-defined. However, it can be seen that formally rewriting the divergent exponential functions as a series,

$$\Delta(N) = \sum_{k=0}^{\infty} c_k(\ln N)\, \alpha_{\mathrm{s}}^k \tag{4.152}$$

with the coefficients $c_k(\ln N)$ being polynomials in $\ln N$, and performing the integration of eq. (4.151) term by term in the expansion, the integral converges for each term separately. Again, the sum of all these integrations diverges due to the Landau pole, and the expansion has to be understood in a formal sense.

On the other hand, evaluating the Mellin transforms in the exponent of $\Delta(N)$ with the prescription of appendix B at an arbitrary logarithmic accuracy renders the integrals finite (but

still not absolutely convergent) for all values of N except for a value $N = N_L := \exp\left[1/(2\alpha_s b_0)\right]$ which denotes the position of the Landau pole[3]. The prescription explicitely excludes the Landau pole from the integration range. It should be noted that the divergencies of the integrals might not even be present if other approximations leading to the form of eqs. (4.85) and (4.93) had not been applied [166]. To distinguish the evaluated form of $\Delta(N)$ at a certain logarithmic accuracy from the full $\Delta(N)$, the former will here be written as $\Delta(N)|_{\mathrm{N^kLL}}$.

Now, the integral

$$\int_{c-i\infty}^{c+i\infty} \frac{\mathrm{d}N}{2\pi i} \rho^{-N} \left[\tilde{f}(N)\right]^2 \Delta(N)|_{\mathrm{N^kLL}} \tag{4.153}$$

is convergent and can be evaluated by again understanding $\Delta(N)|_{\mathrm{N^kLL}}$ as a power expansion in α_s. The authors of ref. [166] then proposed that for a certain choice of $c = C_{\mathrm{MP}}$, the integral with the divergent expansion of eq. (4.152) converges asymptotically to eq. (4.153), meaning that the latter can be understood as an order-by-order inverse Mellin transform of the resummed cross section.

This is called the "*Minimal Prescription*" (MP), and it will be denoted in the integrals as

$$\begin{aligned}\sigma^{(\mathrm{res})}_{h_1h_2\to kl}\left(\rho, \alpha_s(\mu_R^2)\right) &= \int_{C_{\mathrm{MP}}} \frac{\mathrm{d}N}{2\pi i} \rho^{-N} \tilde{\sigma}^{(\mathrm{res})}_{h_1h_2\to kl}\left(N, \alpha_s(\mu_R^2)\right) \\ &= \sum_{i,j} \int_{C_{\mathrm{MP}}} \frac{\mathrm{d}N}{2\pi i} \rho^{-N} \tilde{f}_{i/h_1}(N+1, \mu_F^2)\, \tilde{f}_{j/h_2}(N+1, \mu_F^2) \\ &\qquad \times \tilde{\sigma}^{(\mathrm{res})}_{ij\to kl}\left(N, \alpha_s(\mu_R^2), \mu_F^2\right). \end{aligned} \tag{4.154}$$

C_{MP} has to be chosen in such a way that

$$C_{\tilde{f}} < C_{\mathrm{MP}} < N_L, \tag{4.155}$$

where $C_{\tilde{f}}$ denotes singularities of the PDFs in Mellin space[4] which all lie on the real axis, with the rightmost singularity slightly above $N = 1$. The MP formula, besides achieving the above mentioned asymptotic convergence of the expansion, does not suffer from factorially growing terms which were present in other prescriptions regarding the inverse Mellin transform in the past [178–190], and additionally, the error between the MP formula and the expansion which one introduces due to the asymptotic nature is suppressed by a factor which is stronger than any power suppression.

As the only singularities in the complex N-plane are on the real axis, it is possible to bend the integration contour, a parallel to the imaginary axis, towards a negative real part of N according to Cauchy's integral theorem, resulting in an additional suppression due to the factor ρ^{-N} (with $\rho < 1$) [177]. Figure 4.6 shows the complex N-plane with the original

[3] N_L can easily be determined from observing that e.g. expression $g_i^{(1)}(\lambda)$ of appendix C diverges for $\lambda = 1/2$.

[4] The Mellin transform of a PDF which is parametrised at a starting scale μ_0 as $xf(x, \mu_0^2) = \sum_k A_k\, x^{\delta_k}(1-x)^{\eta_k}$ (e.g. MSTW2008 [20] or MMHT14 [19]) is $\tilde{f}(N+1, \mu_0^2) = \sum_k A_k\, \beta(\delta_k - 1 + N, \eta_k + 1)$ with $\beta(x, y)$ being the Euler beta function which develops singularities at x, y being zero or negative integers.

integration contour as a dotted line going through C_{MP} and the new integration contour as a solid line, bent by an angle $\pm\phi$ with respect to the real axis, with $\phi > \pi/2$. The contribution from the arc line segments vanish as they are moved towards infinity. The grey zig-zag line on the real axis denotes the singularities of the PDFs to the left of the contour, whereas N_L is the Landau pole to the far right. The integration contour can therefore be parametrised as

$$N = C_{\mathrm{MP}} + y\, e^{\pm i\phi}, \tag{4.156}$$

where the lower branch for a negative imaginary part of N is parametrised by $-\infty < y \leq 0$ and a negative sign in front of ϕ, and the upper branch for a positive imaginary part corresponds to $0 \leq y < \infty$ and a positive sign in front of ϕ. Exchanging the integration over N for one over y leads to:

$$\sigma^{(\mathrm{res})}_{h_1h_2\to kl}\left(\rho, \alpha_{\mathrm{s}}(\mu_R^2)\right) = \frac{1}{\pi}\int_0^\infty \mathrm{d}y\, \mathrm{Im}\left[e^{i\phi}\rho^{-C_{\mathrm{MP}}-y\,e^{i\phi}}\tilde{\sigma}^{(\mathrm{res})}_{h_1h_2\to kl}\left(N = C_{\mathrm{MP}} + y\, e^{i\phi}, \alpha_{\mathrm{s}}(\mu_R^2)\right)\right], \tag{4.157}$$

which results from the fact that $\tilde{\sigma}^{(\mathrm{res})}_{h_1h_2\to kl}(N^*) = \left(\tilde{\sigma}^{(\mathrm{res})}_{h_1h_2\to kl}(N)\right)^*$.

4.7 Implementation of the PDFs

As it was already done in eq. (4.105), the resummed total hadronic cross section can again be expressed as a convolution in momentum space,

$$\begin{aligned}\sigma^{(\mathrm{res})}_{h_1h_2\to kl}\left(\rho, \alpha_{\mathrm{s}}(\mu_R^2)\right) &= \sum_{i,j}\int \mathrm{d}\tau\, \mathrm{d}x_1\, \mathrm{d}x_2\, f_{i/h_1}(x_1, \mu_F^2)\, f_{j/h_2}(x_2, \mu_F^2)\, \delta\left(\tau - x_1x_2\right) \\ &\qquad \times \hat{\sigma}^{(\mathrm{res})}_{ij\to kl}\left(\hat{\rho} = \frac{\rho}{\tau}, \alpha_{\mathrm{s}}(\mu_R^2), \mu_F^2\right) \\ &= \sum_{i,j}\int_0^1 \mathrm{d}\tau \int_\tau^1 \frac{\mathrm{d}x}{x} f_{i/h_1}(x, \mu_F^2)\, f_{j/h_2}\left(\frac{\tau}{x}, \mu_F^2\right)\, \hat{\sigma}^{(\mathrm{res})}_{ij\to kl}\left(\frac{\rho}{\tau}, \alpha_{\mathrm{s}}(\mu_R^2), \mu_F^2\right),\end{aligned} \tag{4.158}$$

where $\delta(\tau - x_1x_2) = 1/x_1\, \delta(x_2 - \tau/x_1)$ was used, and with the additional integration over the variable τ instead of $\hat{\rho}$ to make some of the following expressions a little bit more convenient for the numerical implementation. Here, the PDFs and the partonic cross section are formally defined as the inverse Mellin transforms of the type of eq. (4.154), with the inverse Mellin-transformed PDFs of course corresponding to the usual x-space ones. It should be noted, however, that the production cross section would usually vanish for $\tau < \rho$ (which actually denotes the region below the production threshold), while the integration range here goes down to zero. It is an artefact of the "Minimal Prescription" that the inverse Mellin transform does not vanish in the region $\tau \in [0, \rho]$ which originates from the presence of the Landau pole [166] (see also ref. [191]). However, it was shown that the contribution in this region decreases rapidly, making it possible to still apply the QCD factorisation theorem. The angle of eq. (4.156) has to be chosen as $\phi < \pi/2$ in this region in order to obtain the suppression as discussed above (since the inverse Mellin transform in $\hat{\sigma}_{ij\to kl}$ is evaluated with respect to

the variable $\hat{\rho}$ instead of ρ in eq. (4.154), and $\hat{\rho} > 1$ for $\tau < \rho$). This artefact does not affect the treatment of true bound-state contributions as discussed in chapter 9, since the latter do not require an inverse Mellin transform and they will be added separately to the total cross section.

Depending on the application, sometimes eq. (4.154) is more convenient to use, and sometimes eq. (4.158). In particular, for a numerical implementation, eq. (4.154) only requires one integration, but then assumes that the PDFs are available as functions in Mellin-moment space. This is the case for PDFs which are parametrised at an initial scale as polynomials in x or $\sqrt{x}$, like MSTW2008 [20], MMHT14 [19], or CT14 [21]. The evolution to an arbitrary scale is governed by the DGLAP equations [192–194], which is a simple differential equation in Mellin-moment space (contrary to a more complex integro-differential equation in x-space). One computer code implementing the evolution equations and providing the PDFs at an arbitrary scale in Mellin-moment space is `QCD-Pegasus` [195], which is used in this work for the MSTW2008 PDF set.

4.7.1 The "derivative method"

Eq. (4.154) is certainly more general in this sense, as it can also be applied to PDF sets that do not follow a parametrisation which can easily be Mellin-transformed, in particular the PDF sets of the NNPDF collaboration [22]. However, the equation suffers from a highly singular behaviour close to the threshold region $\hat{\rho} \to 1$ (corresponding to $\tau \approx \rho$), see e.g. refs. [166,191]. Although regularised in terms of the plus distributions, this property will cause numerical instabilities. A method proposed in ref. [191] follows from rewriting eq. (4.154) to suppress these singular contributions for $N \to \infty$ in the following sense:

$$\sigma^{(\mathrm{res})}_{h_1 h_2 \to kl}\left(\rho, \alpha_\mathrm{s}(\mu_R^2)\right) = \sum_{i,j} \int_{C_\mathrm{MP}} \frac{\mathrm{d}N}{2\pi i} \rho^{-N} \left[N \tilde{f}_{i/h_1}(N+1, \mu_F^2)\right]\left[N \tilde{f}_{j/h_2}(N+1, \mu_F^2)\right] \times \frac{\tilde{\sigma}^{(\mathrm{res})}_{ij\to kl}\left(N, \alpha_\mathrm{s}(\mu_R^2), \mu_F^2\right)}{N^2}. \tag{4.159}$$

The additional factor of $1/N^2$ leads to a stronger suppression of the partonic cross section containing the resummed logarithms near threshold, providing numerical stability. Furthermore, the combination $N\tilde{f}_{i/h_1}(N+1, \mu_F^2)$ can be rewritten in the following way:

$$\begin{aligned} N\tilde{f}\left(N+1, \mu_F^2\right) &= \int_0^1 \mathrm{d}x\, N x^N f\left(x, \mu_F^2\right) = \int_0^1 \mathrm{d}x\, x f\left(x, \mu_F^2\right) \frac{\mathrm{d}}{\mathrm{d}x} x^N \\ &= \underbrace{\left[x^{N+1} f\left(x, \mu_F^2\right)\right]_0^1}_{=0} - \int_0^1 \mathrm{d}x\, x^N \frac{\mathrm{d}}{\mathrm{d}x}\left[x f\left(x, \mu_F^2\right)\right] \\ &= \int_0^1 \mathrm{d}x\, x^N \mathcal{F}\left(x, \mu_F^2\right) \end{aligned} \tag{4.160}$$

with

$$\mathcal{F}\left(x,\mu_F^2\right) := -\frac{\mathrm{d}}{\mathrm{d}x}\left[xf\left(x,\mu_F^2\right)\right] = \int_{C_{\mathrm{MP}}} \frac{\mathrm{d}N}{2\pi i} x^{-N} N\tilde{f}\left(N+1,\mu_F^2\right), \tag{4.161}$$

where integration by parts was used to rewrite the Mellin transform. The total derivative vanishes due to the PDFs becoming zero at $x = 1$. This result allows eq. (4.158) to be written as:

$$\sigma^{(\mathrm{res})}_{h_1h_2\to kl}\left(\rho,\alpha_{\mathrm{s}}(\mu_R^2)\right) = \sum_{i,j}\int_0^1 \mathrm{d}\tau \int_\tau^1 \frac{\mathrm{d}x}{x}\mathcal{F}_{i/h_1}(x,\mu_F^2)\,\mathcal{F}_{j/h_2}\left(\frac{\tau}{x},\mu_F^2\right)\,\mathcal{S}_{ij\to kl}\left(\hat{\rho}=\rho/\tau,\alpha_{\mathrm{s}}(\mu_R^2),\mu_F^2\right) \tag{4.162}$$

with

$$\mathcal{S}_{ij\to kl}\left(\hat{\rho},\alpha_{\mathrm{s}}(\mu_R^2),\mu_F^2\right) = \int_{C_{\mathrm{MP}}} \frac{\mathrm{d}N}{2\pi i}\hat{\rho}^{-N}\frac{\tilde{\sigma}_{ij\to kl}\left(N,\alpha_{\mathrm{s}}(\mu_R^2),\mu_F^2\right)}{N^2}. \tag{4.163}$$

This "derivative method" can be applied multiple times to obtain a higher suppression of the partonic cross section, requiring higher derivatives of the PDFs, i.e.

$$\begin{aligned}(N+1)N\tilde{f}\left(N+1,\mu_F^2\right) &= \int_0^1 \mathrm{d}x\,(N+1)x^N\mathcal{F}\left(x,\mu_F^2\right) = \int_0^1 \mathrm{d}x\,\mathcal{F}\left(x,\mu_F^2\right)\frac{\mathrm{d}}{\mathrm{d}x}x^{N+1}\\ &= \underbrace{\left[x^{N+1}\mathcal{F}\left(x,\mu_F^2\right)\right]_0^1}_{=0} - \int_0^1 \mathrm{d}x\,x^{N+1}\frac{\mathrm{d}}{\mathrm{d}x}\mathcal{F}\left(x,\mu_F^2\right)\\ &= \int_0^1 \mathrm{d}x\,x^N\mathcal{F}_2\left(x,\mu_F^2\right)\end{aligned} \tag{4.164}$$

with

$$\mathcal{F}_2\left(x,\mu_F^2\right) := x\frac{\mathrm{d}^2}{\mathrm{d}x^2}\left[xf\left(x,\mu_F^2\right)\right] \tag{4.165}$$

and so on. As it turns out, in particular for the squark and gluino production channels with gluon-fusion as an initial state, this higher suppression is needed for numerical stability.

4.8 Matching to a fixed-order calculation

Since resummation only takes threshold-enhanced terms into account, but a cross section can also receive significant contributions from outside the threshold region, it is important to properly include the full fixed-order corrections, which include the non-threshold terms, up to the order to which they are available to obtain the best possible theoretical description of the process. This procedure is called *matching* and, to avoid double counting, requires the subtraction of terms from the resummed cross section up to the order of the fixed-order

cross section, since the latter already includes them. Thus, the best prediction including full fixed-order and threshold-resummed contributions, denoted as N..LO+N..LL, is calculated as follows:

$$\begin{aligned}\sigma^{(\text{f.o.+res})}_{h_1h_2\to kl}\left(\rho,\alpha_\text{s}(\mu_R^2),\mu_F^2\right) &= \sigma^{(\text{f.o.})}_{h_1h_2\to kl}\left(\rho,\alpha_\text{s}(\mu_R^2),\mu_F^2\right)\\ &\quad+\sum_{i,j}\int_{C_\text{MP}}\frac{\mathrm{d}N}{2\pi i}\rho^{-N}\tilde{f}_{i/h_1}(N+1,\mu_F^2)\,\tilde{f}_{j/h_2}(N+1,\mu_F^2)\\ &\quad\times\left[\tilde{\sigma}^{(\text{res})}_{ij\to kl}\left(N,\alpha_\text{s}(\mu_R^2),\mu_F^2\right)-\tilde{\sigma}^{(\text{res})}_{ij\to kl}\left(N,\alpha_\text{s}(\mu_R^2),\mu_F^2\right)\Big|_{\text{f.o.}}\right].\end{aligned} \tag{4.166}$$

5 NLL Threshold Resummation for Future Colliders

After introducing the resummation of soft gluons in the previous chapter, it is possible to use the final expressions that were derived to increase the precision of theoretical calculations, both for the production of already discovered particles to measure their properties more precisely, such as the Higgs boson, top quarks, or electroweak gauge bosons, but also for new particles, such as the supersymmetric squarks ($\tilde{q}$) and gluinos ($\tilde{g}$).

Coloured sparticles are expected to be produced in large numbers at the LHC. It is therefore important to precisely predict their cross sections for experiments to measure them or set mass limits in case they are not found. Heavy particles always receive significant contributions from the partonic threshold region, making it necessary to properly describe this kinematical limit. Therefore, and due to large colour factors entering the calculations, QCD corrections can be large. This chapter and the next one will therefore discuss the impact of threshold-improved calculations on the production of squarks and gluinos. The production channels are:

$$pp \to \tilde{g}\tilde{g},\ \tilde{q}\tilde{q}^*,\ \tilde{q}\tilde{g},\ \tilde{q}\tilde{q},\ \tilde{t}\tilde{t}^*\ +\ X \tag{5.1}$$

In this chapter, NLL threshold resummation for squarks and gluinos will be looked at. After first introducing the colour decomposition of hard and soft functions as needed for the final-state soft-guon emission, predictions for squark and gluino production at future circular colliders will be presented. This work was published in ref. [75], see also ref. [196].

5.1 Ingredients for NLL resummation

The NLO+NLL predictions for all combinations of squark and gluino production have already been calculated a few years ago [109–113]. The ingredients for the resummed part are the exponential functions up to NLL accuracy which includes the one-loop soft anomalous dimension as the only process-dependent quantity. The latter requires the soft and hard functions to be split up into the colour states of the product representation of the final-state

particles, which requires a set of colour basis vectors to be chosen. The next section shortly presents this colour decomposition.

5.1.1 Colour decomposition

For the computation of the soft anomalous dimension, the processes need to be split up into their colour configurations. These are (see eqs. (4.65)–(4.68) for $N_c = 3$)

- for gluino-pair production:

$$q\bar{q} \to \tilde{g}\tilde{g}: \quad \mathbf{3} \otimes \overline{\mathbf{3}} = \mathbf{1} \oplus \mathbf{8_A} \oplus \mathbf{8_S}, \tag{5.2}$$

$$gg \to \tilde{g}\tilde{g}: \quad \mathbf{8} \otimes \mathbf{8} = \mathbf{1} \oplus \mathbf{8_A} \oplus \mathbf{8_S} \oplus \mathbf{27}, \tag{5.3}$$

- for squark-antisquark production:

$$q\bar{q} \to \tilde{q}\tilde{q}^*: \quad \mathbf{3} \otimes \overline{\mathbf{3}} = \mathbf{1} \oplus \mathbf{8}, \tag{5.4}$$

$$gg \to \tilde{q}\tilde{q}^*: \quad \mathbf{8} \otimes \mathbf{8} = \mathbf{1} \oplus \mathbf{8_A} \oplus \mathbf{8_S}, \tag{5.5}$$

- for squark-gluino production:

$$qg \to \tilde{q}\tilde{g}\ (\text{+h.c.}): \quad \mathbf{3} \otimes \mathbf{8} = \mathbf{3} \oplus \overline{\mathbf{6}} \oplus \mathbf{15}, \tag{5.6}$$

- and for squark-pair production:

$$qq \to \tilde{q}\tilde{q}\ (\text{+h.c.}): \quad \mathbf{3} \otimes \mathbf{3} = \overline{\mathbf{3}} \oplus \mathbf{6}. \tag{5.7}$$

Colour channels in a grey colour denote so-called p-wave states (with the special case of the $\overline{\mathbf{3}}$ channel of $\tilde{q}\tilde{q}$, where only the case of equal (s)quark flavours corresponds to a p-wave state). As this distinction will first play a role starting at the NNLL accuracy, its explanation will follow in section 7.2. An s-channel colour basis describing these colour states is chosen, which, as it has been said previously, automatically diagonalises the soft anomalous dimension matrix in the absolute threshold limit. For the calculations, an explicit form of the colour basis vectors is needed. Methods for their calculation are presented in refs. [131, 168] (see also ref. [17]) for arbitrary colour representations of the initial- and final-state particles, and ref. [111] for a more economical method when the particles of the initial and final state are in the same colour representation, as it is the case for squark-gluino and squark-pair production. The results of such a calculation are simply cited here, with the normalisation of the basis vectors given explicitely in ref. [131]. Additionally, the quadratic Casimir invariants $C_2(R_I)$ for each colour representation R_I are given as they are required for the coefficients from the soft anomalous dimension and later also for the Coulomb coefficients. The colour indices correspond to the schematical process

$$i(a_1)\, j(a_2) \to k(a_3)\, l(a_4) \tag{5.8}$$

with a_1, a_2, a_3, a_4 denoting fundamental indices for $i, j, k, l = q, \bar{q}, \tilde{q}, \tilde{q}^*$ and adjoint indices for $i, j, k, l = g, \tilde{g}$:

- gluino-pair production:

$$c_{q\bar{q}\to\tilde{g}\tilde{g},\mathbf{1}} = \frac{1}{\sqrt{N_c(N_c^2-1)}}\delta_{a_1a_2}\delta_{a_3a_4}, \qquad C_2(R_\mathbf{1}) = 0, \tag{5.9}$$

$$c_{q\bar{q}\to\tilde{g}\tilde{g},\mathbf{8_A}} = i\sqrt{\frac{2}{N_c}}f_{a_3a_4c}T^c_{a_2a_1}, \qquad C_2(R_{\mathbf{8_A}}) = N_c, \tag{5.10}$$

$$c_{q\bar{q}\to\tilde{g}\tilde{g},\mathbf{8_S}} = \sqrt{\frac{2N_c}{N_c^2-4}}d_{a_3a_4c}T^c_{a_2a_1}, \qquad C_2(R_{\mathbf{8_S}}) = N_c \tag{5.11}$$

and

$$c_{gg\to\tilde{g}\tilde{g},\mathbf{1}} = \frac{1}{N_c^2-1}\delta_{a_1a_2}\delta_{a_3a_4}, \qquad C_2(R_\mathbf{1}) = 0, \tag{5.12}$$

$$c_{gg\to\tilde{g}\tilde{g},\mathbf{8_A}} = \frac{N_c}{N_c^2-4}d_{a_1a_2c}d_{ca_3a_4}, \qquad C_2(R_{\mathbf{8_A}}) = N_c, \tag{5.13}$$

$$c_{gg\to\tilde{g}\tilde{g},\mathbf{8_S}} = \frac{1}{N_c}f_{a_1a_2c}f_{ca_3a_4}, \qquad C_2(R_{\mathbf{8_S}}) = N_c, \tag{5.14}$$

$$\begin{aligned} c_{gg\to\tilde{g}\tilde{g},\mathbf{27}} = &-\frac{N_c+2}{2N_c(N_c+1)}\delta_{a_1a_2}\delta_{a_3a_4} \qquad C_2(R_\mathbf{27}) = 2(N_c+1), \\ &+\frac{N_c+2}{4N_c}\left(\delta_{a_1a_3}\delta_{a_2a_4}+\delta_{a_1a_4}\delta_{a_2a_3}\right) \\ &-\frac{N_c+4}{4(N_c+2)}d_{a_1a_2c}d_{a_3a_4c} \\ &+\frac{1}{4}\left(d_{a_1a_3c}d_{a_2a_4c}+d_{a_2a_3c}d_{a_1a_4c}\right), \end{aligned} \tag{5.15}$$

- squark-antisquark production:

$$c_{q\bar{q}\to\tilde{q}\tilde{q}^*,\mathbf{1}} = \frac{1}{N_c}\delta_{a_1a_2}\delta_{a_3a_4}, \qquad C_2(R_\mathbf{1}) = 0, \tag{5.16}$$

$$c_{q\bar{q}\to\tilde{q}\tilde{q}^*,\mathbf{8}} = 2T^c_{a_2a_1}T^c_{a_3a_4}, \qquad C_2(R_\mathbf{8}) = N_c \tag{5.17}$$

and

$$c_{gg\to\tilde{q}\tilde{q}^*,\mathbf{1}} = \frac{1}{\sqrt{N_c(N_c^2-1)}}\delta_{a_1a_2}\delta_{a_3a_4}, \qquad C_2(R_\mathbf{1}) = 0, \tag{5.18}$$

$$c_{gg\to\tilde{q}\bar{\tilde{q}}^*,\mathbf{8_A}} = i\sqrt{\frac{2}{N_c}} f_{a_1a_2c} T^c_{a_3a_4}, \qquad C_2(R_{\mathbf{8_A}}) = N_c, \tag{5.19}$$

$$c_{gg\to\tilde{q}\bar{\tilde{q}}^*,\mathbf{8_S}} = \sqrt{\frac{2N_c}{N_c^2-4}} d_{a_1a_2c} T^c_{a_3a_4}, \qquad C_2(R_{\mathbf{8_S}}) = N_c, \tag{5.20}$$

- squark-gluino production:

$$c_{qg\to\tilde{q}\tilde{g},\mathbf{3}} = \frac{2N_c}{N_c^2-1}(T^{a_4}T^{a_2})_{a_3a_1} \qquad C_2(R_{\mathbf{3}}) = \frac{N_c^2-1}{2N_c}, \tag{5.21}$$

$$\begin{aligned} c_{qg\to\tilde{q}\tilde{g},\bar{\mathbf{6}}} = {} & \frac{N_c-2}{2N_c}\delta_{a_2a_4}\delta_{a_1a_3} - d_{ca_4a_2}T^c_{a_3a_1} \qquad C_2(R_{\bar{\mathbf{6}}}) = \frac{(N_c-1)(3N_c+1)}{2N_c}, \\ & + \frac{N_c-2}{N_c-1}(T^{a_4}T^{a_2})_{a_3a_1}, \end{aligned} \tag{5.22}$$

$$\begin{aligned} c_{qg\to\tilde{q}\tilde{g},\mathbf{15}} = {} & \frac{N_c+2}{2N_c}\delta_{a_2a_4}\delta_{a_1a_3} + d_{ca_4a_2}T^c_{a_3a_1} \qquad C_2(R_{\mathbf{15}}) = \frac{(N_c+1)(3N_c-1)}{2N_c}, \\ & - \frac{N_c+2}{N_c+1}(T^{a_4}T^{a_2})_{a_3a_1}, \end{aligned} \tag{5.23}$$

- and squark-pair production:

$$c_{qq\to\tilde{q}\tilde{q},\bar{\mathbf{3}}} = \frac{1}{2}\left(\delta_{a_1a_4}\delta_{a_2a_3} - \delta_{a_1a_3}\delta_{a_2a_4}\right), \qquad C_2(R_{\bar{\mathbf{3}}}) = \frac{(N_c+1)(N_c-2)}{N_c}, \tag{5.24}$$

$$c_{qq\to\tilde{q}\tilde{q},\mathbf{6}} = \frac{1}{2}\left(\delta_{a_1a_4}\delta_{a_2a_3} + \delta_{a_1a_3}\delta_{a_2a_4}\right), \qquad C_2(R_{\mathbf{6}}) = \frac{(N_c-1)(N_c+2)}{N_c}. \tag{5.25}$$

The coefficients δ_{ab}, T^c_{ab}, f_{abc}, and d_{abc} denote the Kronecker delta and the usual colour generators and antisymmetric and symmetric structure constants of SU(N_c). A summation over repeated indices is implied.

The one-loop coefficients of the soft anomalous dimension $D^{(1)}_{ij\to kl,I}$ which are required at NLL accuracy can then be expressed in the absolute threshold limit through the quadratic Casimir invariants of the product representation:

$$D^{(1)}_{ij\to kl,I} = -C_2(R_I). \tag{5.26}$$

The remaining expressions of the exponentials are given in appendix C, while the colour-decomposed LO cross sections are available in ref. [17].

5.2 Predictions for future colliders

While predictions for squark and gluino production have been computed for 7 [197] and 8 TeV including corrections from threshold resummation, it is of interest to provide results for the current and future LHC energies to be used for experimental analyses. While the LHC currently runs at a centre-of-mass energy of 13 TeV and may be upgraded to 14 TeV in the near future, there are plans to further upgrade the LHC in the future to allow for centre-of-mass energies of 33 TeV and 100 TeV with a much higher luminosity. Therefore, we now present total cross sections for squark and gluino production at NLL accuracy and matched to the full NLO result for these present and future energies. The resummed contributions are computed with a self-written code, while the NLO cross sections are computed with the freely available code `Prospino` [74]. The `LHAPDF` [198] library has been used to simplify the computations with the different PDF sets.

The results of these calculations are publicly available as grids including an interpolation code by the name of `NLL-fast` [199]. We provide predictions for the two PDF sets MSTW2008 [20] and CTEQ6L1/CTEQ6.6 [200, 201], including 68% C.L. PDF and α_s uncertainties as well as the uncertainty from simultaneously varying the renormalisation and factorisation scales up and down by a factor of two from their central value, $\mu_R = \mu_F = m_{\text{av}}$, where m_{av} denotes the average mass of the two final-state particles. By now, predictions for the NNPDF3.0 PDF set [22] are also available at 13 TeV, see the next chapter.

The MSTW2008 and CTEQ6.6 results should be combined according to the PDF4LHC recommendations as explained in ref. [75]. In the following, we will present the combined results in an illustrative manner for a few special cases.

5.2.1 Total cross sections for all processes of squark and gluino production

Figure 5.1 shows the total cross sections for squark and gluino production with stop production shown separately, see chapter 8 for a more detailed discussion regarding the special role of stops. We choose 10^{-5} pb as a lower limit for the total cross section, as the expected luminosities of the ATLAS and CMS experiments would still allow for the detection of a few events. With this lower limit, the upper mass limit for a detection of squarks and gluinos lies around m = 2-3.5 TeV for $\sqrt{S}$ = 13, 14 TeV, around m = 4-7 TeV for $\sqrt{S}$ = 33 TeV, and around m = 10-18 TeV for $\sqrt{S}$ = 100 TeV. It can furthermore be seen that while at lower masses, $\tilde{q}\tilde{g}$ and $\tilde{g}\tilde{g}$ dominate as production processes, the dominant processes at high masses are $\tilde{q}\tilde{q}$ and $\tilde{q}\tilde{g}$.

5.2.2 Special cases of squark and gluino production

Experimental analyses often consider simplified models [202] where most of the particles of the supersymmetric spectrum are decoupled, and only a small number of particles is experimentally accessible. We provide results for three such cases: gluino-pair production when assuming squarks to be decoupled, squark production when assuming gluinos to be decoupled, and stop-antistop or sbottom-antisbottom production.

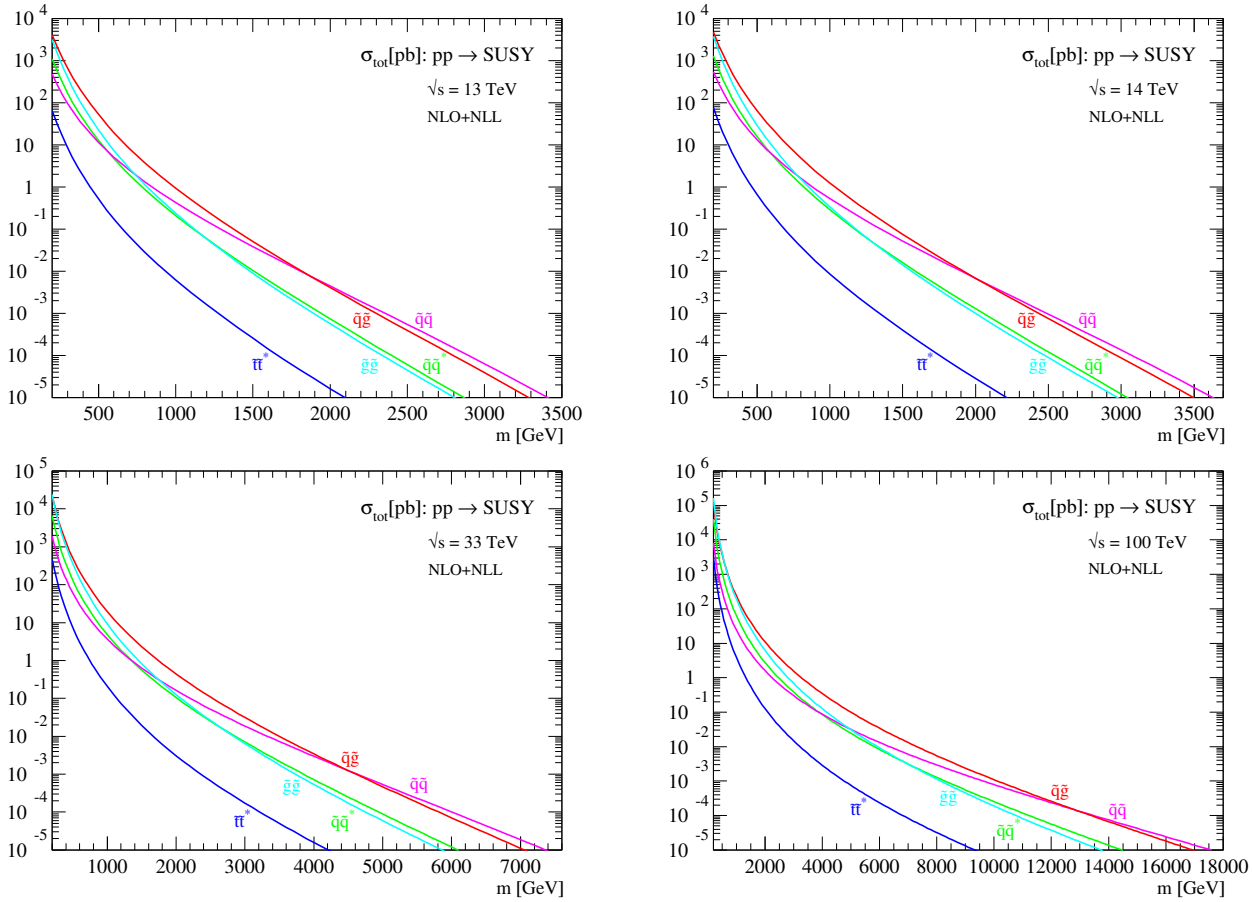

Figure 5.1: NLO+NLL production cross sections for the case of equal squark and gluino masses at collider energies of $\sqrt{S} = 13, 14, 33, 100$ TeV.

5.2.2.1 Gluino-pair production with decoupled squarks

In figure 5.2, the NLO+NLL cross sections for gluino-pair production assuming very heavy squarks are shown for collider energies ranging from 13 TeV to 100 TeV. On the left side, we present the total cross sections including the total uncertainty envelope down to the lower cross section limit of 10^{-5}. On the right side, the total uncertainty band is shown for a smaller mass range and split up into the different contributions from the scale and MSTW and CTEQ PDF and α_s uncertainties. The envelope of the upper most and lower most values constitute the total uncertainty, with the average of the upper most and lower most values being the central value of the prediction. The colour scheme for the different contributions is displayed in the plots. It can be seen that with increasing collider energy, the relative uncertainty shrinks.

5.2.2.2 Squark production with decoupled gluinos

Figure 5.3 shows the NLO+NLL cross sections for squark-antisquark production assuming very heavy gluinos for collider energies ranging from 13 TeV to 100 TeV. The same conventions for displaying the different contributions as in section 5.2.2.1 are used.

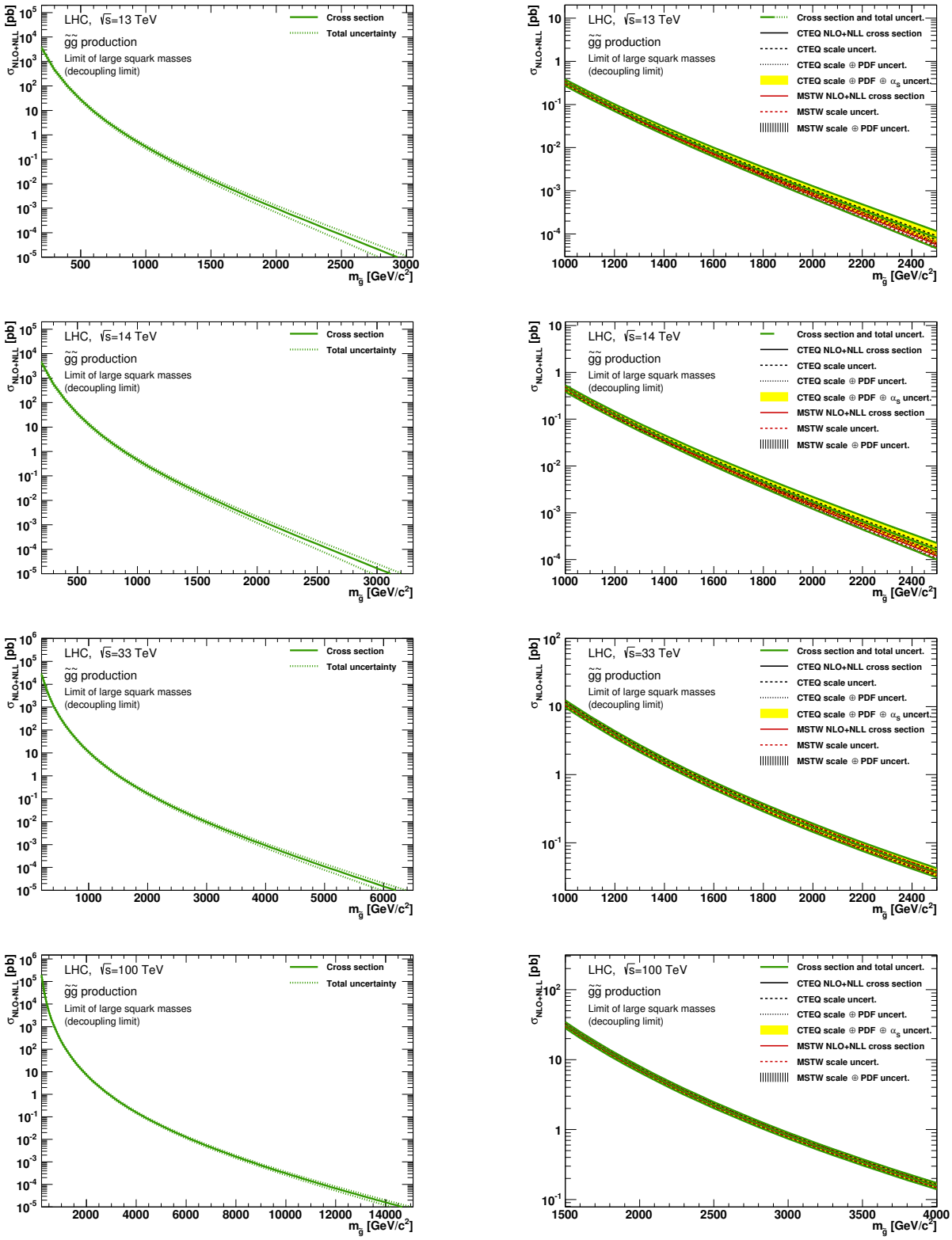

Figure 5.2: NLO+NLL cross sections for gluino-pair production in the case of decoupled squarks, at collider energies of $\sqrt{S} = 13, 14, 33, 100$ TeV.

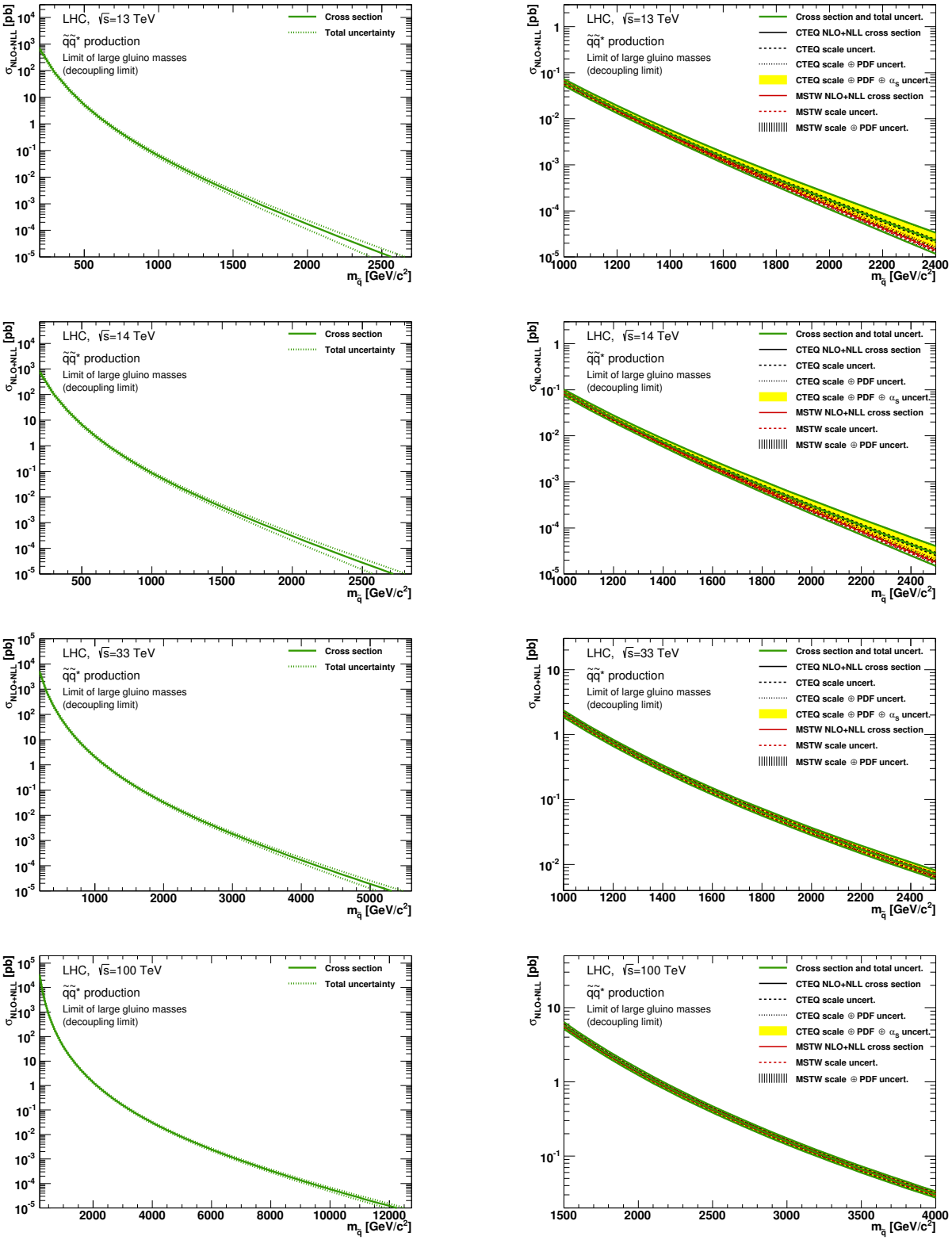

Figure 5.3: NLO+NLL cross sections for squark-antisquark production in the case of decoupled gluinos, at collider energies of $\sqrt{S} = 13, 14, 33, 100$ TeV.

5.2.2.3 Stop-antistop production

The production cross sections for stop-antistop pairs at NLO+NLL accuracy in a scenario where only the lightest stop can be reached experimentally are shown in figure 5.4 again for collider energies from 13 TeV to 100 TeV. The same conventions for displaying the different contributions as in section 5.2.2.1 are used. These cross sections can also be regarded for the production of sbottom-antisbottom pairs in the case where only the lightest sbottom can be reached by experiments, as the differences between stop and sbottom production are numerically negligible [112].

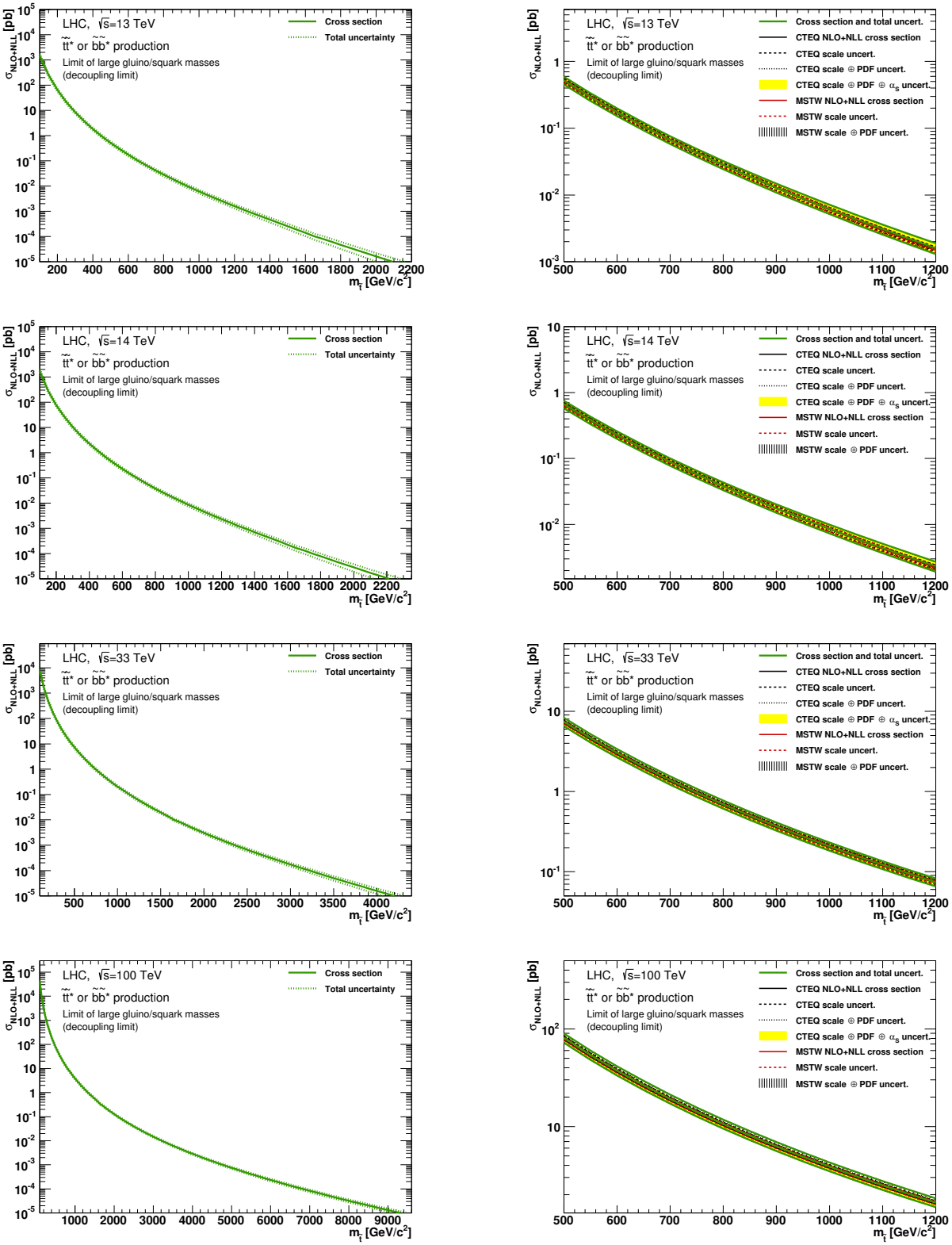

Figure 5.4: NLO+NLL cross sections for stop-antistop or sbottom-antistbottom production at collider energies of $\sqrt{S} = 13, 14, 33, 100$ TeV.

6 NLL Threshold Resummation with Threshold-Improved PDF Sets

The NNPDF collaboration [22] develops PDF sets with a minimal theoretical bias by not choosing a certain parametrisation for a fit function at an initial scale, as it is done by MSTW/MMHT and CTEQ, but instead by using neural networks to obtain a fit of the PDFs from experimental data. One of the main differences to the MSTW and CTEQ PDF sets lies in the determination of the PDF uncertainty: whereas the latter use the Hessian method [203] to generate their eigenvector sets for uncertainty determination leading in general to asymmetric upper and lower uncertainties, the former is based on the Monte Carlo method [204–206] with every replica of equal significance. The latest PDF version is called NNPDF3.0 and includes deep inelastic scattering and Drell-Yan data as well as recent LHC data including W-boson, inclusive jet, and heavy top production collected by the ATLAS, CMS, and LHCb experiments.

For a truthful description of experimental processes, it is necessary to use as many different PDF sets as possible in the calculation of theoretical predictions to minimise the theoretical bias introduced by a specific parametrisation. In that sense, it is of much interest to study in an analysis the effects of the NNPDF set due to its independence from a parametrisation at an initial scale, as up until recently, the data grids of `NLL-fast` were only available for the CTEQ6.6 and MSTW2008 PDF sets.

In this chapter, we will improve the existing results for NLL threshold resummation by, for the first time, analysing the effects of PDFs with threshold resummation, using the recently published threshold-improved NNPDF sets [207]. Threshold-improved PDF sets are of much interest for predictions of the production of new particles such as squarks and gluinos, as it will be seen that these PDFs lead to both a qualitative as well as a quantitative change in the predictions. The results of the collaborative work in this chapter have been published in ref. [142].

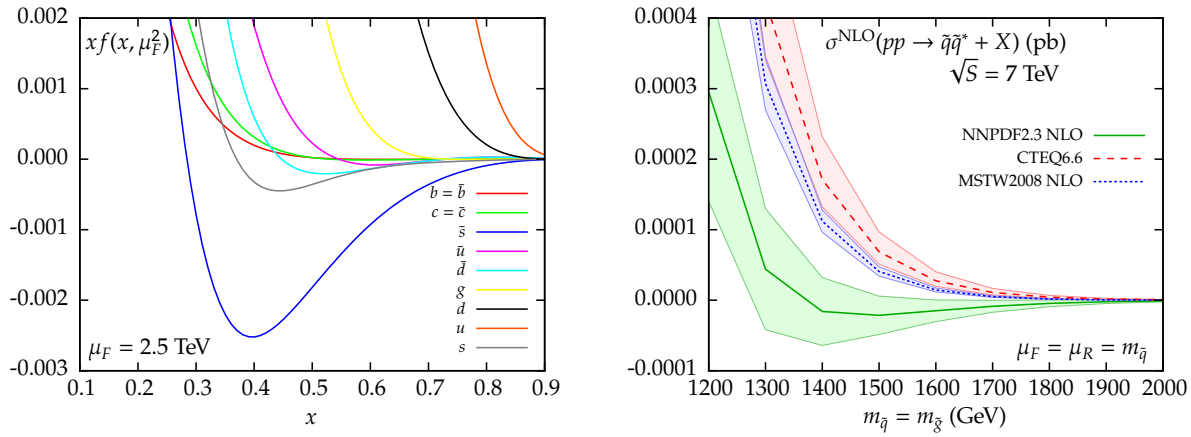

(a) (b)

Figure 6.1: Left: NNPDF2.3 NLO set with $\alpha_s(m_z) = 0.119$ for different parton flavours. The factorisation scale at which the PDF is evaluated is chosen as $\mu_F = 2.5$ TeV. Right: Total cross section for $\tilde{q}\tilde{q}^*$ production at NLO with a centre-of-mass energy of $\sqrt{S} = 7$ TeV. Shown is the high-mass range using the NNPDF2.3, MSTW2008, and CTEQ6.6 PDF sets at NLO. Both the central value as well as the PDF uncertainties of the NNPDF2.3 prediction become negative for $m_{\tilde{q}} > 1.3$ TeV.

6.1 NNPDF2.3 analysis

A main point of the NNPDF3.0 set which differs from its predecessor NNPDF2.3 [208] is, to a lesser degree, the increase in new experimental data taken into account, but more importantly an improvement in positivity constraints: as PDFs beyond LO in the evolution kernel are not required to be positive definite, negative PDF values can arise that, however, should still lead to positive results for observables such as cross sections, see figure 6.1 (a) for the PDFs of the NNPDF2.3 set for the different flavours at a scale of $Q = 2.5$ TeV. In particular, the distributions of the strange quark and its antiparticle are largely negative, and to a lesser amount also the distribution of the down quark. We found that using the NNPDF2.3 set for squark and gluino production leads to negative cross sections for high squark and gluino masses, see figure 6.1 (b) as an exemplary plot which compares the total cross section of $\tilde{q}\tilde{q}^*$ production at NLO for the NNPDF2.3, MSTW2008 and CTEQ6.6 PDF sets, including the range of 68% C.L. PDF uncertainties. The region of high final-state particle masses is indeed the one which is strongly affected by PDF uncertainties due to the lack of experimental data available for large momentum fractions x, making it difficult to provide reliable predictions for cross sections without a prescription to turn off the negative contributions, which, on the other hand, results in an arbitrariness in the definition of the predictions e.g. by reweighting the contributions from certain initial states that contribute differently at LO and NLO.

An improvement in the methology of the positivity constraints was achieved in the creation of the NNPDF3.0 set where the number of constraints introduced was chosen equal to the number of independently parametrised PDFs (i.e. the different flavours), leading to positivity both for the observables used in the fitting process of the PDFs as well as new observables which have not been measured yet, such as in new physics searches [22]. This makes it

applicable to squark and gluino production where due to this new methology, the central value of the cross section always stays positive. Therefore, in the following sections, the impact of the NNPDF3.0 set for NLO+NLL cross sections for squark and gluino production at the LHC will be analysed.

6.2 NLO+NLL cross section predictions at 13 TeV with NNPDF3.0

The following plots present predictions for the four processes $\tilde{g}\tilde{g}$, $\tilde{q}\tilde{q}^*$, $\tilde{q}\tilde{g}$, and $\tilde{q}\tilde{q}$, where the $\tilde{q}$ ($\tilde{q}^*$) denote the supersymmetric partners of the light-flavoured (anti-)quarks only. All squark flavours will be assumed to be mass-degenerate with a common mass $m_{\tilde{q}}$, while the gluino mass is denoted by $m_{\tilde{g}}$. For simplicity, the results in this section are calculated with $m_{\tilde{q}} = m_{\tilde{g}} = m$, although predictions for unequal masses are publicly available in the `NLL-fast` grids. The QCD coupling $\alpha_s(m_Z) = 0.118$ and the NNPDF3.0 PDFs at NLO are defined in the $\overline{\text{MS}}$ scheme with five massless quark flavours. The top mass is set to $m_t = 173.21$ GeV [16]. Unless otherwise specified, the renormalisation and factorisation scales are chosen equal, $\mu_R = \mu_F = \mu$ with $\mu = m$ set to the average mass of the process. To employ the NNPDF sets in our calculations, we use the "derivative method" as described in section 4.7.

For Monte Carlo PDF sets such as NNPDF, the central value of an observable such as a cross section is computed by calculating its value with each replica of the PDF set and then averaging over all of these values:

$$\sigma^{(\text{central})} = \langle\sigma\rangle = \frac{1}{N_{\text{rep}}} \sum_{k=1}^{N_{\text{rep}}} \sigma^{(k)}, \tag{6.1}$$

where N_{rep} denotes the total number of replicas and $\sigma^{(k)}$ is the cross section calculated with replica k. The PDF uncertainty $\Delta\sigma_{\text{PDF}}$ then follows as the value of the standard deviation

$$\Delta\sigma_{\text{PDF}} = \sqrt{\frac{1}{N_{\text{rep}} - 1} \sum_{k=1}^{N_{\text{rep}}} \left(\sigma^{(k)} - \langle\sigma\rangle\right)^2}. \tag{6.2}$$

In our calculations, we use the NNPDF set with $N_{\text{rep}} = 100$ replicas. Furthermore, we apply the prescription that, should a certain replica still lead to a negative cross section, which might happen in the high-uncertainty region for a few replicas, we then set the cross section to zero for this specific replica both in the central value and PDF uncertainty calculations without changing the total number of replicas.

Figure 6.2 shows the total cross section predictions for the four processes as mentioned above at NLO+NLL accuracy and a collider energy of $\sqrt{S} = 13$ TeV. The mass range has been chosen as 1 TeV for the lowest and 3.5 TeV for the highest squark and gluino mass which is motivated by the current upper mass limits from the ATLAS [72, 209] and CMS experiment [210] as well as the plans for future high-luminosity colliders [211] with squark and gluino masses of 3.5 TeV just still being detectable. While the central value of the cross section now always stays positive, the PDF uncertainties blow up for high masses due to the lack of experimental data in this region. In particular, the squark-antisquark cross section

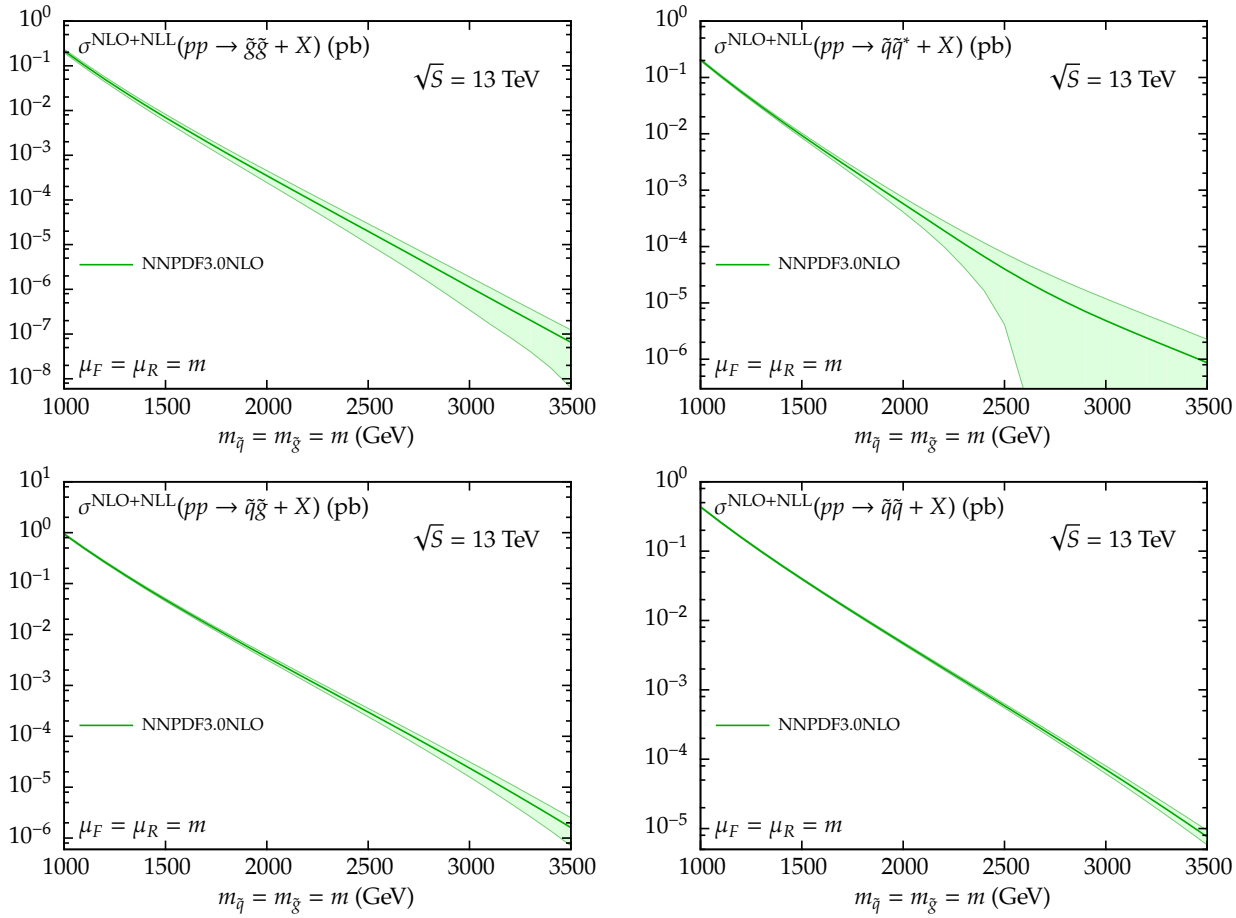

Figure 6.2: The NLO+NLL total cross-sections for all possible production channels of squark and gluino production at the LHC with $\sqrt{S}$ = 13 TeV, obtained with the NNPDF3.0 NLO set. Results are shown as a function of the sparticle mass m and include the one-sigma PDF uncertainties.

suffers from large uncertainties for masses $m \gtrsim 2.5$ TeV which stem from the main initial-state channel $q\bar{q}$. Indeed, we found that this process suffers from negative replicas out of all the processes the most. Nonetheless, applying the prescription of setting these negative replicas to zero only affects the cross section in the very high-mass region with a shift that is well within the intrinsic PDF uncertainties.

Before discussing the cross sections in more detail, it will be useful to first study the importance of different initial-state channels contributing to the four squark and gluino production processes. Figure 6.3 shows the contribution from each initial state to a certain process, normalised to the full cross section being the sum over all initial-state configurations:

$$\frac{\sigma^{\text{NLO+NLL}}(ij \to kl)}{\sigma^{\text{NLO+NLL}}(pp \to kl)}, \tag{6.3}$$

where ij denotes the initial state and kl the final state. This ratio is computed at NLO+NLL accuracy with the NNPDF3.0NLO set. It can be seen that over the whole mass range, all processes have a clearly dominant initial-state channel which defines the behaviour of the

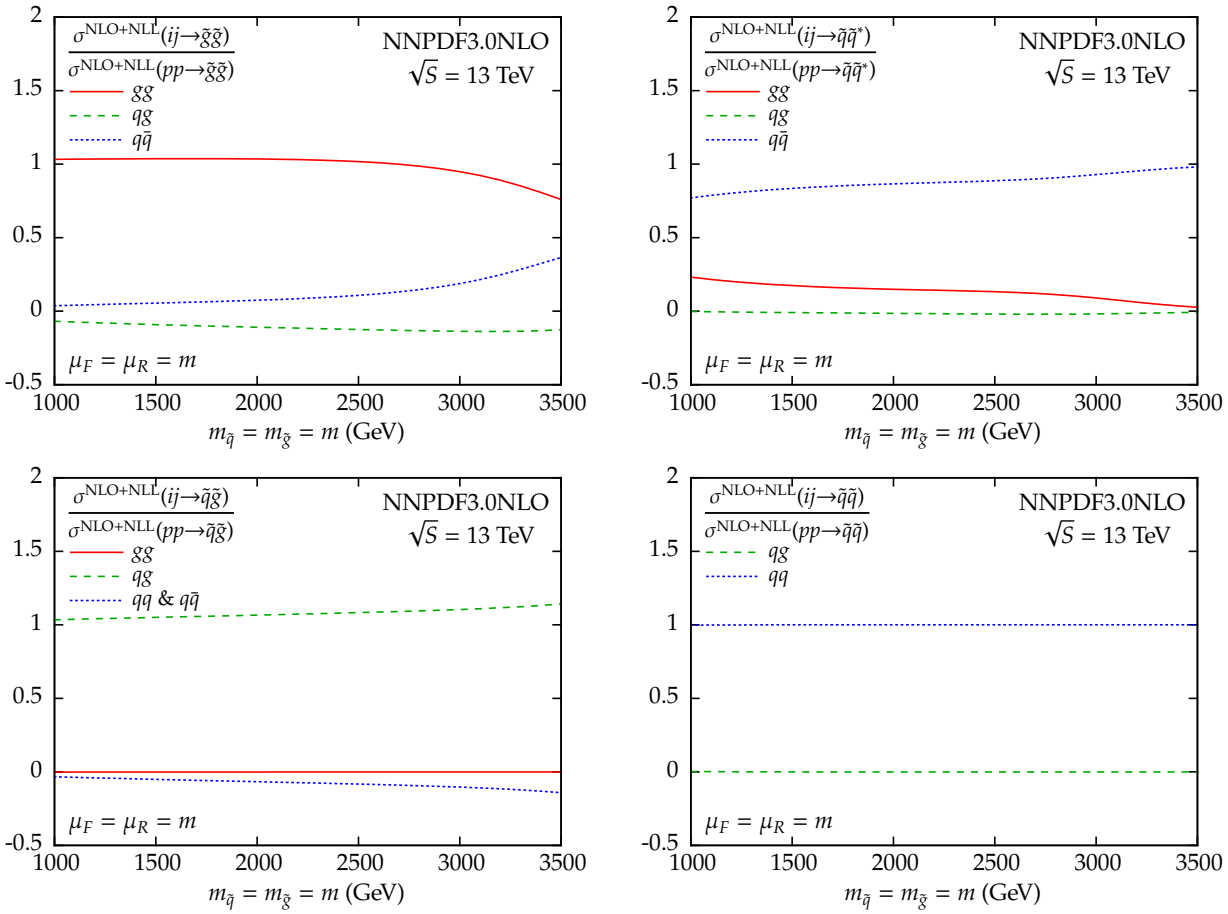

Figure 6.3: Ratio of the different initial-state contributions to the total NLO+NLL cross sections for $\tilde{g}\tilde{g}$, $\tilde{q}\bar{q}^*$, $\tilde{q}\tilde{g}$, and $\tilde{q}\bar{q}$ production depending on the sparticle mass and using NNPDF3.0 NLO PDF sets.

full cross section. Gluino-pair production is dominated by the gluon initial state gg up to sparticle masses of approximately 2.5 TeV, where the contribution from the quark-antiquark annihalation channel $q\bar{q}$ increases towards higher masses. The quark-gluon initial state qg is small compared to the dominant channel, but always leads to a negative contribution. Squark-antisquark production is dominated at high masses by the $q\bar{q}$ channel, with the gg channel contributing roughly by 25% at low masses, but decreasing for higher masses. Squark-gluino production is entirely dominated by the qg channel, with the other channels almost being negligibly small. Lastly, squark-pair production only consists of the quark-quark channel qq, with the other contributions being zero.

A better quantification of the dependence of a cross section on the particle masses and its additional contributions when comparing to a cross section of lower accuracy is given by the K-factor, defined as:

$$K_X = \frac{\sigma^X}{\sigma^{\text{NLO}}}, \tag{6.4}$$

which denotes a normalisation of the cross section at accuracy X to the NLO cross section. The $K_{\text{NLO+NLL}}$-factor, which is of relevance here, then shows the impact of the NLL resummation

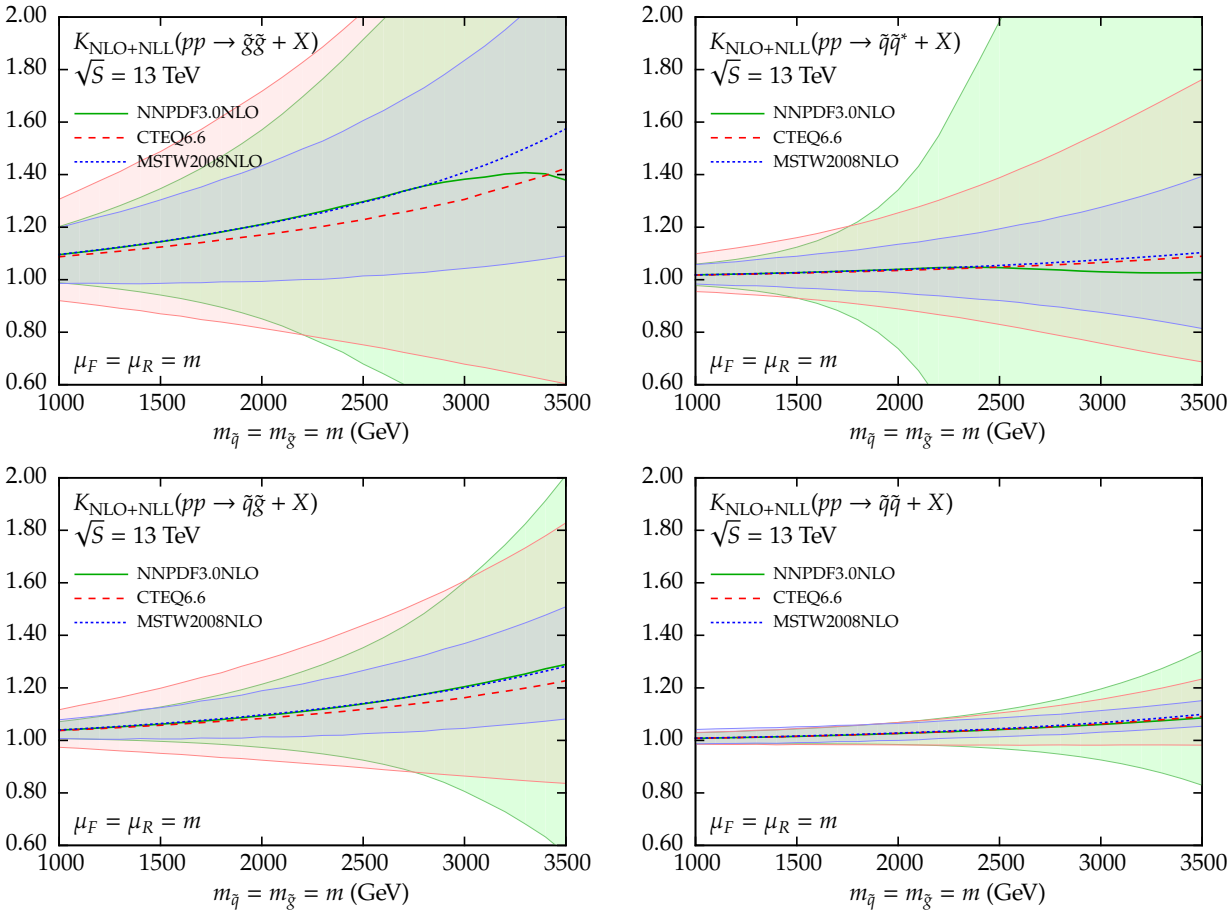

Figure 6.4: Dependence of the $K_{\text{NLO+NLL}}$-factor as defined in eq. (6.4) from the sparticle mass for predictions with the NNPDF3.0 NLO set, also including the results obtained using CTEQ6.6 and MSTW08 NLO, including the corresponding 68% C.L. PDF uncertainties in each case.

corrections to the partonic cross section in case the same PDF set is used both in the numerator and denominator. $K_{\text{NLO+NLL}}$ is expected to be larger than one if the corrections from NLL resummation are positive, and below one for negative corrections. It should be noted that for the denominator, we always choose the central value of the cross section, whereas the PDF uncertainties will only be computed from the numerator, if applicable.

Figure 6.4 shows the K-factor for all four processes in the given mass range, comparing the results from NNPDF3.0NLO to the MSTW2008NLO and CTEQ6.6 PDF sets as the latter are already available at NLO+NLL accuracy. While the NLL contributions for the gluon-initiated processes $\tilde{g}\tilde{g}$ and $\tilde{q}\tilde{g}$ range from approximately 10% at $m = 1$ TeV for $\tilde{g}\tilde{g}$ and 5% for $\tilde{q}\tilde{g}$ to 40-60% at $m = 3.5$ TeV for $\tilde{g}\tilde{g}$ and 20-30% for $\tilde{q}\tilde{g}$, the effect for the quark-initiated processes $\tilde{q}\tilde{q}^*$ and $\tilde{q}\tilde{q}$ is only marginal with 1-2% at $m = 1$ TeV and up to around 10% at $m = 3.5$ TeV. This difference can be explained by the large colour factors of the gluon initial states that appear in the resummed exponents. A second observation is the good agreement between the predictions of the three different PDF sets, in particular for lower masses below 2 TeV, with almost perfect agreement for the quark-initiated processes $\tilde{q}\tilde{q}^*$ and $\tilde{q}\tilde{q}$, while the agreement for $\tilde{g}\tilde{g}$ and $\tilde{q}\tilde{g}$ is still reasonable, in particular for NNPDF3.0 and MSTW2008, and well within

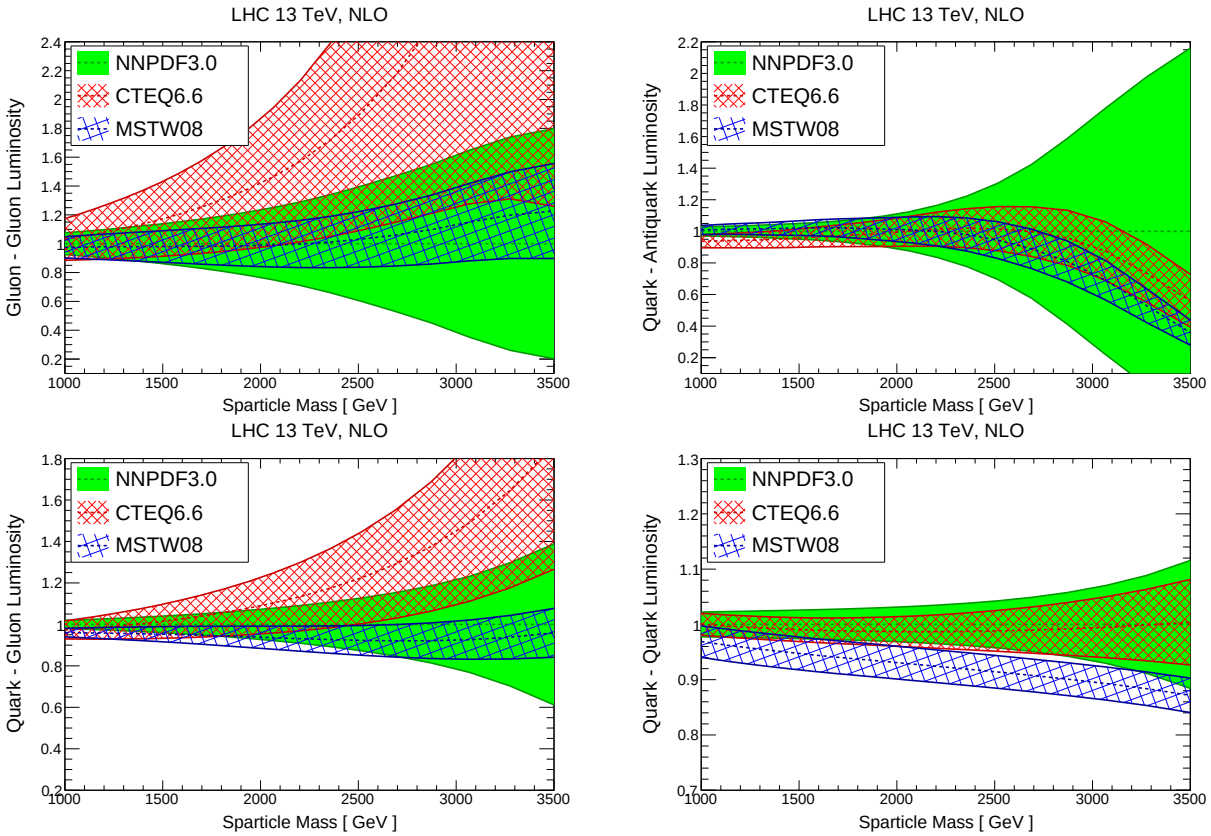

Figure 6.5: Parton luminosities for the NNPDF3.0 NLO, MSTW2008 NLO, and CTEQ6.6 PDF sets, including 68% C.L. PDF uncertainties, depending on the sparticle mass. All luminosities are normalised to the central value of NNPDF3.0 NLO.

the PDF uncertainty bands. Notable are the different sizes of the uncertainty bands: while the NNPDF3.0 band is usually the smallest of the three for $m = 1$ TeV, it grows significantly at higher masses where the other two bands, in particular MSTW2008, somewhat seem to underestimate the theoretical error introduced by the PDF uncertainty.

The behaviour of the PDF uncertainties in the K-factor plots can largely be inferred from the parton luminosities, see e.g. eq. (35) of ref. [22], for the four initial states gg, $q\bar{q}$, qg, and qq, shown in figure 6.5, which offer a closer correspondence to the total cross sections than single PDFs. Plotted are the luminosities for the NNPDF3.0NLO, CTEQ6.6, and MSTW2008NLO PDF sets, normalised to the central value of the NNPDF3.0 set, for varying sparticle masses. The gluon-initiated processes gg and qg show a good agreement between the central values of NNPDF3.0 and MSTW2008, which is reflected in the corresponding K-factors for $\tilde{g}\tilde{g}$ and $\tilde{q}\tilde{g}$, with the MSTW2008 uncertainty band being smaller. The similar size of the NNPDF3.0 and CTEQ6.6 uncertainties for these processes can also be seen, albeit differing in their central value. It should be noted here that since the normalisation in the luminosity plots is always to the NNPDF3.0 set, the difference in central values largely drops out in the K-factors due to the normalisation to the NLO cross section computed with the same PDF set. A good agreement of the sizes of the three uncertainty bands is seen for the quark-initiated processes, while for $q\bar{q}$, the uncertainty band of NNPDF3.0 blows up for high masses.

Due to the immediate availability of the cross sections for MSTW2008 and CTEQ6.6, no comparison has been made for the updated PDF sets MMHT14 [19] and CT14 [21]. However, from the parton luminosities, which are, at least partially, available in ref. [22] for MMHT14 and CT10 as the predecessor of CT14, it can be seen that the agreement between the three sets improves, with the NNPDF3.0 uncertainty band essentially covering the MMHT14 and CT14 luminosities. Therefore, we claim that the results presented here would not change substantially if the combination of NNPDF3.0, MMHT14, and CT14 were used instead of only the NNPDF3.0 set.

The results of the NLO+NLL cross sections with the NNPDF3.0 set have been made publicly available as interpolation grids in the `NLL-fast` format [199].

6.3 NLO+NLL cross sections with threshold-improved NNPDF3.0 sets

One source of theory uncertainty is the mismatch when PDF sets that are obtained from fitting experimental data to fixed-order cross sections are used in calculations with all-order resummation. This was the case in the previous section where the NNPDF3.0NLO sets have been used together with partonic cross sections at NLO+NLL accuracy. Therefore, an improved treatment would require the PDFs to be generated from resummed cross sections. This would result in the typically large corrections from threshold resummation being partially compensated by the PDFs, leading to a more accurate description of production processes, in particular for coloured sparticles where the resummed contributions usually become quite large. It is then important to see if the compensation of contributions from threshold resummations is still in agreement with the theoretical uncertainties when using convential fixed-order PDF sets.

Just recently, the NNPDF collaboration produced a PDF set including threshold-resummed contributions [207], using the same methology as for the NNPDF3.0 analysis. It is the first PDF set of its kind and thus being of great interest for the phenomenological implications to squark and gluino production. The threshold-improved PDF sets have been created based on NLO+NLL and NNLO+NNLL cross sections. The main difference to the NNPDF3.0 set from ref. [22] is a reduced dataset, since resummed calculations are not yet available for all of the processes that flow into the NNPDF3.0 analysis. Therefore, the NNPDF3.0 set will from now on be referred to as "NNPDF3.0 global fit" as a differentiation from the threshold-improved PDF set with a limited dataset. In particular, the processes of inclusive jet as well as charged-current Drell-Yan, i.e. W-boson production, have not yet been calculated with threshold resummation corrections included. The reduced dataset consists of deep inelastic scattering, (neutral-current) Drell-Yan, as well as top quark production data, and we will therefore label both the fixed-order as well as the threshold-improved NNPDF sets created with this dataset with "DIS+DY+top" following the notation of ref. [207]. It is important to emphasise that the fitting methology, input parameters, fixed-order calculations, and the positivity constraints are exactly the same as for the global fit, the only difference being the exclusion of certain experimental datasets. In the following, we explore the effects of the

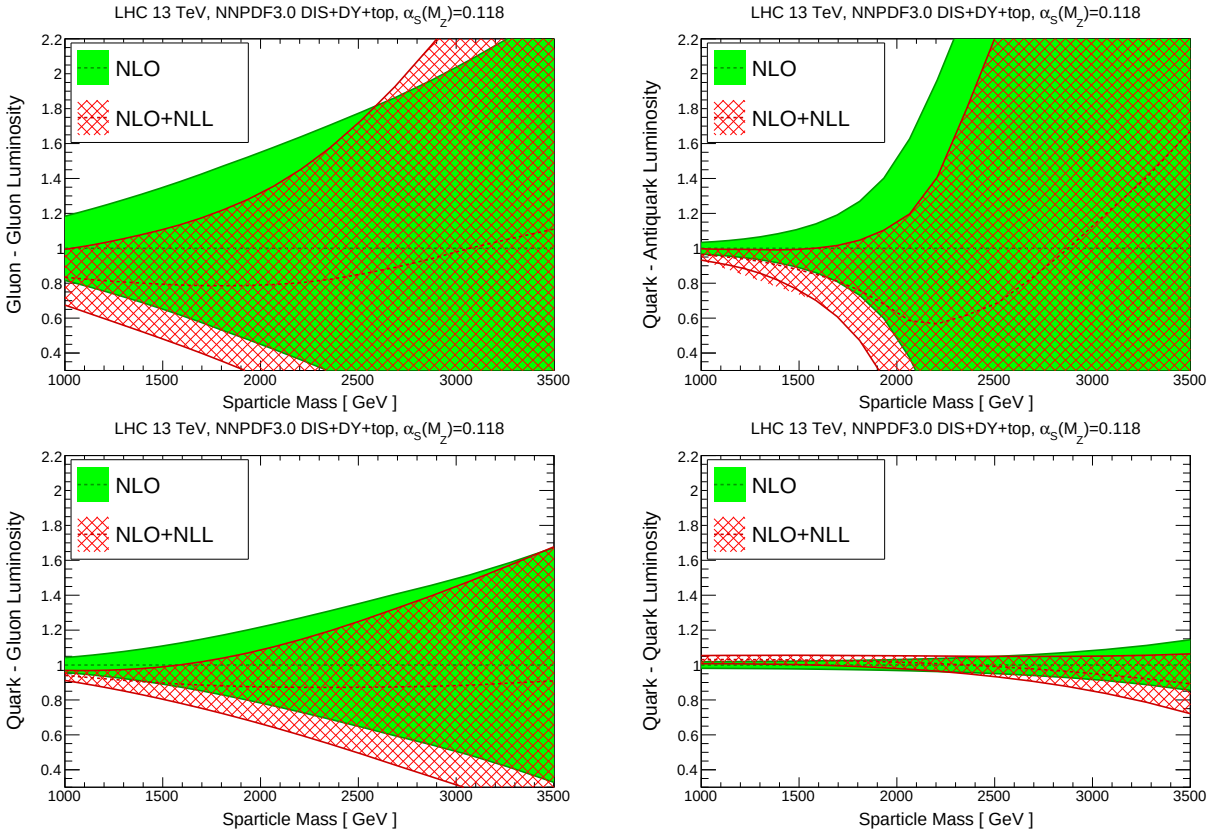

Figure 6.6: Same as figure 6.5, but now comparing the parton luminosities of the NLO+NLL fit to the NLO fit when using the reduced DIS+DY+top dataset.

threshold-improved PDFs on the squark and gluino production at NLO+NLL.

We start by showing the parton luminosities of both the NLO and NLO+NLL fit with the DIS+DY+top dataset in figure 6.6, again normalised to the NLO DIS+DY+top line. One immediate difference which can be seen between the NLO DIS+DY+top fit and the global fit of figure 6.5 is the large increase in PDF uncertainty for all initial-state configurations, most notably for gg and $q\bar{q}$. The origin of this effect is the smaller number of experimental datasets used to constrain the uncertainties, in particular in regions of the momentum fraction parameter space where little data is available. The luminosities of the NLO+NLL fit demonstrate a similar size in PDF uncertainties while their central values are smaller than the ones of the NLO fit for sparticle masses up to around 3 TeV, with the exception of qq, where the behaviour is inverted and the NLO+NLL central value is above the one for NLO up until around 2.5 TeV.

This behaviour of the parton luminosities can immediately be translated into the K-factor defined as:

$$K := \frac{\sigma^{\text{NLO+NLL}}\Big|_{\text{NLL DIS+DY+top}}}{\sigma^{\text{NLO}}\Big|_{\text{NLO DIS+DY+top}}}. \tag{6.5}$$

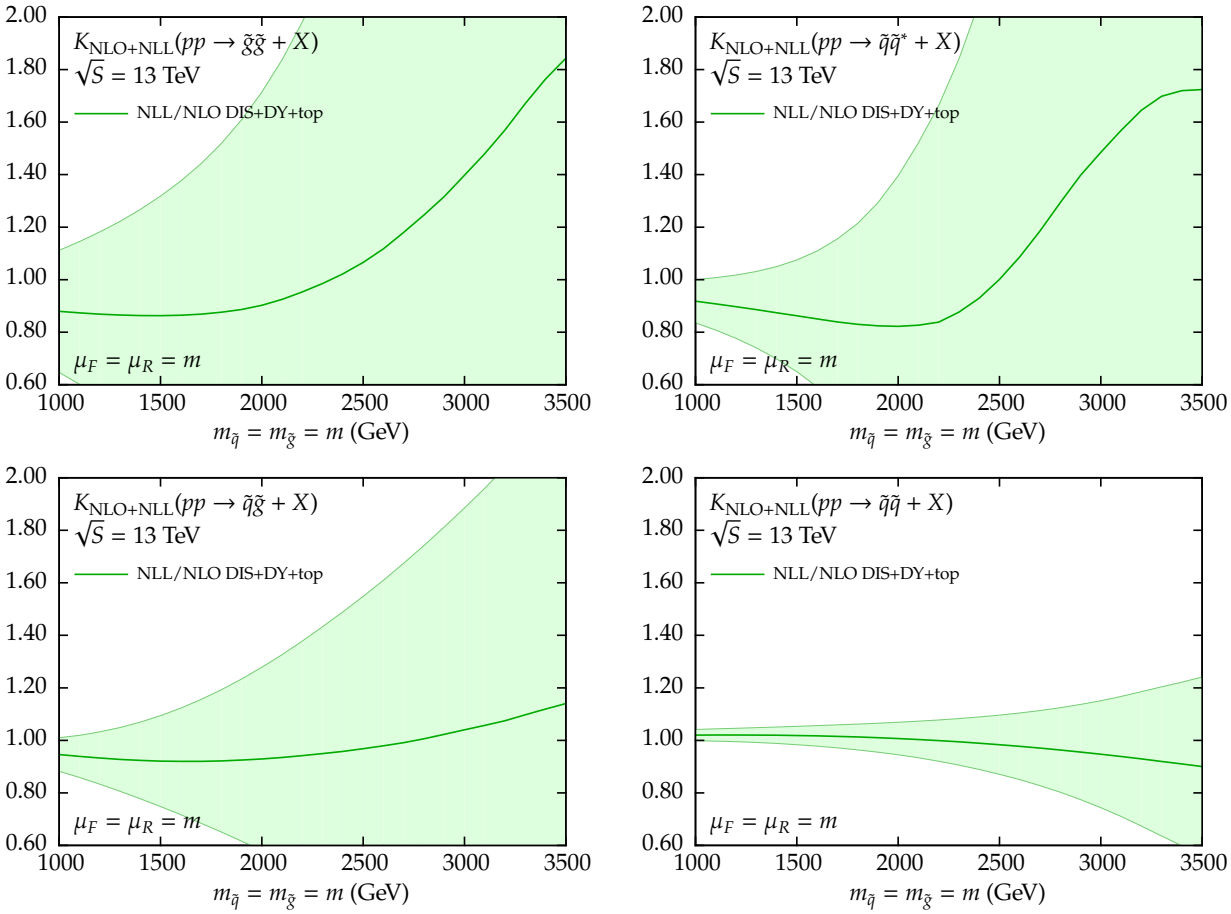

Figure 6.7: Dependence of the $K_{\text{NLO+NLL}}$-factor on the sparticle mass with the NLO+NLL fit used in the numerator, and the reduced DIS+DY+top NLO fit used in the denominator.

This definition exhibits two important differences to the K-factor which was shown in figure 6.4:

- while the NNPDF3.0 line in figure 6.4 was computed with the NNPDF3.0NLO global fit both for the resummed NLO+NLL cross section in the numerator as well as the fixed-order NLO piece in the denominator, here we use the threshold-improved and the fixed-order DIS+DY+top fit in the numerator and the denominator, respectively;

- the perturbative accuracy of the partonic cross sections and the PDF fits now match: resummed in the numerator, fixed-order in the denominator.

We note that for consistency, the reduced NLO DIS+DY+top fit is used in the denominator instead of the global fit. While the latter is more strongly constrained by a larger amount of experimental datasets, one would introduce additional ambiguities due to the mismatch of the datasets used for the fits in the numerator and denominator. It is however desirable to use the more accurate (in terms of experimental data) NLO global fit together with the threshold-improved fit (being more accurate in terms of theory predictions) which is why we will later discuss the application of various prescriptions to combine the two.

The K-factor of eq. (6.5) is shown in figure 6.7. Again, we immediately notice the large PDF uncertainties. Furthermore, the contributions from threshold resummation with the NNPDF3.0NLO global fit always appear to be positive with a K-factor larger than one, see figure 6.4, and monotonically increasing with the sparticle masses, except for $\tilde{g}\tilde{g}$ and $\tilde{q}\tilde{q}^*$ where we observe a turn-over point in the high-mass region in which the PDF uncertainties are anyway very large and the central value, being the average over all replicas, is affected by this large spread. This behaviour is qualitatively different when using threshold-improved PDFs, figure 6.7. We observe a K-factor which is smaller than one for sparticle masses $m \lesssim 2$ TeV for all processes except for $\tilde{q}\tilde{q}$. In particular, for the gluon-dominated processes $\tilde{g}\tilde{g}$ and $\tilde{q}\tilde{g}$, the K-factor is around 0.9-0.95 up to $m \approx 2$ TeV, with the K-factor for $\tilde{q}\tilde{q}^*$ even becoming as small as 0.8 around $m \approx 2$ TeV. The suppression is an effect of threshold-resummed corrections already being present in the PDFs, and therefore . At large masses $m > 2.5$ TeV, however, the K-factor again shows an enhancement of the NLO+NLL cross section with respect to NLO which turns out to be even larger than for the global fit PDFs in $\tilde{g}\tilde{g}$ and $\tilde{q}\tilde{q}^*$ production. This enhancement can be interpreted as the resummation in the partonic cross sections becoming dominant and largely compensating the suppression from the threshold-improved PDFs. For $\tilde{q}\tilde{q}$, the behaviour is inverted, in the sense that at lower masses, the K-factor is slightly above one, while steadily decreasing below one towards higher masses.

This behaviour is in direct agreement with the parton luminosities shown in figure 6.6, with the central lines and uncertainties of the K-factor closely follow the ones of the luminosities, resulting from the fact that each squark and gluino production process has one dominant inital-state channel, see figure 6.3.

6.3.1 The necessity for a prescription

Clearly, it can be seen that threshold-improved PDFs change both the qualitative as well as the quantitative properties of cross sections with threshold resummation corrections included. It is therefore important to take them into account for phenomenological analyses. One issue is however the reduced dataset, leading to a strongly increased PDF uncertainty. This problem will be solved as soon as contributions from threshold resummation have been calculated for the two missing processes, inclusive jet production as well as W-boson production.

Until then, we choose to use a prescription to include the effects of threshold-improved PDFs on squark and gluino production cross sections while keeping as much information from experiments as possible through the use of the global fit PDFs to constrain the region for large momentum fractions. Here, we show two choices for such a prescription which, as we will see, are compatible with the results of figure 6.7 and do not induce any unnaturally

large K-factors[1]. The first prescription defines a K-factor in the following way:

$$K := \frac{\sigma^{\text{NLO+NLL}}\Big|_{\text{NLO global}}}{\sigma^{\text{NLO}}\Big|_{\text{NLO global}}} \times \frac{\sigma^{\text{NLO+NLL}}\Big|_{\text{NLL DIS+DY+top}}}{\sigma^{\text{NLO+NLL}}\Big|_{\text{NLO DIS+DY+top}}}. \tag{6.6}$$

It can be regarded as a rescaling of the K-factor shown in figure 6.4 by a factor that takes the differences of switching from a fixed-order to a threshold-improved PDF fit for a NLO+NLL calculation into account[2]. The second prescription is based on the assumption that it might be more accurate to rescale each initial state separately instead of only the full cross section, and can be described in the following manner:

$$K := \frac{\sigma_{qq}^{\text{NLO+NLL}}\Big|_{\text{rescaled}} + \sigma_{qg}^{\text{NLO+NLL}}\Big|_{\text{rescaled}} + \sigma_{gg}^{\text{NLO+NLL}}\Big|_{\text{rescaled}}}{\sigma^{\text{NLO}}\Big|_{\text{NLO global}}} \tag{6.7}$$

with the "rescaled" cross section given as:

$$\sigma_{ij}^{\text{NLO+NLL}}\Big|_{\text{rescaled}} = \sigma_{ij}^{\text{NLO+NLL}}\Big|_{\text{NLO global}} \times \frac{\sigma_{ij}^{\text{NLO+NLL}}\Big|_{\text{NLL DIS+DY+top}}}{\sigma_{ij}^{\text{NLO+NLL}}\Big|_{\text{NLO DIS+DY+top}}}. \tag{6.8}$$

where ij denotes the specific initial state. Note that in eq. (6.7), qq denotes both the $q\bar{q}$ as well as the qq initial state. The rescaling for both prescriptions only applies to the central value of the cross section, and not the PDF uncertainties.

We mention that, as soon as the remaining processes required for a global fit of the threshold-improved PDFs have been calculated, both prescriptions become:

$$K := \frac{\sigma^{\text{NLO+NLL}}\Big|_{\text{NLL global}}}{\sigma^{\text{NLO}}\Big|_{\text{NLO global}}}, \tag{6.9}$$

which is the desired quantity, combining the threshold-improved (fixed-order) PDF sets with resummed (fixed-order) partonic cross sections.

Figure 6.8 now presents the two prescriptions in comparison to the K-factor of eq. (6.5) and the K-factor for the NLO global fit set, including the PDF uncertainties (light green band) as well as the full theoretical uncertainty (dark green band) which linearly adds the scale uncertainty, obtained from simultaneously varying the renormalisation and factorisation scales up and down by a factor of two with respect to the central scale $\mu = m$, on top of the PDF

[1] We studied various prescriptions and noticed that mixing the global and DIS+DY+top fits in an inconsistent manner leads to cross sections which are not meaningful for predictions.

[2] Alternatively, the K-factor can be interpreted as the true NLO+NLL K-factor with the best PDFs available for the corresponding cross sections (NLO+NLL PDFs for NLO+NLL cross sections, NLO PDFs for NLO cross sections), corrected for the reduced NLO+NLL dataset.

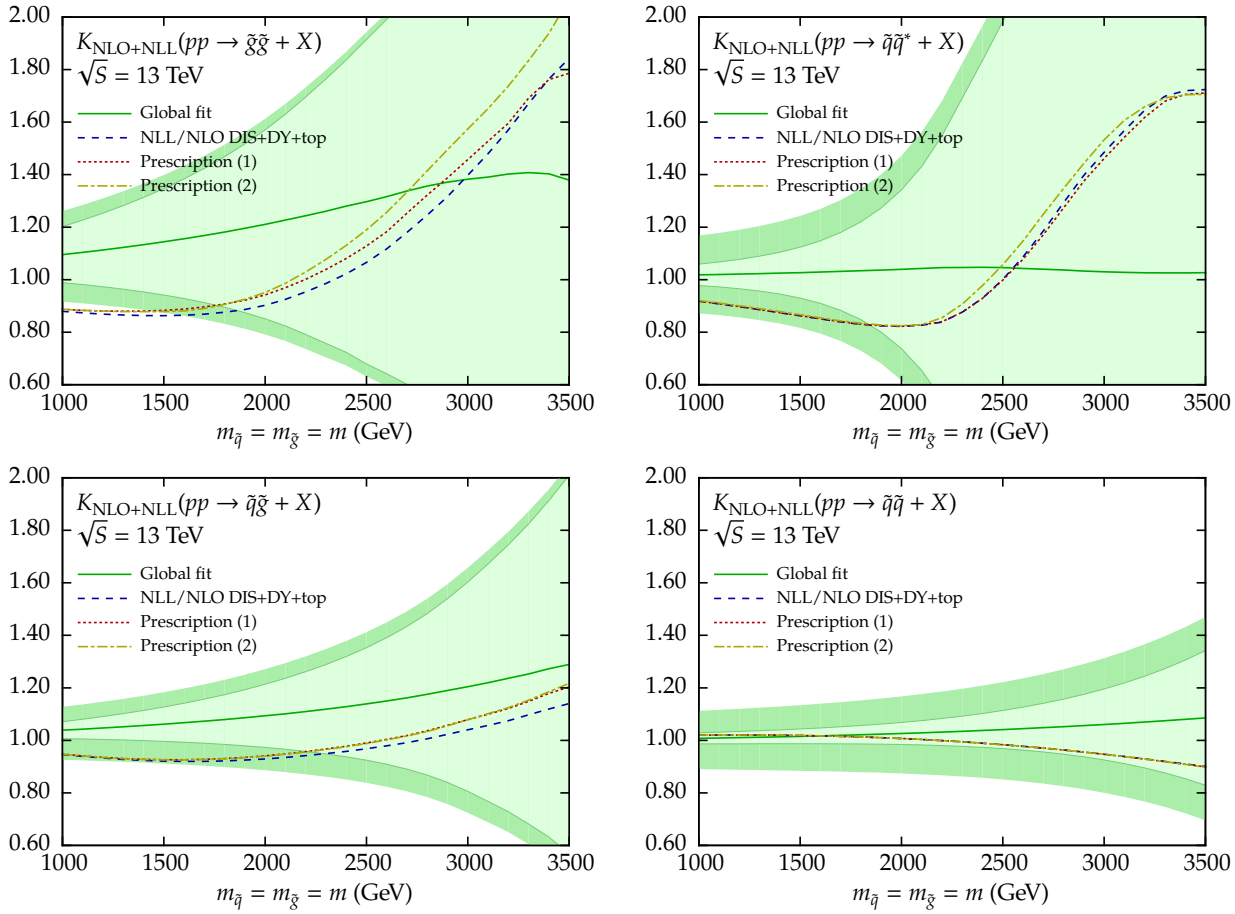

Figure 6.8: Comparison of the $K_{\rm NLO+NLL}$-factors when using the NNPDF3.0 NLO global fit according to eq. (6.4), the NLO+NLL and NLO fits with the reduced DIS+DY+top datasets from eq. (6.5), and the two prescriptions of eqs. (6.6) and (6.7). The light green band denotes the one-sigma PDF uncertainty of the global fit, and the dark green band corresponds to the full theoretical error, i.e. PDF uncertainty linearly added to the scale uncertainty.

uncertainty. First of all, it can be seen that both prescriptions as well as the K-factor of eq. (6.5) give similar results. This property can again be attributed to the behaviour of the luminosities, figure 6.6: dividing both eqs. (6.5) and (6.6) by the "global fit" K-factor (corresponding to the green solid line), we obtain (for eqs. (6.5) only approximately) the ratio of two NLO+NLL cross sections evaluated with the NLL DIS+DY+top and the NLO DIS+DY+top sets. Such a ratio corresponds to what is illustrated in figure 6.6. Furthermore, the prescriptions are consistent with the full theoretical uncertainty band, with the exception of $\tilde{g}\tilde{g}$ for masses $m < 1.5$ TeV, where these K-factors are slightly below the band.

This is an important result, as it demonstrates that the results computed with the NNPDF3.0 global fit are consistent with the additional threshold-improved corrections to the PDF fitting procedure. However, it also shows that, in the case of a further reduction of the intrinsic PDF uncertainty, threshold-improved effects in PDFs, changing the behaviour of the cross sections both qualitatively as well as quantitatively, become more relevant and cannot be neglected in phenomenological predictions. This is particularly true for the event of a detection of squarks

and gluinos some time in the future.

7 NNLL Threshold Resummation for Squarks and Gluinos

Contributions beyond NLL accuracy can be significant, in particular when the production of squarks and gluinos takes place close to threshold. Furthermore, to properly take into account all corrections in the threshold region, it is necessary to also consider higher-order off-shell corrections as well as contributions from Coulomb gluon exchange.

The following chapter presents predictions of squark and gluino production at NNLL accuracy including hard-matching coefficients up to one loop and Coulomb contributions up to two loop. Next to presenting total cross sections and K-factors to show the effect of threshold resummation with respect to NLO, also the scale dependence of the cross sections will be shown. One goal of including threshold resummation corrections is the reduction of this scale dependence, which can give an estimate of the size of higher-order corrections that are yet to be included in the calculations. As more terms in the perturbative series are taken into account, the higher-order scale logarithms should decrease the overall dependence on the renormalisation and factorisation scales. It will be seen that the contributions starting from NNLL can lead to a qualitative change in behaviour of the scale dependence for certain production channels where the the Coulomb contributions and higher-order logarithms are naturally large due to large colour factors.

After discussing the different ingredients needed for increasing the accuracy to NNLL, we present numerical results. It should be noted that only the squarks of the light quark flavours u, d, c, s, b, which we call *light-flavoured squarks*, will be analysed here, with a separate discussion about stops being done in the following chapter. The work presented in this chapter has been published in ref. [140].

7.1 Ingredients for NNLL resummation

For the calculation of soft-gluon resummation up to NNLL accuracy, a few more terms compared to NLL need to be taken into account. First of all, the function $G^{(3)}_{ij\to kl,I}$ of eq. (4.108), collecting the soft-gluon logarithms at NNLL, needs to be included. For its calculation, the A_i and D_i coefficients are required at third and second order in α_s, respectively. Furthermore,

to describe the soft wide-angle gluon emission correctly at NNLL, the two-loop corrections to the soft anomalous dimension $D^{(2)}_{ij\to kl,I}$ need to be known. The full expressions including the coefficients in the absolute threshold limit are given in appendix C.

The matching coefficients of eq. (4.109) will be included up to second order in α_s:

$$C_{ij\to kl,I}\big|_{\text{NNLO}} = 1 + \frac{\alpha_s}{\pi}\left(\mathcal{C}^{\text{Coul},(1)}_{ij\to kl,I} + \mathcal{C}^{(1)}_{ij\to kl,I}\right) + \frac{\alpha_s^2}{\pi^2}\left(\mathcal{C}^{\text{Coul},(1)}_{ij\to kl,I}\mathcal{C}^{(1)}_{ij\to kl,I} + \mathcal{C}^{\text{Coul},(2)}_{ij\to kl,I} + \mathcal{C}^{(2)}_{ij\to kl,I}\right). \quad (7.1)$$

First, the hard-matching coefficients will be discussed, followed by the Coulomb contributions.

7.1.1 Hard-matching coefficients

The hard-matching coefficients require a fixed-order calculation of the virtual corrections to the process of interest. In the case of squark and gluino production, fixed-order corrections are known exactly up to NLO. As the hard-matching coefficients depend on the colour structure, the NLO terms need to be decomposed into the colour configurations of the final state, see section 5.1.1. This procedure is described in refs. [17] and [129, 131], where also explicit expressions for the $\mathcal{O}(\alpha_s)$ hard-matching coefficients of the four squark and gluino production processes are given. The second order coefficient $\mathcal{C}^{(2)}_{ij\to kl,I}$ would require a full NNLO calculation, which is however not yet available for these processes. Therefore, this coefficient will be set to zero, $\mathcal{C}^{(2)}_{ij\to kl,I} = 0$. The hard-matching coefficients are computed in the threshold limit and are constant terms, meaning that they do not depend on β or the Mellin moment N.

7.1.2 Coulomb contributions

The Coulomb corrections are well known and have been derived up to all orders in section section 4.5.2. Here, we only include them up to second order in α_s, while an all-order analysis of the Coulomb contributions will be done later in chapter 9. Expanding the Coulomb Green's function in eq. (4.144) up to first order in α_s, we obtain:

$$\hat{\sigma}^{\text{Coul},(1)}_{ij\to kl,I} = \frac{\alpha_s \pi \mathscr{D}_{ij\to kl,I}}{2\beta}\sqrt{\frac{2m_{\text{red}}}{m_{\text{av}}}}\hat{\sigma}^{(0)}_{ij\to kl,I}. \quad (7.2)$$

The numerical values of $\mathscr{D}_{ij\to kl,I}$ for all production channels of squark and gluino production are listed in table 7.1. The one-loop Coulomb coefficient in Mellin-moment space $\mathcal{C}^{\text{Coul},(1)}_{ij\to kl,I}$ of eq. (7.1) is then defined as:

$$\frac{\alpha_s}{\pi}\mathcal{C}^{\text{Coul},(1)}_{ij\to kl,I}(N) := \frac{1}{\tilde{\sigma}^{(0)}_{ij\to kl,I}(N)}\int_0^1 \mathrm{d}\hat{\rho}\,\hat{\rho}^{N-1}\hat{\sigma}^{\text{Coul},(1)}_{ij\to kl,I}(\beta). \quad (7.3)$$

$\tilde{\sigma}^{(0)}_{ij\to kl,I}(N)$ is the Mellin-transformed partonic LO cross section. The Mellin transforms of the one-loop Coulomb cross sections have been calculated exactly and are listed for the four

Production channel	$\mathscr{D}_{ij\to kl,I}$
$q\bar{q} \to \tilde{g}\tilde{g}$	$\left\{3, \frac{3}{2}, \frac{3}{2}\right\}$
$gg \to \tilde{g}\tilde{g}$	$\left\{3, \frac{3}{2}, \frac{3}{2}, -1\right\}$
$q\bar{q} \to \tilde{q}\tilde{q}^* \, (\tilde{t}\tilde{t}^*)$	$\left\{\frac{4}{3}, -\frac{1}{6}\right\}$
$gg \to \tilde{q}\tilde{q}^* \, (\tilde{t}\tilde{t}^*)$	$\left\{\frac{4}{3}, -\frac{1}{6}, -\frac{1}{6}\right\}$
$qg \to \tilde{q}\tilde{g}$	$\left\{\frac{3}{2}, \frac{1}{2}, -\frac{1}{2}\right\}$
$qq \to \tilde{q}\tilde{q}$	$\left\{\frac{2}{3}, -\frac{1}{3}\right\}$

Table 7.1: Numerical values for the colour factor $\mathscr{D}_{ij\to kl,I}$ appearing in the Coulomb potential eq. (4.135) for all production channels of squark and gluino production, including the production of stops, when setting the number of colours $N_c = 3$. The different numbers in the curly brackets correspond to the different colour configurations denoted by the index I, see section 5.1.1.

processes of squark and gluino production in ref. [140].

The two-loop Coulomb coefficient has been calculated approximately for s-wave states, because it is too difficult in this case to perform the Mellin transform exactly. This is done by approximating the LO cross section according to eq. (4.143) and then applying the Mellin transform in a similar manner to eq. (7.3) with the $\mathcal{O}(\alpha_s^2)$ term of the expansion of the Green's function for a NLO Coulomb potential [140, 212]:

$$\begin{aligned}\frac{\alpha_s^2}{\pi^2}\mathcal{C}^{\mathrm{Coul},(2)} = \frac{\alpha_s^2}{16\pi^2}\Bigg\{&\frac{8}{3}\mathscr{D}_{ij\to kl,I}^2\pi^4 N\frac{2m_{\mathrm{red}}}{m_{\mathrm{av}}} - \mathscr{D}_{ij\to kl,I}\pi^2\sqrt{\frac{N}{\pi}}\sqrt{\frac{2m_{\mathrm{red}}}{m_{\mathrm{av}}}}\Bigg[-16\pi b_0\left(\ln N + \gamma_E\right)\\ &-4a_1 + 32\pi b_0\ln 2 - 16\pi b_0\ln\left(\frac{\mu_C^2}{m_{\mathrm{av}}^2}\right) - 16\pi b_0\ln\left(\frac{2m_{\mathrm{red}}}{m_{\mathrm{av}}}\right)\Bigg]\\ &- 16\pi^2\mathscr{D}_{ij\to kl,I}\left(C_A + 2\mathscr{D}_{ij\to kl,I}(1+v_{\mathrm{spin}})\right)\left(1 - \ln 2 - \frac{1}{2}(\ln N + \gamma_E)\right)\\ &+ \frac{4}{3}\mathscr{D}_{ij\to kl,I}^2\pi^4\frac{2m_{\mathrm{red}}}{m_{\mathrm{av}}}\Bigg\}. \end{aligned} \tag{7.4}$$

The value of v_{spin} depends on the type of particles that are produced as well as their spin configuration. It has been calculated for all processes of squark and gluino production and is given in ref. [134]. In the case of stop production as discussed in chapter 8, the same value as for squark-antisquark production will be used. The remaining coefficients that appear in the formula have already been defined when discussing the Coulomb Green's function in section 4.5.2. We note at this point that the numerical impact of these non-Coulombic

contributions on the cross sections is small.

Alternatively, the Coulomb contributions can be implemented in β-space by performing the Mellin transform of eq. (7.3) numerically. This will also enable us to use the exact two-loop Coulomb coefficient, as opposed to a simplification of the Mellin-transform by approximating the LO cross section[1]. In particular, the numerical Mellin transform will be necessary for the implementation of Coulomb resummation as presented in chapter 9. Another advantage in using a numerical Mellin transform is the fact that the Mellin-transformed one-loop Coulomb cross sections of ref. [134] are defined in terms of hypergeometric functions which, in most cases, are difficult to implement numerically.

7.1.3 Approximated NNLO

As no full NNLO calculations are available for squark and gluino production, dominant terms in the threshold limit of the order $\mathcal{O}(\alpha_s^2)$ relative to LO can be extracted from the resummation formula eq. (4.107), as they are expected to contribute significantly in the case of heavy squarks and gluinos. Here, we use the near-threshold expansion at $\mathcal{O}(\alpha_s^2)$ of appendix A of ref. [128] which is given in β-space. It has been derived from the resummed expressions in the SCET formalism, having the advantage of avoiding an inverse Mellin transform and directly yielding analytical expressions in physical β-space. By adding these $\mathcal{O}(\alpha_s^2)$ terms to the full NLO cross section,

$$\sigma_{h_1h_2\to kl}^{\text{NNLO}_{\text{Approx}}} = \sigma_{h_1h_2\to kl}^{\text{NLO}} + \Delta\sigma_{h_1h_2\to kl}^{\text{NNLO}_{\text{Approx}}}, \tag{7.5}$$

we get an approximation of the NNLO cross section which should be a good description of the full NNLO cross section close to threshold. Furthermore, we have checked that by transforming the β-space expression to Mellin-moment space with the same approximation of the LO cross section as it was used for the two-loop Coulomb coefficient, we obtain the same structure of $\ln(N)$ and one- and two-loop Coulomb terms (which are proportional to $\sqrt{N}$ and N, respectively) as in the expansion of eq. (4.107) at $\mathcal{O}(\alpha_s^4)$, with additional terms proportional to $1/\sqrt{N}$ and higher negative powers of $\sqrt{N}$ that are suppressed for $N \to \infty$. As it will be seen in the case of stop production, however, these subleading terms can become significant when the production takes place further away from threshold.

7.2 Treatment of *p*-wave channels

Before proceeding to the numerical results when performing resummation at NNLL accuracy, the prescription will be presented how the different partial wave contributions are treated. The final state can be produced with different orbital angular momentum quantum numbers L, where $L = 0$ denotes an s-wave state, $L = 1$ a p-wave state, and so on. The dominant contributions near threshold are from s-wave states. However, it might be possible that due

[1] It has been checked at the level of the cross section, however, that the difference between the approximated two-loop Coulomb coefficient in Mellin-moment space and the exact one in β-space is negligible and affects the numerical results by less than a percent, moreso for heavy particles produced close to threshold.

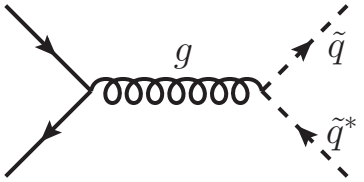

Figure 7.1: LO Feynman diagram for the production of a spin-0 squark-antisquark pair through quark-antiquark annihilation. The intermediate spin-1 gluon forces the squark-antisquark pair to be produced with angular momentum $L = 1$ to conserve the total angular momentum.

to symmetry properties of the final-state particles, the $L = 0$ state is not accessible and the particle pair needs to be produced at $L = 1$ or higher, see for instance figure 7.1.

Different colour configurations of the final-state particles have different symmetry properties. By expanding the LO cross section of a specific colour channel for $\beta \to 0$ and keeping only the leading term, it is immediately possible to distinguish between s- and p-wave channels, as the former are proportional to β, whereas the latter are proportional to β^3 and therefore suppressed by two additional powers. Higher partial wave contributions are then suppressed by even higher powers of β. From this threshold behaviour, it is clear that s-wave states are dominant for resummation. Furthermore, beyond NLL accuracy, the factorisation of soft, hard, and Coulomb contributions has not completely been proven yet. Therefore, we will consider all colour channels with p-wave final states up to NLL accuracy only, setting $C_{ij\to kl,I} = 1$, and not including the approximated NNLO contributions. We have checked for all processes of squark and gluino production that treating the p-wave-suppressed colour channels in the same way as the s-wave channels, i.e. including the full NNLL exponent and taking into account the contributions to $C_{ij\to kl,I}$, does not differ notably from our prescription of considering p-wave channels at NLL accuracy only.

7.3 Numerical results at $\sqrt{S}$ = 8 TeV

Now that all ingredients for NNLL resummation have been discussed and are available, we are in a position to do a numerical analysis of squark and gluino production at the LHC with a centre-of-mass energy of $\sqrt{S} = 8$ TeV. Similar settings as in the previous chapter are adopted: again, we first look at the four processes $\tilde{g}\tilde{g}$, $\tilde{q}\tilde{q}^*$, $\tilde{q}\tilde{g}$, and $\tilde{q}\tilde{q}$ while the production of stops will be considered in the following section. The light squark flavours are chosen to be mass-degenerate, and most of the time, we will also use $m_{\tilde{q}} = m_{\tilde{g}} = m = m_{\text{av}}$ unless specified otherwise. The top quark mass is set to $m_t = 173.07$ GeV [213], which differs slighly from the previous chapter. This change will however have no noticeable numerical impact, as the explicit value of the top mass only appears in loop diagrams. For the central line of the total cross sections and the K-factor plots, the renormalisation and factorisation scales are both chosen equal to the average mass of the final-state particles, $\mu_R = \mu_F = \mu = m_{\text{av}}$.

We will use the the MSTW2008 PDF set [20] and employ `QCD-Pegasus` with the corresponding MSTW2008 parametrisation for the PDFs in Mellin-moment space. For cross sections at NLO and NLL accuracy, NLO PDFs will be used with the corresponding $\alpha_s(m_Z) =$

0.120, while for NNLO and NNLL, NNLO PDFs with $\alpha_s(m_Z) = 0.117$ will be used. The fixed-order computations at NLO will be done with the freely available code `Prospino` [74], while the resummed corrections are implemented in and computed with a self-written computer code, with cross-checks being done by a second independent code.

The plots which we will show use the following labels to denote the accuracy of the cross sections:

- LO and NLO, denoting the leading and next-to-leading order cross section [97],
- NLO+NLL, denoting the resummed soft-gluon corrections at NLL accuracy matched to the NLO cross section, based on the calculations of ref. [109–113],
- $\text{NNLO}_{\text{Approx}}$, denoting the approximated NNLO corrections from threshold-enhanced terms, see section 7.1.3, added to the full NLO cross section,
- NNLL matched, which correspond to the $\text{NNLO}_{\text{Approx}}$+NNLL accuracy for s-wave colour channels, and NLO+NLL accuracy for p-wave colour channels. The numerical impact of using NLO or NNLO PDFs for the p-wave channels was found to be negligible.

The mass ranges in the plots are motivated by the current ATLAS and CMS exclusion limits (see also the previous chapter) and the reported luminosities which would still allow for the detection of a few sparticles with a mass of around 2.5 TeV. Furthermore, it is of interest to study the low and high mass behaviour to quantify the corrections from resummation which are more relevant for higher masses, i.e. closer to the hadronic threshold, due to the partonic threshold region contributing more dominantly to the total hadronic cross section.

Figure 7.2 shows the total cross sections for $\tilde{g}\tilde{g}$, $\tilde{q}\tilde{q}^*$, $\tilde{q}\tilde{g}$, $\tilde{q}\tilde{q}$, and the sum of all four ("inclusive"), including the theoretical uncertainty band. The latter consists of the scale uncertainty, which is obtained by simultaneously varying the renormalisation and factorisation scales up and down by a factor of two with respect to the central scale $\mu = m_{\text{av}}$, added linearly on top of the combined 68% C.L. PDF+α_s uncertainty. The numerical values for some masses are also shown in table 7.2, including the total uncertainties split up into scale, PDF, and α_s uncertainty. For all processes, it can be seen that from values of $\mathcal{O}(1-10\text{ pb})$ at low masses, the cross section quickly drops to values of around $\mathcal{O}(10^{-8} - 10^{-6}\text{ pb})$ towards high masses, with increasing theoretical uncertainty. We have checked that the size of the theoretical uncertainty is dominated by the α_s uncertainty which is obtained from special MSTW2008 NNLO PDF sets with varied values of α_s. Starting from intermediate masses around 1 TeV, $\tilde{q}\tilde{q}$ becomes the dominant process, figure 7.2 (d), and in principle defines the behaviour of figure 7.2 (e). We furthermore show a comparison of the full theoretical and scale uncertainties for NNLL matched and NLO+NLL. While the above mentioned increase in the full theoretical uncertainty is driven by the α_s uncertainty between NLO and NNLO PDF sets, the scale uncertainty decreases for all processes except for $\tilde{g}\tilde{g}$. It can also be seen in table 7.2 that for this process (and also for $\tilde{q}\tilde{g}$), the scale uncertainty behaves in a different way as for the other processes, in the sense that at half the value of the central scale, the cross section decreases, while it increases at twice the value of the central scale (see also later figure 7.5 and the corresponding discussion in the text). For this reason, the scale dependence of gluino-pair production will be analysed in more detail at a later point in this section.

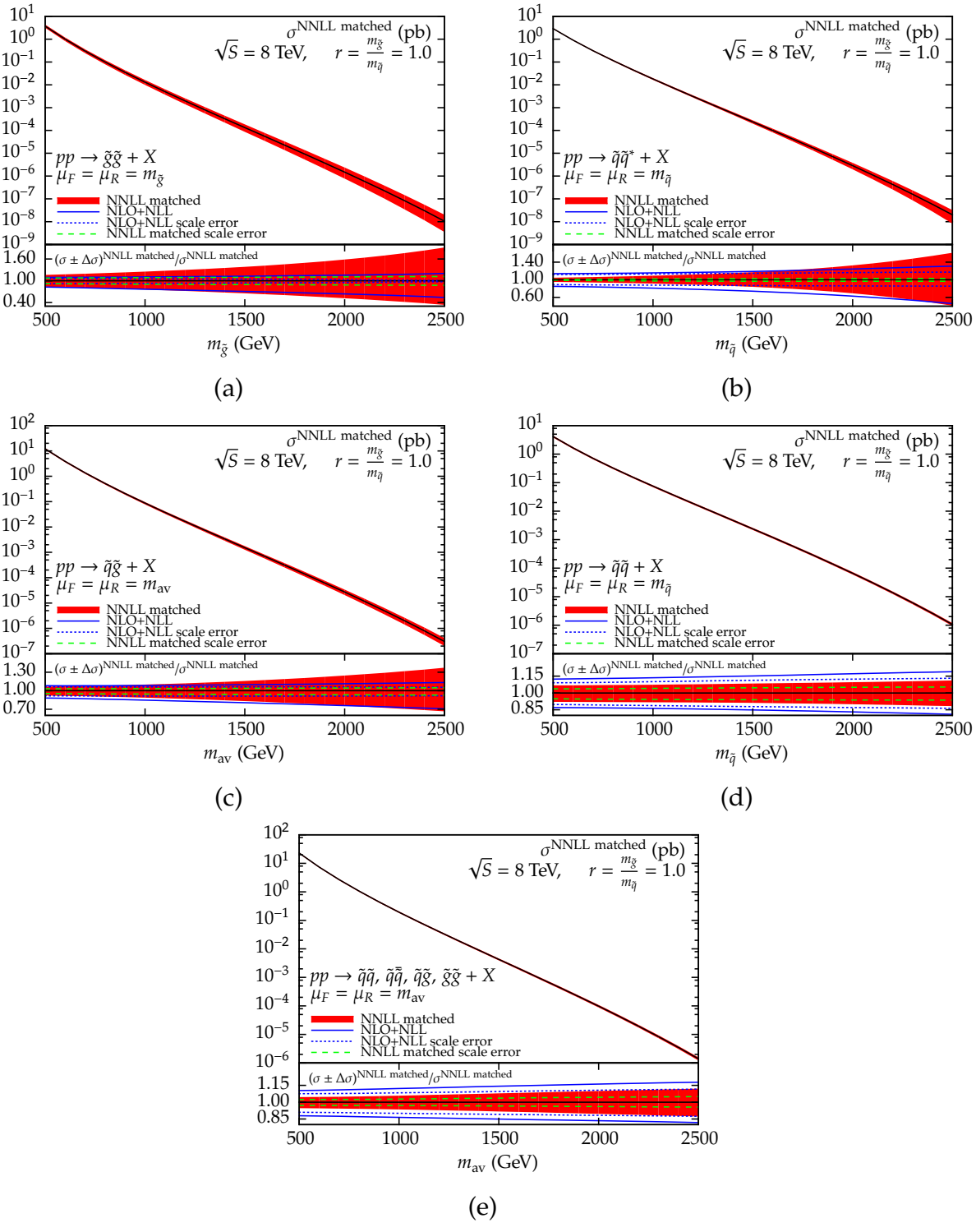

Figure 7.2: Total NNLL matched cross sections for $\tilde{g}\tilde{g}$, $\tilde{q}\tilde{q}^*$, $\tilde{q}\tilde{g}$, $\tilde{q}\tilde{q}$ production as well as the sum of all four at a centre-of-mass energy of $\sqrt{S} = 8$ TeV and including the full theoretical uncertainty band with 68% C.L. PDF+α_s and scale uncertainties. Additionally, the full uncertainties and separately also the scale uncertainties are shown as a ratio to the central value and compared to the NLO+NLL uncertainties.

Process	m (GeV)	$\sigma^{\text{NNLL matched}}$ (pb)	scale unc.	PDF unc.	α_s unc.	total unc.
$\tilde{g}\tilde{g}$	500	3.72	$^{-8.1\%}_{+7.6\%}$	$^{+6.7\%}_{-6.8\%}$	$^{+5.5\%}_{-4.3\%}$	$^{+16\%}_{-16\%}$
$\tilde{g}\tilde{g}$	1000	1.30×10^{-2}	$^{-9.3\%}_{+8.6\%}$	$^{+12\%}_{-13\%}$	$^{+11\%}_{-7.3\%}$	$^{+25\%}_{-24\%}$
$\tilde{g}\tilde{g}$	1500	1.33×10^{-4}	$^{-10\%}_{+9.7\%}$	$^{+20\%}_{-21\%}$	$^{+21\%}_{-12\%}$	$^{+38\%}_{-35\%}$
$\tilde{g}\tilde{g}$	2000	1.49×10^{-6}	$^{-12\%}_{+11\%}$	$^{+31\%}_{-31\%}$	$^{+36\%}_{-19\%}$	$^{+59\%}_{-48\%}$
$\tilde{g}\tilde{g}$	2500	1.05×10^{-8}	$^{-12\%}_{+12\%}$	$^{+49\%}_{-45\%}$	$^{+64\%}_{-30\%}$	$^{+92\%}_{-66\%}$
$\tilde{q}\tilde{q}^*$	500	2.90	$^{+0.37\%}_{-1.2\%}$	$^{+2.6\%}_{-2.3\%}$	$^{+3.2\%}_{-2.8\%}$	$^{+4.5\%}_{-4.8\%}$
$\tilde{q}\tilde{q}^*$	1000	1.80×10^{-2}	$^{+1.7\%}_{-2.8\%}$	$^{+6.0\%}_{-5.3\%}$	$^{+4.5\%}_{-2.9\%}$	$^{+9.2\%}_{-8.8\%}$
$\tilde{q}\tilde{q}^*$	1500	2.37×10^{-4}	$^{+2.4\%}_{-3.3\%}$	$^{+11\%}_{-12\%}$	$^{+9.6\%}_{-5.2\%}$	$^{+17\%}_{-16\%}$
$\tilde{q}\tilde{q}^*$	2000	2.86×10^{-6}	$^{+2.7\%}_{-3.3\%}$	$^{+20\%}_{-25\%}$	$^{+22\%}_{-12\%}$	$^{+33\%}_{-31\%}$
$\tilde{q}\tilde{q}^*$	2500	2.01×10^{-8}	$^{+3.0\%}_{-3.3\%}$	$^{+37\%}_{-50\%}$	$^{+45\%}_{-24\%}$	$^{+61\%}_{-59\%}$
$\tilde{q}\tilde{g}$	500	12.1	$^{-4.7\%}_{+3.2\%}$	$^{+2.3\%}_{-2.1\%}$	$^{+2.7\%}_{-2.3\%}$	$^{+6.7\%}_{-7.8\%}$
$\tilde{q}\tilde{g}$	1000	8.74×10^{-2}	$^{-5.4\%}_{+3.4\%}$	$^{+4.9\%}_{-5.0\%}$	$^{+4.4\%}_{-3.1\%}$	$^{+10\%}_{-11\%}$
$\tilde{q}\tilde{g}$	1500	1.52×10^{-3}	$^{-6.1\%}_{+3.9\%}$	$^{+8.6\%}_{-9.3\%}$	$^{+8.2\%}_{-5.1\%}$	$^{+16\%}_{-17\%}$
$\tilde{q}\tilde{g}$	2000	2.72×10^{-5}	$^{-6.7\%}_{+4.4\%}$	$^{+14\%}_{-15\%}$	$^{+15\%}_{-8.7\%}$	$^{+25\%}_{-24\%}$
$\tilde{q}\tilde{g}$	2500	3.05×10^{-7}	$^{-7.0\%}_{+4.7\%}$	$^{+21\%}_{-22\%}$	$^{+24\%}_{-14\%}$	$^{+37\%}_{-33\%}$
$\tilde{q}\tilde{q}$	500	4.13	$^{+3.7\%}_{-5.2\%}$	$^{+2.6\%}_{-2.0\%}$	$^{+1.7\%}_{-1.7\%}$	$^{+6.8\%}_{-7.9\%}$
$\tilde{q}\tilde{q}$	1000	7.51×10^{-2}	$^{+4.1\%}_{-5.7\%}$	$^{+3.3\%}_{-2.5\%}$	$^{+0.41\%}_{-0.50\%}$	$^{+7.4\%}_{-8.3\%}$
$\tilde{q}\tilde{q}$	1500	2.39×10^{-3}	$^{+4.6\%}_{-6.0\%}$	$^{+3.7\%}_{-2.8\%}$	$^{-0.60\%}_{+0.48\%}$	$^{+8.4\%}_{-8.9\%}$
$\tilde{q}\tilde{q}$	2000	6.66×10^{-5}	$^{+5.0\%}_{-6.2\%}$	$^{+4.3\%}_{-3.5\%}$	$^{-1.5\%}_{+1.5\%}$	$^{+9.6\%}_{-10\%}$
$\tilde{q}\tilde{q}$	2500	1.07×10^{-6}	$^{+5.4\%}_{-6.4\%}$	$^{+5.2\%}_{-4.7\%}$	$^{-2.5\%}_{+2.5\%}$	$^{+11\%}_{-12\%}$
inclusive	500	22.9	$^{+2.2\%}_{-3.0\%}$	$^{+1.7\%}_{-1.6\%}$	$^{+1.8\%}_{-1.5\%}$	$^{+4.7\%}_{-5.2\%}$
inclusive	1000	1.94×10^{-1}	$^{+2.3\%}_{-3.4\%}$	$^{+2.7\%}_{-2.7\%}$	$^{+2.2\%}_{-1.5\%}$	$^{+5.8\%}_{-6.4\%}$
inclusive	1500	4.29×10^{-3}	$^{+2.9\%}_{-4.0\%}$	$^{+3.8\%}_{-3.8\%}$	$^{+3.0\%}_{-1.9\%}$	$^{+7.8\%}_{-8.2\%}$
inclusive	2000	9.81×10^{-5}	$^{+3.6\%}_{-4.6\%}$	$^{+4.9\%}_{-4.9\%}$	$^{+4.3\%}_{-2.7\%}$	$^{+10\%}_{-10\%}$
inclusive	2500	1.40×10^{-6}	$^{+4.2\%}_{-5.1\%}$	$^{+6.2\%}_{-6.1\%}$	$^{+5.7\%}_{-3.6\%}$	$^{+13\%}_{-12\%}$

Table 7.2: The NNLL matched cross section prediction for different SUSY-QCD processes at the LHC with $\sqrt{S}$ = 8 TeV, where "inclusive" corresponds to the sum of all four processes. The scale, PDF, α_s, and total uncertainty are shown separately. The upper number of the scale uncertainty is evaluated at half the value of the central scale, while the lower number is evaluated at twice the value of the central scale.

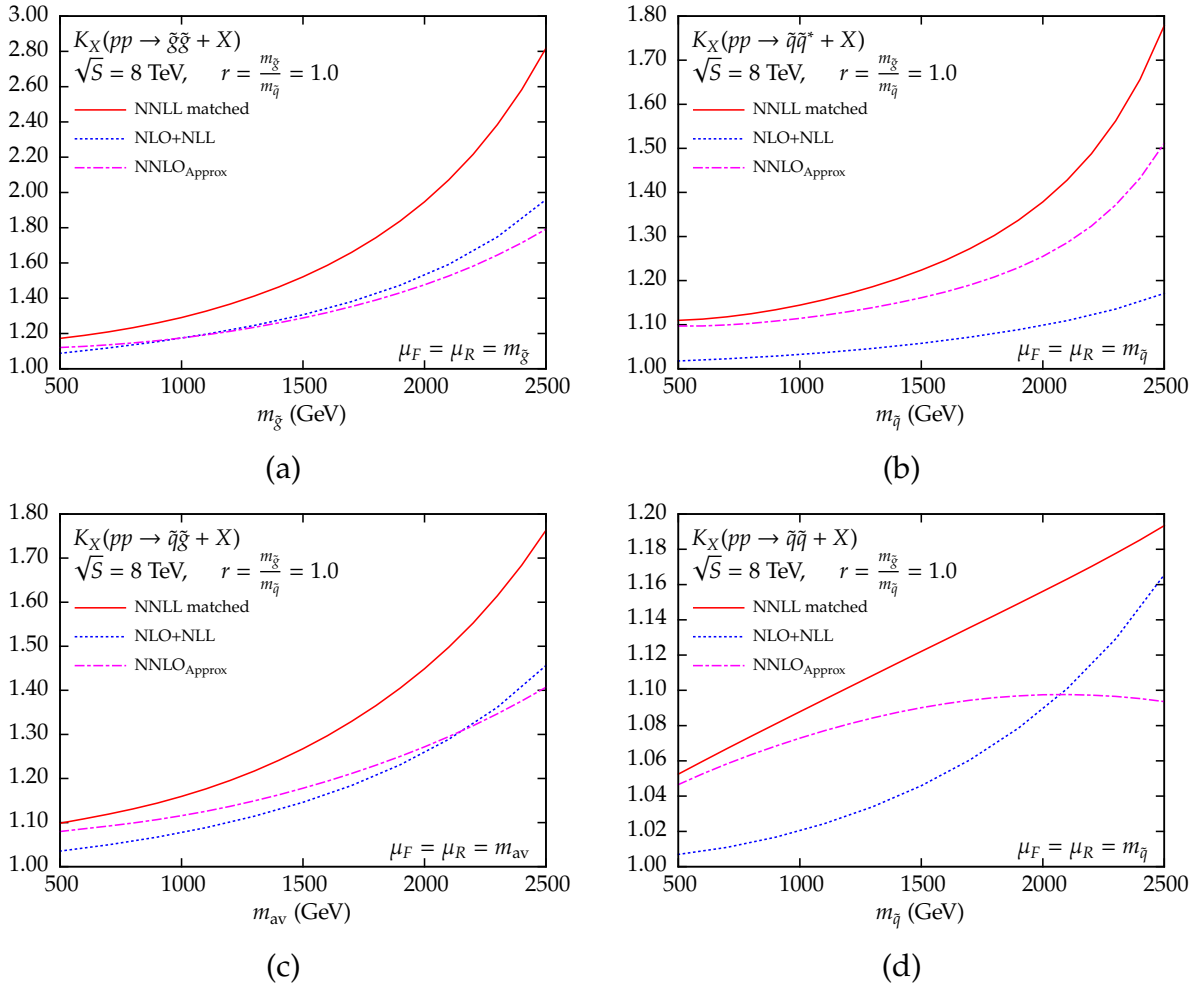

Figure 7.3: K-factors for the NNLL matched cross sections of the four SUSY-QCD processes, comparing to the K-factors of NLO+NLL and NNLO$_{\text{Approx}}$.

The K-factor has been defined in eq. (6.4) as the ratio of a cross section at a certain accuracy and the NLO cross section. It is shown in figure 7.3 for NLO+NLL, NNLO$_{\text{Approx}}$, and NNLL matched when assuming equal masses of squarks and gluinos, $r := m_{\tilde{g}}/m_{\tilde{q}} = 1$. Two different values of r will be shown for NNLL matched in figure 7.5 which we will, however, discuss later.

A first look at the K-factors reveals that the NNLL corrections are positive for the four processes in the given mass range and increase towards higher masses due to the aforementioned closeness to the hadronic threshold. This behaviour is made even clearer when we compare the NNLO$_{\text{Approx}}$ and the NNLL matched lines: far away from the hadronic threshold at low masses, the fixed-order and resummed cross section yield similar results, whereas for high masses, the all-order terms dominate over the fixed-order terms and lead to a much stronger increase of NNLL matched compared to NNLO$_{\text{Approx}}$. The previously calculated NLO+NLL cross sections are in all cases and for the shown mass range smaller than NNLL matched, signifying a strong contribution from the additional logarithmic terms as well as the hard-matching and Coulomb coefficients, where especially the latter are known

to play an important role [123]. The process $\tilde{g}\tilde{g}$, figure 7.3 (a), receives the largest contributions relative to NLO, with a K-factor of slightly below 3 for squark and gluino masses of 2.5 TeV. This can be explained by the larger colour factors for gluinos than the ones for squarks.

The enhancement of the cross section with increasing mass for $\tilde{q}\tilde{q}$ in figure 7.3 (d) which is slower than for the other processes requires some clarification. Squark-pair production proceeds through one initial-state channel in the $\overline{\mathbf{3}}$ and $\mathbf{6}$ representations, see section 5.1.1. Below squark and gluino masses of approximately 1 TeV, the $\overline{\mathbf{3}}$ colour channel is dominant at LO. Above 1 TeV, the $\mathbf{6}$ channel becomes larger than $\overline{\mathbf{3}}$. The Coulomb contributions for the two channels are of a different kind: while $\overline{\mathbf{3}}$ has an attractive Coulomb potential (i.e. $\mathscr{D}_{ij\to kl,I} > 0$) and therefore increases the cross section, the Coulomb potential of $\mathbf{6}$ is repulsive and decreases the cross section. This is exactly what we see in the plot: the strong increase towards higher masses, as it is see for the other processes, is suppressed due to the repulsive colour channel being dominant. A second effect causing this behaviour stems from the ratio of NNLO over NLO PDFs in the K-factor. While the ratio for the gluon distribution becomes larger when the momentum fraction x is increased, the ratio for quark distributions becomes smaller. Since $\tilde{q}\tilde{q}$ is the only process with no gluon in the initial state, its corrections at NNLO and NNLL are slightly suppressed compared to the other three processes. The difference in behaviour for NNLL matched and $\text{NNLO}_{\text{Approx}}$ demonstrates that the enhancement due to higher-order logarithms and their cross terms with the hard-matching coefficients and Coulomb contributions included in NNLL matched partly compensate the suppressing effects closer to threshold.

Figure 7.4 depicts the behaviour of the NNLL matched K-factor for two different ratios r of the squark and gluino masses. The differences between NLO+NLL and NNLL matched in the dependence on r is mainly governed by the product of hard-matching and Coulomb coefficients, which is the only additionally source of r dependence when going from NLL to NNLL. It should be noted that the two-loop Coulomb coefficient in eq. (7.4) only depends on r for $\tilde{q}\tilde{g}$ due to the factors of m_{av} and m_{red} then containing both the squark and the gluino masses instead of only one of those.

At last, we show the scale dependence of the four processes in figure 7.5. While now the common renormalisation and factorisation scale μ is varied up and down by a factor of 5 with respect to the central scale $\mu_0 = m_{\text{av}}$, the squark and gluino mass will be fixed to 1.2 TeV. As it has already been deduced from the total cross section plots of figure 7.2, the scale dependence decreases when including higher order corrections in α_{s} for all processes except for $\tilde{g}\tilde{g}$, figure 7.5 (a), where we observe a slightly stronger scale dependence at the NNLL matched accuracy than for NLO+NLL, and also showing an inverted behaviour compared to the previous accuracies like NLO and NLO+NLL.

7.3.1 Analysis of the scale dependence of gluino-pair production

The origin of the qualitative change in scale behaviour for gluino-pair production can be more easily understood by analysing some intermediate steps of accuracy between NLO+NLL and NNLL matched and by splitting up the NNLL matched cross section into its constituents.

In figure 7.6 (a), we show the intermediate steps with "NLO+NLL with $\mathcal{C}^{(1)}$" denoting NLL

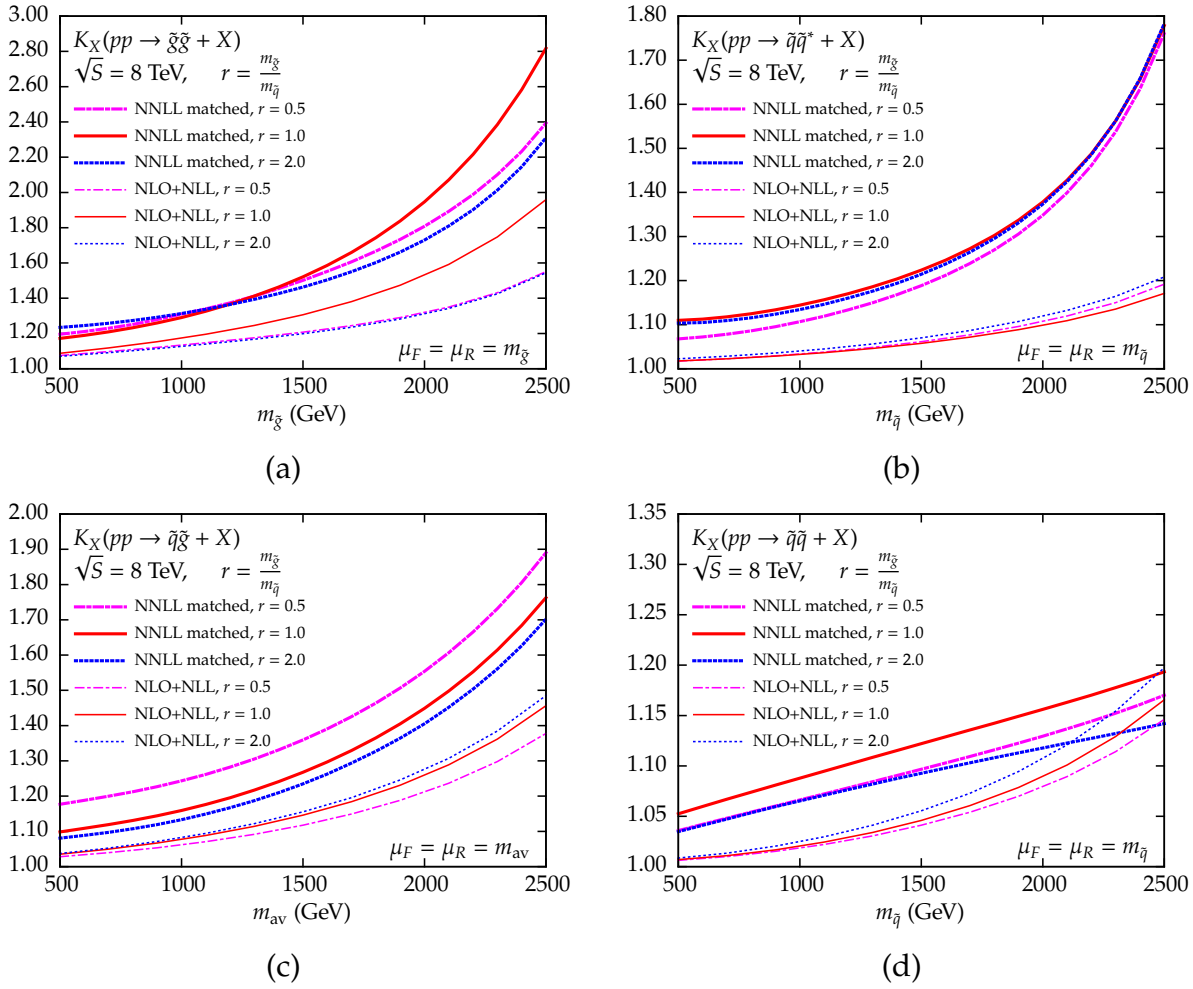

Figure 7.4: *K*-factors for the NNLL matched cross sections of the four SUSY-QCD processes with ratios r of the gluino and squark masses unequal to one, also comparing to the corresponding r-values of NLO+NLL.

resummation in the exponents, but with the one-loop hard-matching coefficient included, keeping the Coulomb contributions equal to zero, "NLO+NLL with $\mathcal{C}^{(1)}$ & $\mathcal{C}^{\text{Coul},(1)}$" denoting the same as above, now including the one-loop Coulomb coefficient also, and lastly also with "$\text{NNLO}_{\text{Approx}}$+NNLL (w/o $\mathcal{C}^{\text{Coul},(1,2)}$)" denoting the approximated NNLO plus NNLL resummation in the exponents, including the one-loop hard-matching coefficients, but keeping both one- and two-loop Coulomb contributions in the resummed equation equal to zero. We observe that there is a very small scale dependence for "NLO+NLL with $\mathcal{C}^{(1)}$"[2]. The notable change in scale behaviour when the one-loop Coulomb contributions are included, in particular for low scales, implies that they are responsible at least partially for the observed scale dependence at the NNLL matched level.

To investigate this behaviour further, we split up the cross sections at the NLO+NLL+$\mathcal{C}^{(1)}$ and NLO+NLL+$\mathcal{C}^{(1)}$+$\mathcal{C}^{\text{Coul},(1)}$ levels into the colour channels to see how the different attractive

[2]We have checked, however, that this behaviour is not preserved for different values of the squark and gluino mass. Its scale dependence is still smaller than for NNLL matched, though.

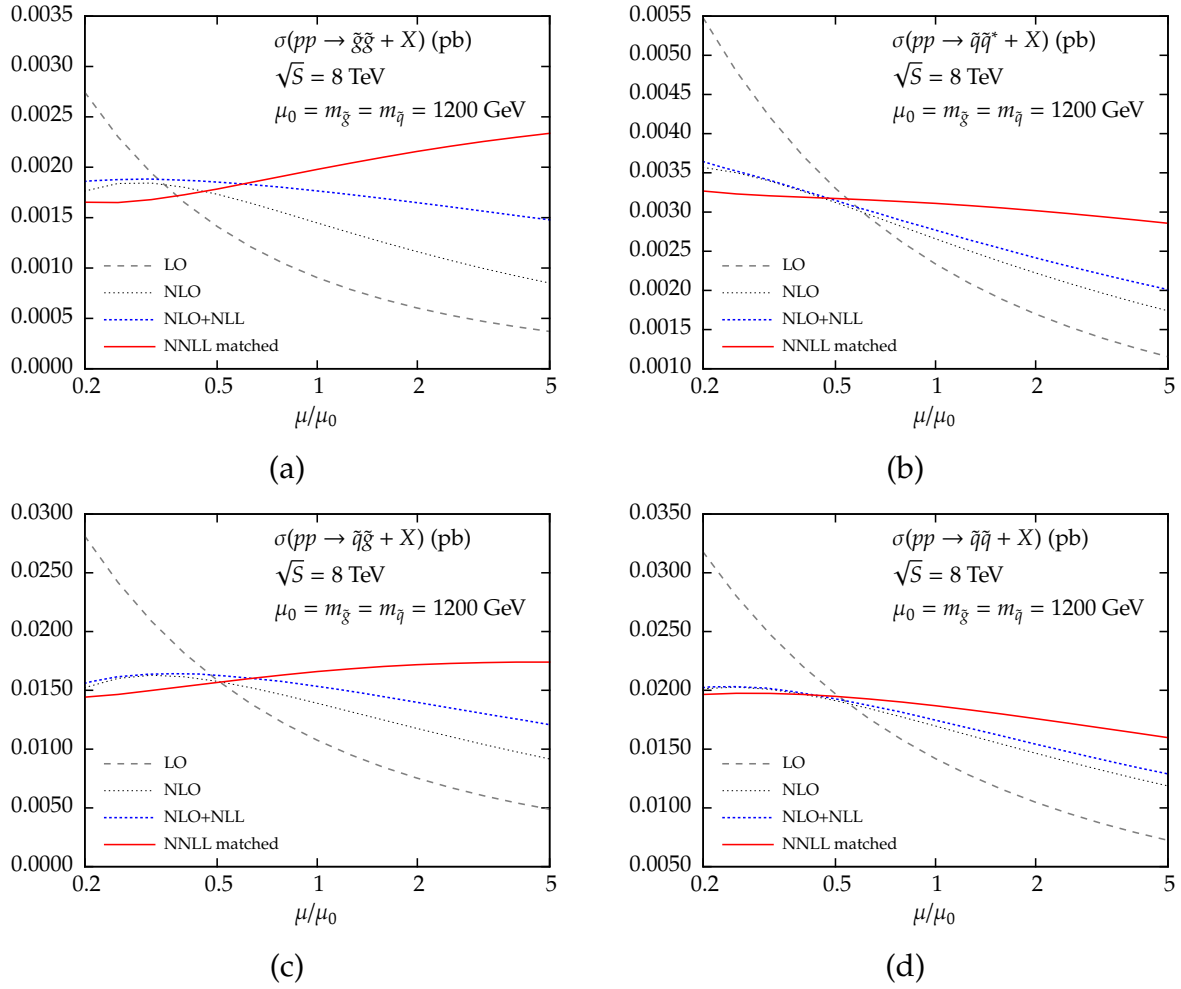

Figure 7.5: Scale dependence of various accuracies of the total cross sections for the four SUSY-QCD processes when simultaneously varying the renormalisation and factorisation scales up and down by a factor of 5 with respect to the central scale.

and repulsive Coulomb interactions affect the scale dependence. Furthermore, we will denote by "purely resummed part" $\sigma^{(\mathrm{res})}$ and "expanded part" $\sigma^{(\mathrm{res})}|_{\mathrm{NLO}}$ the constituents of the proper matching procedure to include the full fixed-order result (see section 4.8). This split-up can be seen in figure 7.7 for the gluon-fusion initial state, as it is the dominant one for gluino-pair production and mainly drives the scale dependence. We show the ratios of the purely resummed and the expanded parts of NLL+$\mathcal{C}^{(1)}$+$\mathcal{C}^{\mathrm{Coul},(1)}$ over NLL+$\mathcal{C}^{(1)}$ for each colour channel separately in figures 7.7 (a) and (b). It can be seen that the inclusion of one-loop Coulomb contributions hardly changes the slope of the colour channels of the purely resummed part, but strongly influences the expanded part at low scales. This can be seen more clearly in figures 7.7 (c) and (d), where we show the absolute values of the purely resummed and expanded cross sections that go into the ratios of (a) and (b). We notice that the Coulomb contributions lead to an almost constant shift for the colour channels of the purely resummed part, while the expanded part is affected strongly at low scales, but only weakly at high scales. This is understood, as the additional term which is added due to the

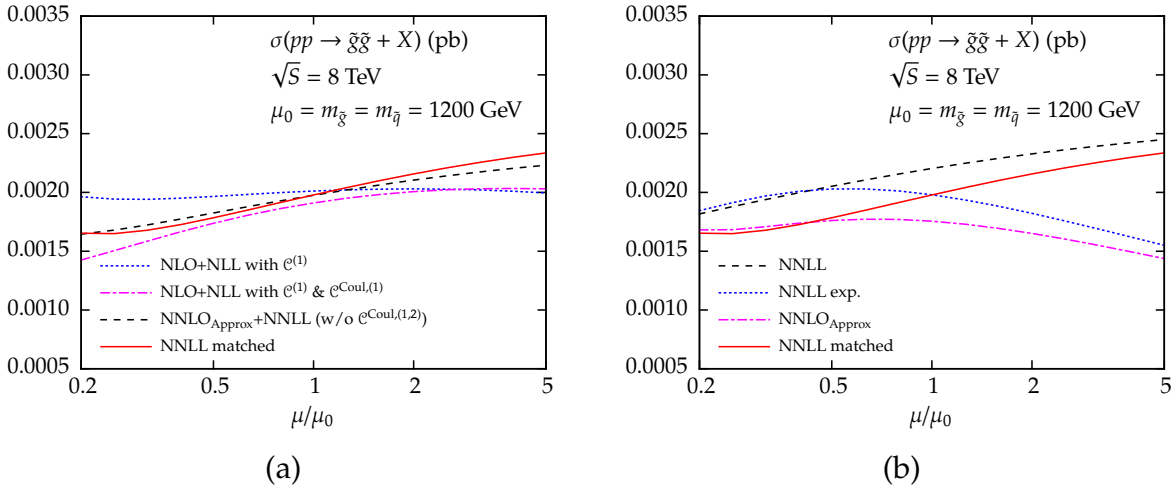

Figure 7.6: Scale dependence of different parts of the gluino pair production cross section: intermediate levels of accuracy (a), and a split-up of the cross section into resummed and expanded parts for NNLL matched, compared to the full NNLL matched result as well as $\mathrm{NNLO}_{\mathrm{Approx.}}$ (b).

one-loop Coulomb contributions is proportional to $\tilde{\sigma}^{\mathrm{LO}} \times \alpha_s \mathcal{C}^{\mathrm{Coul},(1)} \propto \alpha_s^3$, which is sensitive to low scales. The repulsive **27** colour channel plays a special role, as it is the dominant colour channel in the resummed and expanded parts, but also repulsive, so it decreases when the Coulomb contributions are added. This change of the dominant colour channel, affected by a repulsive Coulomb interaction, is the leading effect of the different scale behaviour when adding up all the colour contributions.

Therefore, the interplay between the positive Coulomb contributions for the attractive colour channels and the negative ones for the repulsive **27** channel change the scale behaviour of the expanded part in such a way that, when subtracting it from the full fixed-order calculation at NLO, the scale dependence cancels almost perfectly, see the difference between the thin and thick solid red lines in figure 7.8. This is understood, as adding more NLO terms to the near-threshold expansion such as the one-loop Coulomb contributions brings this approximation closer to the full NLO result. The purely resummed part NLL+$\mathcal{C}^{(1)}$+$\mathcal{C}^{\mathrm{Coul},(1)}$ grows from low scales towards high scales (dashed blue line), which, when added to the almost flat scale dependence originating from the difference between full NLO and the expanded part, results in the scale dependence as seen in the "NLO+NLL with $\mathcal{C}^{(1)}$ & $\mathcal{C}^{\mathrm{Coul},(1)}$" line.

Moving towards NNLL, we see that the difference between the "$\mathrm{NNLO}_{\mathrm{Approx}}$+NNLL (w/o $\mathcal{C}^{\mathrm{Coul},(1,2)}$)" line, which includes one- and two-loop Coulomb terms in the $\mathrm{NNLO}_{\mathrm{Approx}}$, but not in the resummed equation, and NNLL matched is small which tells us that one- and two-loop Coulomb coefficients largely balance each other's effect. In figure 7.6 (b), it is seen that the inclusion of NNLL terms in the exponents seems to mainly affect the high-scale region. Here, we split up the NNLL matched cross section into its purely resummed denoted by "NNLL" and its expanded part up to NNLO denoted by "NNLL exp." and see that for low scales, the resummed and expanded parts agree well, implying that the cross terms between higher-order logarithms, hard-matching coefficients, and Coulomb contributions

in the resummed part only play a minor role for low scales, whereas the two lines disperse at high scales, with the resummed part being significantly larger than the expanded part due to the large logarithmic contributions and their cross terms with the hard-matching coefficients and Coulomb contributions. Thus, we find that due to the similarity of resummed and expanded parts, the scale dependence at lower scales is mainly driven by $\text{NNLO}_{\text{Approx}}$, while mainly the higher-order logarithms drive the scale behaviour at higher scales.

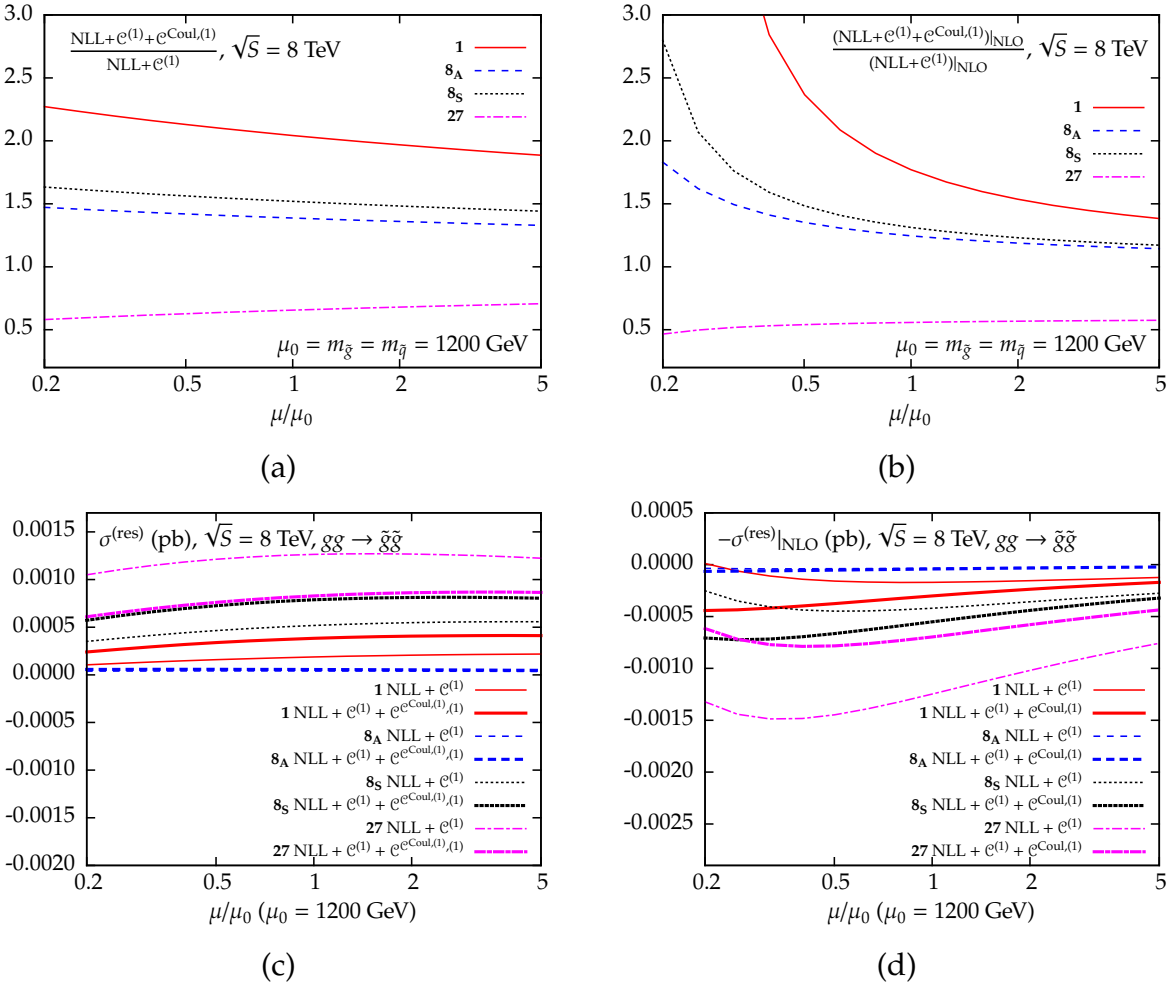

Figure 7.7: Ratio of the NLL+$\mathcal{C}^{(1)}$+$\mathcal{C}^{\text{Coul},(1)}$ cross section over NLL+$\mathcal{C}^{(1)}$ for the gg initial state of $\tilde{g}\tilde{g}$ production, for the purely resummed part (a) and the expanded part (b), split up into the different colour channels. The absolute values of the purely resummed and expanded cross sections are shown in (c) and (d).

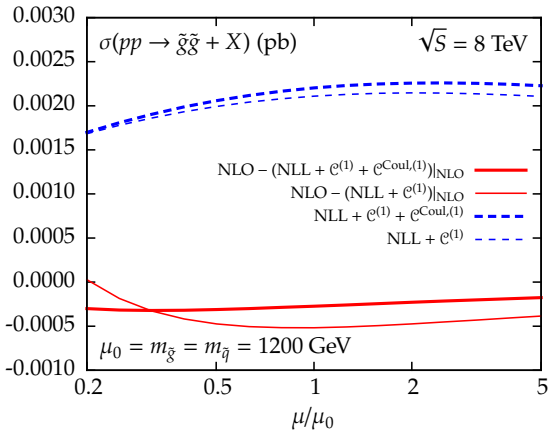

Figure 7.8: Sum of all colour channels for the purely resummed part (dashed blue lines) and NLO minus the expanded part (solid red lines). The "NLO+NLL with $\mathcal{C}^{(1)}$" and "NLO+NLL with $\mathcal{C}^{(1)}$ & $\mathcal{C}^{\text{Coul},(1)}$" lines of figure 7.6 (a) then correspond here to the sum of the thin and thick lines, respectively.

8 NNLL Threshold Resummation for Stops

The production of stops plays a special role as in many supersymmetric scenarios, the lighter mass eigenstate of the stops is amongst the lightest supersymmetric particles in the spectrum, often also being the lightest coloured sparticle, see the discussion of section 3.3.4. In particular, the large top quark mass results in a strong mixing of the weak interaction eigenstates $\tilde{t}_L$ and $\tilde{t}_R$ to give the physical mass eigenstates $\tilde{t}_1 = \tilde{t}_L \cos\theta_{\tilde{t}} + \tilde{t}_R \sin\theta_{\tilde{t}}$ and $\tilde{t}_2 = -\tilde{t}_L \sin\theta_{\tilde{t}} + \tilde{t}_R \cos\theta_{\tilde{t}}$ with the stop mixing angle $\theta_{\tilde{t}}$. The mixing effects also cause a large mass splitting between $\tilde{t}_1$ and $\tilde{t}_2$. For the light-flavoured squarks, this mixing is negligible due to the small quark masses of the first two generations. Sbottoms can in principle be treated in a similar manner to stops, although the mixing and mass splitting effects are much smaller than for the stops. In ref. [112], sbottom production has been analysed at the NLO+NLL level with the conclusion that any additional contributions for sbottoms which are absent for stops are negligibly small, so that the stop production cross section can just as well be used for sbottoms when adjusting the masses and additional parameters. Thus, we will restrict ourselves to the discussion of stop production in this section.

The production process proceeds in a similar manner to light-flavoured squark-antisquark production, the t-channel contribution for the $q\bar{q}$ initial state, as depicted in figure 8.1 (a), is however non-existent due to a negligible effect from top quarks in the initial state. Therefore, stops are only produced through the s-channel diagram of figure 8.1 (b). Due to the gluon always being in an octet state of SU(3), the final state has to be produced in the octet representation also. Furthermore, this type of diagram is exactly corresponding to figure 7.1, resulting in the octet colour channel only contributing as a p-wave. The contributions from gluon fusion are exactly the same as in the light-flavoured case, excluding a factor of $2n_l$ with n_l the number of light quark flavours, since only one type of stop is considered instead of a set of mass-degenerate light-flavoured squarks.

A consequence of the flavour-conserving (SUSY-)QCD interactions and the absence of the gluino exchange graph is furthermore that at LO, only the mass of the stop which is produced ($m_{\tilde{t}_1}$) appears in the cross section, while the masses of the light-flavoured squarks ($m_{\tilde{q}}$), the gluino ($m_{\tilde{g}}$), the other stop mass eigenstate ($m_{\tilde{t}_2}$), as well as the stop mixing angle

Figure 8.1: Feynman diagram for the production of a stop-antistop pair through gluino exchange in the t-channel. This contribution is strongly suppressed due to the flavour-diagonal quark-squark-gluino coupling requiring top quarks to be in the initial state with top quark PDFs being very small and practically zero.

($\theta_{\tilde{t}}$) only start contributing at NLO. Therefore, the effect of a variation of these additional parameters is typically small [98] (see also ref. [112]).

We will now proceed to show the initial-state contributions of stop-antistop production and point out how they differ from light-flavoured squark-antisquark production before discussing the additional ingredients needed for NNLL accuracy. Afterwards, we will present numerical results and compare to ref. [132], where stop production has been calculated at a similar accuracy in the framework of SCET. The work presented in this chapter has been published in ref. [141].

8.1 Initial-state contributions to stop-antistop production

Figure 8.2 shows the contribution of the different initial states and colour channels of stop-antistop and light-flavoured squark-antisquark production to the sum of all colour channels, i.e. the full cross section at LO. In figure 8.2 (a), we see that, despite being p-wave suppressed, the octet channel of the $q\bar{q}$ initial state dominates the cross section by a small amount for stop masses above $m_{\tilde{t}} \approx 1.6$ TeV. Of the gluon initial states, the symmetric octet channel is the dominant colour channel for lower stop masses, and it is slightly below the $q\bar{q}$ octet channel for higher masses. The gg singlet channel contributes at roughly 20%, while the p-wave suppressed antisymmetric octet channel only contributes by a very small amount, in particular for higher masses. We compare to light-flavoured squark-antisquark production in figure 8.2 (b). It is clear that the $q\bar{q}$ singlet channel, which is absent in the case of stops, is strongly dominating the LO cross section. Thus, while light-flavoured squark-antisquark production is almost exclusively driven by the $q\bar{q}$ initial state, stop-antistop production is strongly influenced by the gg initial state which, as we will see later, leads to a difference in the behaviour of the scale dependence.

While so far only the production of a stop-antistop pair of the same mass eigenstate, $\tilde{t}_1\tilde{t}_1^*$ and $\tilde{t}_2\tilde{t}_2^*$, has been discussed, there is also the possibility to produce mixed $\tilde{t}_1\tilde{t}_2^*$ or $\tilde{t}_2\tilde{t}_1^*$ pairs or even equal-charge pairs like $\tilde{t}_1\tilde{t}_1$, $\tilde{t}_2\tilde{t}_2$, $\tilde{t}_1\tilde{t}_2$, $\tilde{t}_1^*\tilde{t}_1^*$ and so on. All of these additional processes can only be realised starting from NNLO or through electroweak channels due to non-existing top quark initial states, which causes them to be strongly suppressed. Furthermore, due

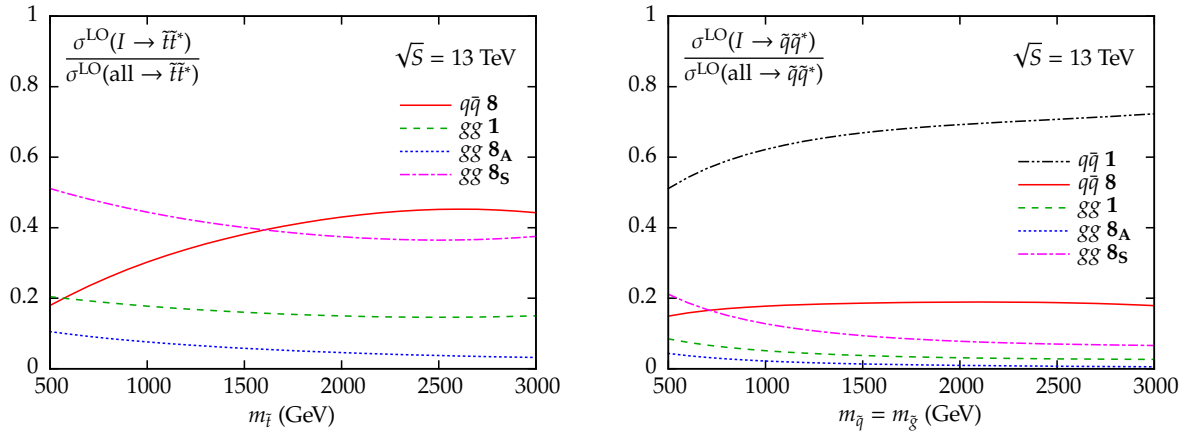

(a) (b)

Figure 8.2: Ratios of the LO cross section for a specific initial state and colour channel I to the full LO cross section at $\sqrt{S}$ = 13 TeV for stop-antistop production (a) and light-flavoured squark-antisquark production (b) when varying the stop and squark masses, respectively. The renormalisation and factorisation scales in both cases are set to the central scale, $\mu_R = \mu_F = \mu = m_{\tilde{t}_1}$. The LO cross sections have been computed with the MSTW2008 NNLO PDF set as it is done in the numerical evaluation of the resummed formulas.

to real emission corrections starting from NLO, new initial-state channels like qg open up. In the threshold limit, these channels will however be very small. As we are interested in performing threshold resummation, we do not take into account all of these suppressed corrections and therefore focus only on the production of $\tilde{t}_1\tilde{t}_1^*$ and $\tilde{t}_2\tilde{t}_2^*$ through the initial-state channels $q\bar{q}$ and gg[1].

8.2 Extraction of the hard-matching coefficient

As the goal of this section is to upgrade the stop-antistop production from NLO+NLL [112] to the same accuracy as squark and gluino production from the previous section, that is $\mathrm{NNLO}_{\mathrm{Approx}}$+NNLL, the hard-matching and Coulomb coefficients need to be determined. The Coulomb contributions are the same as discussed in section 7.1.2. The hard-matching coefficients could in principle be extracted from the NLO calculations [98] of `Prospino`, which, however, is diffcult due to `Prospino` not splitting up the cross sections into their colour channels. Broggio et al. [127] have redone the NLO calculation of the relevant terms from scratch while distiguishing between the different colour channels. In the following, we will describe how we extract the one-loop hard-matching coefficient from their results.

In ref. [127], the authors present an approximated NNLO formula for stop-antistop production, calculated from threshold-enhanced[2] terms in the SCET formalism to resummation.

[1] In the NLO calculations, the additional initial-state channels such as qg, while not being relevant for resummation, are of course taken into account.

[2] Note that the definition of threshold in the referenced paper is not the absolute threshold $\beta \to 0$ that we use, instead, the authors present two ways of defining the threshold through variables from "pair invariant mass" and "one particle inclusive" kinematics.

One of the ingredients for this formula is the hard function, as defined in eq. (26) of ref. [127]. These hard functions are given as matrices in colour configuration space, see the beginning of section 4.3.2, using the same s-channel colour basis which we use. Along with the submission of the paper, the authors bundled a numerical code for the calculation of the approximated NNLO cross section which contains expressions for the one-loop hard function.

The explicit calculation of the hard function requires the virtual one-loop diagrams in (SUSY-)QCD to be evaluated while keeping the colour structure separate (see also ref. [129] for a comment on how to obtain colour-decomposed virtual contributions). Due to the "pair invariant mass" and "one particle inclusive" kinematics having been used in ref. [127], the hard function still depends on differential variables such as the invariant mass and an angle. It should be noted that this hard function was calculated from the full virtual diagrams without taking the threshold limit, so that it is valid in the full kinematical regime and, after integrating over the remaining differential variables, still depends on β. Additionally, as the calculations include all virtual diagrams, the hard function of ref. [127] still contains the Coulomb contributions, and we will need to handle them properly.

For the calculation of a cross section, the hard function is multiplied by the soft function, which also is a matrix in colour configuration space. The NLO terms in the cross section now are constructed from a term where the LO hard function is multiplied with the NLO soft function, which results in the threshold-enhanced logarithms, and another term where the NLO hard function is multiplied with the LO soft function, which we are interested in extracting. Both of these terms are diagonal in colour space.

In ref. [134], the same formalism is used as in ref. [127]. Therefore, we can identify the one-loop hard coefficient $h^{R,(1)}_{pp'}(\mu_h)$ of eq. (3.4) of ref. [134] with the NLO hard function of eq. (26) of ref. [127] by integrating the latter over the remaining differential variables, then dividing it through the LO hard function, and subsequently taking the threshold limit and subtracting the Coulomb contributions. For simplification, we will denote $h^{R,(1)}_{pp'}(\mu_h)$ by $h^{(1)}_I$ in the following. The authors of ref. [134] clarify that the one-loop hard coefficient is the same that appears in their eq. (2.3), i.e. the threshold limit of the NLO cross section. This threshold expansion for $\beta \to 0$ of the partonic NLO cross section is in our notation[3]:

$$\hat{\sigma}^{(1,\mathrm{thr})}_{ij\to\bar{\tilde{t}}\tilde{t}^*,I} = \hat{\sigma}^{(0)}_{ij\to\bar{\tilde{t}}\tilde{t}^*,I} \times \frac{\alpha_s}{4\pi}\Bigg\{\frac{2\pi^2 \mathscr{D}_{ij\to kl,I}}{\beta} + 4(A^{(1)}_i + A^{(1)}_j)\left[\ln^2\left(\frac{8m\beta^2}{\mu_F}\right) + 8 - \frac{11\pi^2}{24}\right] + 4\left(D^{(1)}_{ij\to\bar{\tilde{t}}\tilde{t}^*,I} - 4(A^{(1)}_i + A^{(1)}_j)\right)\ln\left(\frac{8m\beta^2}{\mu_F}\right) - 12D^{(1)}_{ij\to\bar{\tilde{t}}\tilde{t}^*,I} + h^{(1)}_I + \mathcal{O}(\beta)\Bigg\} \tag{8.1}$$

with m the mass of the produced stop $m_{\tilde{t}_1}$, μ_F the factorisation scale, $A^{(1)}_{i,j}$ and $D^{(1)}_{ij\to\bar{\tilde{t}}\tilde{t}^*,I}$ the usual one-loop coefficients appearing in the resummed exponentials, and $\mathscr{D}_{ij\to kl,I}$ the colour coefficient of the Coulomb potential. $\hat{\sigma}^{(0)}_{ij\to\bar{\tilde{t}}\tilde{t}^*,I}$ denotes the colour-decomposed Born cross section. The first term in the curly brackets of eq. (8.1) is the one-loop Coulomb contribution.

[3]The given expansion only holds when stops are produced in an s-wave state. As discussed earlier, higher partial wave contributions for resummation at NNLL are not considered in the implementation presented in this thesis. However, the NLO expansion for these terms is known, see e.g. ref. [123].

Our goal is to obtain the hard-matching coefficient $\mathcal{C}^{(1)}_{ij\to\bar{t}\bar{t}^*,I}$ which is defined in Mellin-moment space through eq. (4.109). It is possible to relate the one-loop hard coefficient $h^{(1)}_I$ to $\mathcal{C}^{(1)}_{ij\to\bar{t}\bar{t}^*,I}$ by taking the Mellin transform of eq. (8.1) and comparing it to the NLO term in the α_s-expansion of eq. (4.107), which is (for a colour channel I):

$$\tilde{\sigma}^{(1,\text{thr})}_{ij\to\bar{t}\bar{t}^*,I} = \tilde{\sigma}^{(0)}_{ij\to\bar{t}\bar{t}^*,I} \times \frac{\alpha_s}{\pi}\Bigg\{(A^{(1)}_i + A^{(1)}_j)\left[\ln N + 2\gamma_E - \ln\left(\frac{4m^2}{\mu_F^2}\right)\right]\ln N - D^{(1)}_{ij\to\bar{t}\bar{t}^*,I}\ln N$$
$$+ \mathcal{C}^{(1)}_{ij\to\bar{t}\bar{t}^*,I} + \mathcal{C}^{\text{Coul},(1)}_{ij\to\bar{t}\bar{t}^*,I}\Bigg\}. \tag{8.2}$$

To simplify the Mellin transform, we approximate the LO cross section according to eq. (4.143), as it was done for the computation of the two-loop Coulomb contribution, and neglect terms that are suppressed by $1/\sqrt{N}$ or higher, which is valid for $N \to \infty$. As the structure of the Coulomb and logarithmic terms in N is the same, we obtain the following relation between our one-loop hard-matching coefficient in Mellin-moment space and the one-loop hard coefficient of SCET, which only differ by constant terms in N:

$$\mathcal{C}^{(1)}_{ij\to\bar{t}\bar{t}^*,I} = \frac{1}{4}h^{(1)}_I + \left(\frac{\pi^2}{24} + (\gamma_E - \ln 2)^2\right)(A^{(1)}_i + A^{(1)}_j) - D^{(1)}_{ij\to\bar{t}\bar{t}^*,I}(\gamma_E + 1 - \ln 2)$$
$$+ \ln\left(\frac{m}{\mu_F}\right)\left((A^{(1)}_i + A^{(1)}_j)\ln\left(\frac{m}{\mu_F}\right) + 2(\ln 2 - \gamma_E)(A^{(1)}_i + A^{(1)}_j) + D^{(1)}_{ij\to\bar{t}\bar{t}^*,I}\right). \tag{8.3}$$

The equations leading to eq. (8.3) are valid only for s-wave states. As we only perform resummation up to NLL accuracy for p-wave states, see section 7.2, this is justified. In fact, we checked that the same expression as eq. (8.3) is obtained when the p-wave variant of eq. (8.1) (see e.g. ref. [123]) is used with the LO cross section approximated as $\propto \beta^3$ instead of $\propto \beta$.

Due to the large number of steps in obtaining a hard-matching coefficient suitable for our application, it feels appropriate to repeat all the steps and present them in chronological order:

1. We extract the term where the NLO hard function is multiplied with the LO soft function from the numerical code of ref. [127].

2. Subsequently, the integration over the invariant mass can be carried out simply by replacing the invariant mass with $\sqrt{\hat{s}}$, the partonic centre-of-mass energy, due to a delta function restricting the phase space for Born and virtual diagrams (see e.g. eq. (4.13)), while the integration over the angle is performed numerically.

3. In order to obtain the absolute threshold limit $\beta \to 0$, we call the code for the hard function with a value of $\hat{s}_{\text{thr}} \approx 4m^2$ (in fact, we have to go slightly above $4m^2$ due to the Coulomb singularity still present; we have checked, however, that the numerical impact of choosing $\hat{s}_{\text{thr}}$ further away from threshold is negligible). We then divide by the partonic LO cross section in β-space evaluated with the same value of $\hat{s}_{\text{thr}}$. The

Benchmark point 40.2.5	(a)	(b)
$m_{\tilde{t}_1}$ (GeV)	1085	1087.15
$m_{\tilde{t}_2}$ (GeV)	1320.85	1319.87
$m_{\tilde{g}}$ (GeV)	1492.57	1489.98
$m_{\tilde{q}}$ (GeV)	1496	1460.3
$\sin 2\theta_{\tilde{t}}$	0.669	0.685

Table 8.1: SUSY parameters used in the calculation of stop cross sections for benchmark point 40.2.5 of ref. [215]. The numerical values of (a) are used in our results ("default values"), while the ones from (b) were used in ref. [132].

partonic LO cross section close to threshold corresponds to the product of LO soft and LO hard function.

4. We subtract numerically the Coulomb contribution $2\pi^2 \mathscr{D}_{ij\to kl,I}/\beta$, where again β is evaluated with the same value of $\hat{s}_{\text{thr}}$. At this point, we have obtained the one-loop hard coefficient $h_I^{(1)}$.

5. Lastly, we use eq. (8.3) to transform the one-loop hard coefficient from SCET into our one-loop hard-matching coefficient in Mellin-moment space.

8.3 Numerical results for stop-antistop production at $\sqrt{S}$ = 8, 13 TeV

With the hard-matching coefficient now available, we are in a position to do a numerical analysis for stop-antistop production at $\text{NNLO}_{\text{Approx}}$+NNLL accuracy with centre-of-mass energies of $\sqrt{S}$ = 8, 13 TeV and compare to the previously calculated NLO+NLL results from ref. [112].

The settings essentially follow the ones from section 7.3. In particular, we also use the MSTW2008 NLO and NNLO PDF sets [20] for the NLO/NLL and $\text{NNLO}_{\text{Approx}}$/NNLL predictions, respectively. We again use the slightly more recent value for the top quark mass, m_t = 173.21 GeV [16]. The NLO cross sections [98] are again calculated with `Prospino`, while the resummed corrections as well as the $\text{NNLO}_{\text{Approx}}$ are computed with a self-written code, cross-checked by a second independently written code [214].

The additional mixing parameters $m_{\tilde{q}}$, $m_{\tilde{g}}$, $m_{\tilde{t}_2}$ and $\theta_{\tilde{t}}$ are chosen according to CMSSM benchmark point 40.2.5 of ref. [215]. We will use the numerical values of table 8.1 (a) in our calculations. In ref. [132], the same benchmark point has been chosen, albeit with slightly different numerical values. Therefore, whenever we compare to the NLO+NNLL results of ref. [132], we will use the values of table 8.1 (b). For our studies, we will generally keep these additionally parameters fixed and only vary the stop-1 mass $m_{\tilde{t}_1}$, unless otherwise specified. As the LO cross section does not depend on the additional parameters, the resummed exponentials will show no parameter dependence either. With the inclusion of the one-loop

hard-matching coefficient, we expect to slightly increase the sensitivity to these parameters, in particular also due to cross terms of higher-order logarithmic terms with the hard-matching coefficient.

The accuracy of the cross sections in the plots and tables will be denoted by the following labels:

- LO and NLO, denoting the leading- and next-to-leading order contributions [98],
- NLO+NLL, denoting the resummed soft-gluon corrections at NLL matched to NLO as calculated in ref. [112],
- NLO+NNLL$_{h+\text{Coul}(1)}$, denoting the resummed NNLL corrections matched to NLO, including the matching coefficient in (4.109) up to $\mathcal{O}(\alpha_s)$, i.e.

$$C_{ij\to\tilde{t}\tilde{t}^*,I}\Big|_{\text{NLO}} = 1 + \frac{\alpha_s}{\pi}\left(\mathcal{C}^{\text{Coul},(1)}_{ij\to\tilde{t}\tilde{t}^*,I} + \mathcal{C}^{(1)}_{ij\to\tilde{t}\tilde{t}^*,I}\right), \tag{8.4}$$

  as a comparison to the results from ref. [132] (with parameters according to table 8.1 (b)),
- NLO+NNLL, denoting the resummed NNLL corrections matched to NLO, including hard-matching coefficients up to $\mathcal{O}(\alpha_s)$ and Coulomb contributions up to $\mathcal{O}(\alpha_s^2)$,

$$C_{ij\to\tilde{t}\tilde{t}^*,I}\Big|_{\text{NNLO}} = 1 + \frac{\alpha_s}{\pi}\left(\mathcal{C}^{\text{Coul},(1)}_{ij\to\tilde{t}\tilde{t}^*,I} + \mathcal{C}^{(1)}_{ij\to\tilde{t}\tilde{t}^*,I}\right) + \frac{\alpha_s^2}{\pi^2}\left(\mathcal{C}^{\text{Coul},(1)}_{ij\to\tilde{t}\tilde{t}^*,I}\mathcal{C}^{(1)}_{ij\to\tilde{t}\tilde{t}^*,I} + \mathcal{C}^{\text{Coul},(2)}_{ij\to\tilde{t}\tilde{t}^*,I}\right). \tag{8.5}$$

  This allows us to investigate the impact of the $\mathcal{O}(\alpha_s^2)$ terms in the matching coefficient, i.e. the two-loop Coulomb contribution as well as the cross-term consisting of the one-loop Coulomb and hard-matching coefficients, as compared to NLO+NNLL$_{h+\text{Coul}(1)}$,
- NNLO$_{\text{Approx}}$, as given by eq. (7.5), denoting the approximated NNLO contributions in the threshold limit from ref. [128] added to the full NLO result,
- NNLO$_{\text{Approx}}$+NNLL, denoting the resummed NNLL corrections matched to the approximated NNLO result, including hard-matching coefficients up to $\mathcal{O}(\alpha_s)$ and Coulomb contributions up to $\mathcal{O}(\alpha_s^2)$ as in eq. (8.5). This prediction differs from NLO+NNLL by terms of $\mathcal{O}\left(1/\sqrt{N}\right)$, i.e. power-suppressed in N. Unless stated otherwise, the values of MSSM parameters listed in table 8.1 (a) are used. We will call this the default prediction.

The p-wave states will be treated in a similar manner to section 7.2.

8.3.1 Threshold behaviour of the partonic cross section

Before discussing total cross sections, we first examine the partonic cross section through means of scaling functions. These are dimensionless functions that allow for an analysis of the partonic cross section without the effects of the convolution with the PDFs. Furthermore, scaling functions of full partonic cross sections can easily be compared to various approximations such as the partonic NLO cross section in the threshold limit. This will be of much interest to us, as it directly shows if the approximations reproduce the full cross

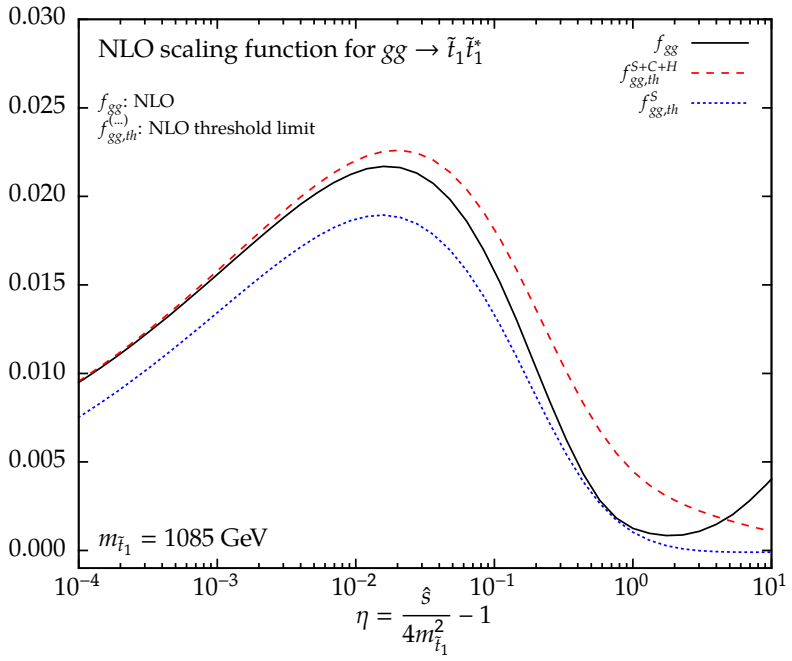

Figure 8.3: NLO scaling function for the gg initial state for different threshold approximations and the full `Prospino` result.

section properly in the kinematical regions in which they are valid. The scaling functions are defined through the partonic cross section [98]:

$$\hat{\sigma}_{ij} = \frac{\alpha_s^2}{m^2_{\tilde{t}_1}} \left\{ f^B_{ij} + 4\pi\alpha_s \left[f_{ij} + \bar{f}_{ij} \ln\left(\frac{\mu^2}{m^2_{\tilde{t}_1}}\right)\right]\right\}, \tag{8.6}$$

where f^B_{ij} is the Born contribution and f_{ij} and $\bar{f}_{ij}$ are the scale-independent and scale-dependent NLO scaling functions.

In figure 8.3, we show the (scale-independent) NLO scaling function f_{gg} for the dominant gg initial state of stop-antistop production both for the full NLO result extracted from `Prospino` (solid black line) as well as for the near-threshold approximation at NLO (dashed red, dotted blue). This approximation is simply the expression in curly brackets from eq. (8.1), taking into account the correct factors of 4π and ignoring the scale-dependent terms. It is clear that, while the approximation when only taking into account the logarithms in β from soft-gluon emission (S) significantly differs from the full result even when moving closer to threshold (which corresponds to $\eta \to 0$), the sum of soft logarithms and the one-loop Coulomb and hard-matching coefficients ($S + C + H$) approaches the full result towards the threshold region and describes it well up to a value of $\eta \approx 10^{-2}$ which corresponds to $\beta \approx 0.1$. It should be noted that especially the Coulomb brings the approximation closer to the full result. It leads to the constant shift between the S and $S + C + H$ lines close to threshold due to the $1/\beta$ from the Coulomb term approximately cancelling the $\propto \beta$ behaviour of the LO cross sectionn in the threshold limit. We conclude that, to describe the threshold region properly, the additional Coulomb and one-loop hard-matching contributions need to be incorporated

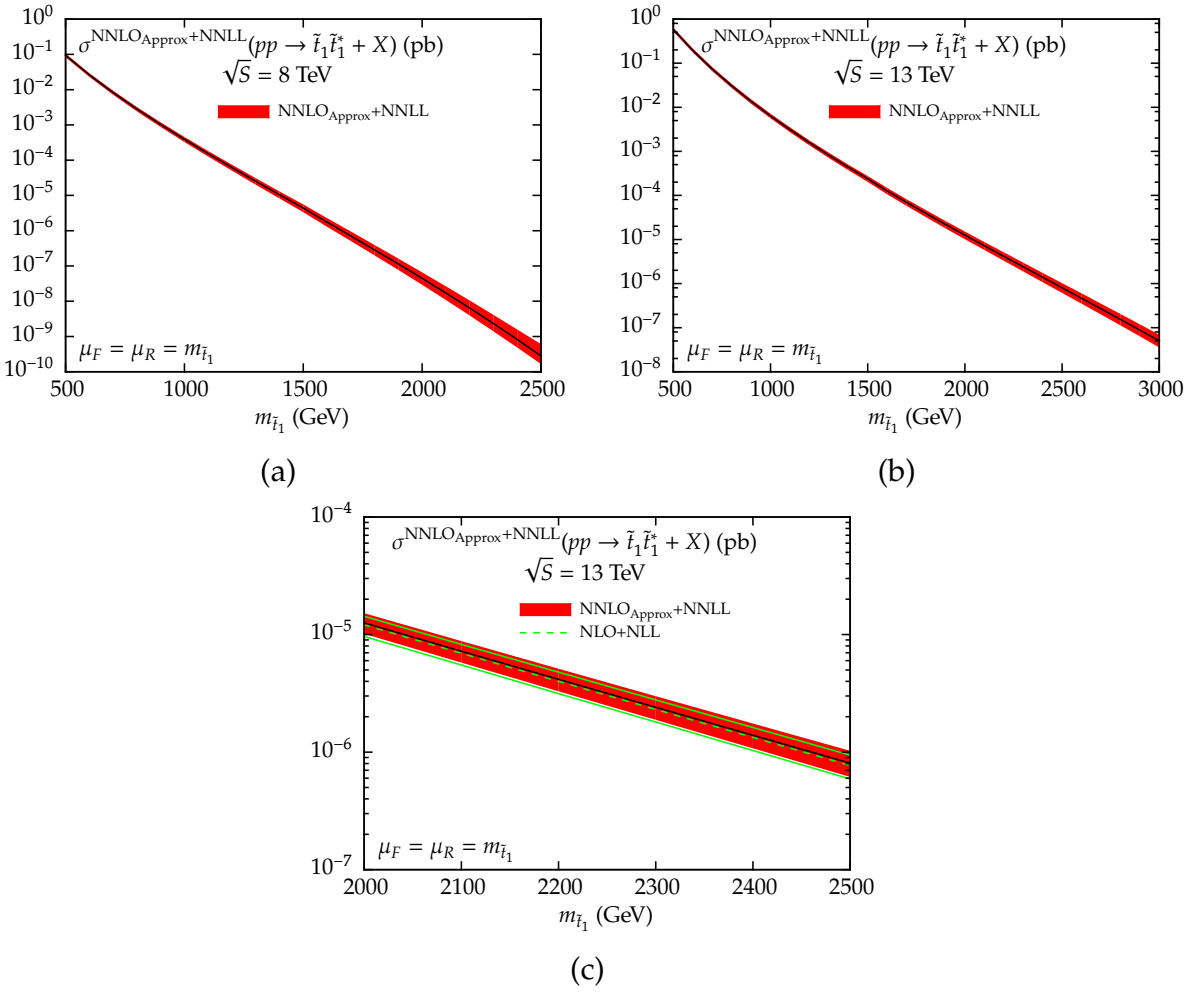

Figure 8.4: The NNLO$_{\text{Approx}}$+NNLL cross section for stop-antistop production for LHC energies of 8 (a) and 13 TeV (b), including the theoretical uncertainty band. Additionally, a comparison with the theoretical uncertainty band at NLO+NLL accuracy is shown (c). The uncertainty band includes the 68% C.L. PDF and α_s uncertanties added quadratically, and the scale uncertainty for $m/2 \leq \mu \leq 2m$ added linearly to the combined PDF and α_s uncertainty. All parameters other than the mass of the produced stop, $m_{\tilde{t}_1}$, have been chosen according to table 8.1 (a).

in the resummed formalism, which we will do by upgrading stop-antistop production to NNLO$_{\text{Approx}}$+NNLL in the following section.

8.3.2 Predictions for stop-antistop production at the LHC

Figure 8.4 and table 8.2 show the total cross section results for the production of $\tilde{t}_1\tilde{t}_1^*$ pairs including the 68% C.L. PDF and α_s uncertainties as well as the theoretical scale uncertainty for varying μ as $m/2 \leq \mu \leq 2m$. The total uncertainty consists of the PDF and α_s uncertainties added in quadrature with the scale uncertainty added linearly on top. We notice that for low stop masses, the three uncertainties are of roughly the same size (a few percent), while above a stop mass of 1 TeV, the PDF and α_s uncertainties start dominating the total uncertainty, with the two uncertainties still being of roughly the same size, up to individual uncertainties

	$\sigma^{\text{NLO+NLL}}$ (pb)	
$m_{\tilde{t}_1}$ (GeV)	8 TeV	13 TeV
500	$86.9^{+(8.8+6.7)\%}_{-(9.2+7.4)\%} \times 10^{-3}$	$53.4^{+(9.2+4.6)\%}_{-(8.6+5.5)\%} \times 10^{-2}$
1200	$57.7^{+(6.1+15.1)\%}_{-(7.7+14.5)\%} \times 10^{-6}$	$14.8^{+(6.7+9.0)\%}_{-(7.7+9.2)\%} \times 10^{-4}$
2000	$40.1^{+(1.9+30.4)\%}_{-(5.0+25.9)\%} \times 10^{-9}$	$12.1^{+(3.6+14.8)\%}_{-(6.2+14.0)\%} \times 10^{-6}$
	$\sigma^{\text{NNLO}_{\text{Approx}}+\text{NNLL}}$ (pb)	
$m_{\tilde{t}_1}$ (GeV)	8 TeV	13 TeV
500	$94.1^{+(4.5+6.9)\%}_{-(5.1+6.6)\%} \times 10^{-3}$	$58.1^{+(5.3+4.8)\%}_{-(4.6+5.1)\%} \times 10^{-2}$
1200	$61.8^{+(3.8+16.2)\%}_{-(5.5+13.2)\%} \times 10^{-6}$	$15.7^{+(4.1+9.0)\%}_{-(5.0+7.9)\%} \times 10^{-4}$
2000	$44.6^{+(6.7+41.1)\%}_{-(8.7+25.9)\%} \times 10^{-9}$	$12.6^{+(4.8+15.9)\%}_{-(6.5+12.8)\%} \times 10^{-6}$

Table 8.2: Total cross section predictions for stop-antistop production for centre-of-mass energies of $\sqrt{S} = 8$ and $\sqrt{S} = 13$ TeV, shown in the format $\sigma \pm \Delta\sigma_\mu[\%] \pm \Delta\sigma_{\text{PDF}+\alpha_s}[\%]$ with $\Delta\sigma_\mu$ being the scale uncertainty and $\Delta\sigma_{\text{PDF}+\alpha_s}$ the combined PDF+α_s uncertainty. For comparison, both the publicly available results for NLO+NLL as well as the new $\text{NNLO}_{\text{Approx}}$+NNLL predictions are presented.

of 50-90% at $\sqrt{S} = 8$ TeV for very high stop masses around 2.5 TeV. The scale uncertainty does not seem to be very sensitive to the mass, with a slight upward trend towards higher masses, and amounts to about 4-9% for the shown values. Interestingly, it seems that the overall size of the uncertainty band stays the same when going from NLO+NLL to $\text{NNLO}_{\text{Approx}}$+NNLL, as seen in figure 8.4 (c) and the numbers of table 8.2. We notice however a slight reduction of the scale uncertainty towards smaller stop masses, and an increase of the scale uncertainty towards higher masses. The scale dependence will be studied thoroughly at a later point.

We now again study the K-factor as defined in eq. (6.4) to more easily see the changes with respect to NLO+NLL. Figure 8.5 shows the K-factor for $\sqrt{S} = 8$ TeV (a) and 13 TeV (b). We see a general upwards trend for both collider energies, with the K-factor of 8 TeV growing from a value of approximately 1.1 at $m_{\tilde{t}_1} = 500$ GeV to 2.0 at $m_{\tilde{t}_1} = 2000$ GeV, while the enhancement at 13 TeV is similar at low masses, but only reaches around 1.3 for $m_{\tilde{t}_1} = 3000$ GeV. This is again in accordance with the process of producing two heavy particles taking place closer to the hadronic threshold at a lower collider energy, and therefore the partonic cross section contributing more significantly in the threshold region. In terms of figure 8.3, this means that we convolute the scaling functions with the PDFs and integrate over η, with the upper integration boundary η_{max} becoming smaller for a lower collider energy. Furthermore, we can see that the NNLL corrections are always larger than the previously known results at NLL accuracy. The growing difference towards higher stop masses between the $\text{NNLO}_{\text{Approx}}$ and the $\text{NNLO}_{\text{Approx}}$+NNLL lines signifies the importance of the formally higher-order logarithms in α_s and their cross terms with the Coulomb and hard-matching coefficients which are not present in the fixed-order calculation.

We observe a peak in the K-factor for both 8 and 13 TeV at a stop mass near $m_{\tilde{t}_1} \approx 1500$

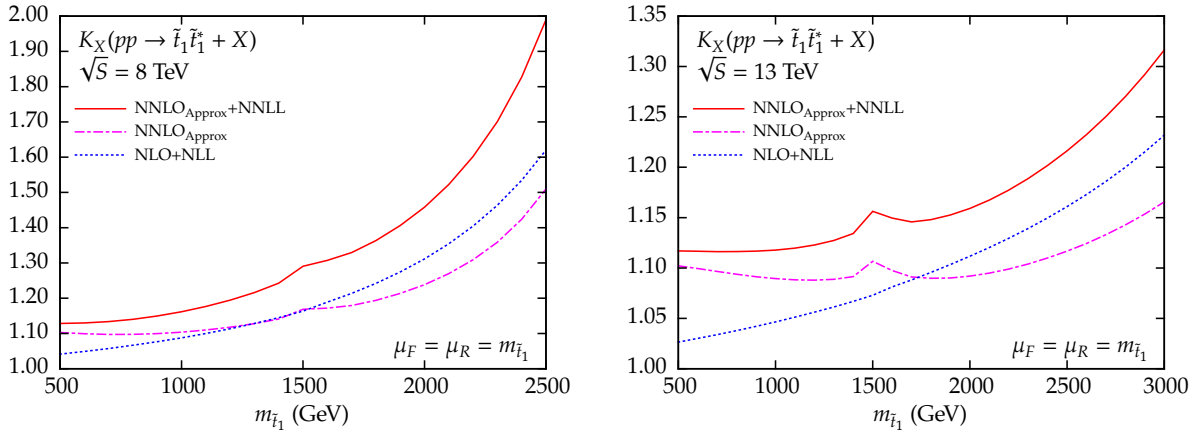

Figure 8.5: The K factor for different orders, as explained in the text. While only the stop-1 mass is being varied, all other parameters are set to the values in table 8.1 (a). The renormalisation and factorisation scales have been set to the stop-1 mass.

GeV. We found that the position of the peak coincides with the gluino mass. While we are going to discuss the parameter dependence of the NNLO$_{\text{Approx}}$+NNLL cross section in a bit, we first clarify the origins of this peak. The hard-matching coefficient of the gg initial state includes two effects which cause the observed behaviour. First, the Mandelstam variable $\hat{s}$ in the NLO calculation develops a threshold at $\hat{s} = 4m_{\tilde{g}}^2$. As we evaluate the hard-matching coefficients from the NLO contributions at threshold, $\hat{s} \to 4m_{\tilde{t}_1}^2$, this directly translate into a threshold for $m_{\tilde{t}_1} = m_{\tilde{g}}$. Second, the stop mass itself has a threshold at $m_{\tilde{t}_1} = m_t + m_{\tilde{g}}$ which is related to an on-shell singularity when the decay of a stop into a top quark and a gluino is kinematically allowed. We checked that in the case of the similar process of light-flavoured squark-antisquark production, the hard-matching coefficient $\mathcal{C}^{(1)}_{gg\to\tilde{q}\bar{\tilde{q}},I}$ (see appendix D of ref. [129], p. 18) develops a similar behaviour at $m_{\tilde{q}} = m_{\tilde{g}}$ (when varying one mass while keeping the other fixed), where the thresholds mainly originate from the $\log^2\left(x_{\tilde{g}\tilde{g}}(4m_{\tilde{q}}^2)\right)$ (with the argument $x_{\tilde{g}\tilde{g}}(4m_{\tilde{q}}^2) = \left[\sqrt{1 - m_{\tilde{g}}^2/m_{\tilde{q}}^2} - 1\right] / \left[\sqrt{1 - m_{\tilde{g}}^2/m_{\tilde{q}}^2} + 1\right]$) and the $\text{Li}_2\left(m_{\tilde{q}}^2/m_{\tilde{g}}^2\right)$ terms. It can be seen that the thresholds denote a transition between two different analytical domains with the argument $m_{\tilde{q}}$ determining if the the functions and their arguments are real or complex valued. Figure 1 of ref. [129] exactly shows this behaviour for the gg initial state.

In figure 8.6, we show the scale dependence for several accuracies of fixed-order and resummed cross sections, again for the two centre-of-mass energies of 8 and 13 TeV.

The common renormalisation and factorisation scale μ is again varied up and down by a factor of 5 around the central value of $\mu_0 = m_{\tilde{t}_1} = 1085$ GeV. At this stop mass, it can be seen that while there is already a notable decrease of the scale dependence at the NLL level with respect to NLO, the behaviour furthermore improves slightly due to the NNLL contributions. In particular towards higher scales, the NNLL contributions cause the slope of the curve to become flatter than NLO+NLL. While the scale uncertainty numbers from table 8.2 suggest that the scale dependence increases for high stop masses when adding the NNLL corrections,

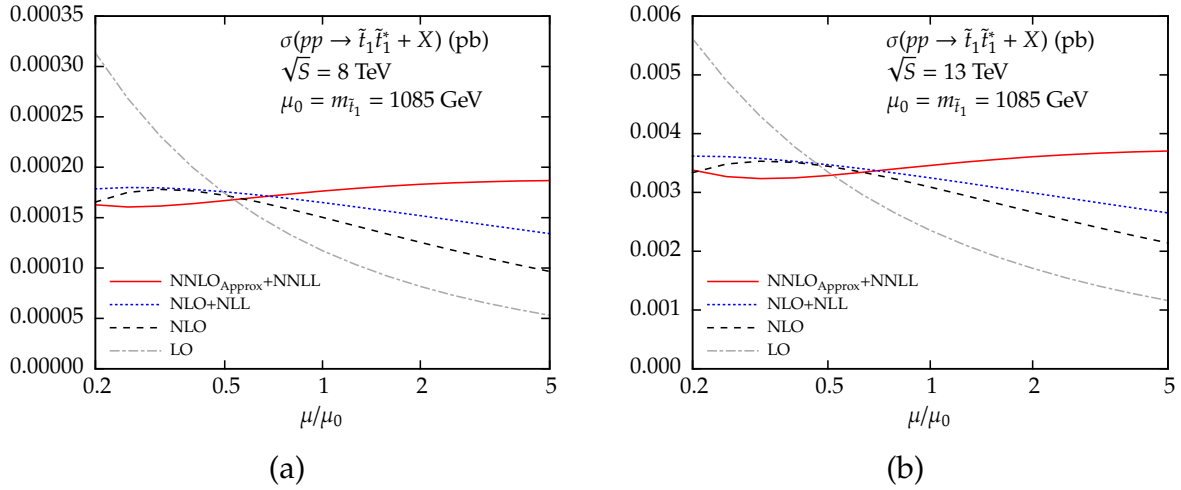

Figure 8.6: Scale dependence of the cross section for different orders. All masses and parameters are set to the values from table 8.1 (a). The central scale is chosen to be the same as the stop-1 mass.

it should be noted that the low scale uncertainty of NLO+NLL or even NLO computed at the two values $\mu = \mu_0/2$ and $\mu = 2\mu_0$ is related to the mass of the stops leading to the turn-over point of the scale dependence (as can be seen in figure 8.6 for NLO in between $\mu = 0.2\mu_0$ and $\mu = 0.5\mu_0$) being close to the central scale $\mu = \mu_0$.

Similarly to what was observed for gluino-pair production in figure 7.5 (a) of section 7.3 and contrary to the previous results at NLO+NLL, the NNLO$_{\text{Approx}}$+NNLL prediction now shows a slight upward slope. We will investigate this behaviour more closely in section 8.3.3, where we compare to the similar production of light-flavoured squark-antisquark pairs and will find that the difference in the behaviour can be traced back to the difference in the contributions to the $q\bar{q}$ initial state, see section 8.1, with mainly the absence of the singlet colour channel being responsible for it.

Before we do that, we still discuss the dependence of the NNLO$_{\text{Approx}}$+NNLL results on the additional SUSY parameters appearing first at NLO. Table 8.3 lists the total cross section for a different choice of parameters. They are first set to the default values of table 8.1 (a), and subsequently varied separately. While the variation of the heavier $\tilde{t}_2$ mass $m_{\tilde{t}_2}$ hardly influences the cross section (even when the $\tilde{t}_2$ is actually lighter than the $\tilde{t}_1$), we observe that a change of the mixing angle or the degenerate light-flavoured squark mass leads to a deviation of at most 1% from using the default parameter values. The main impact comes from the variation of the gluino mass which, depending on the hierarchy between the $\tilde{t}_1$ and $\tilde{g}$ masses, can change the cross section by several percent. One interesting scenario is the case where the lighter stop mass eigenstates are the lightest coloured particles with the other stop and the light-flavoured squarks and the gluino considered to be decoupled[4]. Figure 8.7 shows the K-factor for such a scenario while comparing to the predictions for the default parameter values. It should be noted that the NLO cross section in the denominator of the K-factor is computed with the decoupled parameters for the "dec." lines, but with the default parameters for the default predicitions as in figure 8.5. At high $m_{\tilde{t}_1}$, the K-factor

[4] i.e. their masses are considered much higher than $m_{\tilde{t}_1}$.

Parameter	Value	$\sigma \times 10^{-4}$ (pb)
40.2.5	–	34.60
$m_{\tilde{t}_2}$	100 GeV	34.65
	500 GeV	34.60
	2000 GeV	34.60
	5000 GeV	34.60
$m_{\tilde{g}}$	100 GeV	33.15
	500 GeV	31.98
	2000 GeV	34.63
	5000 GeV	34.80
$m_{\tilde{q}}$	100 GeV	34.85
	500 GeV	34.46
	2000 GeV	34.76
	5000 GeV	35.02
$\sin 2\theta_{\tilde{t}}$	1	34.60
	0	34.67
	-1	34.95

Table 8.3: Parameter dependence of stop-antistop production at $\text{NNLO}_{\text{Approx}}$+NNLL for $\sqrt{S} = 13$ TeV. All parameters are chosen corresponding to benchmark point 40.2.5, and then varied individually for the given values.

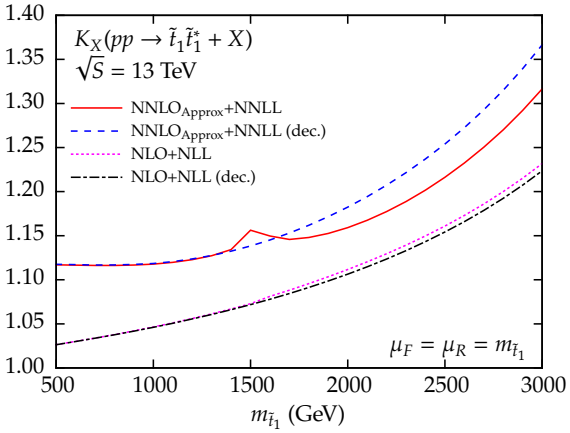

Figure 8.7: Comparison of the K factor when choosing the additional stop parameters according to table 8.1 (a) (solid red for $\text{NNLO}_{\text{Approx}}$+NNLL, pink dotted for NLO+NLL) and when decoupling all masses except for $m_{\tilde{t}_1}$ (dashed blue for $\text{NNLO}_{\text{Approx}}$+NNLL, black dash-dotted for NLO+NLL). For the lines corresponding to the decoupling limit, also the NLO cross section appearing in the denominator of the K factor is computed with the decoupled parameters. For concreteness, we set the decoupled parameters in the plot to $m_{\tilde{q}} = 10$ TeV, $m_{\tilde{t}_2} = 10.01$ TeV, and $m_{\tilde{g}} = 10.02$ TeV, while keeping the mixing angle at its default value.

for $\text{NNLO}_{\text{Approx}}$+NNLL differs by as much as 5%, accentuating the observation that the choice of a particular SUSY model and benchmark point may have a noticeable effect on the stop production cross sections. As discussed before, this difference between the lines is mainly driven by the difference in the gluino mass, while the effect of the differences in the other masses is negligible. In the comparison to the NLO+NLL lines, where the parameter dependence only appears in the NLO cross section in the denominator of the K-factor, we see that this large difference at high masses stems from the hard-matching coefficient as the only additional ingredient at NNLL accuracy that depends on the parameters. In particular the mixing of hard-matching coefficients with the higher-order logarithms of the resummed exponential function and the Coulomb coefficients noticeably increases the difference between the NNLL lines compared to NLO+NLL. We note that the large difference between the NLO+NLL and $\text{NNLO}_{\text{Approx}}$+NNLL behaviour is also a side-effect of the different normalisation of the lines, i.e. using the NLO cross section in the denominator with decoupled parameters for the "dec." lines, and default parameters for the lines of the default predictions. We checked by using the same NLO cross section for all the lines that at high masses, the difference between the two lines at $\text{NNLO}_{\text{Approx}}$+NNLL accuracy is approximately twice as large as the difference for the lines at NLO+NLL accuracy.

8.3.3 Comparison to squark-antisquark production

The scale dependence of a cross section can be best understood when separately analysing its constituents. Therefore, we split up both the $\tilde{t}\tilde{t}^*$ as well as the light-flavour $\tilde{q}\tilde{q}^*$ cross sections in figures 8.8 (a) and (b) into the different initial-state channels $q\bar{q}$, gg, and qg, where the latter only appears starting from NLO and is strongly suppressed close to threshold, therefore not receiving any contributions from resummation, as discussed at the beginning of this section. It is interesting to compare the two processes, as they are very similar in their production mechanisms, yet exhibit a different behaviour when it comes to their scale dependence.

In figure 8.8 (a), we show the scale dependence of $\tilde{t}\tilde{t}^*$ both for the NLO+NLL as well as the $\text{NNLO}_{\text{Approx}}$+NNLL accuracies. It can be seen that the contributions from the gg initial state (dashed red and blue lines) differ at these two levels: while for NLO+NLL, the gg part of the cross section continuously decreases starting from roughly $\mu = 0.5\mu_0$ towards higher scales, gg at $\text{NNLO}_{\text{Approx}}$+NNLL shows a clear upward slope. Adding the p-wave-suppressed $q\bar{q}$ contributions (dotted red and blue lines) does not change the slope of the curve significantly and only increases the cross sections slightly for both accuracies. We note that, even though $q\bar{q}$ is p-wave-suppressed, the absolute size of the gg and $q\bar{q}$ contributions actually does not differ that much, with the former being larger by a modest factor of approximately 1.5 at the given value of the stop mass. Adding the qg contribution from the NLO computation increases the cross section towards lower scales, and decreases it slightly towards higher scales. The solid red line now shows the full $\text{NNLO}_{\text{Approx}}$+NNLL prediction as presented previously. At $\text{NNLO}_{\text{Approx}}$+NNLL, we therefore confirm that the upward slope originates from the behaviour of the dominant gg initial-state channel with the corrections beyond NLO+NLL.

Now, figure 8.8 (b) is the analogous plot for $\tilde{q}\tilde{q}^*$. We immediately observe that, while the

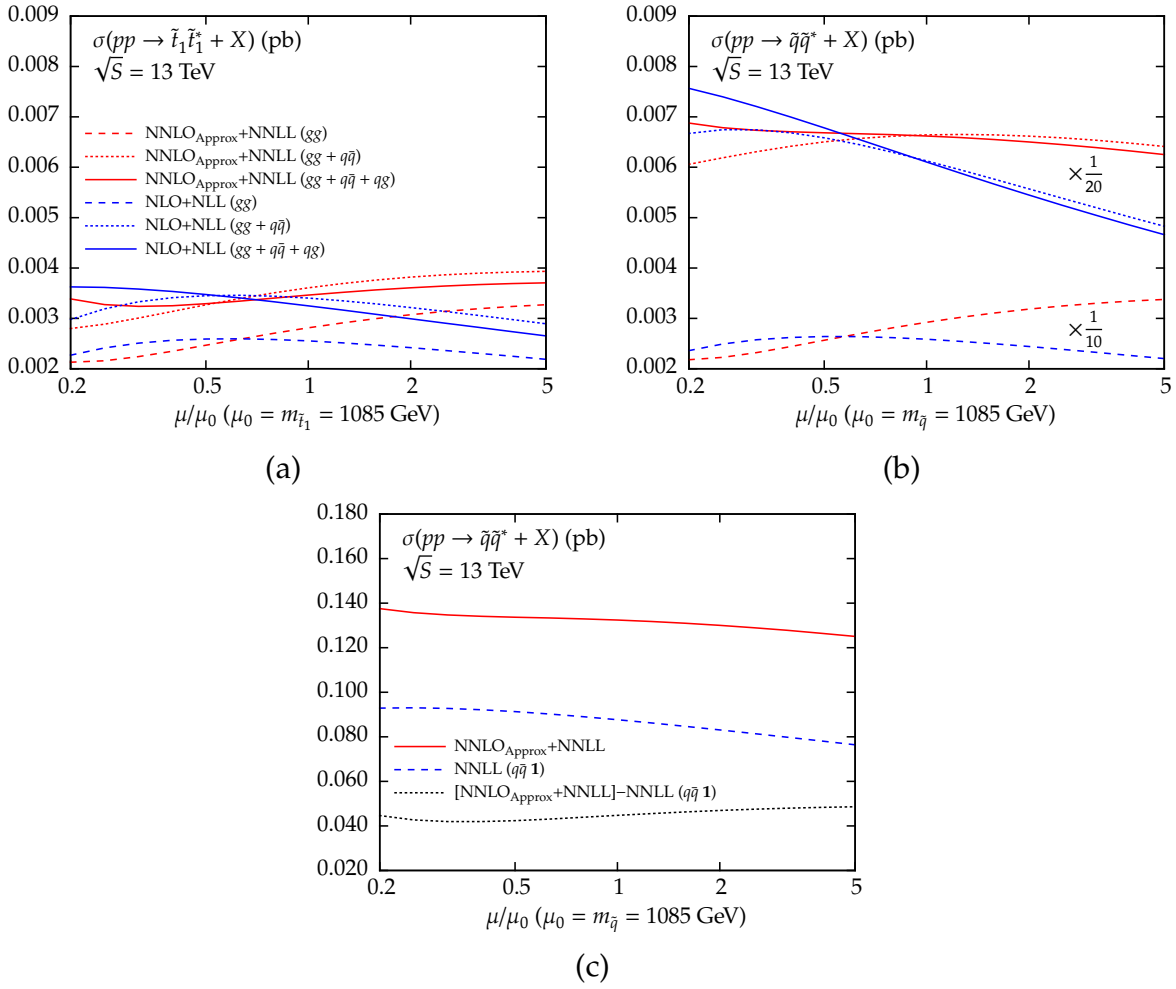

Figure 8.8: Scale dependence for stop-antistop (a) and light-flavoured squark-antisquark production (b) at 13 TeV, split up into the initial-state contributions, both for NLO+NLL as well as NNLO$_{\text{Approx}}$+NNLL. The labelling of the lines in (b) is the same as in (a). It should be noted that for an easier comparison to (a), the lines of (b) have been divided by a factor of 10 for the gg initial state (dashed lines), and by a factor of 20 for the $gg + q\bar{q}$ (dotted lines) and $gg + q\bar{q} + qg$ initial states (solid lines), as indicated on the plot. In (c), the contribution from the singlet channel of the $q\bar{q}$ initial state to $\tilde{q}\tilde{q}^*$ is shown, see the accompanying text for further explanations. The central scales as well as the masses of the produced particles are set in both cases to the $\tilde{t}_1$ mass of table 8.1 (a) for easier comparison.

gg contributions behave in exactly the same way (as they are, in fact, the same aside from the factor $2n_f$), the dominant contribution comes from the $q\bar{q}$ initial state which is much larger than the contribution from the gg initial state as seen in the suppressing factors of 1/10 and 1/20 introduced to be able to compare $\tilde{t}\tilde{t}^*$ and $\tilde{q}\tilde{q}^*$ next to each other. The qg contribution has a similar effect as for $\tilde{t}\tilde{t}^*$ and mainly increases the cross section at lower scales. We have seen the dominance of the $q\bar{q}$ contributions already in section 8.1, with mainly the singlet colour channel of $q\bar{q} \to \tilde{q}\tilde{q}^*$ determining the behaviour of the full cross section. We note that the t-channel diagram which is absent in the case of $\tilde{t}\tilde{t}^*$ also changes the $q\bar{q}$ octet channel slightly, as seen in figure 8.2, in particular also adding an s-wave contribution to it. However, the octet channel only contributes at approximately 20% to the full LO cross section, with the

singlet channel contributing more than 70%. We assume this order to approximately hold also at the NNLO$_{\text{Approx}}$+NNLL level. In any case, we notice that the contributions from the $q\bar{q}$ initial state lead to the pronounced downward slope of the scale dependence at the NLL level. The additional NNLL corrections then lead to an almost flat scale dependence with a slight downward slope towards higher scales remaining.

As a final check to pinpoint the difference in scale dependence for $\tilde{t}\tilde{t}^*$ and $\tilde{q}\tilde{q}^*$ to the absence of the singlet channel in the former, we show figure 8.8 (c) which presents the full NNLO$_{\text{Approx}}$+NNLL prediction for $\tilde{q}\tilde{q}^*$ (solid red line) as already seen in figure 8.8 (b), the purely resummed[5] contributions for the singlet channel of the $q\bar{q}$ initial state labelled "NNLL ($q\bar{q}$ **1**)" (dashed blue line), and the latter subtracted from the former (dotted black line). This last line is an approximation for removing all $q\bar{q}$-singlet contributions from the $\tilde{q}\tilde{q}^*$ cross section[6]. We notice from the last line that doing this subtraction leads to a notable decrease in the cross section, as expected with the $q\bar{q}$ singlet channel being the dominant one, and it furthermore changes the scale behaviour in such a sense that it now exhibits an upward slope, which is very similar to $\tilde{t}\tilde{t}^*$. We therefore conclude that the absence of the $q\bar{q}$ singlet channel in the case of $\tilde{t}\tilde{t}^*$ production leads to a dominance of the gg initial state, resulting in an upward slope of the scale dependence at the NNLO$_{\text{Approx}}$+NNLL accuracy. Additionally, we note that the results for $\tilde{g}\tilde{g}$ and $\tilde{q}\tilde{g}$ production from the previous section, which also mainly proceed through dominant channels with gluons in the initial state, behave in a similar manner, with the scale dependence showing an upward slope.

8.3.4 Comparison to SCET results

Results for stop-antistop production including corrections from threshold resummation at NNLL accuracy have already been calculated within the SCET formalism and are available in ref. [132]. It should furthermore be noted that the authors use two different kinematical schemes to define their threshold, which differs from the absolute threshold used here by subleading terms. Our work presents results at NNLL accuracy with a slightly higher accuracy by including also $\mathcal{O}(\alpha_s^2)$ effects in the matching coefficient, i.e. cross terms between the one-loop hard-matching and Coulomb coefficients as well as the two-loop Coulomb contributions. Due to the different approaches to threshold resummation, i.e. the Mellin-moment space approach for us and SCET for them, it is of interest to see how well the results from both approaches agree.

We now present the comparison in table 8.4 as well as figure 8.9. As mentioned previously, we use the parameter points of table 8.1 (b) for the calculation of the numbers in the table and figure to reproduce the settings of ref. [132] as closely as possible. While the authors use two different PDF sets, we only compare to the numbers at $\sqrt{S} = 8, 14$ TeV that are computed with the MSTW2008 PDF set. The various accuracies used in table 8.4 and figure 8.9 are defined in the beginning of section 8.3. The given uncertainties only denote the theoretical scale

[5] Purely resummed means that neither a full fixed-order cross section is added to it, nor the fixed-order expansion of the threshold-enhanced terms is subtracted from it, see also the discussion in the text regarding figure 7.6.

[6] It is an approximation, as it is not possible to switch off only certain colour channels in `Prospino`, so only the threshold-enhanced NLO terms of the $q\bar{q}$-singlet, contained within NNLL ($q\bar{q}$ **1**), are removed.

	8 TeV	
$m_{\tilde{t}_1}$ (GeV)	500	1087.17
$(\sigma \pm \Delta\sigma_\mu)_{\text{NLO}}$ (pb)	$83.4^{+10.5}_{-12.1} \times 10^{-3}$	$14.7^{+2.1}_{-2.4} \times 10^{-5}$
$(\sigma \pm \Delta\sigma_\mu)_{\text{NLO+NNLL}}$ (pb) from ref. [132]	$79.9^{+6.2}_{-3.9} \times 10^{-3}$	$15.2^{+1.7}_{-0.9} \times 10^{-5}$
$(\sigma \pm \Delta\sigma_\mu)_{\text{NLO+NNLL}_{h+\text{Coul(1)}}}$ (pb)	$85.2^{+0.8}_{-0.2} \times 10^{-3}$	$15.9^{+0.2}_{-0.2} \times 10^{-5}$
$(\sigma \pm \Delta\sigma_\mu)_{\text{NLO+NNLL}}$ (pb)	$86.4^{+0.2}_{-0.0} \times 10^{-3}$	$16.2^{+0.3}_{-0.3} \times 10^{-5}$
$(\sigma \pm \Delta\sigma_\mu)_{\text{NNLO}_{\text{Approx}}+\text{NNLL}}$ (pb)	$94.1^{+4.3}_{-4.8} \times 10^{-3}$	$17.3^{+0.7}_{-0.9} \times 10^{-5}$
	14 TeV	
$m_{\tilde{t}_1}$ (GeV)	500	1087.17
$(\sigma \pm \Delta\sigma_\mu)_{\text{NLO}}$ (pb)	$66.5^{+7.5}_{-8.5} \times 10^{-2}$	$44.2^{+4.9}_{-5.9} \times 10^{-4}$
$(\sigma \pm \Delta\sigma_\mu)_{\text{NLO+NNLL}}$ (pb) from ref. [132]	$62.9^{+3.5}_{-3.2} \times 10^{-2}$	$43.1^{+3.5}_{-1.8} \times 10^{-4}$
$(\sigma \pm \Delta\sigma_\mu)_{\text{NLO+NNLL}_{h+\text{Coul(1)}}}$ (pb)	$67.2^{+1.5}_{-0.4} \times 10^{-2}$	$45.3^{+0.1}_{-0.0} \times 10^{-4}$
$(\sigma \pm \Delta\sigma_\mu)_{\text{NLO+NNLL}}$ (pb)	$68.0^{+1.0}_{-0.1} \times 10^{-2}$	$45.9^{+0.3}_{-0.2} \times 10^{-4}$
$(\sigma \pm \Delta\sigma_\mu)_{\text{NNLO}_{\text{Approx}}+\text{NNLL}}$ (pb)	$74.3^{+4.0}_{-3.4} \times 10^{-2}$	$49.3^{+2.2}_{-2.4} \times 10^{-4}$

Table 8.4: Stop-antistop production cross sections for different accuracies at centre-of-mass energies of $\sqrt{S} = 8, 14$ TeV using MSTW2008 PDF sets. Only the scale variation uncertainties are shown. Refer to the accompanying text for more explanation on these uncertainties. For all numbers, the parameter values from table 8.1 (b) are used.

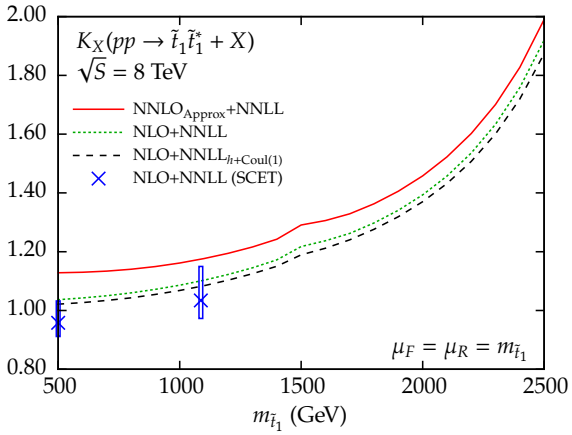

Figure 8.9: Comparison of the K factor to the SCET results [132]. Shown is the NNLO$_{\text{Approx}}$+NNLL prediction of this work (solid red), the NLO+NNLL$_{h+\text{Coul(1)}}$ cross section mimicking the method of [132] (dashed black), the NLO+NNLL cross section including $\mathcal{O}(\alpha_s^2)$ terms in the matching coefficient (dotted green), and two points for the SCET results including their uncertainties from table 8.4. All lines and points in this plot have been calculated using the values of table 8.1 (b).

uncertainties for the various cross sections. In the case of ref. [132], the authors obtain their uncertainties from varying all the scales individually for the two different kinematics and then computing the envelope of the minimum and maximum values, leading to significantly larger uncertainties than for the numbers from our approach. Nonetheless, we can see a good agreement of our predictions with their results within the given uncertainties when we change our default prediction in such a way that we match to the full NLO instead of the $\text{NNLO}_{\text{Approx}}$ result and disable the $\mathcal{O}(\alpha_s^2)$ terms in the matching coefficients $C_{ij\to\bar{t}t^*,I}$. This is important as it shows that with different methods of defining the threshold region, similar results can be obtained. We note, however, that for a stop mass of 500 GeV, the central value of the NNLL corrections of the SCET formalism decrease the cross sections with respect to NLO, albeit being compatible with a K factor larger than 1 within uncertainties. The same behaviour is not seen for our results. On the other hand, we notice that with our description of $\text{NLO+NNLL}_{h+\text{Coul(1)}}$ and NLO+NNLL, the results exhibit very small scale uncertainties.

The results of ref. [132] are not compatible with our default prediction $\text{NNLO}_{\text{Approx}}$+NNLL, however. In fact, we notice a non-negligible difference between $\text{NNLO}_{\text{Approx}}$+NNLL and NLO+NNLL. As the contributions to the resummed exponentials and the Coulomb and hard-matching coefficients are the same in the two accuracies, the only difference stems from the matching procedure to the fixed-order cross section. We will therefore discuss this difference a bit more in detail in the following.

8.3.5 Subleading terms in $\text{NNLO}_{\text{Approx}}$

It has been argued in section 7.1.3 that the threshold-enhanced $\mathcal{O}(\alpha_s^4)$ terms in β-space ref. [128] multiplied by the LO cross section can be Mellin-transformed to obtain the same $\ln(N)$ and Coulomb terms that follow from an expansion of eq. (4.107) up to NNLO. Additionally, the Mellin transform of the logarithms $\ln(\beta)$ of ref. [128] generate terms which are constant in N and contributions proportional to $N^{-1/2}, N^{-1}, N^{-3/2}, \ldots$, both of which are formally subleading in the threshold limit $N \to \infty$. These are the only terms in which the two accuracies $\text{NNLO}_{\text{Approx}}$+NNLL and NLO+NNLL differ. Schematically, this difference is:

$$\begin{aligned}
&\Delta\sigma^{\text{NNLO}_{\text{Approx}}}(\beta) - \int_{\text{inv.}} \mathrm{d}N\, \Delta\tilde{\sigma}^{\text{NNLO}_{\text{Approx}}}(N) \\
&\quad = \int_{\text{inv.}} \mathrm{d}N \left[\int \mathrm{d}\beta\, \beta^{N-1} \Delta\sigma^{\text{NNLO}_{\text{Approx}}}(\beta) - \Delta\tilde{\sigma}^{\text{NNLO}_{\text{Approx}}}(N) \right] \\
&\quad = \int_{\text{inv.}} \mathrm{d}N \left[\text{const.} + \underbrace{\frac{1}{\sqrt{N}} + \frac{1}{N} + \ldots}_{\text{subl.}} \right]
\end{aligned} \tag{8.7}$$

with $\Delta\sigma^{\text{NNLO}_{\text{Approx}}}(\beta)$ the threshold-enhanced NNLO terms in β-space, $\Delta\tilde{\sigma}^{\text{NNLO}_{\text{Approx}}}(N)$ the NNLO terms in Mellin-moment space of the expansion of eq. (4.107), and $\int_{\text{inv.}}$ the inverse Mellin transform. Therefore, we attempt to reduce this difference by calculating the constant as well as the first few subleading terms analytically and then subtracting them from the

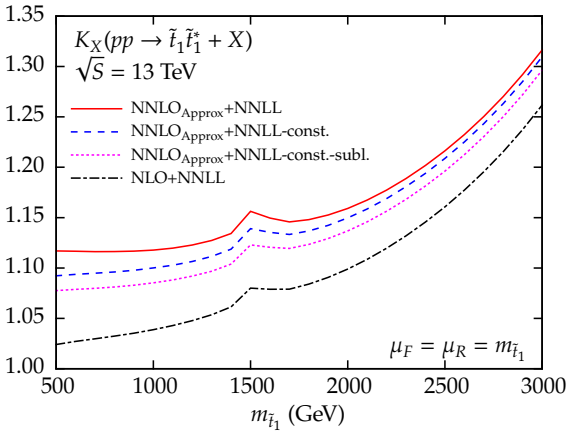

Figure 8.10: Comparison of the NNLO$_{\text{Approx}}$+NNLL and NLO+NNLL accuracies, with two intermediate lines where terms that are constant in N and subleading for $N \to \infty$ are considered. The first three subleading powers of N have been considered in the computation.

NNLO$_{\text{Approx}}$+NNLL cross section. In figure 8.10, we show first the K-factor for the default NNLO$_{\text{Approx}}$+NNLL prediction (solid red line) as well as the default prediction with constant terms subtracted, denoted by "-const." (dashed blue line), with additionally the first three subleading powers of N subtracted, denoted by "-const.-subl." (dotted pink line), and at last the NLO+NNLL prediction (dash-dotted black line). We see that, while the considered constant and subleading terms are not yet enough to fill the gap, we are able to reduce the difference between the NNLO$_{\text{Approx}}$+NNLL and NLO+NNLL predictions by a substantial amount, corresponding to a difference in the K-factors between the solid red and dotted pink curves of almost 5% at a stop mass of $m_{\tilde{t}_1} = 500$ GeV and 1-2% for $m_{\tilde{t}_1} = 3000$ GeV. It is furthermore noticeable that the difference between NNLO$_{\text{Approx}}$+NNLL and NLO+NNLL is large for small stop masses far away from the hadronic threshold (almost 10%), but becomes smaller for high stop masses when approaching the hadronic threshold (around 5%) where the subleading terms are less relevant.

8.3.6 Estimating the *p*-wave contributions at higher logarithmic accuracies

As a last discussion, we estimate how big the unknown p-wave contributions for NNLL resummation are and if our treatment of taking the p-wave contributions into account only at the NLL level is justified. As it has already been said, the factorisation of soft and hard parts as well as the Coulomb contributions has not yet fully been proven at the NNLL level. Nevertheless, we can try to simply treat p-wave states in a similar manner to the s-wave contributions. Fortunately, the hard functions required for our hard-matching coefficients, see section 8.3, have also been calculated in ref. [127] for the two p-wave-suppressed colour channels $q\bar{q}$ **8** and gg $\mathbf{8_A}$. While the one-loop Coulomb contributions are the same as for s-wave states, the two-loop Coulomb contributions receive an extra term (see eq. (2.22) of ref. [123]). The non-Coulombic terms of eq. (4.145) which appear inside eq. (7.4) have naively been included in the same way as for s-wave states. With these ingredients, we can also perform NNLL resummation for the p-wave-suppressed colour channels. Figure 8.11 shows

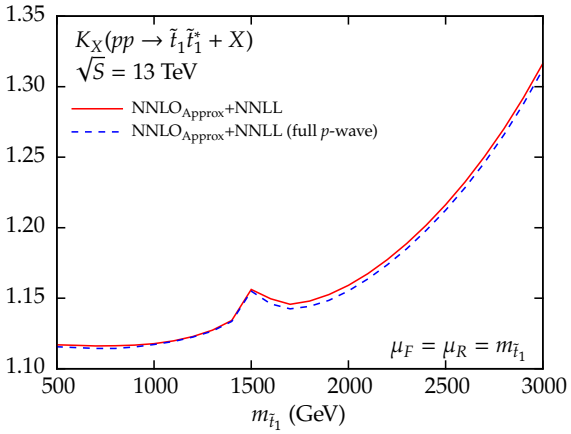

Figure 8.11: Comparison of the default NNLO$_{\text{Approx}}$+NNLL with the treatment of p-wave states as outlined in section 7.2, and an estimate for including the p-wave states at NNLL accuracy.

the comparison of the default NNLO$_{\text{Approx}}$+NNLL prediction with p-wave states treated as in section 7.2 (solid red line) and with p-wave states taken into account at NNLL accuracy (dashed blue line). It can immediately be seen that the p-wave states treated in the same way as the s-wave states only receive very small corrections below one percent at the NNLL level, which justifies our prescription of section 7.2.

9 Coulomb Resummation and Bound-State Contributions

Up until now, only the threshold logarithms were resummed to all orders and the matching coefficients were taken at a fixed order. With the methods presented in this thesis, it is possible to also take the contributions from Coulomb gluon exchange up to all orders in perturbation theory into account. In particular, the Green's function derived in section 4.5 allows for an all-order description of the Coulomb contributions in β-space. While the soft-gluon and Coulomb contributions can be resummed separately, it is more interesting to combine the two to provide the Coulomb gluons with information about already emitted soft gluons which slightly change the remaining kinetic energy available for the produced particles. This procedure should lead to a more precise description of the process near the production threshold. A proof that these higher-order Coulomb contributions factorise from the soft and hard parts has been shown up to NNLL accuracy for s-wave states in ref. [122], with arguments of such a factorisation for the case of leading p-wave states in ref. [123] (such as the $q\bar{q}$ initial state for $\tilde{t}\tilde{t}^*$).

Furthermore, in the case of an attractive Coulomb interaction, bound states can form. They manifest as a discrete number of poles in the Green's function for energies below the threshold. As we will assume the squarks and gluinos to be stable by setting $\Gamma = 0$, we use the narrow-width approximation to describe the bound states as a sum of delta functions. Finite-width effects for $\Gamma \neq 0$ have been studied in ref. [135].

After discussing the implementation of Coulomb resummation and bound-state contributions, we present numerical results. We also compare to the results of ref. [134] which have been calculated in the formalism of SCET.

9.1 Implementation of Coulomb resummation into the framework in Mellin-moment space

For an all-order description in the Mellin-moment space, the Coulomb coefficients would be required at all orders:

$$\begin{aligned}
&1 + \frac{\alpha_s}{\pi} \mathcal{C}^{\text{Coul},(1)}_{ij\to kl,I}(N) + \frac{\alpha_s^2}{\pi^2} \mathcal{C}^{\text{Coul},(2)}_{ij\to kl,I}(N) + ... \\
&\qquad = \frac{1}{\tilde{\sigma}^{(0)}_{ij\to kl,I}(N)} \int_0^1 \mathrm{d}\hat{\rho}\, \hat{\rho}^{N-1} \left(\hat{\sigma}^{\text{Coul},(0)}_{ij\to kl,I}(\hat{\rho}) + \hat{\sigma}^{\text{Coul},(1)}_{ij\to kl,I}(\hat{\rho}) + \hat{\sigma}^{\text{Coul},(2)}_{ij\to kl,I}(\hat{\rho}) + ... \right) \\
&\qquad = \frac{1}{\tilde{\sigma}^{(0)}_{ij\to kl,I}(N)} \int_0^1 \mathrm{d}\hat{\rho}\, \hat{\rho}^{N-1} \hat{\sigma}^{(0)}_{ij\to kl,I}(\hat{\rho}) \frac{\operatorname{Im} G(0,0;E)}{\operatorname{Im} G^{\text{free}}(0,0;E)}
\end{aligned} \tag{9.1}$$

with $\hat{\sigma}^{\text{Coul},(0)}_{ij\to kl,I} = \hat{\sigma}^{(0)}_{ij\to kl,I}$ the Born cross section, and $E = \sqrt{\hat{s}} - 2m_{\text{av}} \approx m_{\text{av}}\beta^2 = m_{\text{av}}(1-\hat{\rho})$. The right-hand side of the equation is simply an expansion of eq. (4.144) in α_s. The Coulomb Green's function provides an all-order expression for the Coulomb contributions with a Coulomb potential at a given accuracy. The Mellin-transform of the Green's function times the leading order cross section is very difficult to be carried out analytically, which is why we choose to keep the explicit Mellin-integral and evaluate it numerically.

By combining eqs. (4.100) (in the case of absolute theshold), (4.144), (4.109), and (4.157), we now obtain a formula for the total hadronic cross section which includes the Coulomb Green's function:

$$\begin{aligned}
\sigma^{(\text{res,Coul})}_{h_1h_2\to kl}(\rho) = \frac{1}{\pi} \sum_{i,j} \sum_I \int_0^\infty \mathrm{d}y \operatorname{Im} \Bigg[& e^{i\phi} \rho^{-N} \tilde{f}_{i/h_1}(N+1,\mu_F^2)\, \tilde{f}_{j/h_2}(N+1,\mu_F^2) \\
& \times \Delta_i \Delta_j \Delta^{(\text{s})}_{ij\to kl,I}(N+1,Q^2,\mu_R^2,\mu_F^2) \left(1 + \frac{\alpha_s}{\pi} \mathcal{C}^{(1)}_{ij\to kl,I} + ... \right) \\
& \times \int_0^1 \mathrm{d}\hat{\rho}\, \hat{\rho}^{N-1} \hat{\sigma}^{(0)}_{ij\to kl,I}(\hat{\rho}) \frac{\operatorname{Im} G(0,0;E)}{\operatorname{Im} G^{\text{free}}(0,0;E)} \Bigg]
\end{aligned} \tag{9.2}$$

where N is parametrised as before, $N = N(y) = C_{\text{MP}} + y\, e^{i\phi}$. We will consider eq. (9.2) as our final formula for the numerical implementation, combining both the effects from soft-gluon emission as well as Coulomb exchange between slowly moving final-state particles up to all orders.

9.2 Implementation of bound-state contributions

In section 4.5.3, it was shown that the Coulomb Green's function develops poles for energies below the production threshold. These poles manifest as bound-states for an attractive Coulomb potential, and can be written as a sum over δ-peaks in the narrow-width approximation, as it was done in eq. (4.150). We start with eq. (4.158), but, instead of regarding the

resummed soft-gluon corrections, only taking the Coulomb Green's function via eq. (4.144) into account:

$$\begin{aligned}\sigma^{(\text{Coul+BS})}_{h_1h_2\to kl}(\rho) &= \sum_{i,j}\sum_{I}\int_0^1 \mathrm{d}\tau \int_\tau^1 \frac{\mathrm{d}x}{x} f_{i/h_1}(x,\mu_F^2)\, f_{j/h_2}\left(\frac{\tau}{x},\mu_F^2\right) \hat{\sigma}^{\text{Coul}}_{ij\to kl,I}\left(\frac{\rho}{\tau}\right) \\ &= \sum_{i,j}\sum_{I}\int_0^1 \mathrm{d}\tau\, \mathscr{L}_{ij}(\tau)\, \hat{\sigma}^{(0)}_{ij\to kl,I}\left(\frac{\rho}{\tau}\right) \frac{\operatorname{Im} G(0,0;E)}{\operatorname{Im} G^{\text{free}}(0,0;E)} \end{aligned} \tag{9.3}$$

with the luminosity function

$$\mathscr{L}_{ij}(\tau) := \int_\tau^1 \frac{\mathrm{d}x}{x} f_{i/h_1}(x,\mu_F^2)\, f_{j/h_2}\left(\frac{\tau}{x},\mu_F^2\right). \tag{9.4}$$

As it has already been discussed in section 4.7, while the integration range $\tau \in [\rho, 1]$ corresponds to the region above threshold where the definitions of eqs. (4.137) and (4.140) can be used and which is already taken into account in eq. (9.2) together with soft-gluon resummation, we are now more interested in the integration range $\tau \in [0, \rho]$ that denotes the region below threshold where we apply first of all eq. (4.143) to rewrite the cross section close to threshold into the hard function and the free Green's function and to immediately cancel the latter with the corresponding term in the fraction, and subsequently replace $\operatorname{Im} G(0,0;E)$ with eq. (4.150) to obtain:

$$\begin{aligned}\sigma^{\text{BS}}_{h_1h_2\to kl}(\rho) &= \sum_{i,j}\sum_{I}\int_0^\rho \mathrm{d}\tau\, \mathscr{L}_{ij}(\tau)\, \mathcal{H}^{(0)}_{ij\to kl,I} \cancel{\operatorname{Im} G^{\text{free}}(0,0;E)} \frac{\operatorname{Im} G^{\text{BS}}(0,0;E)}{\cancel{\operatorname{Im} G^{\text{free}}(0,0;E)}} \\ &= \sum_{i,j}\sum_{I}\int_0^\rho \mathrm{d}\tau\, \mathscr{L}_{ij}(\tau)\, \mathcal{H}^{(0)}_{ij\to kl,I} \sum_{n=1}^{\infty} \delta(E-E_n) \left(\frac{\alpha_{\text{s}} \mathscr{D}_{ij\to kl,I} m_{\text{red}}}{n}\right)^3. \end{aligned} \tag{9.5}$$

The energy difference to the threshold E can be expressed through τ because of $\hat{s} = \tau S$ (with S the squared hadronic centre-of-mass energy),

$$E = \sqrt{\hat{s}} - 2m_{\text{av}} = \sqrt{\tau S} - 2m_{\text{av}} \Rightarrow \tau = \frac{(E+2m_{\text{av}})^2}{S}, \tag{9.6}$$

and when we also rewrite the delta function,

$$\delta(E-E_n) = \delta\left(\sqrt{\tau S} - 2m_{\text{av}} - E_n\right) = \delta(\tau-\tau_n)\frac{2(E_n+2m_{\text{av}})}{S} \tag{9.7}$$

with $\tau_n = (E_n + 2m_{\text{av}})^2/S$, the integration over τ can be performed trivially (because it is always true that $\tau_n < \rho$) and we arrive at the following expression:

$$\sigma^{\text{BS}}_{h_1h_2\to kl}(\rho) = \sum_{i,j}\sum_{I}\sum_{n=1}^{\infty} \mathscr{L}_{ij}(\tau_n)\, \mathcal{H}^{(0)}_{ij\to kl,I} \frac{2(E_n+2m_{\text{av}})}{S} \left(\frac{\alpha_{\text{s}} \mathscr{D}_{ij\to kl,I} m_{\text{red}}}{n}\right)^3, \tag{9.8}$$

where E_n is given in eq. (4.148). It should be noted that in the definition of the luminosity function, there is still one integration to perform which, at its lower bound, depends on n through τ_n. A substitution of the integration variable to render the integration bounds independent of n leads to a final expression for bound-state contributions which can easily be implemented numerically.

The partonic cross section always contains a factor of $1/\hat{s}$, which is the flux factor for massless initial-state particles when computing the cross section $\mathrm{d}\hat{\sigma}$ from the matrix elements $\mathcal{M}$ and the phase space dPS_n,

$$\mathrm{d}\hat{\sigma} = \frac{1}{2\hat{s}} |\mathcal{M}|^2 \, \mathrm{dPS}_n. \tag{9.9}$$

In the threshold limit, this factor becomes $1/\hat{s}_{\mathrm{thr}} \approx 1/(4m_{\mathrm{av}}^2)$. To slightly improve the description of the partonic cross section near threshold, we take into account the exact flux factor by multiplying the terms of eq. (9.8) with a factor $4m_{\mathrm{av}}^2/\hat{s} = 4m_{\mathrm{av}}^2/(\tau_n S)$ to obtain:

$$\begin{aligned}\sigma^{\mathrm{BS,imp}}_{h_1h_2\to kl}(\rho) &= \sum_{i,j}\sum_{I}\sum_{n=1}^{\infty} \mathscr{L}_{ij}(\tau_n)\,\frac{4m_{\mathrm{av}}^2}{\tau_n S}\,\mathcal{H}^{(0)}_{ij\to kl,I}\,\frac{2(E_n+2m_{\mathrm{av}})}{S}\left(\frac{\alpha_{\mathrm{s}}\mathscr{D}_{ij\to kl,I}m_{\mathrm{red}}}{n}\right)^3 \\ &= \sum_{i,j}\sum_{I}\sum_{n=1}^{\infty} \mathscr{L}_{ij}(\tau_n)\,\mathcal{H}^{(0)}_{ij\to kl,I}\,\frac{8m_{\mathrm{av}}^2}{(E_n+2m_{\mathrm{av}})S}\left(\frac{\alpha_{\mathrm{s}}\mathscr{D}_{ij\to kl,I}m_{\mathrm{red}}}{n}\right)^3.\end{aligned} \tag{9.10}$$

It should be noted that in the sum over the colour channels I, only channels correspond to an attractive Coulomb potential, $\mathscr{D}_{ij\to kl,I} > 0$, are summed over. The bound-state contributions below threshold are then added to the $\mathrm{NNLO}_{\mathrm{Approx}}$+NNLL predictions including Coulomb resummation in the Mellin-moment space formalism above threshold.

9.3 Choice of the scale

The relevant scale for bound-state effects is related to the Bohr radius r_B of the corresponding bound states. The latter can be computed from finding the radius of the minimal total energy corresponding to the Hamiltonian eq. (4.127), and is for a LO Coulomb potential:

$$r_B = \frac{1}{m_{\mathrm{red}}\left|\mathscr{D}_{ij\to kl,I}\right|\alpha_{\mathrm{s}}}. \tag{9.11}$$

The Bohr scale is now defined as twice the inverse Bohr radius,

$$\mu_B^{[I]} := \frac{2}{r_B} = 2m_{\mathrm{red}}\left|\mathscr{D}_{ij\to kl,I}\right|\alpha_{\mathrm{s}}\left(\mu_B^{[I]}\right), \tag{9.12}$$

where α_{s} is evaluated at the Bohr scale itself, requiring this equation to be solved iteratively. It should be noted that the Bohr scale depends on the colour channel. Eq. (9.12) defines the scale which is used for the bound-state contributions, eq. (9.10). We note that in eq. (9.10), the α_{s} factors of $\mathcal{H}^{(0)}_{ij\to kl,I}$, stemming from the off-shell interactions, are evaluated at the usual

value renormalisation scale μ_R close to the typical hard scale $\sim m_{\text{av}}$ of the process, whereas the α_s factors originating from the Green's function are evaluated at the Bohr scale as defined in eq. (9.12) for the colour channels where $\mathscr{D}_{ij\to kl,I} > 0$. The Bohr scale has already been used in previous studies, see refs. [122, 123, 136, 175, 216]

As argued in refs. [122, 123] using momentum power-counting of the Coulomb gluons and also by analysing the scale dependence of the terms in eq. (4.138), the natural scale of Coulomb interactions turns out to be

$$\mu_C \sim 4m_{\text{red}}v \approx 2\sqrt{2m_{\text{red}}m_{\text{av}}}\beta = 2\sqrt{m_k m_l}\beta \tag{9.13}$$

in order to minimise the effect of a residual higher-order scale dependence from a truncation of the perturbative expansion of α_s. The Coulomb scale appears both explicitely in the Green's function as well as in the factors of α_s. Such a scale choice also leads to the inclusion of some of the mixed soft $\ln(\beta)$ and Coulomb $1/\beta$ terms such as $\alpha_s \ln(\beta) \times \alpha_s/\beta$, which are formally of NLL accuracy [122]. The scale choice of eq. (9.13) needs to be bounded from below, since, besides hitting the Landau pole when β is integrated over, bound-state effects become important in the vicinity of the threshold. Therefore, we use the Bohr scale of eq. (9.12) to bound the Coulomb scale from below. While bound states only arise for an attractive Coulomb potential, $\mathscr{D}_{ij\to kl,I} > 0$, we also use the Bohr scale as a lower boundary for a repulsive potential, which is not completely justified, but leads to negligible effects for the total cross section above threshold [123]. The Coulomb scale is consequently chosen to be:

$$\mu_C := \max\left\{\mu_B^{[I]}, 2\sqrt{m_k m_l}\beta\right\}, \tag{9.14}$$

which ensures that, as soon as the bound-state effects become relevant, the Bohr scale is used.

We stress that eq. (9.12) is used for the contributions below threshold, while eq. (9.14) applies to the contributions above threshold.

9.4 Numerical results and comparison to SCET

The parameters for the numerical evaluation have been chosen equal to those in sections 7.3 and 8.3. We again use the MSTW2008 PDF set, with NLO PDFs for results at NLO and NLO+NLL accuracy, and NNLO PDFs for results at $\text{NNLO}_{\text{Approx}}$+NNLL accuracy. We present our predictions at a collider energy of $\sqrt{S} = 8$ TeV to simplify comparisons to the results of ref. [134] which were computed in the SCET formalism.

We will show predictions for the $\text{NNLO}_{\text{Approx}}$+NNLL accuracy presented in chapters 7 (corresponding to "NNLL matched") and 8 with additional contributions from Coulomb resummation with a NLO Coulomb potential ("Coul") and bound states ("BS"). We also show some results of the plots from ref. [134], namely "NNLL (SCET)" which corresponds to the currently best result within the SCET formalism for squark and gluino production, including the soft exponentials up to NNLL, one-loop hard-matching coefficients, Coulomb resummation with a NLO Coulomb potential, bound states, and matching to $\text{NNLO}_{\text{Approx}}$,

as well as "$\text{NNLL}_{\text{fixed}-C}$ (SCET)" which is the same as above, however with the Coulomb contributions expanded up to $\mathcal{O}(\alpha_s^2)$. Comparing our predictions in the Mellin-moment space formalism to the SCET formalism, "$\text{NNLO}_{\text{Approx}}$+NNLL+Coul+BS" corresponds to "NNLL (SCET)" and "$\text{NNLO}_{\text{Approx}}$+NNLL" roughly corresponds to "$\text{NNLL}_{\text{fixed}-C}$ (SCET)"; this is no exact correspondence, as there are the following differences between our predictions and the ones from ref. [134]:

- The SCET formalism has more scales that can be varied independently. In particular the soft scale can be chosen independently, while it is fixed to the value Q/N in the Mellin-moment space formalism.
- The authors of ref. [134] convolute the bound-state contributions with their soft function as described in ref. [217]. This is not doable in the same manner in the Mellin-moment space formalism. Furthermore, they also include bound-state effects from a NLO Coulomb potential, causing a small shift in the bound-state energies and residues, while we only include bound-state effects originating from a LO potential.
- The SCET results include a constant term to account for unknown NNLO corrections beyond the threshold limit, while we set the two-loop hard-matching coefficient to zero.

It is of much interest to see how well the two independent approaches of threshold resummation agree, and how much the contributions which are subleading in the threshold limit and in which the two formalisms differ play a role.

Figure 9.1 shows the K-factor as defined in eq. (6.4) for the above-mentioned accuracies. We first focus on the impact of Coulomb resummation and bound-state contributions, and will then compare to the SCET results. We see that for all processes of squark and gluino production, the impact of including Coulomb resummation is small, implying that the inclusion of the second-order Coulomb corrections already account for the dominant terms. The largest impact of Coulomb resummation can be seen for $\tilde{g}\tilde{g}$ and $\tilde{q}\tilde{q}^*$ where the effect of the Coulomb terms beyond second order, being roughly independent of the mass, is a few percent in the K-factor, whereas for $\tilde{q}\tilde{g}$, $\tilde{q}\tilde{q}$, and $\tilde{t}\tilde{t}^*$ it is below a percent. The bound-state contributions can contribute quite significantly again for $\tilde{g}\tilde{g}$ and $\tilde{q}\tilde{q}^*$ in particular, with an effect at high masses of up to 20% and 10%, respectively, and $\tilde{t}\tilde{t}^*$ with approximately 1% for the whole mass range, while for the other two processes, the bound-state contributions are negligibly small. This is in partial agreement with ref. [123], where bound-state contributions have been found to be largest for $\tilde{g}\tilde{g}$ and $\tilde{q}\tilde{q}^*$ and very small for $\tilde{q}\tilde{q}$. The exception is $\tilde{q}\tilde{g}$, where our results show that bound-state contributions are negligible, while the authors of ref. [123] found that they contribute by roughly 5% to the NLL K-factor at large masses for $\sqrt{S} = 7$ TeV. It is possible that this difference to our results is however related to the difference in the implementation of the bound-state contributions, in particular the convolution with the soft function, as discussed at the beginning of this section.

Comparing our predictions to the SCET numbers, we see that, taking into account the differences at the beginning of the chapter, the best predictions "$\text{NNLO}_{\text{Approx}}$+NNLL+Coul+BS" and "NNLL (SCET)" lead to similar results and differ at most by 10-20% for $\tilde{g}\tilde{g}$ at high masses,

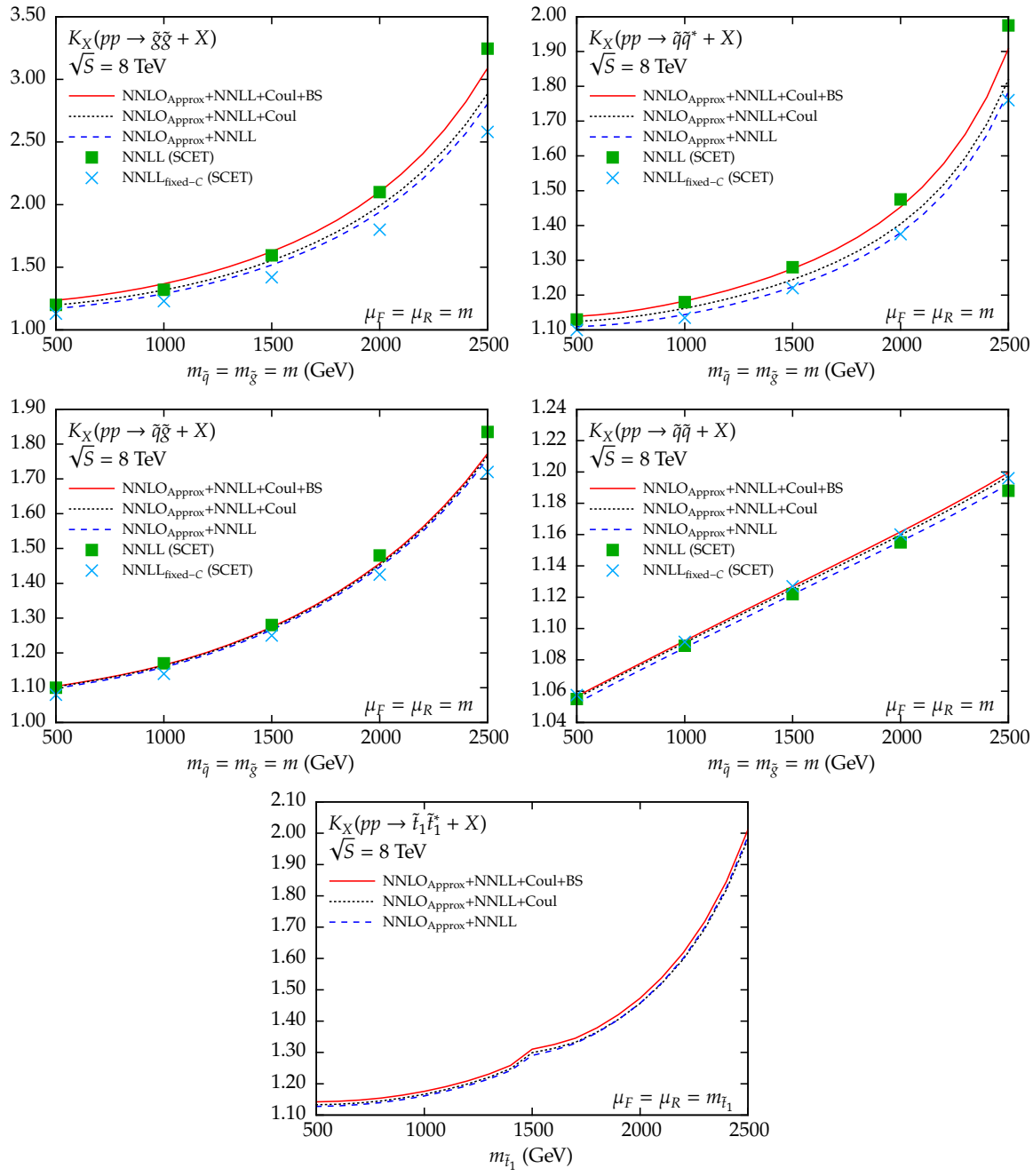

Figure 9.1: Comparison between the best results for squark and gluino production at NNLO$_{\text{Approx}}$+NNLL accuracy, including Coulomb resummation with a NLO Coulomb potential and bound states, of the Mellin-space approach and SCET, at a collider energy of $\sqrt{S}$ = 8 TeV and using MSTW2008 NNLO PDF sets. The SCET numbers are read off from the corresponding plots in [134].

while the agreement at lower masses, also for the other processes, is generally much better and within a few percent difference. While the predictions at $\text{NNLO}_{\text{Approx}}$+NNLL accuracy differ by a larger amount to "$\text{NNLL}_{\text{fixed}-C}$ (SCET)" for the two processes $\tilde{g}\tilde{g}$ and $\tilde{q}\tilde{g}$, the agreement improves when also including Coulomb resummation and bound-state contributions. It should be noted that, while we see that contributions from Coulomb resummation and bound states are generally positive, the effect of Coulomb resummation and bound states in SCET leads to a decrease of the K-factor for $\tilde{q}\tilde{q}$, which should, however, agree within the theoretical scale uncertainty, see figure 9.3.

It is also interesting to see how much impact Coulomb resummation and the bound-state contributions have on the scale dependence. In figure 9.2, we vary the scales around their central value μ_0. While for $\text{NNLO}_{\text{Approx}}$+NNLL, the only two accessible scales are the renormalisation and factorisation scales which are varied simultaneously, for Coulomb resummation and bound states, we also have the Coulomb and the Bohr scales, respectively. Thus, while for the renormalisation and factorisation scales, the central value μ_0 corresponds to the mass of the produced particles $m_{\tilde{q}} = m_{\tilde{g}} = 1200$ GeV and $m_{\tilde{t}_1} = 1085$ GeV, the central values of the Coulomb and Bohr scales are defined by eq. (9.14) and eq. (9.12), respectively, which we vary up and down by a factor of 5 simultaneously. While there is no impact of Coulomb resummation and bound-state contributions for $\tilde{q}\tilde{q}$ and only a small impact for $\tilde{q}\tilde{g}$ and $\tilde{t}\tilde{t}^*$ in particular for very low and very high scales, the scale dependence changes more clearly for $\tilde{g}\tilde{g}$ and $\tilde{q}\tilde{q}^*$, in particular at low scales. First, adding Coulomb resummation to $\text{NNLO}_{\text{Approx}}$+NNLL shifts the scale dependence up for high scales and down for low scales. Then, bound states raise the cross sections at low scales, by a significant amount for $\tilde{g}\tilde{g}$. This is due to the low value of the Bohr scale at which the factors of α_s are evaluated, with α_s changing more rapidly at low scales, in addition to the large logarithmic contributions and colour factors for gluinos in the final state. Compared to the scale dependence at NLO and NLO+NLL accuracy, the new ingredients at NNLL accuracy lead to a significantly different behaviour for all processes.

The plots of figure 9.2 are not available for the SCET results, where a comparison would be difficult anyway due to the larger amount of scales which can be varied independently for SCET than for the Mellin-moment space approach. We however look in figure 9.3 at the dependence of the scale uncertainty, evaluated from varying the central values of all appearing scales up and down by a factor of 2, from the mass of the produced particles. We furthermore adopt for $\tilde{g}\tilde{g}$, $\tilde{q}\tilde{q}^*$, and $\tilde{q}\tilde{q}$ unequal squark and gluino masses, as denoted in the plots, to enable us to compare to the SCET results of ref. [134]. We see that for all processes except for $\tilde{g}\tilde{g}$ and also $\tilde{t}\tilde{t}^*$ at high masses, the $\text{NNLO}_{\text{Approx}}$+NNLL scale uncertainty is smaller than the one of NLO+NLL. The inclusion of Coulomb resummation and bound-state contributions only lead to a slight improvement for $\tilde{g}\tilde{g}$ (with the contributions from Coulomb resummation alone actually worse the scale dependence slightly), while for $\tilde{q}\tilde{q}^*$ and $\tilde{t}\tilde{t}^*$, the effects of Coulomb resummation and bound states mainly cancel themselves, leading to a similar scale uncertainty as for $\text{NNLO}_{\text{Approx}}$+NNLL. As it was seen in figure 9.2, the scale dependence slightly increases for $\tilde{q}\tilde{g}$, while it is negligibly affected by Coulomb resummation and bound states for $\tilde{q}\tilde{q}$. The special process of $\tilde{t}\tilde{t}^*$ shows that above a stop mass of approximately 1500 GeV, which corresponds to the gluino mass in the benchmark scenario,

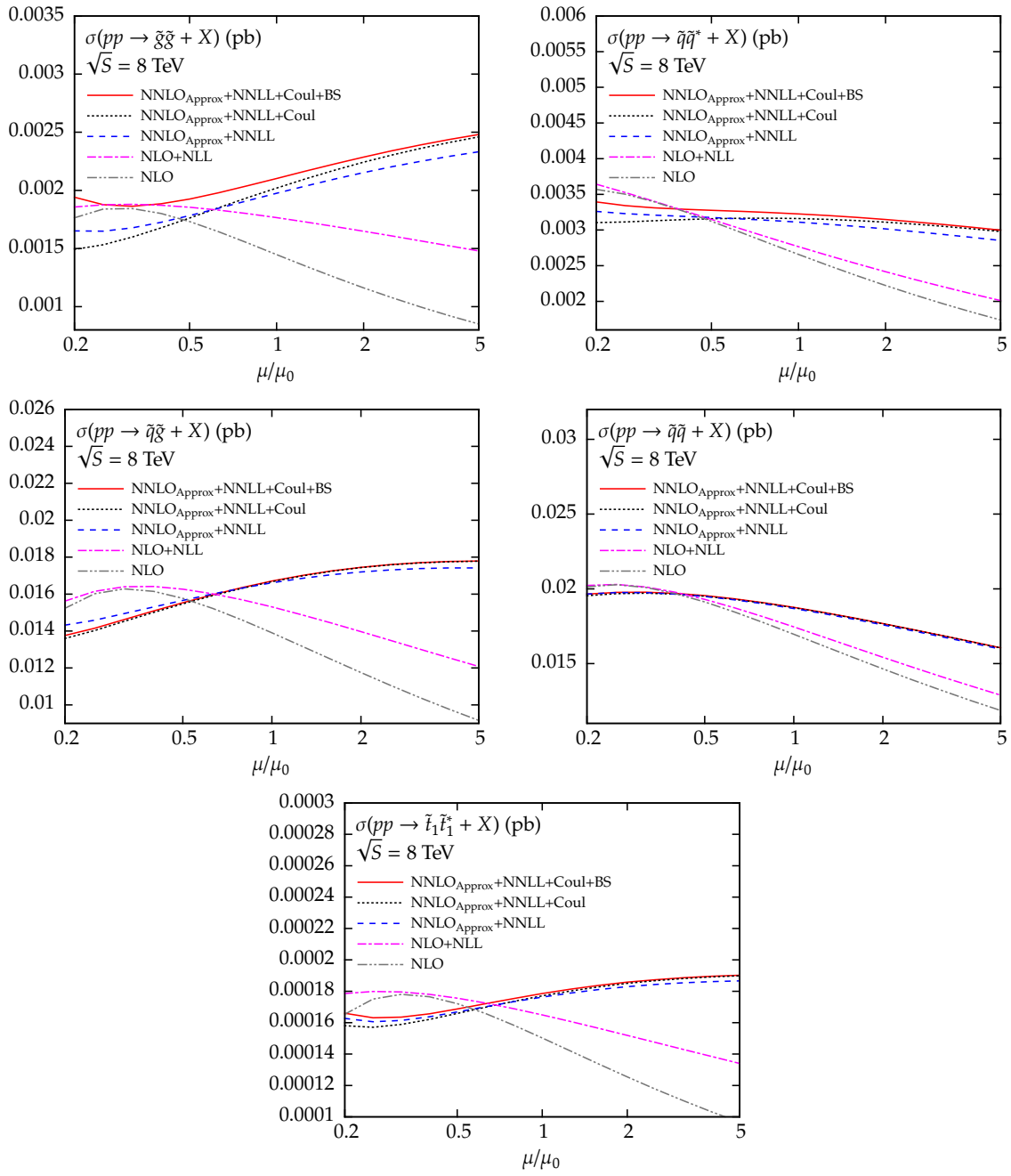

Figure 9.2: Scale dependence of the cross sections at NNLO$_{\text{Approx}}$+NNLL accuracy, also including Coulomb resummation with a NLO Coulomb potential and bound-state contributions. The renormalisation and factorisation scales are set equal, all appearing scales are varied up and down by a factor of 5 with respect to their central scale values.

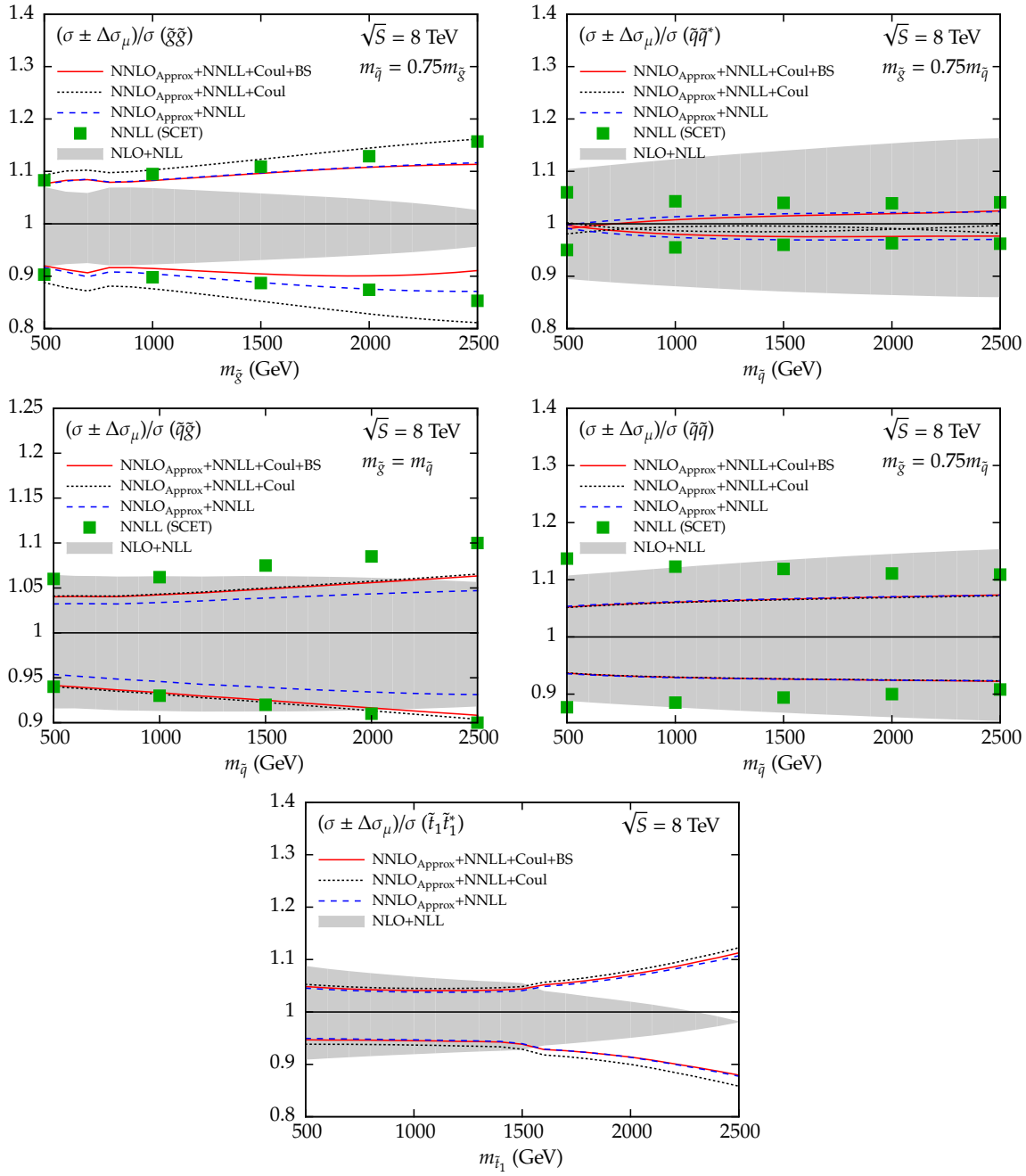

Figure 9.3: Mass dependence of the scale uncertainty for the NNLO$_{\text{Approx}}$+NNLL accuracy, including Coulomb resummation and bound states, when varying all scales around their central values up and down by a factor of two. All lines are normalised to their corresponding central values. Additionally, the scale uncertainties of NLO+NLL and the SCET formalism are shown.

the scale dependence for $\text{NNLO}_{\text{Approx}}$+NNLL starts to increase with an increasing stop mass, while the NLO+NLL scale dependence becomes very small at high stop masses. This very small scale uncertainty of NLO+NLL should be regarded with precaution, as it is related to the turn-over point of the scale dependence moving towards the central value of the scale for higher masses, as discussed in section 8.3.2 in the accompanying text to figure 8.6. We stress that the increased scale dependence in some cases can also be explained from the introduction of the Bohr scale for the bound states and the Coulomb scale which have not been used for the predictions at NLO+NLL and $\text{NNLO}_{\text{Approx}}$+NNLL accuracy.

Lastly, when comparing our results to SCET, we see a reasonable agreement in the scale uncertainty, with our results enveloped inside the "NNLL (SCET)" uncertainty band. This is expected, as the additional variation of the soft scale which is present in SCET will in general lead to a larger scale uncertainty. Figures 9.1, 9.2, and 9.3 have shown that results obtained in the two independent methods of carrying out threshold resummation in Mellin-moment space and using SCET leads to compatible results, with the agreement between the two approaches being improved at $\text{NNLO}_{\text{Approx}}$+NNLL accuracy including Coulomb resummation and bound states.

10 Double Parton Scattering for J/ψ-Pair Production

An important ingredient in searches for SUSY particles at the LHC is the correct determination of background from the Standard Model. With increasing collider energy, the so-called *underlying event*, denoting everything which happens next to the primary hard scattering process, becomes more probable. One contribution to the underlying event comes from multi-parton interactions (MPI), those are additional scattering processes of partons from the same collision of protons next to the primary scattering. In particular, double parton scattering (DPS), where two distinct parton interactions arise from the same proton-proton collision, can become likely enough to compete with the usual single parton scattering (SPS) processes, see figure 10.1. Therefore, a thorough understanding of these additional contributions is needed for a precise theoretical description of the background at the LHC and will also help to explore the inner structure of protons and nucleons, not being accessible by perturbative calculations.

Double parton scattering has been searched for both in pre-LHC experiments like AFS, UA2, CDF, and D0 as well as by the LHCb and ATLAS collaborations, in 4-jet [218–220], γ + 3-jet [221–223], W + 2-jets [224], J/ψ + W [225], 4-charm [226], J/ψ+charm [226], and J/ψ + J/ψ [227] final states. Both on the theoretical as well on the experimental side, a lot of progress is being made to uncover the structure of DPS [228], in particular the correlations and interference between the two hard scatterings, the latter which are often assumed to be independent.

The work presented in this chapter serves as an update to previous studies of J/ψ pair-production done in ref. [229], which were performed as a response to experimental results presented in ref. [230], now including updated fiducial volumes for ongoing analyses by the LHCb and ATLAS experiments. A J/ψ pair is a very good candidate to study double parton scattering as its subsequent decay into muons gives a clear and easily distinguishable signal. Results for the production of J/ψ pairs have been published by LHCb in ref. [230], by D0 in ref. [227], and by CMS in ref. [231].

The authors of ref. [229] included effects from *parton showering* or *initial-state radiation*. This is in a certain sense similar to the resummation of soft gluons up to all orders in

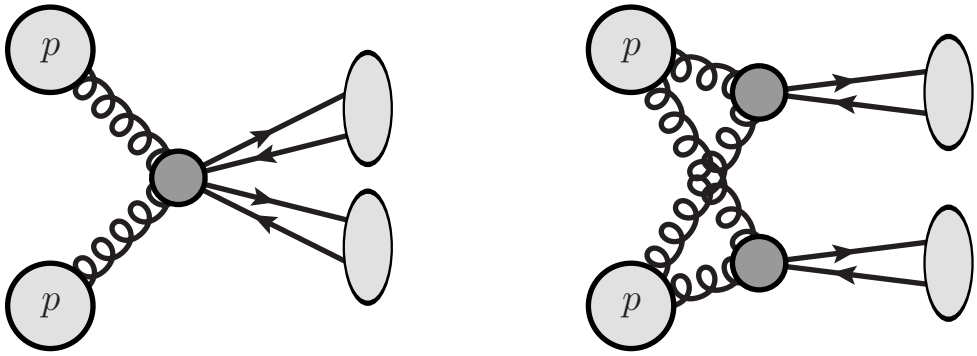

Figure 10.1: Schematical representation of SPS (left) and DPS (right) for a proton-proton collision. Whereas in the SPS case, the two final-state particles (grey ellipses) originate from the same scattering process (dark grey circle), in the DPS case, two scattering processes of two independent partons from each proton occur.

perturbation theory. Contrary to the fully analytical resummation requiring information about the structure of the process, parton showers offer a numerical and more manageable way of including soft-gluon emission at LL and partially also NLL accuracy up to all orders in α_s in an arbitrary process. The technique of parton showers relies on unitarity, which is why parton showers do not affect the total cross section, if no parameter cuts are taken into account. It however changes the shape of distributions such as for the transverse momentum of the final-state particle system.

We will start with describing the theoretical setup used in ref. [229] both for the SPS and DPS cross section calculations. Afterwards, we show numerical results for total cross sections and the kinematic distributions for a choice of experimentally accessible variables.

10.1 Theoretical setup

The calculation of conventional single parton scattering contributions to J/ψ pair-production is non-trivial and requires specific methods to account for the non-perturbative mechanisms involved in meson production. Two widely applied methods are the colour-singlet model (CSM) [232–234] and non-relativistic quantum chromodynamics (NRQCD) [235]. Full NLO and partial NNLO contributions in the CSM framework have been studied in ref. [236,237], as well as the impact of colour-octet contributions. Here, the SPS contributions will be considered utilising a leading-order (LO) colour-singlet result presented in ref. [238] and including radiative corrections from parton showering. In the following section, the calculation of the DPS contributions will be outlined.

10.1.1 Factorisation approach for double parton scattering

DPS production of a J/ψ-pair is described using an approximation in which the DPS cross section factorises into a product of two hard-scattering cross sections describing single-J/ψ

production which are independent from each other:

$$\mathrm{d}\sigma^{2J/\psi}_{\mathrm{DPS}} = \frac{\mathrm{d}\sigma^{J/\psi}_{\mathrm{SPS}}\,\mathrm{d}\sigma^{J/\psi}_{\mathrm{SPS}}}{2\sigma_{\mathrm{eff}}}. \tag{10.1}$$

The SPS cross section for single-J/ψ production is given as

$$\mathrm{d}\sigma^{J/\psi}_{\mathrm{SPS}} = \sum_{i,j} f_i(x_i, \mu_F^2)\, f_j(x_j, \mu_F^2)\, \mathrm{d}\hat{\sigma}^{J/\psi}_{\mathrm{SPS}}\, \mathrm{d}x_i\, \mathrm{d}x_j \tag{10.2}$$

with a sum over the initial state flavours i, j and the parton distribution functions $f_i(x_i, \mu_F^2)$ and

$$\mathrm{d}\hat{\sigma}^{J/\psi}_{\mathrm{SPS}} = \sum_{a,b} \frac{1}{2\hat{s}} \overline{|\mathcal{M}_{ab\to J/\psi+X}|^2}\, \mathrm{dPS}_{J/\psi+X} \tag{10.3}$$

the partonic cross section for single J/ψ production with the corresponding matrix elements $\mathcal{M}_{ab\to J/\psi+X}$ and the phase space $\mathrm{dPS}_{J/\psi+X}$. X denotes any additional final state which is not a J/ψ, and therefore not of interest for J/ψ production. The factor σ_{eff} is assumed to only depend on the transverse structure of the proton, and should therefore be process and energy independent if the factorisation of eq. (10.1) holds. It is the main quantity to be extracted by a DPS experiment. A study of γ + 3-jet production by CDF suggests a value of $\sigma_{\mathrm{eff}} = 14.5 \pm 1.7^{+1.7}_{-2.3}$ mb [222], whereas a more recent double-J/ψ study by D0 reports a lower value of $4.8 \pm 0.5 \pm 2.5$ mb [227], suggesting that the observed discrepancy could be related to the different dominant inital states for the corresponding process.

Single-J/ψ production is not well described by fixed-order calculations [239–246] at low transverse momentum p_T, as it requires non-perturbative methods. Therefore, the same setup as in ref. [229] is used, and shall be reminded here. The matrix element as in eq. (10.3) is given by:

$$\overline{|\mathcal{M}_{ab\to J/\psi+X}|^2} = \begin{cases} K \exp\left(-\kappa \frac{p_T^2}{m^2_{J/\psi}}\right) & \text{for } p_T \le \langle p_T \rangle \\ K \exp\left(-\kappa \frac{\langle p_T\rangle^2}{m^2_{J/\psi}}\right)\left[1 + \frac{\kappa}{n}\frac{p_T^2 - \langle p_T\rangle^2}{m^2_{J/\psi}}\right]^{-n} & \text{for } p_T > \langle p_T \rangle, \end{cases} \tag{10.4}$$

which describes a fit of data from the LHCb [247], ATLAS [248], CMS [249], and CDF [250] experiments to a Crystal Ball function. In eq. (10.4), $K = \lambda^2 \kappa \hat{s}/m^2_{J/\psi}$, and the fit parameters are determined to be $\kappa = 0.6$ and $\lambda = 0.327$ for $n = 2$ and $\langle p_T \rangle = 4.5$ GeV.

10.2 Monte Carlo simulation

The public Monte Carlo event generator `Herwig++-2.7.1` [251] has been used to simulate J/ψ production at the LHC using MSTW2008 LO and MSTW2008 NLO parton distribution functions [20]. The factorisation scale is chosen as the transverse mass of a single J/ψ, $\mu_F =$

$m_T = \sqrt{m_{J/\psi}^2 + p_T^2}$. The J/ψ mesons are assumed to decay isotropically into a pair of opposite-sign (OS) muons with a branching ratio of BR($J/\psi \to 2\mu$) = 0.05935. Out of the two possible combinations of choosing OS muon pairs, the one with an invariant mass closest to the physical J/ψ mass $m_{J/\psi} = 3.096$ GeV is chosen. From these pairs, all properties of the J/ψ are reconstructed. To optimise the data samples collected by the experiments for a DPS analysis, a certain set of cuts on transverse momentum and (pseudo)rapidity of the J/ψ as well as their decay products are applied.

One parameter appearing in the calculation of the SPS cross section of ref. [238] is the charm quark mass which we set to $m_c = m_{J/\psi}/2$. Another input parameter entering the SPS calculation is the non-perturbative wave function of the J/ψ meson at the origin. In the following computations, it will be set to $|R(0)|^2 = 0.92\ \text{GeV}^3$. It should be noted that a variation of this parameter can be achieved by multiplying the SPS cross section by a factor of $\left(|R(0)_{\text{new}}|^2/|R(0)|^2\right)^2$, where $|R(0)_{\text{new}}|^2$ is the new value of the wave function. Similarly, the value of σ_{eff} enters the DPS calculation and can be changed by multiplying the DPS cross section with a factor of $\sigma_{\text{eff}}/\sigma_{\text{eff,new}}$.

As it was pointed out in ref. [237], the prompt production of J/ψ mesons comprises feed-down from the decay of χ_c and ψ' at a non-negligible amount of roughly 85%. The SPS calculation of ref. [238] is for direct production of J/ψ pairs only, so in the following, all SPS cross sections will be considered for prompt production, $\sigma^{\text{prompt}} = 1.85 \times \sigma^{\text{direct}}$. The DPS results implicitely include feed-down contributions due to the fit to experimental data.

10.2.1 LHCb cuts

The LHCb experiment, being a forward spectrometer, mainly selects events in the forward scattering region with low transverse momentum. The cuts are[1]:

- $p_{T,J/\psi} < 10$ GeV,
- $2 < y_{J/\psi} < 4.2$,

with $p_{T,J/\psi}$ being the transverse momentum and $y_{J/\psi}$ the rapidity of one J/ψ. Any further cuts on the muons as the decay products of the di-J/ψ are not relevant for the theoretical predictions presented in this work, as they are already taken into account in the efficiency correction of the data.

10.2.2 ATLAS cuts

The ATLAS experiment probes the J/ψ in the central region imposing a minimum transverse momentum and a more central rapidity region. Additionally, several cuts are also applied to the muons[2]:

1) $p_{T,J/\psi} > 8.5$ GeV,

[1] From private communications with Andrew Cook.
[2] From private communications with Ben Weinert.

σ in pb	LO	LO (NLO PDFs)	PS+σ(2 GeV)	DPS
LHCb (7 TeV)	74.8	11.0	11.4	12.1
ATLAS (7 TeV)	8.25×10^{-3}	2.70×10^{-3}	3.89×10^{-3}	4.01×10^{-3}
LHCb (8 TeV)	84.8	11.9	12.4	14.4
ATLAS (8 TeV)	9.55×10^{-3}	3.03×10^{-3}	4.44×10^{-3}	5.12×10^{-3}
LHCb (13 TeV)	133	15.5	16.1	25.5
ATLAS (13 TeV)	16.0×10^{-3}	4.48×10^{-3}	6.98×10^{-3}	12.0×10^{-3}

Table 10.1: Total cross sections for SPS and DPS production of a J/ψ pair for different centre-of-mass energies and cuts. The first column (LO) is computed with the MSTW2008 LO PDF set, whereas the remaining three columns are computed with the MSTW2008 NLO PDF set. All numbers include the branching ratio factor of $\mathrm{BR}^2(J/\psi \to 2\mu)$.

2) $|y_{J/\psi}| < 2.1$,

3) $p_{T,\mu} > 2.5$ GeV,

4) $|\eta_\mu| < 2.3$,

5) at least 1 J/ψ with both $p_{T,\mu} > 4$ GeV,

with $p_{T,\mu}$ being the transverse momentum and η_μ the pseudorapidity of one muon.

10.3 Cross sections and kinematic distributions

Table 10.1 and figure 10.2 show the total cross sections for SPS and DPS production of J/ψ pairs with the LHCb and the ATLAS cuts at different centre-of-mass energies. First of all, it can be seen in table 10.1 that the switch from LO to NLO PDFs causes the cross sections to become significantly smaller. Despite the calculation for SPS J/ψ production being of LO, we use NLO PDFs due to the inclusion of higher-order effects from parton showering. Furthermore, while the LHCb cuts only moderately affect the total cross section when adding parton showering and intrinsic p_T of the partons to the LO calculation, the total cross section for the ATLAS cuts increases due to parton showering and intrinsic p_T by a factor of approximately 1.5 for both centre-of-mass energies. From figure 10.2, it can clearly be see that, while at 7 and 8 TeV, the SPS and DPS contributions are of roughly the same size, the DPS contributions grow more rapidly with increasing collider energy, and will be larger by almost a factor of 2 with respect to the SPS cross sections at 13 TeV. This is important for the current LHC run, as it shows that DPS processes will occur more prevalently and that they will be more easily distinguishable from SPS.

Another thing to note is the large difference in magnitude of the LHCb and ATLAS values, being much smaller in the case of the predictions for ATLAS. We checked that mainly cut no. 5 of section 10.2.2, requiring both muons that stem from the same decay of one J/ψ to have

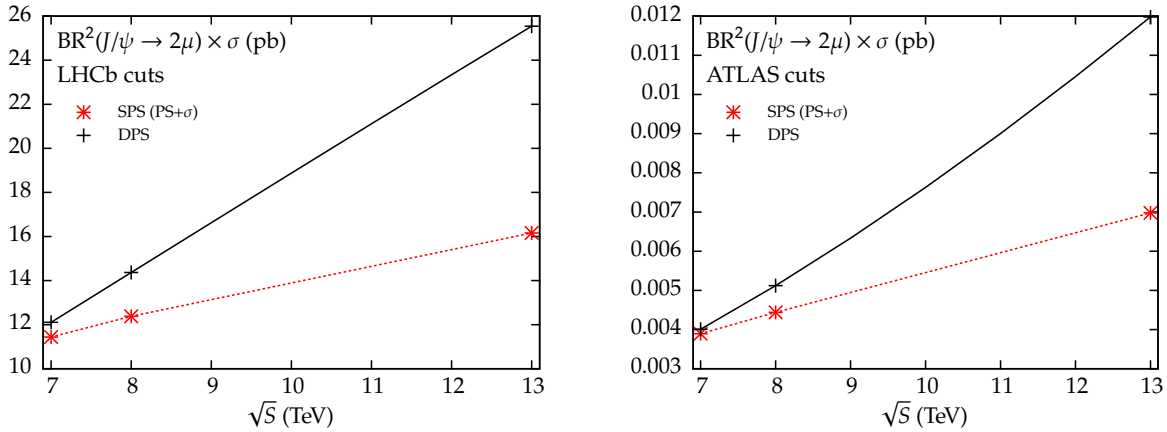

Figure 10.2: Total cross section dependence of the centre-of-mass energy of the collider for the LHCb (a) and the ATLAS cuts (b). Shown are the SPS prediction with parton showering and intrinsic transverse momentum of the partons, and the DPS contribution. The lines for SPS are interpolated between the points.

$p_{T,\mu} > 4$ GeV, and to a lesser amount cut no. 1, requiring each J/ψ to have a $p_{T,J/\psi} > 8.5$ GeV, lower the cross section values significantly.

Since for DPS, the fit to the Crystal Ball function has been performed including Tevatron and 7 TeV LHC data, we checked that for the available measurement of single-J/ψ production at 13 TeV from the LHCb experiment [252] with $\sigma^{J/\psi}_{\text{exp}} = 15.30 \pm 0.03 \pm 0.86$ µb, the fit parameters still produce results at 13 TeV consistent with the LHCb measurement, $\sigma^{J/\psi}_{\text{fit}} = 15.83$ µb.

10.3.1 LHCb predictions

The LHCb collaboration made a first measurements of double-J/ψ production over four years ago with data collected at a centre-of-mass energy of $\sqrt{S} = 7$ TeV [230]. They found a total cross section of $\sigma^{2J/\psi}_{\text{exp}} = 5.1 \pm 1.0 \pm 1.1$ nb in the fiducial volume defined by the rapidity range $2 < y_{J/\psi} < 4.5$ and a maximum transverse momentum $p_{T,J/\psi} < 10$ GeV. Despite the slightly changed fiducial volume in regard to the rapidity of the J/ψ, our result for SPS with parton showering and intrinsic transverse momentum added to DPS agrees with the experimental measurement within errors. The previous theoretical study in ref. [229] analysed these results and concluded that it is possible to separate the DPS component from the data by using correlations in the longitudinal direction of the J/ψ and imposing constraints on a minimum rapidity separation. In this section, we analyse the updated fiducial volume as defined by the cuts in section 10.2.1.

In figure 10.3, a selection of four differential distributions is shown: invariant mass, transverse momentum of the di-J/ψ system, azimuthal angular separation, and rapidity separation. Shown are predictions for SPS production including only parton showering/initial-state radiation (PS) and both initial-state radiation as well as intrinsic transverse momentum of the initial-state partons (PS+σ). The DPS predictions are calculated as outlined in section 10.1.1.

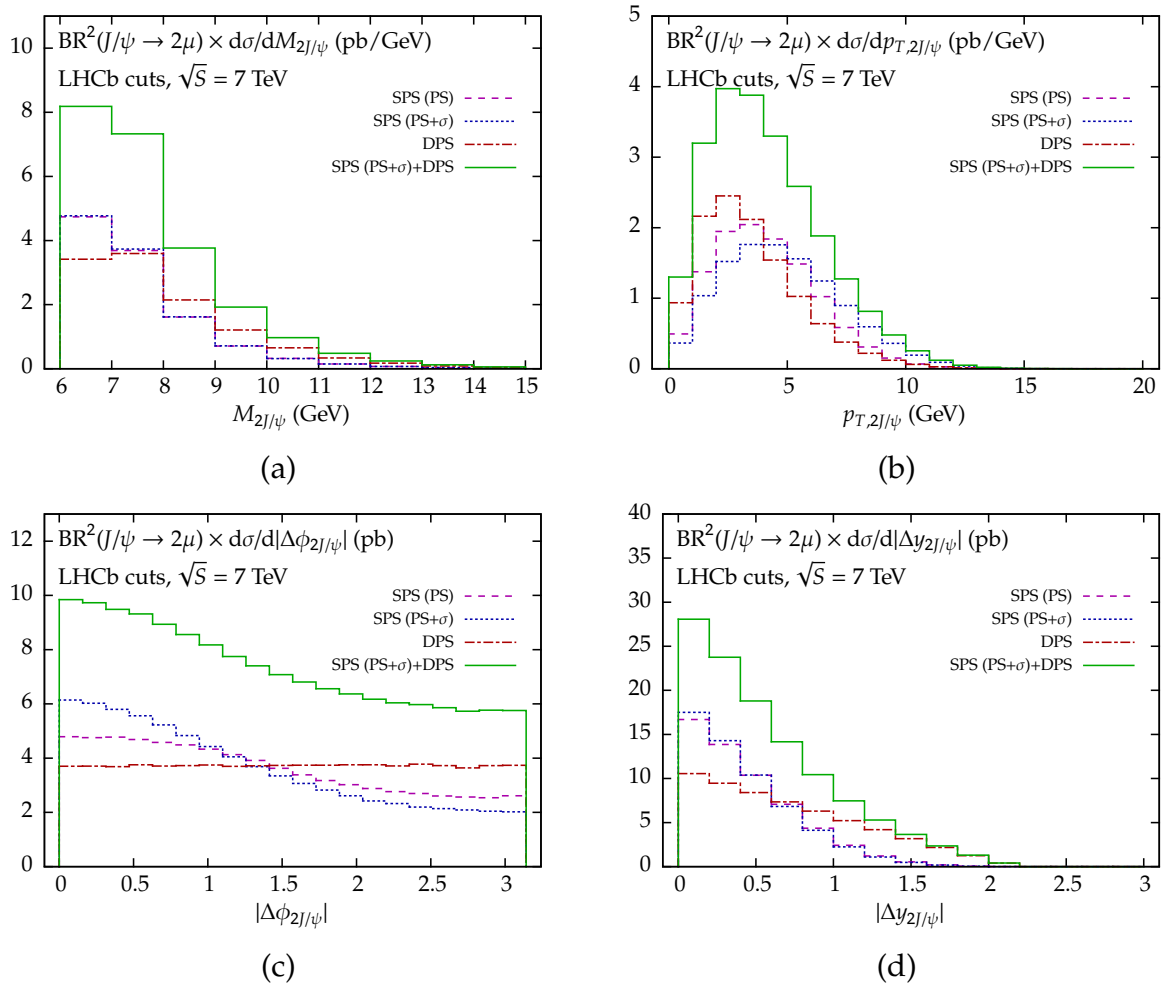

Figure 10.3: Differential distributions for the LHCb cuts at a collider energy of $\sqrt{S} = 7$ TeV. Shown are the invariant mass spectrum (a), the transverse momentum of the di-J/ψ system (b), the azimuthal angular separation (c), and the rapidity separation (d) for various SPS and DPS predictions, see the accompanying text for an explanation of the lines.

It can be seen that the DPS contributions make up a significant part of the full signal+background predictions (denoted by SPS (PS+σ)+DPS), and is comparable in size with the SPS background. In particular, for the invariant mass and p_T spectra of the di-J/ψ system, figures 10.3 (a) and (b), the DPS contribution makes up the major part at intermediate-high $M_{2J/\psi}$ and low $p_{T,2J/\psi}$. Apart from roughly the similar size of SPS and DPS contributions, it is difficult to differentiate the DPS signal from the background also in terms of the shape of these two distributions. The azimuthal angular separation between the two J/ψ mesons, shown in figure 10.3 (c), is not very well suited either for this distinction, as the DPS signal shows a uniform distribution in the transverse direction, which, although strongly differing from the pure SPS LO result only allowing back-to-back scattering (not shown here, see ref. [229] for the corresponding histogram), is made less significant by higher-order radiation strongly distorting the SPS background, even peaking towards no angular separation at all. We found that this is due to the upper p_T cut applied to both J/ψ mesons. As it was noted in

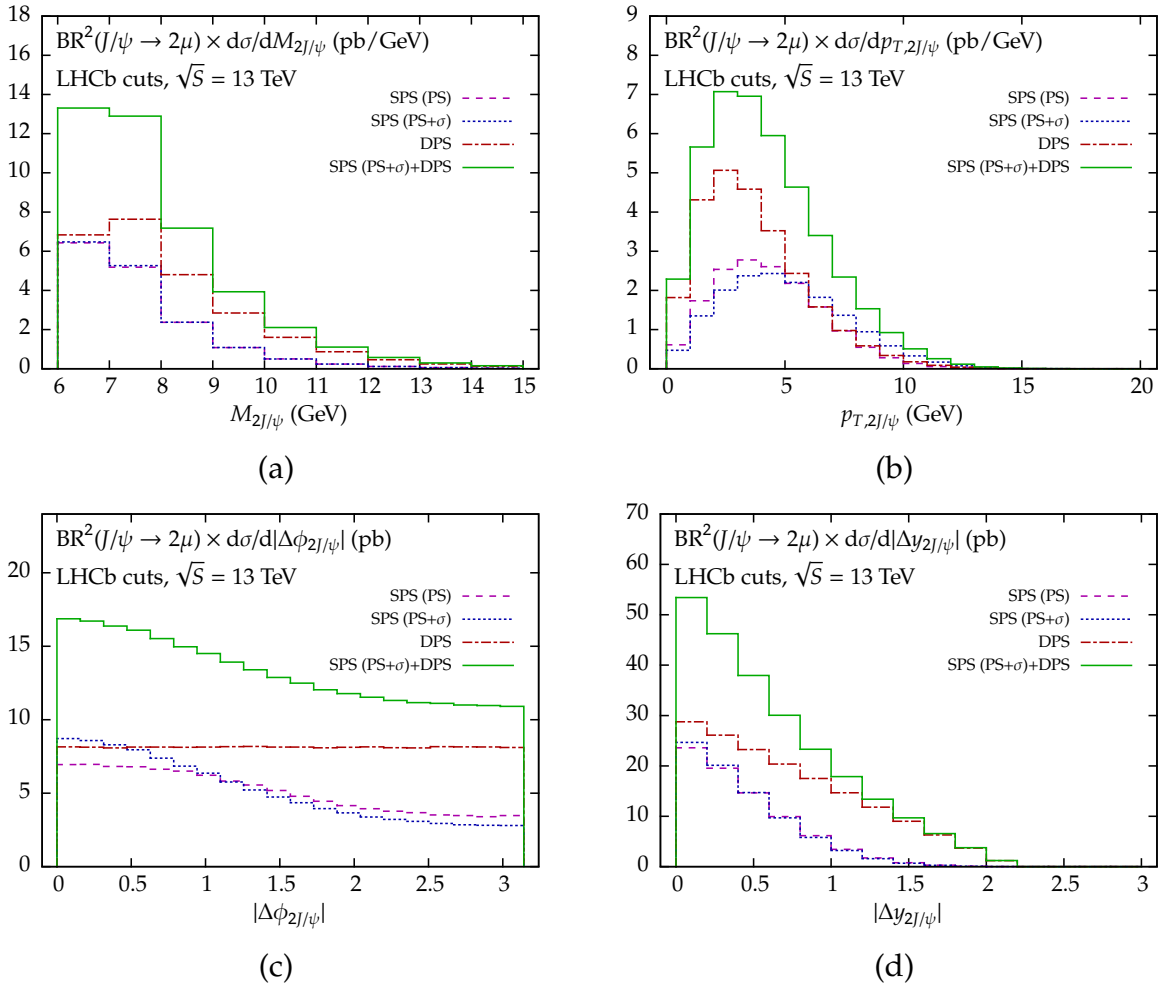

Figure 10.4: Differential distributions for the LHCb cuts at a collider energy of $\sqrt{S}$ = 13 TeV. The distributions are the same as for figure 10.3.

ref. [229], an analysis of the longitudinal components such as the rapidity separation between the two J/ψ in figure 10.3 (d) leads to more conclusive results, because at a high rapidity separation, the full signal+background predictions are primarily made up by the DPS signal with almost no SPS background expected.

The new fiducial volume with a slightly lower maximum rapidity of a J/ψ does not change the results significantly compared to the ones in ref. [229]. We note that, while in ref. [229], also muon cuts have been taken into account, our results do not include muon cuts, but prompt J/ψ production, increasing the SPS numbers by a factor of 1.85 with respect to direct J/ψ production. Thus, while the absolute values of the cross sections differ, the shapes of the distributions stay approximately the same.

10.3.1.1 Predictions at 13 TeV

At a collider energy of 13 TeV, shown in figure 10.4, we see that the DPS contributions now dominate over SPS in almost all of the bins in the distributions. While the invariant mass

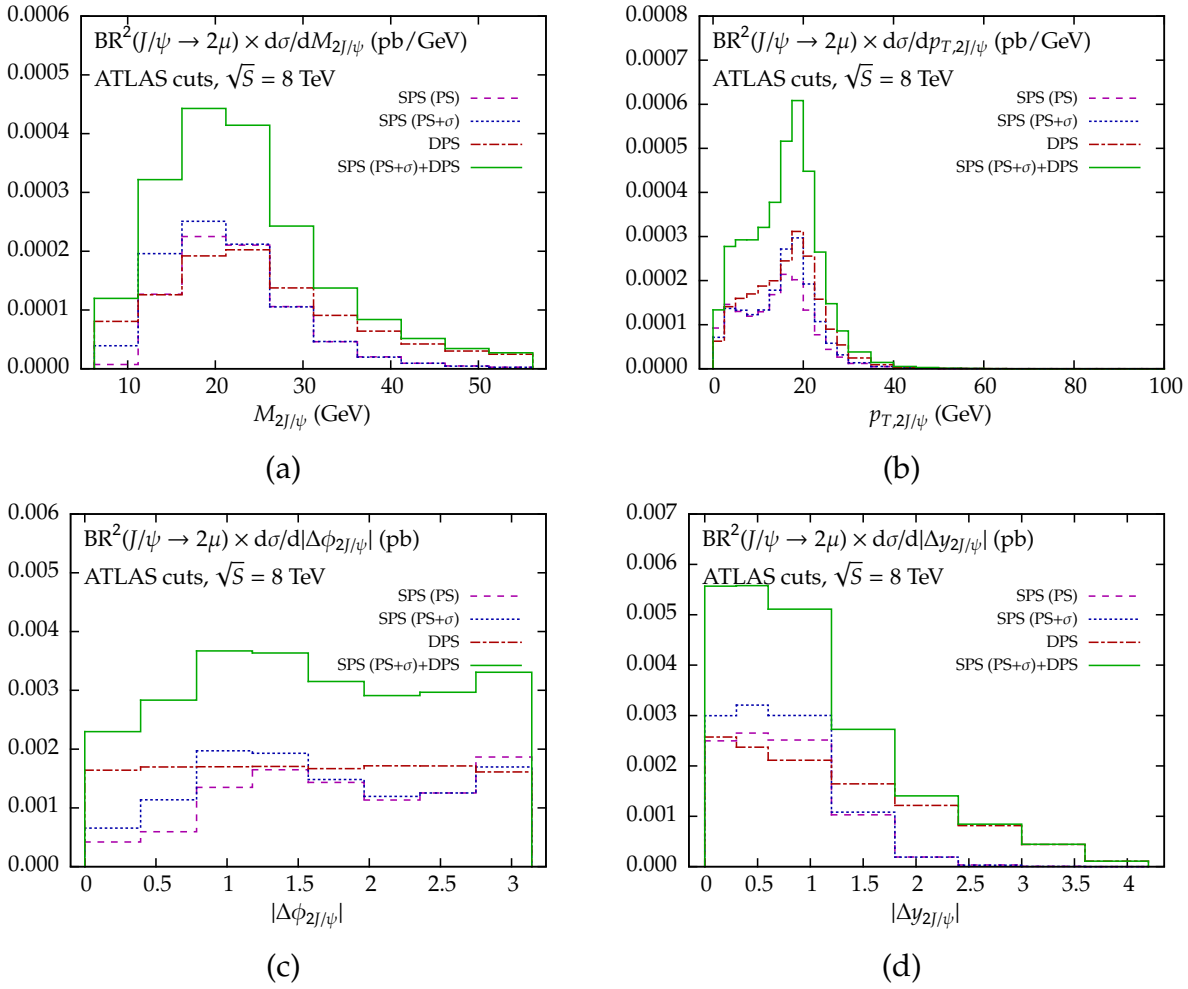

Figure 10.5: Differential distributions for the ATLAS cuts at a collider energy of $\sqrt{S} = 8$ TeV. The distributions are the same as for figure 10.3.

distribution of figure 10.4 (a) and the azimuthal angular separation of figure 10.4 (c) still do not serve well to distinguish between DPS and SPS, the lower p_T range of figure 10.4 (b) and the higher y range of figure 10.4 (d) are now dominated much more strongly by DPS. We stress, however, that the p_T distribution is very susceptible to higher-order corrections which can change the shape significantly, and we do not use a full NLO calculation for our predictions. The invariant mass and rapidity distributions are more stable with respect to the higher-order corrections, as will also be seen later in section 10.3.4.

10.3.2 ATLAS predictions

The ATLAS cuts mainly differ from the LHCb ones by imposing a minimum transverse momentum for each J/ψ, effectively probing the high-p_T region unlike the LHCb experiment. Furthermore, the predictions are now for $\sqrt{S} = 8$ TeV.

In figure 10.5, the same set of distributions as in the case for LHCb is shown. Figure 10.5 (a) shows the invariant mass distribution of the di-J/ψ system. A major difference to the LHCb

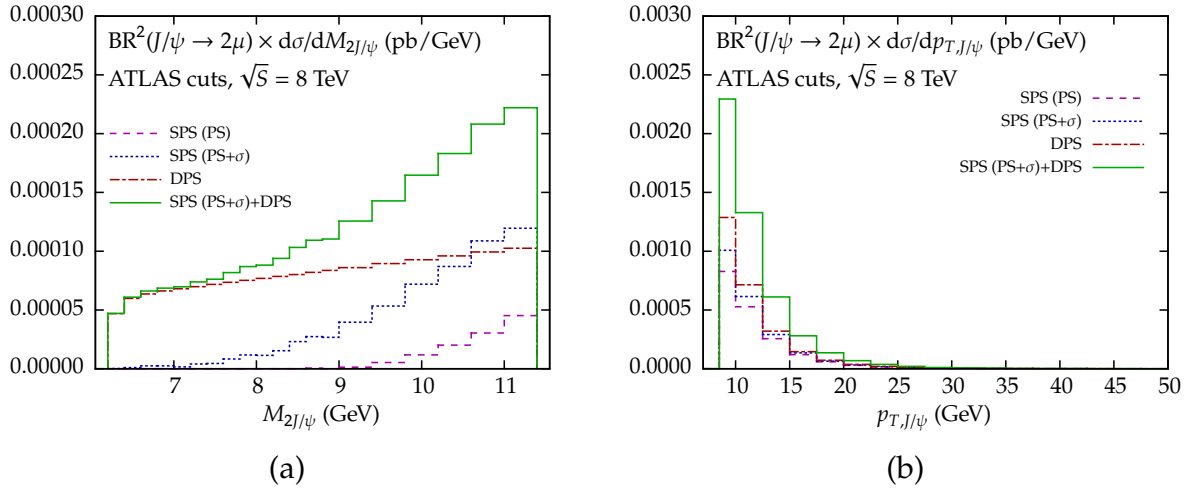

Figure 10.6: Zoomed in version of the invariant mass distribution, figure 10.5 (a), for the lowest mass bin, as well as the distribution showing the transverse momentum of a single J/ψ.

cuts is that the distribution is peaked at a much higher value of $M_{2J/\psi}$, allowing for a low-mass tail. Zooming into the lowest mass bin, see figure 10.6 (a), one notices the dominance of the DPS effects over the SPS background, providing a possibility for a clean DPS signal to experimental searches. However, the cross sections are very small in this mass range, requiring a sufficiently large integrated luminosity for events to occur. The transverse momentum of the di-J/ψ system is shown in figure 10.5 (b). In the structure of the SPS distributions, two peaks are visible. This behaviour can be understood by looking at the azimuthal angular separation, figure 10.5 (c), where the SPS distributions favour two regions: back-to-back scattering with $|\Delta\phi_{2J/\psi}| = \pi$, and a forward-scattering region slightly below $|\Delta\phi_{2J/\psi}| = \pi/2$. Since the p_T cut on the J/ψ mesons requires them to have a transverse momentum of at least 8.5 GeV, and the p_T distribution of a single J/ψ is peaked towards the lowest possible values, see figure 10.6 (b), the back-to-back configuration mainly contributes to the first peak of the $p_{T,2J/\psi}$ plot. The forward-scattering configuration does not play a role for low $p_{T,2J/\psi}$, but it contributes to the second peak, approximately at twice the p_T cut on the J/ψ. It has been checked that the local minimum in between the peaks is a consequence of the p_T cut on the J/ψ and moves when the cut is varied. The DPS signal does not show the two-peak structure, as its azimuthal angular separation is again uniformly distributed. The rapidity separation distribution in figure 10.5 (d) shows a similar behaviour as for the LHCb case: a clean DPS signal at high rapidity separations.

10.3.2.1 Predictions at 13 TeV

Also for the ATLAS predictions, the dominance of the DPS contributions at 13 TeV leads to an easier distinction between SPS and DPS. Despite the transverse momentum distribution of the di-J/ψ system now offering a clearer possibility to separate SPS and DPS contributions for low p_T, we again note that higher-order corrections which are not included here can change the shape of the distribution significantly.

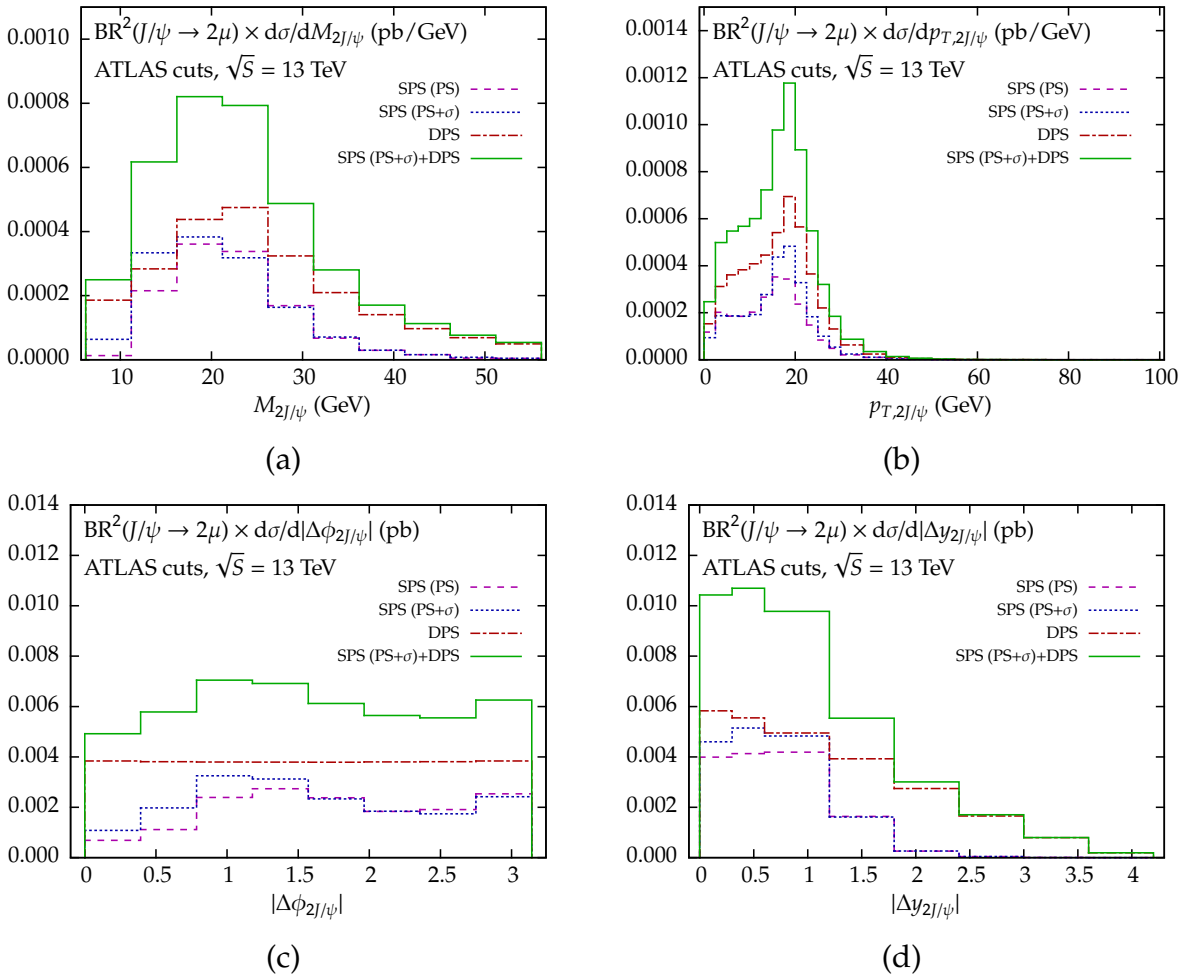

Figure 10.7: Differential distributions for the ATLAS cuts at a collider energy of $\sqrt{S}$ = 13 TeV. The distributions are the same as for figure 10.3.

10.3.3 Comparison to CMS measurement

The CMS experiment has recently measured J/ψ-pair production at 7 TeV [231]. They applied the following cuts to their data:

1) $p_{T,J/\psi} > 6.5$ GeV for $|y_{J/\psi}| < 1.2$,

2) $p_{T,J/\psi} > 6.5 \to 4.5$ GeV for $1.2 < |y_{J/\psi}| < 1.43$,

3) $p_{T,J/\psi} > 4.5$ GeV for $1.43 < |y_{J/\psi}| < 2.2$.

The p_T cut in point 2 scales linearly from 6.5 GeV to 4.5 GeV with the value of $|y_{J/\psi}|$ from 1.2 to 1.43. No further cuts on the muons are applied.

In figure 10.8, we compare our predictions to the CMS data. We show all bins normalised to the corresponding total cross section of a line to only compare the shape of the distributions and approximately remove the dependence on a specific PDF set. Shown are the invariant mass distribution, the transverse momentum of the di-J/ψ system, and the rapidity separation

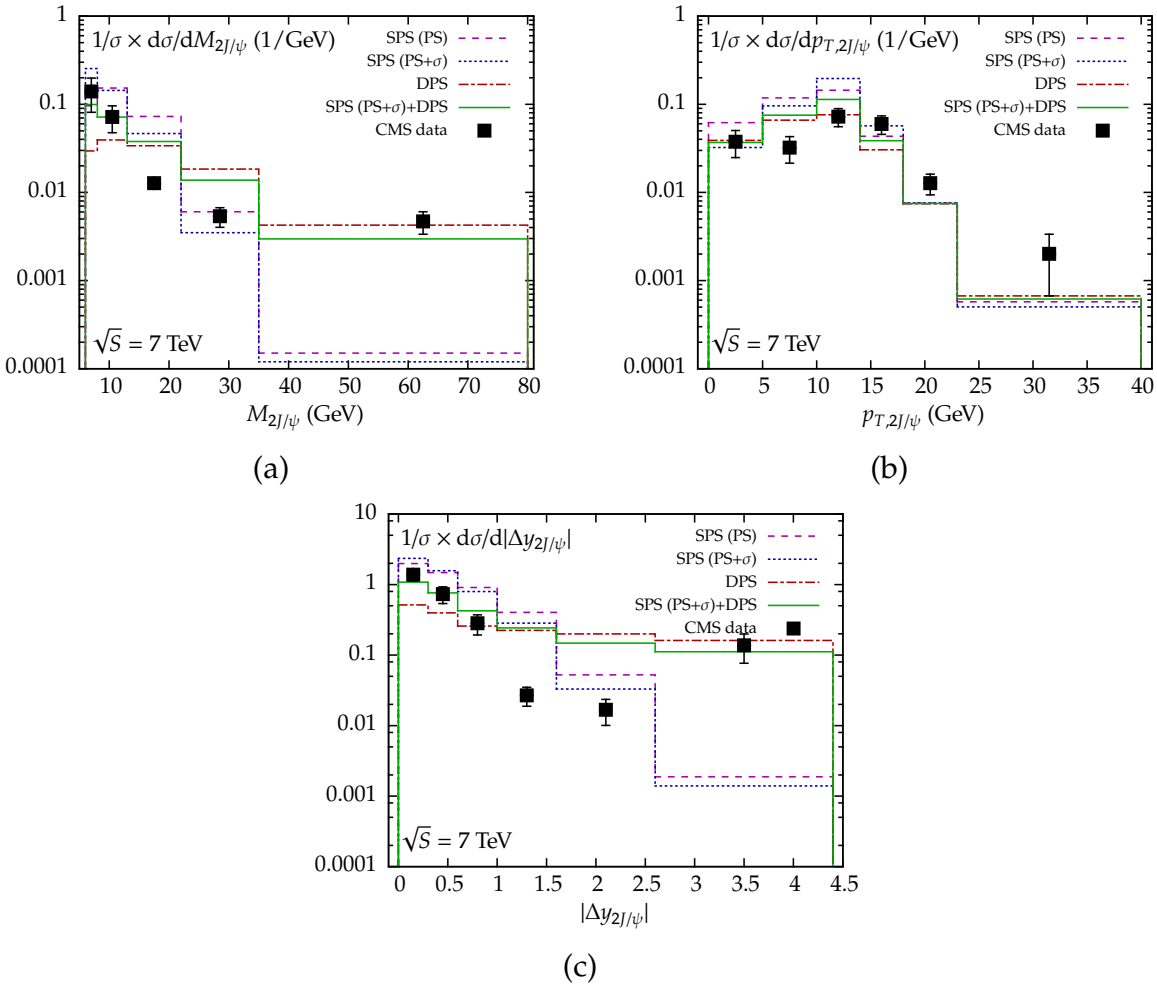

Figure 10.8: Comparison of SPS and DPS predictions to the CMS data at 7 TeV for the invariant mass (a), the transverse momentum of the di-J/ψ system (b), and the rapidity separation (c). Shown are bins which are normalised to the corresponding total cross sections of the different SPS and DPS distributions and the data.

of the two J/ψ. We see that our predictions describe the CMS data reasonably well, in particular also when further sources of uncertainty like the exact choice of the parameters which appear in the SPS and DPS calculations are taken into account. Especially for the invariant mass and the rapidity separation distributions, figures 10.8 (a) and (c), we notice that for a high invariant mass/rapidity separation, DPS contributions are vital to describe the data, whereas the low invariant mass/rapidity region is dominated by the shape of the SPS contributions.

10.3.4 Comparison to Lansberg et al.

At last, we compare our results to the recently published ones from Lansberg et al., ref. [237]. The authors present predictions for similar scenarios of J/ψ-pair production at the LHCb and ATLAS experiments, with the difference of using full calculations of real gluon emission

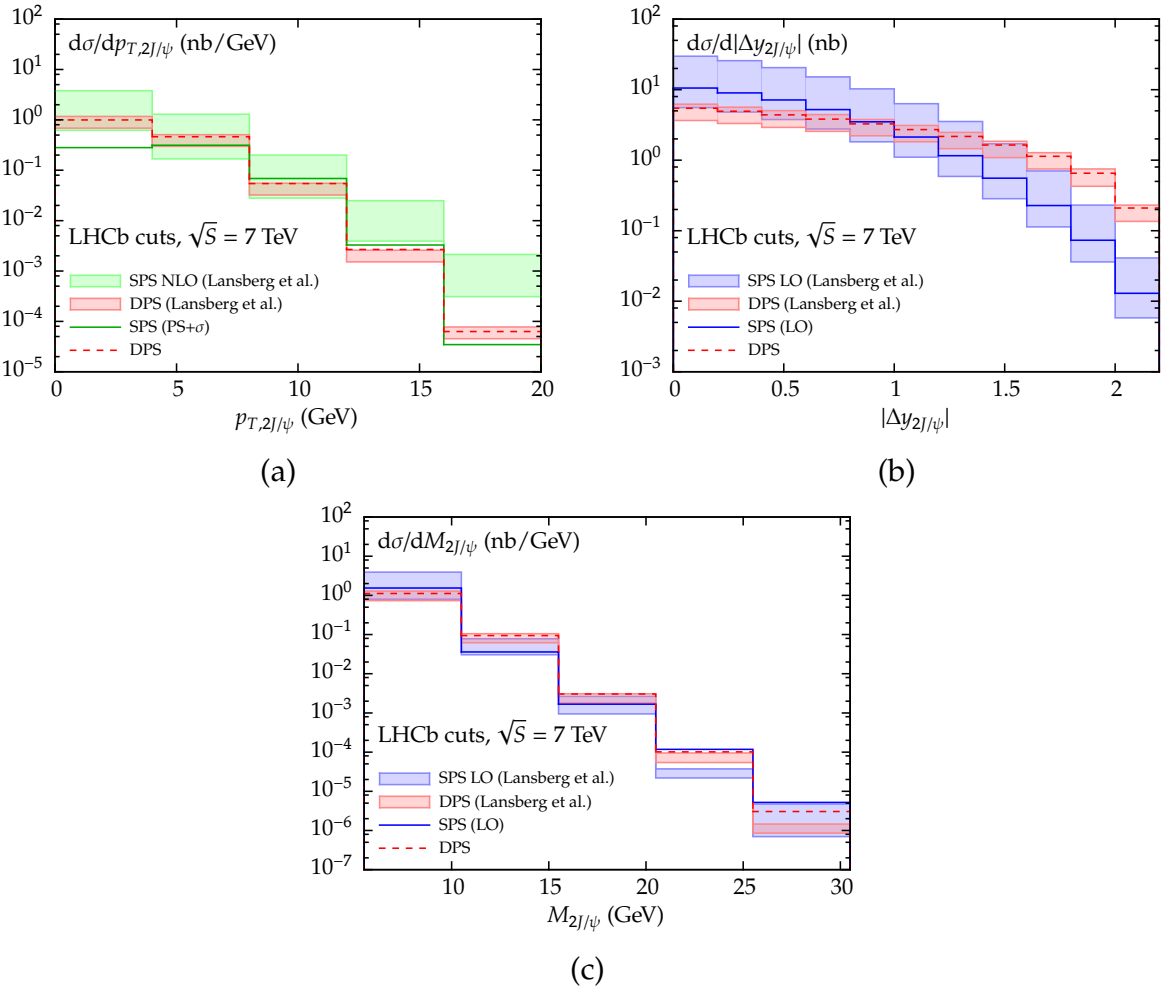

Figure 10.9: Comparison between our results and ref. [237] for the LHCb cuts. Shown are the transverse momentum distribution of the di-J/ψ system (a), the rapidity separation (b), and the invariant mass (c). The "SPS NLO (Lansberg et al.)" and "DPS (Lansberg et al.)" uncertainty bands are read off from the corresponding plots in ref. [237]. The cross sections here are not multiplied by the squared branching ratio $\mathrm{BR}^2(J/\psi \to 2\mu)$.

at NLO (without the virtual corrections, though). This method differs from ours by also taking into account hard gluon emission, while parton showering only considers soft gluons, however to all orders in α_s. In this regard, it is interesting to see how the two approaches compare for the LHCb and ATLAS cuts. In order to minimise the sources of uncertainty, we choose the same parameters and PDF sets as Lansberg et al. These are the wave function of the J/ψ meson at origin $|R(0)|^2 = 0.81\ \mathrm{GeV}^3$, the charm mass $m_c = 1.5$ GeV, the effective DPS cross section $\sigma_{\mathrm{eff}} = 8.2$ mb, and the PDF sets CTEQ6L1 for LO [200], CTEQ6M for SPS (PS+σ) [200], and MSTW2008 NLO for DPS. We note that we still use the fit parameters as specified at the end of section 10.1.1, while Lansberg et al. use a slightly changed fit with $\kappa = 0.65$ and $\lambda = 0.32$.

Figure 10.9 shows the comparison of the prediction for the LHCb cuts at 7 TeV. While the rapidity separation (b) and invariant mass distributions (c) agree (except for small deviations

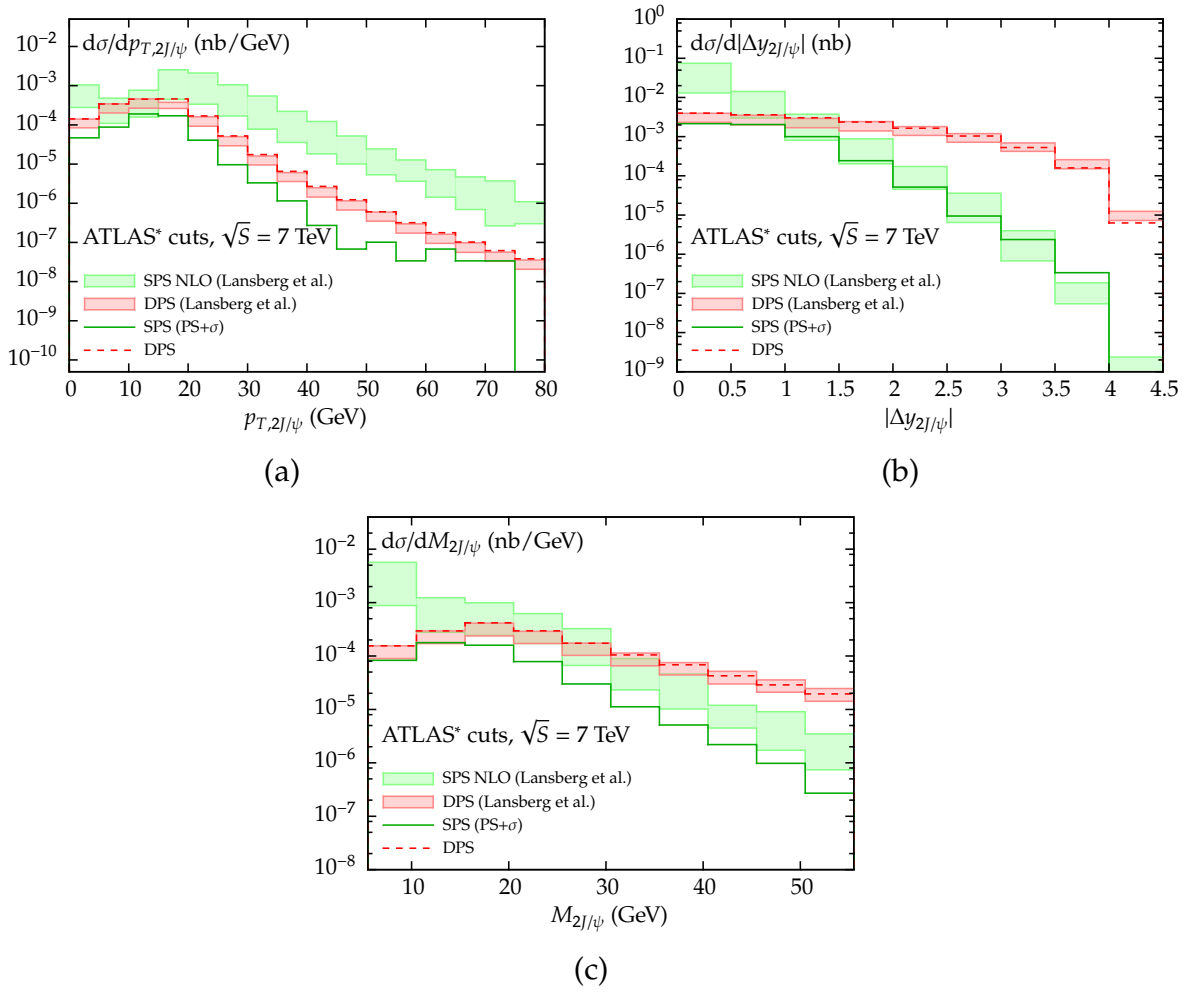

Figure 10.10: Same as figure 10.9 for the case of the ATLAS* cuts. These differ from the ATLAS cuts defined in section 10.2.2 by imposing a lower $p_{T,J/\psi}$ cut of $p_{T,J/\psi} > 5$ GeV instead of $p_{T,J/\psi} > 8.5$ GeV. Furthermore, the predictions are shown for $\sqrt{S} = 7$ TeV instead of 8 TeV.

for a large invariant mass) due to the same input calculations used for LO and DPS, the transverse momentum distribution (a) of SPS differs at low and high p_T, but agrees for intermediate values. We see at low p_T the typical suppression from the all-order structure of parton showering, while the NLO prediction of figure 10.9 is growing towards small p_T. The inclusion of soft-gluon emission at all orders of parton showering describes the region of low p_T better than a fixed-order calculation at NLO, only taking into account real emission corrections. On the other hand, the high-p_T region cannot be described properly by parton showering due to hard gluon emission not taken into account.

The ATLAS* predictions in figure 10.10 at 7 TeV show the same set of distributions. It should be noted that the asterisk denotes a changed lower $p_{T,J/\psi}$ cut of $p_{T,J/\psi} > 5$ GeV instead of $p_{T,J/\psi} > 8.5$ GeV. The transverse momentum distribution of figure 10.10 (a) show a larger $p_{T,2J/\psi}$ range, which shows that for large values of $p_{T,2J/\psi} > 20$ GeV, the parton shower and NLO results differ by a large amount, while there is again an agreement for $p_{T,2J/\psi} \approx$ 5-10 GeV. Interestingly, while there is a difference for a low rapidity separation, figure 10.10 (b), the

two predictions agree within the uncertainty for $|\Delta y_{2J/\psi}| > 1$. The invariant mass distribution of figure 10.10 (c) shows that the lack of hard gluon emission leads to the parton shower result always being below the NLO result. We note that our fit parameters for the Crystal Ball function used in the DPS calculation lead to results that are compatible with the different fit parameters of figure 10.10.

From these comparisons, we see that the rapidity separation distribution is most stable with respect to higher-order corrections from hard-gluon emission that are not included in our approach, while the transverse momentum distribution of the di-J/ψ system is most strongly affected by them. We however expect that a variation of our parameters and the factorisation and renormalisation scales will lead to uncertainty bands which should reduce the discrepancy between our results and the ones from ref. [237].

11 Conclusions

The production of squarks and gluinos at the LHC is an important discovery channel for supersymmetry due to large cross sections. We have discussed the application of soft-gluon and Coulomb resummation with bound-state formation close to threshold for all processes of squark and gluino production, while additionaly analysing effects of double parton scattering, which is important for estimating Standard Model background for new physics searches.

Applying the framework derived in chapters 2, 3, and 4, we first updated the state-of-the-art predictions for squark and gluino production at NLO+NLL accuracy used in experimental analyses to LHC energies of 13 TeV and 14 TeV, while also discussing the predictions for future upgrades of the LHC and new circular colliders at 33 TeV and 100 TeV in chapter 5. We have seen that squark and gluino masses can be probed up to approximately 3 TeV and stop masses up to 2 TeV for collider energies of 13 and 14 TeV, while future colliders with 33 and 100 TeV will be able to search for squarks and gluinos with masses around 6 to 18 TeV and stop with masses ranging from approximately 4 to 9 TeV, assuming a sufficiently high integrated luminosity. We provide numerical tables for a wide range of squark and gluino masses, including theoretical uncertainties from scale variation, PDF and α_s errors, using the MSTW2008 and CTEQ6.6 PDF sets, together with an interpolation code, which is made public as the package `NLL-fast` [199] for the usage in SUSY searches of the ATLAS and CMS experiments.

In a collaboration together with the members of the NNPDF collaboration, we computed predictions for squark and gluino production at a collider energy of 13 TeV with the recently published NNPDF3.0 NLO set. It has been seen in chapter 6 that the predictions with the NNPDF3.0 set are well in agreement with the MSTW2008 NLO and CTEQ6.6 computations, where at large masses, the PDF uncertainties of the NNPDF3.0 set become very large due to a lack of experimental data for PDFs at large momentum fraction x and envelop the other predictions. Furthermore, for the first time, we analysed the impact of threshold-improved PDF fits within the NNPDF framework for squark and gluino production and saw that the effects are non-negligible, leading to a decrease of the NLO+NLL cross sections with respect to NLO for low masses, and a stronger increase at high masses. As not all of the processes

that go into the NNPDF analysis have been computed with threshold resummation included, the predictions were made with a reduced dataset, causing the PDF uncertainties to become larger than for the global fit with the full dataset. As the effects of threshold-improved PDFs are within the PDF uncertainty of the NNPDF3.0 NLO set, the latter are preferred in the calculations for the time being in order to determine mass exclusion limits in experimental searches for supersymmetry. At the point where the PDF uncertainties can be reduced significantly, or when supersymmetric particles are found, we state that threshold-improved PDF sets will be necessary to properly describe the production of squarks and gluinos.

The increase in logarithmic accuracy to NNLL for squark and gluino produciton has been worked out in chapter 7, while the production of stops has been analysed separately in chapter 8 due to their special role as being amongst the lighest supersymmetric particles in a lot of scenarios. We included hard-matching coefficients up to one loop and Coulomb contributions up to two loop, and saw that for all processes, the additional contributions at NNLL accuracy significantly increase the total cross sections, with the strongest relative enhancement being seen for gluino-pair production due to large colour factors. Additionally, we analysed the dependence on the renormalisation and factorisation scales and found that, with the exception of gluino-pair production, the scale behaviour improves due to the higher-order corrections being taken into account. We discussed the increased scale dependence of gluino-pair production in much detail and found that, while at low scales, mainly the Coulomb contributions have a strong effect on the cross section, the high-scale behaviour is driven by the large higher-order logarithms in the exponentials, enhancing the importance of soft-gluon resummation for this process. Additional contributions which would require a full NNLO calculation might improve this behaviour.

The production of stops at NNLL accuracy required the extraction of the one-loop hard-matching coefficients from a calculation done in the formalism of SCET. We found that also the cross sections for stop production are enhanced due to the higher-order logarithms, hard-matching coefficients and Coulomb contributions, in particular when approaching the threshold region. We have seen in the study of the NLO scaling functions that in particular the Coulomb contributions strongly influence the behaviour of the cross section, bringing the NLO threshold expansion much closer to the full NLO result near threshold. We also noticed an increase compared to NLO+NLL in the dependence on the specific SUSY parameters appearing as a result of the stop mixing, and being included in the hard-matching coefficients. In particular, the hierarchy between the stop and gluino masses influences the cross sections noticeably. We have also analysed the different behaviour of the scale dependence from NLO+NLL, now showing a slight upward slope towards higher scales, and compared to the similar process of light-flavoured squark-antisquark production. It has been seen that the main difference lies in the absence of the singlet colour channel of the $q\bar{q}$ initial state which is the dominant contribution to light-flavoured squark-antisquark production. The scale dependence of stop-antistop production is therefore driven by the dominant gg initial state which leads to a decrease of the cross sections for lower values of the scale, and an increase for higher values of the scale. It has also been of interest to compare our results to a similar calculation done in the SCET formalism in ref. [132]. We found that within the given theoretical uncertainties, our results agree, emphasising that with different methods

of threshold resummation, similar results, obtained in two independent approaches, can be achieved. We furthermore noted that additional uncertainties come from subleading terms which can change the cross sections by several percent.

Being in a position to combine soft-gluon and Coulomb resummation and include contributions from bound-state formation below threshold, we discussed the additional effects on squark and gluino production compared to the predictions of the previous two chapters in chapter 9. We found that, while the inclusion of Coulomb resummation does not significantly change the predictions with Coulomb contributions being considered up to two loop, the formation of bound states for attractive colour channels between the squarks and gluinos lead to effects of several percent, mainly affecting gluino-pair and squark-antisquark production. We saw that in all cases, the higher-order Coulomb and bound-state contributions are positive. As a similar study including both soft-gluon and Coulomb resummation as well as bound-state contributions has been done in SCET by the authors of ref. [134], we were able to compare to their results and found that the agreement between our two approaches improves and that the results are compatible within the theoretical uncertainties.

At last, we have studied DPS effects for the case of J/ψ-pair production in chapter 10. DPS is important for a proper description of background processes from Standard Model particles. Background analyses in general are important for searches for new physics models such as supersymmetry. This work has been an update to a previous study of ref. [229] to provide predictions for ongoing DPS analyses of the LHCb and ATLAS collaborations. We have updated the fiducial volumes and provided differential distributions for several kinematical variables, finding that at collider energies of 7 and 8 TeV, the DPS contributions are of similar size as the SPS contributions, with the former increasing more quickly than the latter for higher energies. Similar to the study of ref. [229], we found that mainly longitudinal variables such as the rapidity separation are suited for a separation of DPS and SPS contributions, with the separation made easier at higher energies due to the larger contributions from DPS. Additionally, the ATLAS analysis allows for a separation at low invariant mass and high rapidity separation of the di-J/ψ system. We compared our predictions to recently published CMS results and saw that DPS should be included for a better description of the distributions. Lastly, a comparison of our results including parton showering to a NLO calculation showed that the lack of hard gluon emission in parton showering leads to a difference in the predictions mainly for higher values of the transverse momentum of the di-J/ψ system, as it was expected.

To summarise the results of this thesis, we have analysed the effects of threshold resummation up to NNLL including hard-matching coefficients up to one loop and Coulomb contributions both up to two loop and resummed to all orders, together with bound-state contributions from below threshold, on all processes of coloured SUSY particle production, leading to noticeable enhancements and effects on the total cross sections. Additionally, we studied DPS contributions to J/ψ-pair production which will become significant at the current and future runs of the LHC. While some of the results are already publicly available, we will, in the near future, provide an interface for the experimental community to easily access our results and use them in future analyses. Further publications for the remaining results are currently in preparation.

A Full scale dependence of the resummed expressions

In this chapter, it will be outlined how to readd the full dependence on the renormalisation and factorisation scales of the functions in eq. (4.100). From eq. (4.47), the renormalisation scale dependence of the jet functions is given as:

$$\mu_R \frac{\mathrm{d}}{\mathrm{d}\mu_R} \ln \tilde{\psi}_{i/i}\left(N, \mu_R^2, \varepsilon\right) = -\gamma_{\psi_i}\left(\alpha_\mathrm{s}(\mu_R^2)\right) = 2\gamma_i\left(\alpha_\mathrm{s}(\mu_R^2)\right). \tag{A.1}$$

As the jet functions do not require a separate renormalisation as composite operators, the second equal sign relates the anomalous dimensions of the jet functions with the ones from the initial-state fields with flavour i. Furthermore, as also stated earlier, this anomalous dimension does not depend on the Mellin moment variable N. The difference in the minus sign has been taken to follow the convention of ref. [158].

The light-cone parton-in-parton distributions follow the evolution equations with respect to the factorisation scale [158, 263]:

$$\mu_F \frac{\mathrm{d}}{\mathrm{d}\mu_F} \ln \tilde{f}_{i/i}\left(N, \mu_F^2, \varepsilon\right) = 2\gamma_{i/i}\left(N, \alpha_\mathrm{s}(\mu_F^2)\right). \tag{A.2}$$

The anomalous dimension of the light-cone parton-in-parton functions depends on N. As already mentioned earlier, only flavour-diagonal splittings are of relevance for the large-N case, which is why flavour-mixing terms are not written explicitely.

Solving the two differential equations leads to additional terms in the exponent of the resummed expression describing separately the renormalisation and factorisation scale dependence:

$$\begin{aligned}\frac{\tilde{\psi}_{i/i}(N, \mu_R^2, \varepsilon)}{\tilde{f}_{i/i}(N, \mu_F^2, \varepsilon)} &= \frac{\tilde{\psi}_{i/i}(N, Q^2, \varepsilon)}{\tilde{f}_{i/i}(N, Q^2, \varepsilon)} \\ &\quad \times \exp\left\{-2\int_{\mu_R}^{Q} \frac{\mathrm{d}\lambda}{\lambda} \gamma_i\left(\alpha_\mathrm{s}(\lambda^2)\right) + 2\int_{\mu_F}^{Q} \frac{\mathrm{d}\lambda}{\lambda} \gamma_{i/i}\left(N, \alpha_\mathrm{s}(\lambda^2)\right)\right\}. \end{aligned} \tag{A.3}$$

Expressions for the anomalous dimensions of the parton-in-parton distribution functions may be found in ref. [263].

Lastly, the coupling of the N-independent prefactor $R_i\left(\alpha_s(Q^2)\right)$ in eq. (4.84) may be replaced in the $\overline{\text{MS}}$ scheme by the running coupling depending on μ_R, $R_i\left(\alpha_s(\mu_R^2)\right)$.

B Evaluation of the integrals in the exponentiated expressions

The evaluation of the integrals in eqs. (4.85) and (4.93) requires the choice of a logarithmic accuracy, as the full integrals diverge due to the argument of α_s being integrated over and hitting the Landau pole. This chapter will follow a proposed prescription in ref. [264] which is valid to all logarithmic accuracies.

In ref. [157], it has been shown that integrals of the type

$$I_n(N) := \int_0^1 \mathrm{d}z\, z^{N-1} \left[\frac{\ln^n(1-z)}{1-z}\right]_+ = \int_0^1 \mathrm{d}z\, \frac{z^{N-1}-1}{1-z} \ln^n(1-z), \tag{B.1}$$

encountered in the exponentiated expressions, can be evaluated by a small trick: rewriting the logarithms as

$$\ln^n(1-z) = \lim_{\epsilon\to 0} \left(\frac{\partial}{\partial \epsilon}\right)^\epsilon (1-z)^\epsilon \tag{B.2}$$

and exchanging the integral with the limes and derivative with respect to ϵ turns the integral into two terms that can be written as the Euler beta function $\beta(x,y) = \int_0^1 \mathrm{d}t\, t^{x-1}(1-t)^{y-1}$:

$$\begin{aligned} I_n(N) &= \lim_{\epsilon\to 0} \left(\frac{\partial}{\partial \epsilon}\right)^\epsilon \int_0^1 \mathrm{d}z \left(z^{N-1}-1\right)(1-z)^{\epsilon-1} \\ &= \lim_{\epsilon\to 0} \left(\frac{\partial}{\partial \epsilon}\right)^\epsilon \left[\beta(N,\epsilon) - \beta(1,\epsilon)\right] \\ &= \lim_{\epsilon\to 0} \left(\frac{\partial}{\partial \epsilon}\right)^\epsilon \left\{\frac{1}{\epsilon}\left[\frac{\Gamma(N)\Gamma(1+\epsilon)}{\Gamma(N+\epsilon)} - 1\right]\right\}. \end{aligned} \tag{B.3}$$

In the large-N limit, terms suppressed by at least $1/N$ can be neglected, so that eq. (B.3) turns

into

$$I_n(N) = \lim_{\epsilon\to 0}\left(\frac{\partial}{\partial\epsilon}\right)^{\epsilon}\left\{\frac{1}{\epsilon}\left[e^{-\epsilon\ln N}\Gamma(1+\epsilon)-1\right]\right\}+\mathcal{O}\left(\frac{1}{N}\right). \tag{B.4}$$

The remaining gamma function can be written in terms of another exponential function,

$$\Gamma(1+\epsilon) = \exp\left\{-\gamma_E\epsilon+\sum_{n=2}^{\infty}(-1)^n\frac{\zeta(n)}{n}\epsilon^n\right\}. \tag{B.5}$$

Expanding the exponential functions and applying the derivative with respect to ϵ term by term, the well-known polynomial in $\ln N$ for $N\to\infty$ up to an arbitrary accuracy is obtained:

$$I_n(N) = \frac{(-1)^{n+1}}{n+1}\ln^{n+1}\bar{N}+\frac{(-1)^{n-1}}{2}n\zeta(2)\ln^{n-1}\bar{N}+\sum_{m=0}^{n-2}a_{mn}\ln^k\bar{N}+\mathcal{O}\left(\frac{1}{N}\right) \tag{B.6}$$

with $\bar{N} = N\exp(\gamma_E)$ and a_{mn} numerical constants. Comparing eq. (B.1) to this result, it can be seen that the first term can be reproduced by applying the following replacement:

$$z^{N-1}-1 \approx -\Theta\left(1-z-\frac{1}{\bar{N}}\right). \tag{B.7}$$

This approximation reproduces all logarithms in N to NLL accuracy correctly, strongly simplifying the evaluation of integrals such as

$$\int_0^1 \mathrm{d}z\frac{z^{N-1}-1}{1-z}F\left(\alpha_\mathrm{s},\ln(1-z)\right)\overset{(\mathrm{NLL})}{\approx}\int_0^{1-1/\bar{N}}\mathrm{d}z\frac{F\left(\alpha_\mathrm{s},\ln(1-z)\right)}{1-z} \tag{B.8}$$

with a function F which has the following perturbative expansion:

$$F\left(\alpha_\mathrm{s},\ln(1-z)\right) = \sum_{m=1}^{\infty}\alpha_\mathrm{s}^m\sum_{n=0}^{2m-1}F_{mn}\ln^n(1-z) \tag{B.9}$$

where F_{mn} are α_s- and z-independent coefficients.

A generalisation of this prescription has been suggested by the authors of ref. [264]. By rewriting the term

$$e^{-\epsilon\ln N}\Gamma(1+\epsilon) = \Gamma\left(1-\frac{\partial}{\partial\ln N}\right)e^{-\epsilon\ln N}, \tag{B.10}$$

where the right-hand side has to be understood in a formal sense, and with the gamma function defined through eq. (B.5), the all-order prescription becomes:

$$z^{N-1}-1 = -\Gamma\left(1-\frac{\partial}{\partial\ln N}\right)\Theta\left(1-z-\frac{1}{N}\right)+\mathcal{O}\left(\frac{1}{N}\right). \tag{B.11}$$

A more practicable way of using this prescription is given by the expansion of the differential

operator

$$\Gamma\left(1-\frac{\partial}{\partial \ln N}\right)=1+\gamma_E\frac{\partial}{\partial \ln N}+\frac{1}{2}\left(\gamma_E^2+\zeta(2)\right)\left(\frac{\partial}{\partial \ln N}\right)^2+\ldots. \tag{B.12}$$

Truncating the series and then using eq. (B.11) to replace the first factor in integrals of the type of eq. (B.8) will result in terms up to LL, NLL, NNLL, …being obtained.

C Resummed exponential functions up to NNLL

The full expressions for the soft-collinear and wide-angle soft terms in eq. (4.107) are listed here for the general case of unequal renormalisation and factorisation scales, $\mu_R \neq \mu_F$. The expressions shown here are based on refs. [129, 264]. Using the variable $\lambda = b_0 \alpha_s(\mu_R^2) \ln N$, eq. (4.108) can be written as:

$$\Delta_i \Delta_j \Delta^{(s)}_{ij\to kl,I} = \exp\left[G^{(1)}_{ij}(\lambda) \ln N + G^{(2)}_{ij\to kl,I}(\lambda) + \alpha_s G^{(3)}_{ij,kl}(\lambda) + \mathcal{O}(\mathrm{N^3LL}) \right], \tag{C.1}$$

$$G^{(1)}_{ij}(\lambda) = g^{(1)}_i(\lambda) + g^{(1)}_j(\lambda), \tag{C.2}$$

$$G^{(2)}_{ij\to kl,I}(\lambda) = g^{(2)}_i(\lambda, Q^2, \mu_R^2, \mu_F^2) + g^{(2)}_j(\lambda, Q^2, \mu_R^2, \mu_F^2) + h^{(2)}_{ij\to kl,I}(\lambda), \tag{C.3}$$

$$G^{(3)}_{ij\to kl,I}(\lambda) = g^{(3)}_i(\lambda, Q^2, \mu_R^2, \mu_F^2) + g^{(3)}_j(\lambda, Q^2, \mu_R^2, \mu_F^2) + h^{(3)}_{ij\to kl,I}(\lambda, Q^2, \mu_R^2). \tag{C.4}$$

The functions $g^{(1)}_i$, $g^{(2)}_i$, and $g^{(3)}_i$ stem from soft-collinear gluon emission and only depend on the flavour of the initial-state parton, whereas the functions $h^{(2)}_{ij\to kl,I}$ and $h^{(3)}_{ij\to kl,I}$, originating from wide-angle soft gluon emission, additionally depend on the colour structure of the process. They are defined as:

$$g^{(1)}_i(\lambda) = \frac{A^{(1)}_i}{2\pi b_0 \lambda} \left[2\lambda + (1-2\lambda)\ln(1-2\lambda) \right], \tag{C.5}$$

$$\begin{aligned} g^{(2)}_i(\lambda, Q^2, \mu_R^2, \mu_F^2) = &-\frac{A^{(1)}_i \gamma_E}{\pi b_0} \ln(1-2\lambda) + \frac{A^{(1)}_i b_1}{2\pi b_0^3} \left[2\lambda + \ln(1-2\lambda) + \frac{1}{2}\ln^2(1-2\lambda) \right] \\ &- \frac{A^{(2)}_i}{2\pi^2 b_0^2} \left[2\lambda + \ln(1-2\lambda) \right] + \frac{A^{(1)}_i}{2\pi b_0} \left[\ln(1-2\lambda) \ln\left(\frac{Q^2}{\mu_R^2}\right) + 2\lambda \ln\left(\frac{\mu_F^2}{\mu_R^2}\right) \right], \end{aligned} \tag{C.6}$$

$$h^{(2)}_{ij\to kl,I}(\lambda) = \frac{\ln(1-2\lambda)}{2\pi b_0} D^{(1)}_{ij\to kl,I}, \tag{C.7}$$

$$\begin{aligned} g^{(3)}_i(\lambda, Q^2, \mu_R^2, \mu_F^2) = {} & \frac{A^{(1)}_i b_1^2}{2\pi b_0^4} \frac{1}{1-2\lambda}\left[2\lambda^2 + 2\lambda\ln(1-2\lambda) + \frac{1}{2}\ln^2(1-2\lambda)\right] \\ & + \frac{A^{(1)}_i b_2}{2\pi b_0^3}\left[2\lambda + \ln(1-2\lambda) + \frac{2\lambda^2}{1-2\lambda}\right] \\ & - \frac{A^{(1)}_i b_1 \gamma_E}{\pi b_0^2}\frac{2\lambda + \ln(1-2\lambda)}{1-2\lambda} + \frac{2A^{(1)}_i}{\pi}\left(\zeta(2) + \gamma_E^2\right)\frac{\lambda}{1-2\lambda} \\ & - \frac{A^{(2)}_i b_1}{2\pi^2 b_0^3}\frac{1}{1-2\lambda}\left[2\lambda(\lambda+1) + \ln(1-2\lambda)\right] \\ & + \frac{2A^{(2)}_i \gamma_E}{\pi^2 b_0}\frac{\lambda}{1-2\lambda} + \frac{A^{(3)}_i}{\pi^3 b_0^2}\frac{\lambda^2}{1-2\lambda} - \frac{D^{(2)}_i}{2\pi^2 b_0}\frac{\lambda}{1-2\lambda} \\ & + \left[\frac{A^{(1)}_i b_1}{2\pi b_0^2}\frac{2\lambda + \ln(1-2\lambda)}{1-2\lambda} - \frac{2A^{(1)}_i \gamma_E}{\pi}\frac{\lambda}{1-2\lambda}\right]\ln\left(\frac{Q^2}{\mu_R^2}\right) \\ & + \frac{A^{(1)}_i}{2\pi}\left[\frac{\lambda}{1-2\lambda}\ln^2\left(\frac{Q^2}{\mu_R^2}\right) - \lambda\ln^2\left(\frac{\mu_F^2}{\mu_R^2}\right)\right] \\ & - \frac{A^{(2)}_i}{\pi^2 b_0}\left[\frac{\lambda}{1-2\lambda}\ln\left(\frac{Q^2}{\mu_R^2}\right) - \lambda\ln\left(\frac{\mu_F^2}{\mu_R^2}\right)\right], \end{aligned} \tag{C.8}$$

$$\begin{aligned} h^{(3)}_{ij\to kl,I}(\lambda, Q^2, \mu_R^2, \mu_F^2) = {} & \frac{D^{(1)}_{ij\to kl,I} b_1}{2\pi b_0^2}\frac{2\lambda + \ln(1-2\lambda)}{1-2\lambda} - \frac{2D^{(1)}_{ij\to kl,I}\gamma_E}{\pi}\frac{\lambda}{1-2\lambda} - \frac{D^{(2)}_{ij\to kl,I}}{\pi^2 b_0}\frac{\lambda}{1-2\lambda} \\ & + \frac{D^{(1)}_{ij\to kl,I}}{\pi}\frac{\lambda}{1-2\lambda}\ln\left(\frac{Q^2}{\mu_R^2}\right) \end{aligned} \tag{C.9}$$

with the process independent coefficients

$$A^{(1)}_i = C_i, \tag{C.10}$$

$$A^{(2)}_i = \frac{1}{2}C_i\left[\left(\frac{67}{18} - \zeta(2)\right)C_A - \frac{5}{9}n_l\right], \tag{C.11}$$

$$\begin{aligned} A^{(3)}_i = {} & \frac{1}{4}C_i\left[C_A^2\left(\frac{245}{24} - \frac{67}{9}\zeta(2) + \frac{11}{6}\zeta(3) + \frac{11}{5}\zeta(2)^2\right) + C_F n_l\left(-\frac{55}{24} + 2\zeta(3)\right)\right. \\ & \left. + C_A n_l\left(-\frac{209}{108} + \frac{10}{9}\zeta(2) - \frac{7}{3}\zeta(3)\right) - \frac{n_l^2}{27}\right], \end{aligned} \tag{C.12}$$

and

$$D_i^{(2)} = C_i \left[C_A \left(-\frac{101}{27} + \frac{11}{3}\zeta(2) + \frac{7}{2}\zeta(3) \right) + n_l \left(\frac{14}{27} - \frac{2}{3}\zeta(2) \right) \right], \tag{C.13}$$

where C_i is a colour factor defined as

$$C_i = \begin{cases} C_F = \frac{N_c^2 - 1}{2N_c} & \text{for } i = q, \bar{q} \\ C_A = N_c & \text{for } i = g \end{cases} \tag{C.14}$$

and n_l is the number of light quark flavours. The process dependent coefficients are

$$D_{ij\to kl,I}^{(1)} = -C_2(R_I), \tag{C.15}$$

$$\begin{aligned} D_{ij\to kl,I}^{(2)} &= C_2(R_I) \left[-C_A \left(\frac{115}{36} - \frac{1}{2}\zeta(2) + \frac{1}{2}\zeta(3) \right) + \frac{11}{18} n_l \right] \\ &= -C_2(R_{ij\to kl,I}) \left(\frac{1}{2} \left[\left(\frac{67}{18} - \zeta(2) \right) C_A - \frac{5}{9} n_l \right] + \frac{C_A}{2} (\zeta(3) - 1) + 2\pi b_0 \right) \end{aligned} \tag{C.16}$$

where $C_2(R_I)$ are the quadratic Casimir invariants of the colour representation I of a certain process, see section 5.1.1.

Bibliography

[1] S. L. Glashow, "*Partial Symmetries of Weak Interactions*," Nucl. Phys. **22** (1961) 579.

[2] S. Weinberg, "*A Model of Leptons*," Phys. Rev. Lett. **19** (1967) 1264.

[3] A. Salam, "*Weak and Electromagnetic Interactions*," Conf. Proc. C **680519** (1968) 367.

[4] S. L. Glashow, J. Iliopoulos and L. Maiani, "*Weak Interactions with Lepton-Hadron Symmetry*," Phys. Rev. D **2** (1970) 1285.

[5] H. Fritzsch, M. Gell-Mann and H. Leutwyler, "*Advantages of the Color Octet Gluon Picture*," Phys. Lett. B **47** (1973) 365.

[6] D. J. Gross and F. Wilczek, "*Asymptotically Free Gauge Theories. 1*," Phys. Rev. D **8** (1973) 3633.

[7] S. Weinberg, "*Nonabelian Gauge Theories of the Strong Interactions*," Phys. Rev. Lett. **31** (1973) 494.

[8] P. W. Higgs, "*Broken Symmetries and the Masses of Gauge Bosons*," Phys. Rev. Lett. **13** (1964) 508.

[9] F. Englert and R. Brout, "*Broken Symmetry and the Mass of Gauge Vector Mesons*," Phys. Rev. Lett. **13** (1964) 321.

[10] G. S. Guralnik, C. R. Hagen and T. W. B. Kibble, "*Global Conservation Laws and Massless Particles*," Phys. Rev. Lett. **13** (1964) 585.

[11] G. Aad *et al.* [ATLAS Collaboration], "*Observation of a new particle in the search for the Standard Model Higgs boson with the ATLAS detector at the LHC*," Phys. Lett. B **716** (2012) 1 [arXiv:1207.7214].

[12] S. Chatrchyan *et al.* [CMS Collaboration], "*Observation of a new boson at a mass of 125 GeV with the CMS experiment at the LHC*," Phys. Lett. B **716** (2012) 30 [arXiv:1207.7235].

[13] T. Nakano and K. Nishijima, "*Charge Independence for V-particles*," Prog. Theor. Phys. **10** (1953) 581.

[14] M. Gell-Mann, "*The interpretation of the new particles as displaced charge multiplets*," Nuovo Cim. **4** (1956) S2, 848.

[15] S. Bethke, "*The 2009 World Average of alpha(s)*," Eur. Phys. J. C **64** (2009) 689 [arXiv:0908.1135].

[16] K. A. Olive *et al.* [Particle Data Group Collaboration], "*Review of Particle Physics*," Chin. Phys. C **38** (2014) 090001.

[17] I. Niessen, "*Improving Predictions for SUSY Cross Sections*," PhD thesis (2012).

[18] R. Ellis, W. Stirling, and B. Webber, "*QCD and Collider Physics*," Cambridge University Press, 1996.

[19] L. A. Harland-Lang, A. D. Martin, P. Motylinski and R. S. Thorne, "*Parton distributions in the LHC era: MMHT 2014 PDFs*," Eur. Phys. J. C **75** (2015) 5, 204 [arXiv:1412.3989].

[20] A. D. Martin, W. J. Stirling, R. S. Thorne and G. Watt, "*Parton distributions for the LHC*," Eur. Phys. J. C **63** (2009) 189 [arXiv:0901.0002].

[21] S. Dulat *et al.*, "*The CT14 Global Analysis of Quantum Chromodynamics*," [arXiv:1506.07443].

[22] R. D. Ball *et al.* [NNPDF Collaboration], "*Parton distributions for the LHC Run II*," JHEP **1504** (2015) 040 [arXiv:1410.8849].

[23] J. Butterworth *et al.*, "*PDF4LHC recommendations for LHC Run II*," J. Phys. G **43** (2016) 023001 [arXiv:1510.03865].

[24] J. Wess and B. Zumino, "*Supergauge Transformations in Four-Dimensions*," Nucl. Phys. B **70** (1974) 39.

[25] S. P. Martin, "*A Supersymmetry primer*," Adv. Ser. Direct. High Energy Phys. **21** (2010) 1 [Adv. Ser. Direct. High Energy Phys. **18** (1998) 1] [hep-ph/9709356].

[26] I. J. R. Aitchison, "*Supersymmetry and the MSSM: An Elementary introduction*," [hep-ph/0505105].

[27] S. Weinberg, "*Implications of Dynamical Symmetry Breaking*," Phys. Rev. D **13** (1976) 974.

[28] E. Gildener, "*Gauge Symmetry Hierarchies*," Phys. Rev. D **14** (1976) 1667.

[29] L. Susskind, "*Dynamics of Spontaneous Symmetry Breaking in the Weinberg-Salam Theory*," Phys. Rev. D **20** (1979) 2619.

[30] S. Weinberg, "*Implications of Dynamical Symmetry Breaking: An Addendum*," Phys. Rev. D **19** (1979) 1277.

[31] G. 't Hooft, C. Itzykson, A. Jaffe, H. Lehmann, P. K. Mitter, I. M. Singer and R. Stora, "*Recent Developments in Gauge Theories. Proceedings, Nato Advanced Study Institute, Cargese, France, August 26 - September 8, 1979*," NATO Sci. Ser. B **59** (1980) pp.1.

[32] G. F. Smoot *et al.*, "*Structure in the COBE differential microwave radiometer first year maps*," Astrophys. J. **396** (1992) L1.

[33] C. L. Bennett *et al.* [WMAP Collaboration], "*First year Wilkinson Microwave Anisotropy Probe (WMAP) observations: Preliminary maps and basic results*," Astrophys. J. Suppl. **148** (2003) 1 [astro-ph/0302207].

[34] N. Jarosik *et al.* [WMAP Collaboration], "*Three-year Wilkinson Microwave Anisotropy Pr (WMAP) observations: beam profiles, data processing, radiometer characterization and systematic error limits*," Astrophys. J. Suppl. **170** (2007) 263 [astro-ph/0603452].

[35] G. Hinshaw *et al.* [WMAP Collaboration], "*Five-Year Wilkinson Microwave Anisotropy Probe (WMAP) Observations: Data Processing, Sky Maps, and Basic Results*," Astrophys. J. Suppl. **180** (2009) 225 [arXiv:0803.0732].

[36] N. Jarosik *et al.*, "*Seven-Year Wilkinson Microwave Anisotropy Probe (WMAP) Observations: Sky Maps, Systematic Errors, and Basic Results*," Astrophys. J. Suppl. **192** (2011) 14 [arXiv:1001.4744].

[37] G. Hinshaw *et al.* [WMAP Collaboration], "*Nine-Year Wilkinson Microwave Anisotropy Probe (WMAP) Observations: Cosmological Parameter Results*," Astrophys. J. Suppl. **208** (2013) 19 [arXiv:1212.5226].

[38] A. Mennella *et al.*, "*Planck pre-launch status: Low Frequency Instrument calibration and expected scientific performance*," Astron. Astrophys. **520** (2010) A5 [arXiv:1001.4562].

[39] P. A. R. Ade *et al.* [Planck Collaboration], "*Planck Early Results XVIII: The power spectrum of cosmic infrared background anisotropies*," Astron. Astrophys. **536** (2011) A18 [arXiv:1101.2028].

[40] P. A. R. Ade *et al.* [Planck Collaboration], "*Planck 2013 results. I. Overview of products and scientific results*," Astron. Astrophys. **571** (2014) A1 [arXiv:1303.5062].

[41] P. A. R. Ade *et al.* [Planck Collaboration], "*Planck 2013 results. XVI. Cosmological parameters*," Astron. Astrophys. **571** (2014) A16 [arXiv:1303.5076].

[42] R. Adam *et al.* [Planck Collaboration], "*Planck 2015 results. I. Overview of products and scientific results*," [arXiv:1502.01582].

[43] P. A. R. Ade *et al.* [Planck Collaboration], "*Planck 2015 results. XIII. Cosmological parameters*," [arXiv:1502.01589].

[44] S. R. Coleman and J. Mandula, "*All Possible Symmetries of the S Matrix*," Phys. Rev. **159** (1967) 1251.

[45] R. Haag, J. T. Lopuszanski and M. Sohnius, "*All Possible Generators of Supersymmetries of the s Matrix*," Nucl. Phys. B **88** (1975) 257.

[46] L. Girardello and M. T. Grisaru, "*Soft Breaking of Supersymmetry*," Nucl. Phys. B **194** (1982) 65.

[47] A. H. Chamseddine, R. L. Arnowitt and P. Nath, "*Locally Supersymmetric Grand Unification*," Phys. Rev. Lett. **49** (1982) 970.

[48] R. Barbieri, S. Ferrara and C. A. Savoy, "*Gauge Models with Spontaneously Broken Local Supersymmetry*," Phys. Lett. B **119** (1982) 343.

[49] L. E. Ibanez, "*Locally Supersymmetric SU(5) Grand Unification*," Phys. Lett. B **118** (1982) 73.

[50] L. J. Hall, J. D. Lykken and S. Weinberg, "*Supergravity as the Messenger of Supersymmetry Breaking*," Phys. Rev. D **27** (1983) 2359.

[51] N. Ohta, "*Grand Unified Theories Based On Local Supersymmetry*," Prog. Theor. Phys. **70** (1983) 542.

[52] J. R. Ellis, D. V. Nanopoulos and K. Tamvakis, "*Grand Unification in Simple Supergravity*," Phys. Lett. B **121** (1983) 123.

[53] L. Alvarez-Gaume, J. Polchinski and M. B. Wise, "*Minimal Low-Energy Supergravity*," Nucl. Phys. B **221** (1983) 495.

[54] M. Dine and W. Fischler, "*A Phenomenological Model of Particle Physics Based on Supersymmetry*," Phys. Lett. B **110** (1982) 227.

[55] C. R. Nappi and B. A. Ovrut, "*Supersymmetric Extension of the SU(3) x SU(2) x U(1) Model*," Phys. Lett. B **113** (1982) 175.

[56] L. Alvarez-Gaume, M. Claudson and M. B. Wise, "*Low-Energy Supersymmetry*," Nucl. Phys. B **207** (1982) 96.

[57] M. Dine and A. E. Nelson, "*Dynamical supersymmetry breaking at low-energies*," Phys. Rev. D **48** (1993) 1277 [hep-ph/9303230].

[58] M. Dine, A. E. Nelson and Y. Shirman, "*Low-energy dynamical supersymmetry breaking simplified*," Phys. Rev. D **51** (1995) 1362 [hep-ph/9408384].

[59] M. Dine, A. E. Nelson, Y. Nir and Y. Shirman, "*New tools for low-energy dynamical supersymmetry breaking*," Phys. Rev. D **53** (1996) 2658 [hep-ph/9507378].

[60] V. A. Rubakov and M. E. Shaposhnikov, "*Do We Live Inside a Domain Wall?*," Phys. Lett. B **125** (1983) 136.

[61] V. A. Rubakov and M. E. Shaposhnikov, "*Extra Space-Time Dimensions: Towards a Solution to the Cosmological Constant Problem*," Phys. Lett. B **125** (1983) 139.

[62] L. Randall and R. Sundrum, "*A Large mass hierarchy from a small extra dimension*," Phys. Rev. Lett. **83** (1999) 3370 [hep-ph/9905221].

[63] L. Randall and R. Sundrum, "*An Alternative to compactification*," Phys. Rev. Lett. **83** (1999) 4690 [hep-th/9906064].

[64] E. A. Mirabelli and M. E. Peskin, "*Transmission of supersymmetry breaking from a four-dimensional boundary*," Phys. Rev. D **58** (1998) 065002 [hep-th/9712214].

[65] D. E. Kaplan, G. D. Kribs and M. Schmaltz, "*Supersymmetry breaking through transparent extra dimensions*," Phys. Rev. D **62** (2000) 035010 [hep-ph/9911293].

[66] Z. Chacko, M. A. Luty, A. E. Nelson and E. Ponton, "*Gaugino mediated supersymmetry breaking*," JHEP **0001** (2000) 003 [hep-ph/9911323].

[67] M. Schmaltz and W. Skiba, "*Minimal gaugino mediation*," Phys. Rev. D **62** (2000) 095005 [hep-ph/0001172].

[68] M. Schmaltz and W. Skiba, "*The Superpartner spectrum of gaugino mediation*," Phys. Rev. D **62** (2000) 095004 [hep-ph/0004210].

[69] L. Randall and R. Sundrum, "*Out of this world supersymmetry breaking*," Nucl. Phys. B **557** (1999) 79 [hep-th/9810155].

[70] G. F. Giudice, M. A. Luty, H. Murayama and R. Rattazzi, "*Gaugino mass without singlets*," JHEP **9812** (1998) 027 [hep-ph/9810442].

[71] J. R. Ellis and S. Rudaz, "*Search for Supersymmetry in Toponium Decays*," Phys. Lett. B **128** (1983) 248.

[72] G. Aad *et al.* [ATLAS Collaboration], "*Summary of the searches for squarks and gluinos using* $\sqrt{s} = 8$ *TeV pp collisions with the ATLAS experiment at the LHC*," JHEP **1510** (2015) 054 [arXiv:1507.05525].

[73] CMS Supersymmetry Physics Results, https://twiki.cern.ch/twiki/bin/view/CMSPublic/PhysicsResultsSUS.

[74] W. Beenakker, R. Höpker, and M. Spira, "*PROSPINO: A Program for the production of supersymmetric particles in next-to-leading order QCD*," [hep-ph/9611232]. See http://www.thphys.uni-heidelberg.de/~plehn/index.php?show=prospino or http://tiger.web.psi.ch/prospino/, 1996.

[75] C. Borschensky, M. Krämer, A. Kulesza, M. Mangano, S. Padhi, T. Plehn and X. Portell, "*Squark and gluino production cross sections in pp collisions at* $\sqrt{s} = 13, 14, 33$ *and 100 TeV*," Eur. Phys. J. C **74** (2014) 12, 3174 [arXiv:1407.5066].

[76] W. Beenakker, M. Klasen, M. Kramer, T. Plehn, M. Spira and P. M. Zerwas, "*The Production of charginos / neutralinos and sleptons at hadron colliders*," Phys. Rev. Lett. **83** (1999) 3780 [Phys. Rev. Lett. **100** (2008) 029901] [hep-ph/9906298].

[77] M. Spira, "*Higgs and SUSY particle production at hadron colliders*," [hep-ph/0211145].

[78] T. Plehn, "*Measuring the MSSM Lagrangean*," Czech. J. Phys. **55** (2005) B213 [hep-ph/0410063].

[79] G. Bozzi, B. Fuks and M. Klasen, "*Transverse-momentum resummation for slepton-pair production at the CERN LHC*," Phys. Rev. D **74** (2006) 015001 [hep-ph/0603074].

[80] G. Bozzi, B. Fuks and M. Klasen, "*Threshold Resummation for Slepton-Pair Production at Hadron Colliders*," Nucl. Phys. B **777** (2007) 157 [hep-ph/0701202].

[81] G. Bozzi, B. Fuks and M. Klasen, "*Joint resummation for slepton pair production at hadron colliders*," Nucl. Phys. B **794** (2008) 46 [arXiv:0709.3057].

[82] J. Debove, B. Fuks and M. Klasen, "*Transverse-momentum resummation for gaugino-pair production at hadron colliders*," Phys. Lett. B **688** (2010) 208 [arXiv:0907.1105].

[83] J. Debove, B. Fuks and M. Klasen, "*Threshold resummation for gaugino pair production at hadron colliders*," Nucl. Phys. B **842** (2011) 51 [arXiv:1005.2909].

[84] J. Debove, B. Fuks and M. Klasen, "*Joint Resummation for Gaugino Pair Production at Hadron Colliders*," Nucl. Phys. B **849** (2011) 64 [arXiv:1102.4422].

[85] B. Fuks, M. Klasen, D. R. Lamprea and M. Rothering, "*Gaugino production in proton-proton collisions at a center-of-mass energy of 8 TeV*," JHEP **1210** (2012) 081 [arXiv:1207.2159].

[86] B. Fuks, M. Klasen, D. R. Lamprea and M. Rothering, "*Precision predictions for electroweak superpartner production at hadron colliders with Resummino*," Eur. Phys. J. C **73** (2013) 2480 [arXiv:1304.0790].

[87] D. Lamprea, M. Rothering: Resummino, an open-source code providing resummation predictions for Beyond the Standard Model particle production at hadron colliders up to the NLO+NLL level, http://www.resummino.org.

[88] H. P. Nilles, "*Supersymmetry, Supergravity and Particle Physics*," Phys. Rept. **110** (1984) 1.

[89] H. E. Haber and G. L. Kane, "*The Search for Supersymmetry: Probing Physics Beyond the Standard Model*," Phys. Rept. **117** (1985) 75.

[90] G. L. Kane and J. P. Leveille, "*Experimental Constraints on Gluino Masses and Supersymmetric Theories*," Phys. Lett. B **112** (1982) 227.

[91] P. R. Harrison and C. H. Llewellyn Smith, "*Hadroproduction of Supersymmetric Particles*," Nucl. Phys. B **213** (1983) 223 [Nucl. Phys. B **223** (1983) 542].

[92] E. Reya and D. P. Roy, "*SUPERSYMMETRIC PARTICLE PRODUCTION AT p anti-p COLLIDER ENERGIES*," Phys. Rev. D **32** (1985) 645.

[93] S. Dawson, E. Eichten and C. Quigg, "*Search for Supersymmetric Particles in Hadron - Hadron Collisions*," Phys. Rev. D **31** (1985) 1581.

[94] H. Baer and X. Tata, "*Component Formulae for Hadroproduction of Left-handed and Right-handed Squarks*," Phys. Lett. B **160** (1985) 159.

[95] W. Beenakker, R. Hopker, M. Spira and P. M. Zerwas, "*Squark production at the Tevatron*," Phys. Rev. Lett. **74** (1995) 2905 [hep-ph/9412272].

[96] W. Beenakker, R. Hopker, M. Spira and P. M. Zerwas, "*Gluino pair production at the Tevatron*," Z. Phys. C **69** (1995) 163 [hep-ph/9505416].

[97] W. Beenakker, R. Hopker, M. Spira and P. M. Zerwas, "*Squark and gluino production at hadron colliders*," Nucl. Phys. B **492** (1997) 51 [hep-ph/9610490].

[98] W. Beenakker, M. Kramer, T. Plehn, M. Spira and P. M. Zerwas, "*Stop production at hadron colliders*," Nucl. Phys. B **515** (1998) 3 [hep-ph/9710451].

[99] G. Bozzi, B. Fuks and M. Klasen, "*Non-diagonal and mixed squark production at hadron colliders*," Phys. Rev. D **72** (2005) 035016 [hep-ph/0507073].

[100] A. T. Alan, K. Cankocak and D. A. Demir, "*Squark pair production in the MSSM with explicit CP violation*," Phys. Rev. D **75** (2007) 095002 [Phys. Rev. D **76** (2007) 119903] [hep-ph/0702289].

[101] S. Bornhauser, M. Drees, H. K. Dreiner and J. S. Kim, "*Electroweak contributions to squark pair production at the LHC*," Phys. Rev. D **76** (2007) 095020 [arXiv:0709.2544].

[102] W. Hollik, M. Kollar and M. K. Trenkel, "*Hadronic production of top-squark pairs with electroweak NLO contributions*," JHEP **0802** (2008) 018 [arXiv:0712.0287].

[103] W. Hollik and E. Mirabella, "*Squark anti-squark pair production at the LHC: The Electroweak contribution*," JHEP **0812** (2008) 087 [arXiv:0806.1433].

[104] W. Hollik, E. Mirabella and M. K. Trenkel, "*Electroweak contributions to squark-gluino production at the LHC*," JHEP **0902** (2009) 002 [arXiv:0810.1044].

[105] E. Mirabella, "*NLO electroweak contributions to gluino pair production at hadron colliders*," JHEP **0912** (2009) 012 [arXiv:0908.3318].

[106] J. Germer, W. Hollik, E. Mirabella and M. K. Trenkel, "*Hadronic production of squark-squark pairs: The electroweak contributions*," JHEP **1008** (2010) 023 [arXiv:1004.2621].

[107] J. Germer, W. Hollik and E. Mirabella, "*Hadronic production of bottom-squark pairs with electroweak contributions*," JHEP **1105** (2011) 068 [arXiv:1103.1258].

[108] J. Germer, W. Hollik, J. M. Lindert and E. Mirabella, "*Top-squark pair production at the LHC: a complete analysis at next-to-leading order*," JHEP **1409** (2014) 022 [arXiv:1404.5572].

[109] A. Kulesza and L. Motyka, "*Threshold resummation for squark-antisquark and gluino-pair production at the LHC*," Phys. Rev. Lett. **102** (2009) 111802 [arXiv:0807.2405].

[110] A. Kulesza and L. Motyka, "*Soft gluon resummation for the production of gluino-gluino and squark-antisquark pairs at the LHC*," Phys. Rev. D **80** (2009) 095004 [arXiv:0905.4749].

[111] W. Beenakker, S. Brensing, M. Krämer, A. Kulesza, E. Laenen and I. Niessen, "*Soft-gluon resummation for squark and gluino hadroproduction*," JHEP **0912** (2009) 041 [arXiv:0909.4418].

[112] W. Beenakker, S. Brensing, M. Krämer, A. Kulesza, E. Laenen and I. Niessen, "*Supersymmetric top and bottom squark production at hadron colliders*, JHEP **1008** (2010) 098 [arXiv:1006.4771].

[113] W. Beenakker, S. Brensing, M. Krämer, A. Kulesza, E. Laenen, L. Motyka and I. Niessen, "*Squark and Gluino Hadroproduction*," Int. J. Mod. Phys. A **26** (2011) 2637 [arXiv:1105.1110].

[114] C. W. Bauer, S. Fleming and M. E. Luke, "*Summing Sudakov logarithms in B —> X(s gamma) in effective field theory*," Phys. Rev. D **63** (2000) 014006 [hep-ph/0005275].

[115] C. W. Bauer, S. Fleming, D. Pirjol and I. W. Stewart, "*An Effective field theory for collinear and soft gluons: Heavy to light decays*," Phys. Rev. D **63** (2001) 114020 [hep-ph/0011336].

[116] C. W. Bauer and I. W. Stewart, "*Invariant operators in collinear effective theory*," Phys. Lett. B **516** (2001) 134 [hep-ph/0107001].

[117] C. W. Bauer, D. Pirjol and I. W. Stewart, "*Soft collinear factorization in effective field theory*," Phys. Rev. D **65** (2002) 054022 [hep-ph/0109045].

[118] M. Beneke, A. P. Chapovsky, M. Diehl and T. Feldmann, "*Soft collinear effective theory and heavy to light currents beyond leading power*," Nucl. Phys. B **643** (2002) 431 [hep-ph/0206152].

[119] M. Beneke and T. Feldmann, "*Multipole expanded soft collinear effective theory with non-Abelian gauge symmetry*," Phys. Lett. B **553** (2003) 267 [hep-ph/0211358].

[120] R. J. Hill and M. Neubert, "*Spectator interactions in soft collinear effective theory*," Nucl. Phys. B **657** (2003) 229 [hep-ph/0211018].

[121] T. Becher, A. Broggio and A. Ferroglia, "*Introduction to Soft-Collinear Effective Theory*," [arXiv:1410.1892].

[122] M. Beneke, P. Falgari and C. Schwinn, "*Threshold resummation for pair production of coloured heavy (s)particles at hadron colliders*," Nucl. Phys. B **842** (2011) 414 [arXiv:1007.5414].

[123] P. Falgari, C. Schwinn and C. Wever, "*NLL soft and Coulomb resummation for squark and gluino production at the LHC*," JHEP **1206** (2012) 052 [arXiv:1202.2260].

[124] U. Langenfeld and S. O. Moch, "*Higher-order soft corrections to squark hadro-production*," Phys. Lett. B **675** (2009) 210 [arXiv:0901.0802].

[125] U. Langenfeld, "*Threshold Improved QCD Corrections for Stop-Antistop production at Hadron colliders*," JHEP **1107** (2011) 052 [arXiv:1011.3341].

[126] U. Langenfeld, S. O. Moch and T. Pfoh, "*QCD threshold corrections for gluino pair production at hadron colliders*," JHEP **1211** (2012) 070 [arXiv:1208.4281].

[127] A. Broggio, A. Ferroglia, M. Neubert, L. Vernazza and L. L. Yang, "*Approximate NNLO Predictions for the Stop-Pair Production Cross Section at the LHC*," JHEP **1307** (2013) 042 [arXiv:1304.2411].

[128] M. Beneke, M. Czakon, P. Falgari, A. Mitov and C. Schwinn, "*Threshold expansion of the gg(qq-bar) —> QQ-bar + X cross section at O(alpha(s)**4)*," Phys. Lett. B **690** (2010) 483 [arXiv:0911.5166].

[129] W. Beenakker, S. Brensing, M. Kramer, A. Kulesza, E. Laenen and I. Niessen, "*NNLL resummation for squark-antisquark pair production at the LHC*," JHEP **1201** (2012) 076 [arXiv:1110.2446].

[130] T. Pfoh, "*Phenomenology of QCD threshold resummation for gluino pair production at NNLL*," JHEP **1305** (2013) 044 [JHEP **1310** (2013) 090] [arXiv:1302.7202].

[131] W. Beenakker *et al.*, "*Towards NNLL resummation: hard matching coefficients for squark and gluino hadroproduction*," JHEP **1310** (2013) 120 [arXiv:1304.6354].

[132] A. Broggio, A. Ferroglia, M. Neubert, L. Vernazza and L. L. Yang, "*NNLL Momentum-Space Resummation for Stop-Pair Production at the LHC*," JHEP **1403** (2014) 066 [arXiv:1312.4540].

[133] M. Beneke, P. Falgari, J. Piclum, C. Schwinn and C. Wever, "*Higher-order soft and Coulomb corrections to squark and gluino production at the LHC*," PoS RADCOR **2013** (2013) 051 [arXiv:1312.0837].

[134] M. Beneke, P. Falgari, J. Piclum, C. Schwinn and C. Wever, "*Higher-order soft and Coulomb corrections to squark and gluino production at the LHC*," PoS LL **2014** (2014) 060.

[135] P. Falgari, C. Schwinn and C. Wever, "*Finite-width effects on threshold corrections to squark and gluino production*," JHEP **1301** (2013) 085 [arXiv:1211.3408].

[136] K. Hagiwara and H. Yokoya, "*Bound-state effects on gluino-pair production at hadron colliders*," JHEP **0910** (2009) 049 [arXiv:0909.3204].

[137] M. R. Kauth, J. H. Kühn, P. Marquard and M. Steinhauser, "*Gluinonia: Energy Levels, Production and Decay*," Nucl. Phys. B **831** (2010) 285 [arXiv:0910.2612].

[138] M. R. Kauth, J. H. Kühn, P. Marquard and M. Steinhauser, "*Gluino Pair Production at the LHC: The Threshold*," Nucl. Phys. B **857** (2012) 28 [arXiv:1108.0361].

[139] M. R. Kauth, A. Kress and J. H. Kühn, "*Gluino-Squark Production at the LHC: The Threshold*," JHEP **1112** (2011) 104 [arXiv:1108.0542].

[140] W. Beenakker, C. Borschensky, M. Krämer, A. Kulesza, E. Laenen, V. Theeuwes and S. Thewes, "*NNLL resummation for squark and gluino production at the LHC*," JHEP **1412** (2014) 023 [arXiv:1404.3134].

[141] W. Beenakker, C. Borschensky, R. Heger, M. Krämer, A. Kulesza and E. Laenen, "*NNLL resummation for stop pair-production at the LHC*," [arXiv:1601.02954].

[142] W. Beenakker, C. Borschensky, M. Krämer, A. Kulesza, E. Laenen, S. Marzani and J. Rojo, "*NLO+NLL squark and gluino production cross-sections with threshold-improved parton distributions*," Eur. Phys. J. C **76** (2016) 2, 53 [arXiv:1510.00375].

[143] C. D. White, "*An Introduction to Webs*," J. Phys. G **43** (2016) 3, 033002 [arXiv:1507.02167].

[144] F. Bloch and A. Nordsieck, "*Note on the Radiation Field of the electron*," Phys. Rev. **52** (1937) 54.

[145] T. Kinoshita, "*Mass singularities of Feynman amplitudes*," J. Math. Phys. **3** (1962) 650.

[146] T. D. Lee and M. Nauenberg, "*Degenerate Systems and Mass Singularities*," Phys. Rev. **133** (1964) B1549.

[147] R. Brock *et al.* [CTEQ Collaboration], "*Handbook of perturbative QCD: Version 1.0*," Rev. Mod. Phys. **67** (1995) 157.

[148] G. Luisoni and S. Marzani, "*QCD resummation for hadronic final states*," J. Phys. G **42** (2015) 10, 103101 [arXiv:1505.04084].

[149] L. D. Landau, "*On analytic properties of vertex parts in quantum field theory*," Nucl. Phys. **13** (1959) 181.

[150] S. Coleman and R. E. Norton, "*Singularities in the physical region*," Nuovo Cim. **38** (1965) 438.

[151] G. F. Sterman, "*An Introduction to quantum field theory*," Cambridge University Press (1994).

[152] S. D. Drell and T. M. Yan, "*Massive Lepton Pair Production in Hadron-Hadron Collisions at High-Energies*," Phys. Rev. Lett. **25** (1970) 316 [Phys. Rev. Lett. **25** (1970) 902].

[153] G. Altarelli, R. K. Ellis and G. Martinelli, "*Large Perturbative Corrections to the Drell-Yan Process in QCD*," Nucl. Phys. B **157** (1979) 461.

[154] M. Aicher, "*Threshold Resummation Effects on the Parton Distribution Function of the Pion and Time-Reversal-Odd Single-Spin Asymmetries*," PhD thesis (2011).

[155] T. O. Eynck, "*Soft gluons and hard scales in QCD – Heavy quarks at finite and all orders*," PhD thesis (2003).

[156] G. F. Sterman, "*Summation of Large Corrections to Short Distance Hadronic Cross-Sections*," Nucl. Phys. B **281** (1987) 310.

[157] S. Catani and L. Trentadue, "*Resummation of the QCD Perturbative Series for Hard Processes*," Nucl. Phys. B **327** (1989) 323.

[158] N. Kidonakis, G. Oderda and G. F. Sterman, "*Threshold resummation for dijet cross-sections*," Nucl. Phys. B **525** (1998) 299 [hep-ph/9801268].

[159] H. Contopanagos, E. Laenen and G. F. Sterman, "*Sudakov factorization and resummation*," Nucl. Phys. B **484** (1997) 303 [hep-ph/9604313].

[160] H. Jones, "*Groups, Representations and Physics*," Adam Hilger (1990).

[161] W. Fulton, "*Young Tableaux*," Cambridge University Press (1997).

[162] M. Czakon, A. Mitov and G. F. Sterman, "*Threshold Resummation for Top-Pair Hadroproduction to Next-to-Next-to-Leading Log*," Phys. Rev. D **80** (2009) 074017 [arXiv:0907.1790].

[163] N. Kidonakis, G. Oderda and G. F. Sterman, "*Evolution of color exchange in QCD hard scattering*," Nucl. Phys. B **531** (1998) 365 [hep-ph/9803241].

[164] N. Kidonakis and G. F. Sterman, "*Resummation for QCD hard scattering*," Nucl. Phys. B **505** (1997) 321 [hep-ph/9705234].

[165] S. Forte and G. Ridolfi, "*Renormalization group approach to soft gluon resummation*," Nucl. Phys. B **650**, 229 (2003) [hep-ph/0209154].

[166] S. Catani, M. L. Mangano, P. Nason and L. Trentadue, "*The Resummation of soft gluons in hadronic collisions*," Nucl. Phys. B **478** (1996) 273 [hep-ph/9604351].

[167] R. Bonciani, S. Catani, M. L. Mangano and P. Nason, "*NLL resummation of the heavy quark hadroproduction cross-section*," Nucl. Phys. B **529** (1998) 424 [Nucl. Phys. B **803** (2008) 234] [hep-ph/9801375].

[168] M. Beneke, P. Falgari and C. Schwinn, "*Soft radiation in heavy-particle pair production: All-order colour structure and two-loop anomalous dimension*," Nucl. Phys. B **828** (2010) 69 [arXiv:0907.1443].

[169] V. S. Fadin, V. A. Khoze and T. Sjöstrand, "*On the Threshold Behavior of Heavy Top Production*," Z. Phys. C **48** (1990) 613.

[170] W. k. Kwong, "*Threshold production of $t\bar{t}$ pairs by e^+e^- collisions*," Phys. Rev. D **43** (1991) 1488.

[171] M. J. Strassler and M. E. Peskin, "*The Heavy top quark threshold: QCD and the Higgs*," Phys. Rev. D **43** (1991) 1500.

[172] E. E. Salpeter and H. A. Bethe, "*A Relativistic equation for bound state problems*," Phys. Rev. **84** (1951) 1232.

[173] M. Beneke, A. Signer and V. A. Smirnov, "*Top quark production near threshold and the top quark mass*," Phys. Lett. B **454** (1999) 137 [hep-ph/9903260].

[174] A. Pineda and A. Signer, "*Heavy Quark Pair Production near Threshold with Potential Non-Relativistic QCD*," Nucl. Phys. B **762** (2007) 67 [hep-ph/0607239].

[175] Y. Kiyo, J. H. Kuhn, S. Moch, M. Steinhauser and P. Uwer, "*Top-quark pair production near threshold at LHC*," Eur. Phys. J. C **60** (2009) 375 [arXiv:0812.0919].

[176] M. Beneke, Y. Kiyo and K. Schuller, "*Third-order Coulomb corrections to the S-wave Green function, energy levels and wave functions at the origin*," Nucl. Phys. B **714** (2005) 67 [hep-ph/0501289].

[177] D. Graudenz, M. Hampel, A. Vogt and C. Berger, "*The Mellin transform technique for the extraction of the gluon density*," Z. Phys. C **70** (1996) 77 [hep-ph/9506333].

[178] G. Parisi and R. Petronzio, "*Small Transverse Momentum Distributions in Hard Processes*," Nucl. Phys. B **154** (1979) 427.

[179] G. Curci and M. Greco, "*Large Infrared Corrections in QCD Processes*," Phys. Lett. B **92** (1980) 175.

[180] G. Curci and M. Greco, "*Soft Corrections to the Drell-Yan Process in QCD*," Phys. Lett. B **102** (1981) 280.

[181] D. Appell, G. F. Sterman and P. B. Mackenzie, "*Soft Gluons and the Normalization of the Drell-Yan Cross-section*," Nucl. Phys. B **309** (1988) 259.

[182] E. Laenen, J. Smith and W. L. van Neerven, "*All order resummation of soft gluon contributions to heavy quark production in hadron hadron collisions*," Nucl. Phys. B **369** (1992) 543.

[183] E. Laenen, J. Smith and W. L. van Neerven, "*Top quark production cross-section*," Phys. Lett. B **321** (1994) 254 [hep-ph/9310233].

[184] H. Contopanagos and G. F. Sterman, "*Principal value resummation*," Nucl. Phys. B **419** (1994) 77 [hep-ph/9310313].

[185] L. Alvero and H. Contopanagos, "*Nonleading logarithms in principal value resummation*," Nucl. Phys. B **436** (1995) 184 [hep-ph/9407293].

[186] H. Contopanagos, L. Alvero and G. F. Sterman, "*Principal value resummation for dilepton production*," [hep-ph/9408393].

[187] L. Alvero and H. Contopanagos, "*The Dilepton production cross-section in principal value resummation*," Nucl. Phys. B **456** (1995) 497 [hep-ph/9411294].

[188] L. Alvero, "*Nonperturbative corrections to the dilepton cross-section*," [hep-ph/9412335].

[189] E. L. Berger and H. Contopanagos, "*Perturbative gluon resummation of the top quark production cross-section*," Phys. Lett. B **361** (1995) 115 [hep-ph/9507363].

[190] E. L. Berger and H. Contopanagos, "*The Perturbative resummed series for top quark production in hadron reactions*," Phys. Rev. D **54** (1996) 3085 [hep-ph/9603326].

[191] A. Kulesza, G. F. Sterman and W. Vogelsang, "*Joint resummation in electroweak boson production*," Phys. Rev. D **66** (2002) 014011 [hep-ph/0202251].

[192] Y. L. Dokshitzer, "*Calculation of the Structure Functions for Deep Inelastic Scattering and e+ e- Annihilation by Perturbation Theory in Quantum Chromodynamics.*," Sov. Phys. JETP **46** (1977) 641 [Zh. Eksp. Teor. Fiz. **73** (1977) 1216].

[193] V. N. Gribov and L. N. Lipatov, "*Deep inelastic e p scattering in perturbation theory*," Sov. J. Nucl. Phys. **15** (1972) 438 [Yad. Fiz. **15** (1972) 781].

[194] G. Altarelli and G. Parisi, "*Asymptotic Freedom in Parton Language*," Nucl. Phys. B **126** (1977) 298.

[195] A. Vogt, "*Efficient evolution of unpolarized and polarized parton distributions with QCD-PEGASUS*," Comput. Phys. Commun. **170** (2005) 65 [hep-ph/0408244].

[196] https://twiki.cern.ch/twiki/bin/view/LHCPhysics/SUSYCrossSections

[197] M. Kramer, A. Kulesza, R. van der Leeuw, M. Mangano, S. Padhi, T. Plehn and X. Portell, "*Supersymmetry production cross sections in pp collisions at* $\sqrt{s} = 7$ *TeV*," [arXiv:1206.2892].

[198] http://lhapdf.hepforge.org.

[199] http://pauli.uni-muenster.de/~akule_01/nllwiki/index.php/NLL-fast

[200] J. Pumplin, D. R. Stump, J. Huston, H. L. Lai, P. M. Nadolsky and W. K. Tung, "*New generation of parton distributions with uncertainties from global QCD analysis*," JHEP **0207** (2002) 012 [hep-ph/0201195].

[201] P. M. Nadolsky, H. L. Lai, Q. H. Cao, J. Huston, J. Pumplin, D. Stump, W. K. Tung and C.-P. Yuan, "*Implications of CTEQ global analysis for collider observables*," Phys. Rev. D **78** (2008) 013004 [arXiv:0802.0007].

[202] D. Alves *et al.* [LHC New Physics Working Group Collaboration], "*Simplified Models for LHC New Physics Searches*," J. Phys. G **39** (2012) 105005 [arXiv:1105.2838].

[203] J. Pumplin, D. Stump, R. Brock, D. Casey, J. Huston, J. Kalk, H. L. Lai and W. K. Tung, "*Uncertainties of predictions from parton distribution functions. 2. The Hessian method*," Phys. Rev. D **65** (2001) 014013 [hep-ph/0101032].

[204] L. Del Debbio *et al.* [NNPDF Collaboration], "*Unbiased determination of the proton structure function F(2)**p with faithful uncertainty estimation*," JHEP **0503** (2005) 080 [hep-ph/0501067].

[205] L. Del Debbio *et al.* [NNPDF Collaboration], "*Neural network determination of parton distributions: The Nonsinglet case*," JHEP **0703** (2007) 039 [hep-ph/0701127].

[206] R. D. Ball *et al.* [NNPDF Collaboration], "*A Determination of parton distributions with faithful uncertainty estimation*," Nucl. Phys. B **809** (2009) 1 [Nucl. Phys. B **816** (2009) 293] [arXiv:0808.1231].

[207] M. Bonvini *et al.*, "*Parton distributions with threshold resummation*," JHEP **1509** (2015) 191 [arXiv:1507.01006].

[208] R. D. Ball *et al.*, "*Parton distributions with LHC data*," Nucl. Phys. B **867** (2013) 244 [arXiv:1207.1303].

[209] G. Aad *et al.* [ATLAS Collaboration], "*Summary of the ATLAS experiment's sensitivity to supersymmetry after LHC Run 1 — interpreted in the phenomenological MSSM*," JHEP **1510** (2015) 134 [arXiv:1508.06608].

[210] V. Khachatryan *et al.* [CMS Collaboration], "*Search for Physics Beyond the Standard Model in Events with Two Leptons, Jets, and Missing Transverse Momentum in pp Collisions at sqrt(s) = 8 TeV*," JHEP **1504** (2015) 124 [arXiv:1502.06031].

[211] [CMS Collaboration], "*Projected Performance of an Upgraded CMS Detector at the LHC and HL-LHC: Contribution to the Snowmass Process*," [arXiv:1307.7135.].

[212] V. M. Theeuwes, "*Soft Gluon Resummation for Heavy Particle Production at the Large Hadron Collider*," PhD thesis (2015).

[213] J. Beringer *et al.* [Particle Data Group Collaboration], "*Review of Particle Physics (RPP)*," Phys. Rev. D **86** (2012) 010001.

[214] R. Heger, master's thesis (2016).

[215] S. S. AbdusSalam, B. C. Allanach, H. K. Dreiner, J. Ellis, U. Ellwanger, J. Gunion, S. Heinemeyer and M. Kraemer *et al.*, "*Benchmark Models, Planes, Lines and Points for Future SUSY Searches at the LHC*," Eur. Phys. J. C **71** (2011) 1835 [arXiv:1109.3859].

[216] K. Hagiwara, Y. Sumino and H. Yokoya, "*Bound-state Effects on Top Quark Production at Hadron Colliders*," Phys. Lett. B **666** (2008) 71 [arXiv:0804.1014].

[217] M. Beneke, P. Falgari, S. Klein and C. Schwinn, "*Hadronic top-quark pair production with NNLL threshold resummation*," Nucl. Phys. B **855** (2012) 695 [arXiv:1109.1536].

[218] T. Akesson *et al.* [Axial Field Spectrometer Collaboration], "*Double Parton Scattering in pp Collisions at* $\sqrt{s}$ = 63-*GeV*," Z. Phys. C **34** (1987) 163.

[219] J. Alitti *et al.* [UA2 Collaboration], "*A Study of multi - jet events at the CERN anti-p p collider and a search for double parton scattering*," Phys. Lett. B **268** (1991) 145.

[220] F. Abe *et al.* [CDF Collaboration], "*Study of four jet events and evidence for double parton interactions in* $p\bar{p}$ *collisions at* $\sqrt{s}$ = 1.8 *TeV*," Phys. Rev. D **47** (1993) 4857.

[221] F. Abe *et al.* [CDF Collaboration], "*Measurement of double parton scattering in* $\bar{p}p$ *collisions at* $\sqrt{s}$ = 1.8 *TeV*," Phys. Rev. Lett. **79** (1997) 584.

[222] F. Abe *et al.* [CDF Collaboration], "*Double parton scattering in $\bar{p}p$ collisions at $\sqrt{s} = 1.8TeV$*," Phys. Rev. D **56** (1997) 3811.

[223] V. M. Abazov *et al.* [D0 Collaboration], "*Double parton interactions in γ+3 jet events in pp^- bar collisions $\sqrt{s} = 1.96$ TeV.*," Phys. Rev. D **81** (2010) 052012 [arXiv:0912.5104].

[224] G. Aad *et al.* [ATLAS Collaboration], "*Measurement of hard double-parton interactions in $W(\rightarrow lv)$+ 2 jet events at $\sqrt{s}$=7 TeV with the ATLAS detector*," New J. Phys. **15** (2013) 033038 [arXiv:1301.6872].

[225] G. Aad *et al.* [ATLAS Collaboration], "*Measurement of the production cross section of prompt J/ψ mesons in association with a $W^{\pm}$ boson in pp collisions at $\sqrt{s} = 7$ TeV with the ATLAS detector*," JHEP **1404** (2014) 172 [arXiv:1401.2831].

[226] R. Aaij *et al.* [LHCb Collaboration], "*Observation of double charm production involving open charm in pp collisions at $\sqrt{s} = 7$ TeV*," JHEP **1206** (2012) 141 [JHEP **1403** (2014) 108] [arXiv:1205.0975].

[227] V. M. Abazov *et al.* [D0 Collaboration], "*Observation and studies of double J/ψ production at the Tevatron*," Phys. Rev. D **90** (2014) 11, 111101 [arXiv:1406.2380].

[228] S. Bansal *et al.*, "*Progress in Double Parton Scattering Studies*," [arXiv:1410.6664].

[229] C. H. Kom, A. Kulesza and W. J. Stirling, "*Prospects for observation of double parton scattering with four-muon final states at LHCb*," Eur. Phys. J. C **71** (2011) 1802 [arXiv:1109.0309].

[230] R. Aaij *et al.* [LHCb Collaboration], "*Observation of J/ψ pair production in pp collisions at $\sqrt{s} = 7TeV$*," Phys. Lett. B **707** (2013) 52 [arXiv:1109.0963].

[231] V. Khachatryan *et al.* [CMS Collaboration], "*Measurement of prompt J/ψ pair production in pp collisions at $\sqrt{s} = 7$ Tev*," JHEP **1409** (2014) 094 [arXiv:1406.0484].

[232] C. H. Chang, "*Hadronic Production of J/ψ Associated With a Gluon*," Nucl. Phys. B **172** (1980) 425.

[233] R. Baier and R. Ruckl, "*Hadronic Production of J/psi and Upsilon: Transverse Momentum Distributions*," Phys. Lett. B **102** (1981) 364.

[234] R. Baier and R. Ruckl, "*Hadronic Collisions: A Quarkonium Factory*," Z. Phys. C **19** (1983) 251.

[235] G. T. Bodwin, E. Braaten and G. P. Lepage, "*Rigorous QCD analysis of inclusive annihilation and production of heavy quarkonium*," Phys. Rev. D **51** (1995) 1125 [Phys. Rev. D **55** (1997) 5853] [hep-ph/9407339].

[236] J. P. Lansberg and H. S. Shao, "*Production of $J/\psi+\eta_c$ versus $J/\psi+J/\psi$ at the LHC: Importance of Real α_s^5 Corrections*," Phys. Rev. Lett. **111** (2013) 122001 [arXiv:1308.0474].

[237] J. P. Lansberg and H. S. Shao, "*J/ψ-Pair Production at Large Momenta: Indications for Double Parton Scatterings and Large α_s^5 Contributions*," Phys. Lett. B **751** (2015) 479 [arXiv:1410.8822].

[238] R. Li, Y. J. Zhang and K. T. Chao, "*Pair Production of Heavy Quarkonium and B(c)(*) Mesons at Hadron Colliders*," Phys. Rev. D **80** (2009) 014020 [arXiv:0903.2250].

[239] J. M. Campbell, F. Maltoni and F. Tramontano, "*QCD corrections to J/psi and Upsilon production at hadron colliders*," Phys. Rev. Lett. **98** (2007) 252002 [hep-ph/0703113].

[240] B. Gong, X. Q. Li and J. X. Wang, "*QCD corrections to J / psi production via color octet states at Tevatron and LHC*," Phys. Lett. B **673** (2009) 197 Erratum: [Phys. Lett. **693** (2010) 612] [arXiv:0805.4751].

[241] M. Butenschoen and B. A. Kniehl, "*Reconciling J/ψ production at HERA, RHIC, Tevatron, and LHC with NRQCD factorization at next-to-leading order*," Phys. Rev. Lett. **106** (2011) 022003 [arXiv:1009.5662].

[242] Y. Q. Ma, K. Wang and K. T. Chao, "*$J/\psi(\psi')$ production at the Tevatron and LHC at $\mathcal{O}(\alpha_s^4 v^4)$ in nonrelativistic QCD*," Phys. Rev. Lett. **106** (2011) 042002 [arXiv:1009.3655].

[243] V. A. Khoze, A. D. Martin, M. G. Ryskin and W. J. Stirling, "*Inelastic J/ψ and υ hadroproduction*," Eur. Phys. J. C **39** (2005) 163 [hep-ph/0410020].

[244] P. Artoisenet, J. P. Lansberg and F. Maltoni, "*Hadroproduction of J/ψ and υ in association with a heavy-quark pair*," Phys. Lett. B **653** (2007) 60 [hep-ph/0703129].

[245] P. Artoisenet, J. M. Campbell, J. P. Lansberg, F. Maltoni and F. Tramontano, "*Υ Production at Fermilab Tevatron and LHC Energies*," Phys. Rev. Lett. **101** (2008) 152001 [arXiv:0806.3282].

[246] S. J. Brodsky and J. P. Lansberg, "*Heavy-Quarkonium Production in High Energy Proton-Proton Collisions at RHIC*," Phys. Rev. D **81** (2010) 051502 [arXiv:0908.0754].

[247] R. Aaij *et al.* [LHCb Collaboration], "*Measurement of J/ψ production in pp collisions at $\sqrt{s}$ = 7 TeV*," Eur. Phys. J. C **71** (2011) 1645 [arXiv:1103.0423].

[248] G. Aad *et al.* [ATLAS Collaboration], "*Measurement of the differential cross-sections of inclusive, prompt and non-prompt J/ψ production in proton-proton collisions at $\sqrt{s}$ = 7 TeV*," Nucl. Phys. B **850** (2011) 387 [arXiv:1104.3038].

[249] V. Khachatryan *et al.* [CMS Collaboration], "*Prompt and non-prompt J/ψ production in pp collisions at $\sqrt{s}$ = 7 TeV*," Eur. Phys. J. C **71** (2011) 1575 [arXiv:1011.4193].

[250] D. Acosta *et al.* [CDF Collaboration], "*Measurement of the J/ψ meson and b−hadron production cross sections in $p\bar{p}$ collisions at $\sqrt{s}$ = 1960 GeV*," Phys. Rev. D **71** (2005) 032001 [hep-ex/0412071].

[251] M. Bahr *et al.*, "*Herwig++ Physics and Manual*," Eur. Phys. J. C **58** (2008) 639 [arXiv:0803.0883].

[252] R. Aaij *et al.* [LHCb Collaboration], "*Measurement of forward J/ψ production cross-sections in pp collisions at $\sqrt{s}$ = 13 TeV*," JHEP **1510** (2015) 172 [arXiv:1509.00771].

[253] J. R. Gaunt, "*Single Perturbative Splitting Diagrams in Double Parton Scattering*," JHEP **1301** (2013) 042 [arXiv:1207.0480].

[254] J. R. Gaunt, R. Maciula and A. Szczurek, "*Conventional versus single-ladder-splitting contributions to double parton scattering production of two quarkonia, two Higgs bosons and $c\bar{c}c\bar{c}$*," Phys. Rev. D **90** (2014) 5, 054017 [arXiv:1407.5821].

[255] B. Blok, Y. Dokshitzer, L. Frankfurt and M. Strikman, "*Perturbative QCD correlations in multi-parton collisions*," Eur. Phys. J. C **74** (2014) 2926 [arXiv:1306.3763].

[256] G. Sterman and M. Zeng, "*Quantifying Comparisons of Threshold Resummations*," JHEP **1405** (2014) 132 [arXiv:1312.5397].

[257] L. G. Almeida, S. D. Ellis, C. Lee, G. Sterman, I. Sung and J. R. Walsh, "*Comparing and counting logs in direct and effective methods of QCD resummation*," JHEP **1404** (2014) 174 [arXiv:1401.4460].

[258] M. Bonvini, S. Forte, G. Ridolfi and L. Rottoli, "*Resummation prescriptions and ambiguities in SCET vs. direct QCD: Higgs production as a case study*," JHEP **1501** (2015) 046 [arXiv:1409.0864].

[259] M. Bonvini, S. Forte, M. Ghezzi and G. Ridolfi, "*The scale of soft resummation in SCET vs perturbative QCD*," Nucl. Phys. Proc. Suppl. **241-242** (2013) 121 [arXiv:1301.4502].

[260] M. Bonvini, S. Forte, M. Ghezzi and G. Ridolfi, "*Threshold Resummation in SCET vs. Perturbative QCD: An Analytic Comparison*," Nucl. Phys. B **861** (2012) 337 [arXiv:1201.6364].

[261] M. Bonvini and L. Rottoli, "*Three loop soft function for N^3LL' gluon fusion Higgs production in soft-collinear effective theory*," Phys. Rev. D **91** (2015) 5, 051301 [arXiv:1412.3791].

[262] V. Ahrens, A. Ferroglia, M. Neubert, B. D. Pecjak and L. L. Yang, "*Renormalization-Group Improved Predictions for Top-Quark Pair Production at Hadron Colliders*," JHEP **1009** (2010) 097 [arXiv:1003.5827].

[263] N. Kidonakis, E. Laenen, S. Moch and R. Vogt, "*Sudakov resummation and finite order expansions of heavy quark hadroproduction cross-sections*," Phys. Rev. D **64** (2001) 114001 [hep-ph/0105041].

[264] S. Catani, D. de Florian, M. Grazzini and P. Nason, "*Soft gluon resummation for Higgs boson production at hadron colliders*," JHEP **0307** (2003) 028 [hep-ph/0306211].

Acknowledgements

At the end of this thesis, I would like to thank everyone who helped and supported me throughout my time as a PhD student.

My special thanks go to my supervisor Anna Kulesza. I am grateful to her for giving me the possibility to work on my PhD thesis in Münster. Her door was always open for questions, and the input and suggestions that she gave me regarding my work were always very useful. She guided me through many stages of becoming a better researcher.

I would also like to thank Michael Klasen for agreeing to be my second examiner.

I thank the members of the institute as a whole for the pleasant atmosphere, in particular the secretaries Anne and Katharina who were always extremely helpful whenever I needed something or had a general question.

Many thanks go to my friends from Münster who made my time at and outside of the institute much more enjoyable. In random order: Marcel, for regularly distracting me from work and also for the very useful discussions about resummation, especially towards the end of my time at the institute; David, for teaching me a little bit of Spanish and daily providing a random fact about mathematics; Florian, for always letting me decide on the route of the hiking trips; Vincent, for being a great office mate and bringing me Dutch cookies; Christian, for the jokes; Pietro, for discussing world affairs while eating pizza; Sonja and Manuel, for convincing me to go swimming; Moritz and Peter (together with Sonja and Manuel), for the jam sessions at the top of the institute; Saskia, for lending me her notes about statistical physics; and also to everyone else who I forgot to mention!

Additionally, I want to thank Eric Laenen for the stay at NIKHEF. His discussions about infrared singularities and resummation helped my understanding a lot, and I enjoyed the atmosphere in the Netherlands. I also thank the rest of the "resummation gang," Michael Krämer and Wim Beenakker, for the fruitful meetings and discussions.

Without the constant encouragement from my family, this work would not have been possible. Therefore, a lot of thanks go to my family (including Fido) and Alejandra, for enduring my bad mood whenever I was stressed, and for the nice words that always cheered me up, even from far (~500 km) and very far (~8000 km) away.

Lebenslauf

Persönliche Daten

Name: Christoph Julian Borschensky
Geburtsdatum und -ort: 03. Februar 1988 in Offenburg
Staatsangehörigkeit: deutsch

Studium

Seit Oktober 2012	**Promotion in Physik** *Precision Calculations for Coloured Supersymmetric Particle Production at the Large Hadron Collider* Betreuerin: Jun. Prof. Dr. Anna Kulesza, Institut für Theoretische Physik Westfälische Wilhelms-Universität (WWU) Münster
Februar 2011 – Februar 2012	**Diplomarbeit** *Einschränkungen an Annihilationsprozesse dunkler Materie aus dem seltenen $B_s \to \mu^+\mu^-$-Zerfall im Minimalen Supersymmetrischen Standardmodell* Betreuer: Prof. Dr. Ulrich Nierste, Institut für Theoretische Teilchenphysik Karlsruher Institut für Technologie (KIT), ehemals Universität Karlsruhe
Oktober 2006 – März 2012	**Physik-Studium, Abschluss: Diplom** Karlsruher Institut für Technologie (KIT), ehemals Universität Karlsruhe

Schulausbildung

Juni 2006	**Abitur**
September 1998 – Juni 2006	**Oken-Gymnasium** Offenburg
September 1994 – Juli 1998	**Grundschule Griesheim** Offenburg

Berufstätigkeit

Oktober 2012 – März 2016	**Wissenschaftlicher Mitarbeiter** Institut für Theoretische Physik, WWU Münster
April 2012 – September 2012	**Wissenschaftliche Hilfskraft** Institut für Angewandte und Numerische Mathematik, KIT
Januar 2011 – März 2012	**Studentische Hilfskraft** Institut für Angewandte und Numerische Mathematik, KIT

Münster, den 29. März 2016